Time-lapse super-resolution imaging reveals key principles for cis-limited Xist RNA localisation



Lisa Rodermund

St. Anne's College

University of Oxford

Supervised by

Prof. Neil Brockdorff

Dr. Lothar Schermelleh

Dr. Heather Coker

Submitted: Michaelmas Term 2020

A thesis submitted for the degree of

Doctor of Philosophy Biochemistry

Acknowledgements

My heartfelt gratitude goes to my supervisors Professor Neil Brockdorff and Dr. Lothar Schermelleh for their ongoing support, expertise and guidance. Their passion and brilliance have kept me inspired, motivated and engaged throughout the entire project. Secondly, I would like to thank my day-to-day supervisor Heather Coker for her patience, reassurance, and generous sharing of her vast scientific knowledge and practical skills. She showed me that there was a solution to every problem, and kind-heartedly took over every single chromatin TRIzol extraction when I succumbed to my fear of needles. Many thanks also to Roel Oldenkamp, without whose problem-solving skills and creativity the set-up of the image analysis workflow would have been impossible. I am extremely grateful to Guifeng Wei for his important and generous support performing computational analyses of the chromatin RNA sequencing and SLAM-seq data. Moreover, I would like to thank Joseph Bowness and Guifeng Wei for the generation of the SPOC mut cell line. My whole-hearted thanks go to Tatyana Nesterova, who has inspired me with her passionate work ethic, for her supportive scientific and practical advice. I would like to express my gratitude to both the Brockdorff and the Schermelleh group for the many fruitful scientific discussions, constructive feedback, and many outings, which have made my time in Oxford special.

Warmest thanks also to my thesis committee members Prof. David Sherratt and Dr. Alfredo Castello, who have accompanied the project with valuable advice and scientific input. They were able to look at the project from a different angle, when it

was most needed. Finally, I would like to thank Prof. Edith Heard and Prof. Rob Klose for taking the time to examine this thesis.

In addition, I would like to acknowledge a number of people, who have picked me up when times were hard and made the easy times even more enjoyable. I would like to thank my brother Luca for his unwavering support. From helping me move to Oxford despite just having undergone surgery to writing our theses in solidarity during a global pandemic – I knew he was always just a phone call away. I am also extremely grateful to my partner Konstantinos for enduring the many late nights of image processing, being the best lockdown companion (fb) and always having an open ear and open mind, scientifically and personally. I would like to thank my parents, Birgit and Erik, for their constant encouragement and especially for gifting me my first microscope and sparking my interest in biology twenty years ago. Many thanks also to my grandparents Lilo and Lothar for always supporting my educational career. I am grateful to have been part of the St. Anne's MCR, which has given me a sense of community, and where I have formed many important friendships and found my lovely housemates of three years, Antje, Nicole and Gabi. Finally, I would like to mention my nocturnal and furry buddy Hippo, who has cheered me up countless times.

Table of contents

Acknowledgements 2

Table of figures 7

Abbreviations 9

Abstract 13

1 Introduction 14

1.1 Overview 14

1.2 Features of the Xi 17

1.2.1 Chromatin features 17

1.2.2 Chromosome structure 19

1.3 XCI is driven by Xist RNA 21

1.3.1 Regulation of Xist expression 22

1.3.2 *Cis*-limited Xist RNA localisation 26

1.3.3 Xist mediated silencing of the Xi 34

1.4 CIZ-1 role in XCI and Xist localisation 38

1.5 Xist RNA silencing factor SPEN 42

1.6 Imaging RNA 47

1.7 Aims 52

2 Methods 53

2.1 Generation of cell lines 53

2.1.1 Tissue culture 55

2.1.2 ChrX ES cell line 56

2.1.3 Autosomal transgene ES cell line 58

2.1.4 Ciz-1 KO ES cell line 59

2.1.5 SPEN RRM del ES cell line 61

2.1.6 SPOC mut ES cell line 62

2.1.7 PCR screen of gDNA and agarose gel analysis 64

2.1.8 NPC derivation 66

2.2 Xist RNA FISH 68

2.2.1 FISH probe preparation and agarose gel 68

2.2.2 RNA FISH for scoring 69

2.2.3 RNA FISH for 3D-SIM 70

2.3 Fluorescence staining 72

2.3.1 Immunofluorescence staining 72

2.3.2 HaloTag staining 73

2.4 3D-SIM 75

2.4.1 Acquisition 75

2.4.2 Reconstruction 75

2.4.3 Alignment 76

2.5 Live cell imaging 77

2.5.1 3D-SIM live cell imaging 77

2.5.2 PALM-TIRF single particle tracking ... 77
2.6 RNA-SPLIT (Sequential Pulse Localisation Imaging over Time) ... 79
2.6.1 Sample preparation ... 79
2.6.2 Nascent Xist RNA dynamics ... 80
2.6.3 Xist turnover on chromatin ... 80
2.6.4 Image analysis workflow ... 81
2.6.5 Dual colour control ... 85
2.6.6 Dox washout experiment ... 85
2.7 SLAM-seq ... 87
2.7.1 Sample preparation ... 87
2.7.2 Data Analysis ... 90
2.8 Chromatin RNA sequencing to assess silencing ... 91
2.8.1 Sample preparation ... 91
2.8.2 Data analysis ... 92
2.9 Western blot ... 94
2.10 Southern blot ... 96
2.11 Statistical analysis ... 100
3 Super-resolution RNA-SPLIT – a new method to assess RNA dynamics and localisation ... 101
3.1 Bgl-stem-loop tagging of Xist RNA in combination with HaloTag technology and 3D-SIM allows for detection of individual Xist foci ... 101
3.1.1 Generation and characterisation of the ChrX ES cell line ... 101
3.1.2 Generation and characterisation of the autosomal transgene ES cell line ... 110
3.2 Live imaging to investigate Xist RNA dynamics ... 115
3.3 Development of RNA-SPLIT as an alternative approach to live imaging ... 120
3.4 Xist RNA stability is defined by its chromatin environment and rate of transcription ... 125
3.5 Newly transcribed Xist spreads in 3D from the transcription site towards the periphery of the Xi territory ... 135
3.6 The Xist transcription site relocates from the centre of the Xi territory towards the periphery over time ... 138
3.7 Coupling of newly transcribed Xist with previously bound Xist ... 142
3.8 Summary: Fundamental principles of Xist spreading revealed ... 148
4 Application of RNA-SPLIT to investigate Xist dynamics and behaviour in Ciz-1 knockout cells ... 156
4.1 CRISPR mediated knockout of ClZ-1 in BglG-Halo-Xist mESCs ... 156
4.2 KO of ClZ-1 has a minor effect on Xist localisation in mESCs ... 160
4.3 Xist dynamics are largely unaffected in Ciz-1 KO mESCs ... 164
4.4 Xist coupling is unaffected in Ciz-1 KO mESCs ... 167
4.5 Xist is fully delocalised in Ciz-1 KO NPCs ... 169

4.6 Minimal effects on silencing in Ciz-1 KO NPCs 173

4.7 Xist transcription is increased in Ciz-1 KO NPCs 176

4.8 Xist coupling is evident in NPCs and is independent of Xist localisation to the X chromosome in Ciz-1 KO cells 180

4.9 Summary: New insights into the role of CIZ-1 in Xist localisation and dynamics 183

5 SPEN plays a key role in Xist localisation, dynamics and coupling 190

5.1 Generation of SPEN RRM deletion in BglG-Halo-Xist mESCs 190

5.2 Generation of SPEN SPOC domain mutations in BglG-Halo-Xist mESCs 194

5.3 SPEN plays an important role in Xist localisation 197

5.4 Perturbation of SPEN binding to Xist leads to increased Xist transcription and decreased stability 201

5.5 SPEN binding to Xist but not SPOC domain function is essential for Xist coupling 205

5.6 Summary: SPEN plays a SPOC domain independent key role in Xist localisation, dynamics and coupling 209

6 Discussion 216

6.1 RNA-SPLIT – a powerful tool to study Xist RNA behaviour 217

6.2 *Cis*-limited localisation of Xist RNA 222

6.3 New insights into Xist RNA kinetics 231

6.4 Xist RNA spreading across the Xi 237

6.5 About the curious phenomenon of Xist coupling 240

References 245

Table of figures

Figure 1: Organisation of the inactive X chromosome. 18
Figure 2: Xist gene regulation 24
Figure 3: The Xist repeats A-F and cis-limited Xist localisation 28
Figure 4: Xist RNA spreading 31
Figure 5: The Xist repeats A-F and Xist-mediated gene silencing 36
Figure 6: Generation of XX mESCs with inducible endogenous BglG-Halo-Xist. 104
Figure 7: Bgl-stem-loop tagging of Xist in combination with HaloTag technology and 3D-SIM allows for visualisation of single Xist foci 107
Figure 8: Insertion of the Bgl-stem-loop array does not alter Xist functionality 109
Figure 9: Generation of XY mESCs with inducible autosomal transgenic BglG-Halo-Xist on chromosome 15. 112
Figure 10: Xist molecule number and induction efficiency of ChrX and autosomal transgene cells during expansion and steady state. 113
Figure 11: Live cell imaging of BglG-Halo-Xist. 117
Figure 12: RNA-SPLT – a new method to assess RNA localisation and dynamics. 122
Figure 13: Xist RNA stability determined by RNA-SPLIT varies depending on stage of XCI and chromatin environment. 126
Figure 14: Validation of RNA-SPLIT by SLAM-seq 129
Figure 15: Xist RNA stability is defined by its rate of transcription. 133
Figure 16: RNA-SPLIT reveals 3D spreading behaviour of Xist during expansion. 136
Figure 17: The Xist TS relocates towards the periphery of the Xi territory over time in ChrX cells. 139
Figure 18: The Xist TS relocates towards the centre of the Xi territory over time in autosomal transgene cells. 141
Figure 19: RNA-SPLIT shows that newly synthesised Xist couples with pre-synthesised Xist 144
Figure 20: Generation of Ciz-1 KO mESCs. 157
Figure 21: Xist is efficiently induced and Xist-mediated transcriptional silencing is unaffected in Ciz-1 KO cells. 159
Figure 22: Perturbation of CIZ-1 has a minor effect on Xist localisation in mESCs. 161
Figure 23: Xist dynamics are largely unaffected in Ciz-1 KO mESCs. 165
Figure 24: Xist coupling is unaffected in Ciz-1 KO mESCs. 168
Figure 25: Differentiation of WT and Ciz-1 KO mESCs into NPCs. 170
Figure 26: Xist is fully delocalised in Ciz-1 KO NPCs. 172
Figure 27: Ciz-1 KO NPCs show no H2AK119ub1 enrichment on the Xi, but with no significant defect in X chromosomal silencing 174
Figure 28: Xist transcription dynamics and stability in WT and Ciz-1 KO NPCs assessed by RNA-SPLIT. 178

Figure 29: Xist coupling occurs in WT and Ciz-1 KO NPCs. 181
Figure 30: Generating a SPEN RRM deletion. 191
Figure 31: SPEN RRM del cells display a major silencing defect and slightly decreased induction efficiency.....192
Figure 32: Generating and characterising SPOC mut mESCs 195
Figure 33: Analysis of Xist localisation in SPEN RRM del and SPOC mut cells.....198
Figure 34: Perturbation of SPEN binding to Xist affects Xist expression and density. 200
Figure 35: SPEN RRM del but not SPOC mut cells show increased Xist RNA transcription.....202
Figure 36: SPEN RRM del but not SPOC mut cells show significantly decreased Xist RNA stability. 204
Figure 37: Deletion of the SPEN RRM domains but not mutation of the SPOC domain leads to abrogated Xist coupling.....206
Figure 38: CIZ-1 and SPEN play a role in cis-limited Xist localisation. 226
Figure 39: A novel promoter-independent feedback mechanism regulates Xist stability in response to Xist transcription rates throughout XCI.....234
Figure 40: Model of Xist spreading in WT mESCs and upon perturbation of SPEN. 238
Figure 41: Model of coupling of newly synthesised and pre-synthesised Xist molecules. 242

Abbreviations

3D-SIM – 3D structured illumination microscopy

AU-rich elements; AREs – adenylate-uridylate-rich elements

CHART – capture hybridisation analysis of RNA targets

ChIP – chromatin immunoprecipitation

CIZ-1 – Cip1-interacting zinc finger protein 1

CRISPR – clustered regularly interspaced short palindromic repeats

EZH2 – enhancer of zeste homolog 2

FISH – fluorescence in situ hybridisation

FRAP – fluorescence recovery after photobleaching

gDNA – genomic DNA

HDAC – histone deacetylase

hnRNPU – heterogenous nuclear ribonucleoprotein U

iCLIP – individual-nucleotide resolution cross-linking and immunoprecipitation

Jarid2 – jumonji, AT rich interacting domain 2

KO – knock out

LBR – lamin B receptor

LINE1 – long interspersed nuclear elements 1

m6A – N6-Methyladenosine

MCN – modulation contrast

MCNR – modulation contrast-to-noise ratio

MEFs – mouse embryonic fibroblasts

mESC – mouse embryonic stem cells

METTL3 – N6-adenosine-methyltransferase 70 kDa subunit

N-CoR – nuclear co-repressor complex

NEAT-1 – nuclear paraspeckle assembly transcript 1

NNA – nearest neighbour analysis

NPCs – neural progenitor cells

NuRD – nucleosome remodelling and deacetylase complex

Oct 3/4 – octamer-binding transcription factor 3/4

OTFs – optical transfer functions

PALM/TIRF – photoactivated localisation microscopy/total internal reflection

PBST – PBS, 0.1% Tween

PEFs – primary embryonic fibroblasts

PRC – polycomb repressive complex

PVDF – polyvinylidene difluoride

RAP – RNA antisense purification

Rbm15 – RNA Binding Motif Protein 15

RID – nuclear receptor interaction domain

RIs – refractive indices

RNA-SPLIT – sequential pulse localisation imaging over time

Rnf12 – RING finger 12

RNPs – ribonucleoprotein particles

RRMs – RNA binding domains

SAF-A – scaffold attachment factor A

SDS – sodium dodecyl sulphate

SELEX – selectively evolved by exponential enrichment

sgRNA – single guide RNA

SMCHD1 – structural maintenance of chromosomes flexible hinge domain containing 1

SMRT – silencing mediator of retinoic acid and thyroid hormone receptor

SNPs – single nucleotide polymorphisms

Sox2 – sex determining region Y-box 2

SPEN – split ends

SPEN RRM del – SPEN RRM deletion

SPOC mut – SPOC mutant

SPOC – SPEN paralog and ortholog C-terminal

SRA – steroid receptor RNA activator

STORM – stochastic optical reconstruction microscopy

TAD – topologically associated domain

TS – transcription site

WT – wild type

Xa – active X chromosome

XCI – X chromosome inactivation

Xi – inactive X chromosome elect

Xic – X-chromosome-inactivation centre

Xist – X inactive specific transcript

XR-PID – Xist RNA polycomb interaction domain

YY1 – yin yang 1

Abstract

Dosage compensation in XX female mammals is achieved by X chromosome inactivation (XCI). The key player in this process is the long noncoding RNA Xist (X inactive specific transcript), which associates *in cis* with the inactive X chromosome elect (Xi) to mediate gene silencing and heterochromatization. Xist spreads across the entire Xi, but little is known about the dynamics of this process, particularly in the context of single cells. This thesis documents the development of a new, time-resolved super-resolution imaging methodology: RNA-SPLIT (Sequential Pulse Localisation Imaging over Time) combining Bgl-stem-loop labelling, HaloTag technology and 3D structured illumination microscopy (3D-SIM) to detect individual Xist RNA molecules in single mouse embryonic stem cells (mESC) with high spatial and temporal resolution.

XY and XX mESCs expressing inducible autosomal transgenic or endogenous Bgl-stem-loop tagged Xist in tandem with BglG-Halo fusion protein were used to visualise distinct, functional Xist foci and analyse their spreading behaviour across the Xi during early XCI. RNA-SPLIT yielded important insights into Xist RNA kinetics, localisation and spreading behaviour during XCI and a feedback mechanism linking Xist RNA synthesis and degradation. RNA-SPLIT also uncovered novel coupling behaviour of Xist RNA molecules which, using perturbation experiments with CIZ-1 and SPEN, was shown to be independent of Xist localisation to the Xi, but dependent upon SPEN. In depth analysis demonstrated SPEN to have separable, SPOC domain independent functions in Xist RNA localisation, stability and coupling behaviour.

CHAPTER I

1 Introduction

1.1 Overview

In order to achieve a balanced gene expression in XX females as compared to XY males, different species evolved distinct dosage compensation mechanisms [reviewed by (Disteche 2012)]. To reach X-linked gene dosage compensation in eutherian mammals, one of the X chromosomes in XX female cells is transcriptionally silenced early during embryonic development, normally at random (Lyon 1961) [reviewed by (Graves 2016)]. This complex process is called X chromosome inactivation (XCI). Dosage compensation is essential with failure to achieve XCI being lethal in female embryos [reviewed by (Brockdorff and Turner 2015)]. XCI is not only necessary, but also provides an evolutionary advantage for female mammals: Random XCI creates a mosaic pattern of cells with either the maternal or the paternal X chromosome undergoing XCI, which masks the effect of deleterious mutations and can thereby increase the reproductive fitness (Franco and Ballabio 2006).

Xist (X inactive specific transcript) RNA is indispensable for the process of XCI and is expressed from the future inactive X chromosome (Xi) as XCI is initiated (Brown et al. 1991; Brockdorff et al. 1991; Borsani et al. 1991), eventually spreading to accumulate across the whole length of the Xi elect (Sheardown et al. 1997). Xist RNA initiates transcriptional gene silencing and chromatin remodelling *in cis* by

recruiting epigenetic modifiers, as well as other secondary silencing factors, to the Xi. For a recent review see (Brockdorff, Bowness, and Wei 2020). However, this recruitment of silencing factors is crucial only for the initiation of XCI, since loss of Xist after XCI does not interfere with maintenance of the inactive state (Costanzi et al. 2000; Csankovszki, Nagy, and Jaenisch 2001), suggesting that the stably propagated epigenetic marks are able to maintain transcriptional silencing.

Initiation of random XCI occurs in early female embryos and can be modelled in XX mouse embryonic stem cells (mESCs). In mESCs Xist RNA is repressed, and is then expressed randomly from one of the X chromosomes during differentiation (Wutz and Jaenisch 2000). The choice of which Xist locus gets activated, and therefore of which X chromosome gets inactivated, is stochastic and the probability of inactivation is directly proportional to the X chromosome: ploidy ratio (Monkhorst et al. 2008). In some placental mammals, including mice, there is imprinted XCI during early embryogenesis, with random XCI occurring later in postimplantation embryos [reviewed by (Avner and Heard 2001)]. In imprinted XCI the paternal X chromosome is always inactivated during differentiation of cells that subsequently make up the extra-embryonic tissues (Takagi and Sasaki 1975). When Xist RNA is ectopically expressed in mESCs, X-linked gene silencing can be initiated, but it is reversible during the early differentiation time window (Wutz and Jaenisch 2000).

In summary, the process of XCI can be understood as a coordinated switch of chromatin structure and chromosome organisation initiated by Xist RNA expression and resulting in gene silencing. Once, XCI has occurred, it is irreversible and stably maintained throughout all cell divisions (Wutz and Jaenisch 2000; Jonkers et al.

2008). After spreading of Xist across the Xi a transcriptionally silent nuclear compartment is formed and RNA polymerase II is excluded from the chromatin (Chaumeil et al. 2006). In the mouse, only 3-7% of genes, so called escapees, remain transcriptionally active throughout XCI in a tissue-specific manner (Berletch et al. 2015). The resulting unique chromatin features and chromosome structure of the Xi will be discussed in section 1.2. This project focuses on using super-resolution microscopy to study Xist RNA and the Xist localisation factor Cip1-interacting zinc finger protein 1 (CIZ-1), as well as the Xist interacting silencing factor split ends (SPEN). Hence, Xist RNA gene regulation, *cis*-limited localisation and gene silencing will be introduced in detail in section 1.3, followed by overviews of CIZ-1 and SPEN proteins in sections 1.4 and 1.5, respectively. Finally, different RNA labelling and imaging approaches, which are relevant to the methodology used in this project, are introduced in section 1.6.

1.2 Features of the Xi

The compacted Xi displays some unique chromatin features, such as characteristic histone modifications and 3D chromatin structure. Moreover, it has a distinctive chromosome structure and organisation, which distinguishes it from the active X chromosome (Xa). In fact, the Xi is structurally so distinct that Murray Barr first noticed its existence in 1949 in female cat neurons using only a compound microscope and simple tissue staining (Barr and Bertram 1949). The following section introduces the different features of the Xi.

1.2.1 Chromatin features

The Xi is characterised by the enrichment of histone modifications associated with gene repression, for example H2AK119ub and H3K27me3 catalysed by polycomb repressive complex (PRC)1 and PRC2, respectively (Silva et al. 2003; Plath et al. 2003; de Napoles et al. 2004), and depletion of histone modifications associated with gene activity, for example acetylation of histones H2A, H2B, H3, and H4 (Jeppesen and Turner 1993; Belyaev, Keohane, and Turner 1996). Histone deacetylation on the Xi is achieved, at least in part, by the recruitment of histone deacetylase (HDAC) 3 through the Xist interacting silencing factor SPEN (see section 1.5) (McHugh et al. 2015; Żylicz et al. 2019; Nesterova et al. 2019; Dossin et al. 2020). Other repressive chromatin marks on the Xi include the histone modifications H3K9me2/3 and H4K20me3 (Heard et al. 2001; Kohlmaier et al. 2004), the histone variant macroH2A (Mermoud et al. 1999; Costanzi et al. 2000), and DNA methylation at promotor linked CpG islands of X-linked genes (Norris, Brockdorff, and Rastan 1991). Concurrent with changes to the chromatin

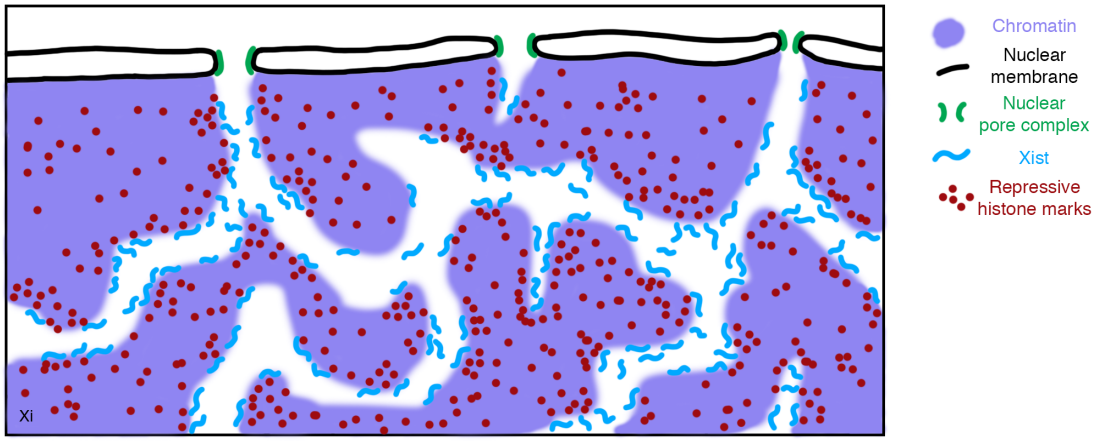

Figure 1: Organisation of the inactive X chromosome. Schematic illustrating the organisation of the Xi including Xist found in the interchromatin channels and repressive histone marks found in the dense chromatin regions.

landscape, RNA polymerase II and associated co-factors are excluded from the Xi chromatin as XCI progresses, accompanied by a loss of nascent transcripts (Chaumeil et al. 2006).

Chromatin compaction of the Xi has been reported to be 1.2-fold higher as compared to the Xa (Naughton et al. 2010; Teller et al. 2011; Giorgetti et al. 2016). In line with this, 3D structured illumination microscopy (SIM) analysis of the Xi has revealed that, while the Xi is more compacted than the Xa, its heterochromatic structure is not entirely compacted and impermeable (Smeets et al. 2014) (Figure 1). Instead, the chromatin is organised in 3D such that interchromatin channels connect to nuclear pores (Smeets et al. 2014) (Figure 1). PRC2-mediated histone modifications were found to be localised to dense chromatin regions, while Xist RNA was found in the interchromatin channels and less dense perichromatin region (Smeets et al. 2014) (Figure 1).

1.2.2 Chromosome structure

Using super-resolution microscopy, DNA fluorescence in situ hybridisation (FISH) and 3C technologies, it has been shown that the Xi forms a separate compartment from the rest of the genome, whose 3D organisation is determined by the formation of transcriptionally active and inactive compartments (Rao et al. 2014; Wang et al. 2016; Lieberman-aiden et al. 2009) [reviewed by (da Rocha and Heard 2017)]. Moreover, escapee genes on the Xi have been found to interact with one another, as well as with active compartments in the rest of the genome (Splinter et al. 2011). In neural progenitor cells (NPCs), escapees have been found preferentially located at the periphery of the Xi territory (Splinter et al. 2011). In addition to being more compacted, it has been shown that the inter-loci distances on the Xi are relatively homogenous (Wang et al. 2016). A similar chromatin folding configuration has been observed in Polycomb-repressed chromatin by super-resolution microscopy (Boettiger et al. 2016).

Hi-C and 3D DNA FISH studies have demonstrated that, while the Xi shows an overall loss of topologically associated domains (TADs), it folds into two mega domains divided by a boundary containing the unusually conserved DXZ4 macrosatellite (Rao et al. 2014; Deng et al. 2015; Giorgetti et al. 2016). This DXZ4 locus contains several CpG island rich tandem repeats and CTCF-binding sites, which are exclusive to the Xi (Chadwick 2008; Horakova et al. 2012; Deng et al. 2015). Deletion of the DXZ4 boundary leads to the loss of the partition of the Xi into the two mega domains and causes massive structural reorganisation (Giorgetti et al. 2016; Darrow et al. 2016). The organisation of the Xi has been shown to be dependent on Xist RNA mediated silencing, since the boundary between the mega

domains disappears upon deletion of the Xist RNA A-repeats, which are essential for its silencing ability (Giorgetti et al. 2016). While deletion of Xist RNA from the already formed Xi leads to a reorganisation of the chromosome conformation resembling that of the Xa, this does not seem to have an effect on the maintenance of gene silencing (Splinter et al. 2011). Hence, both Xist RNA and the CTCF rich DXZ4 locus play an important role in establishing the structure of the Xi [reviewed by (da Rocha and Heard 2017)].

1.3 XCI is driven by Xist RNA

Early studies demonstrated that a genomic region on the X chromosome, referred to as the X-chromosome-inactivation centre (Xic), functions in *cis* to initiate and establish XCI (Allderdice et al. 1978; Rastan 1983). Studies on the human X chromosome narrowed this region to around 1Mb (Brown 1991a), and led to the identification of a candidate gene, XIST (Brown et al. 1991b), which is expressed exclusively from the Xi. Subsequent work identified the mouse homologue, Xist (Brockdorff et al. 1991; Borsani et al. 1991). Other elements within the mouse Xic region, the DXPas34 locus and the Xist antisense gene Tsix were found to be involved in the regulation of Xist expression during XCI (Debrand et al. 1999; J T Lee, Davidow, and Warshawsky 1999; Cohen et al. 2007). Xist gene knock out (KO) and transgene studies demonstrated that Xist RNA is both necessary and sufficient for the initiation of XCI [reviewed by (Avner and Heard 2001; Loda and Heard 2019)]. Interestingly, induction of autosomal Xist transgenes in mESCs can lead to reversible Xist-mediated gene silencing of the chromosome *in cis* (Lee et al. 1996; Lee and Jaenisch 1997; Wutz and Jaenisch 2000), but is less efficient than the silencing on the Xi by endogenous Xist (Tang et al. 2010; Loda et al. 2017).

When XCI is initiated, Xist, which is a 17 kb spliced, polyadenylated and capped long noncoding RNA, is expressed on the Xi elect, and subsequently localises to and spreads across the Xi in *cis* to initiate a cascade of chromatin changes resulting in transcriptional silencing of the Xi (C. J. Brown et al. 1991; Brockdorff et al. 1991; Borsani et al. 1991; Brockdorff et al. 1992; C. J. Brown et al. 1992; Kay et al. 1993). Xist is expressed in all placental mammals and shows a reasonable level of primary

sequence conservation, including in several conserved segments of short tandem repeats, which in subsequent work have been found to confer critical functions (Brown et al. 1992; Brockdorff et al. 1992; Nesterova et al. 2001; Wutz, Rasmussen, and Jaenisch 2002).

Understanding how Xist RNA functions can be reduced to three major questions, which will be discussed in the following sections: How is Xist regulated in development to achieve the silencing of a single chromosome? How is Xist RNA limited to and spreads across a single chromosome territory? How does Xist induce chromatin modifications and gene silencing resulting in XCI? Of note, a seminal study using inducible Xist transgenes with deletions of different regions demonstrated that *cis*-limited localisation of Xist and its silencing function are, at least in part, separable processes (Wutz, Rasmussen, and Jaenisch 2002).

1.3.1 Regulation of Xist expression

Xist expression is tightly regulated. Some important elements that influence Xist expression are located outside of the Xist gene but within the Xic. Examples include the Xist activators Jpx, and Ftx, noncoding RNAs, located 5' of Xist (Tian, Sun, and Lee 2010; Chureau et al. 2011; Nora et al. 2012) (Figure 2). The protein coding RING finger 12 (Rnf12) gene approximately 500 kb upstream of the Xist gene has been shown to activate Xist in a dose-dependent fashion (Jonkers et al. 2009; Barakat et al. 2014) (Figure 2). Key pluripotency factors, such as Nanog, octamer-binding transcription factor (Oct) 3/4, and sex determining region Y-box 2 (Sox2) have been found to bind to the Xist intron 1 in mESCs (Navarro et al. 2008; Schulz et al. 2014) (Figure 2). Mutations of Oct3/4 and Sox2 affecting the binding to Xist

caused the release of Nanog from Xist, as well as ectopic Xist expression (Navarro et al. 2008). This suggests that pluripotency factors cooperatively repress Xist in mESCs (Figure 2).

An important negative regulator of Xist RNA expression is Tsix, a 40 kb long noncoding RNA that is transcribed from the antisense strand, spanning 15kb downstream of Xist and the entire Xist locus itself (Lee, Davidow, and Warshawsky 1999) (Figure 2). Tsix is part of the Xic and its RNA is retained in the nucleus like Xist RNA. In undifferentiated mESCs before XCI, Tsix is expressed biallelically from both X chromosomes (Lee, Davidow, and Warshawsky 1999). However, its expression is switched to monoallelic expression from the Xa when XCI is initiated, from which it maintains high levels of expression until Xist is completely silenced (Lee, Davidow, and Warshawsky 1999). It has been suggested that Tsix regulates Xist expression *in cis* by repressive antisense transcription, which modifies the chromatin environment of the Xist locus, especially of the Xist promoter (Lee and Lu 1999; Luikenhuis, Wutz, and Jaenisch 2001; Stavropoulos, Lu, and Lee 2001). Both KO and overexpression experiments using Xist and Tsix have demonstrated the important influence they have on the probability of each X chromosome initiating XCI [reviewed by (Avner and Heard 2001)]. It has been proposed that a certain threshold set by Tsix has to be overcome by Xist such that XCI can be initiated. In line with this, in cells lacking Tsix RNA a skewing of Xist expression and initiation of XCI towards the mutant X chromosome was found (Lee and Lu 1999; Luikenhuis, Wutz, and Jaenisch 2001). On the other hand, X chromosomes that contain a Tsix locus which is overexpressed, preferentially inactivate the wild type (WT) X chromosome (Luikenhuis, Wutz, and Jaenisch 2001). Thus, Tsix can be understood

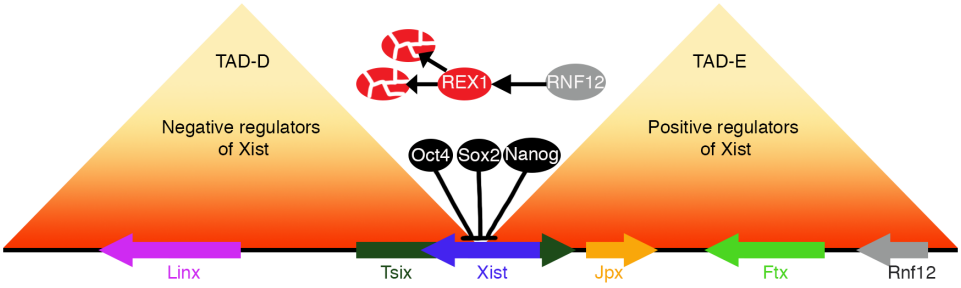

Figure 2: Xist gene regulation. Scheme illustrating positive and negative regulators of the Xist gene, divided into two TADs.

as a negative regulator of Xist *in cis*, not directly affecting silencing, but rather preventing ectopic silencing after the initiation of XCI.

Disruption of Tsix impairs the establishment of repressive epigenetic modifications such as hypomethylation of the Xist locus (Takashi Sado, Hoki, and Sasaki 2005), again suggestive of Xist being regulated by the induction of chromatin structure modifications through Tsix and its transcription. It has been suggested that the Xic locus is in a semi-stable transcriptional state, which predicts the outcome of XCI (Loos et al. 2016). Here, the X-to-autosome ratio is thought to influence these transcriptional states through regulating the nuclear concentration of trans-acting regulators of XCI (Loos et al. 2016). It has been discovered that the promoters of Xist and its positive regulators lie in a distinct TAD adjacent to a second TAD containing the Tsix promoter (Nora et al. 2012; van Bemmel et al. 2019) (Figure 2). Moreover, the promoter of the long noncoding RNA Linx, which is located in the same TAD as Tsix (Nora et al. 2017), has recently been identified as a long range silencer of Xist (Galupa et al. 2020) (Figure 2).

X-encoded regulators of Tsix initiate the dose-dependent repression or activation of Xist RNA expression, whereas other factors suppress Xist expression in a dose

dependent manner to inhibit the onset of XCI. For instance, RNF12 and REX1 have been shown to regulate XCI by repression of Tsix and activation of Xist (Gontan et al. 2012). Rnf12 is located around 500 kb upstream of the Xist gene and encodes the E3 ubiquitin ligase RING finger protein 12 (Jonkers et al. 2009; Gontan et al. 2012) (Figure 2). It has been found to regulate Xist RNA expression by targeting the Xist repressor REX1 for degradation (Gontan et al. 2012) (Figure 2). REX1 has several binding sites on Xist and Tsix RNA in regulatory regions and therefore can act directly as a negative regulator of Xist or indirectly by regulating Tsix (Navarro et al. 2010; Gontan et al. 2012). Degradation of REX1 facilitates binding of yin yang 1 (YY1), which usually competes with REX1 for regulatory binding sites on Xist, activating Xist RNA expression, notably within a major enhancer region located in Xist exon 1 (Makhlouf et al. 2014).

Adding copies of Rnf12 to the genome has been shown to lead to the initiation of XCI in male mESCs and a majority of female mESCs, while a heterozygous KO of Rnf12 in mESCs has been found to cause a reduction of the ability to initiate XCI, suggesting that Rnf12 acts in a dose-dependent fashion in the initiation of XCI (Jonkers et al. 2009). The Rnf12 gene is itself regulated by pluripotency factors, which underlines their impact on Xist and Tsix control in undifferentiated mESCs (Navarro et al. 2011).

Recently, RNF12 has been found to act in two steps: Firstly, two active copies of RNF12 facilitate the initiation of XCI (Barakat et al. 2014), then subsequently, one copy remains active during the maintenance of XCI (Barakat et al. 2014). This

mechanism prevents XCI of both X chromosomes and allows fine-tuning of the process.

1.3.2 *Cis*-limited Xist RNA localisation

Xist RNA has the remarkable ability to localise and spread across a single chromosome *in cis* (Clemson et al. 1996). Early work analysing X autosome translocations led to the idea that an X inactivation signal spreads bidirectionally from the Xic, initially to nearby sites and then progressively to more distant sites (Duthie et al. 1999). Whilst spread of X inactivaiton does occur into autosomal segments, it is apparently less efficient than on the X chromosome (Popova et al. 2006). The idea of progressive bidirectional spread of an inactivating signal was extrapolated to Xist RNA following its discovery (Brockdorff et al. 1992). However, that transgenic Xist expressed from autosomes can localise and induce transcriptional silencing in *cis*, demonstrates that *cis*-limited Xist localisation and functionality does not require sequence specific binding (Lee and Jaenisch 1997).

Xist localisation to a defined nuclear territory is maintained in cells following extensive extraction and digestion of chromatin, suggesting a role for insoluble nuclear proteins referred to as the nuclear matrix (Clemson et al. 1996), and candidate proteins have been identified (see below). Little is known about the mechanism of *in cis* localisation of Xist, its spreading across the Xi and the dynamics of this process. The following sections will elaborate on what is currently known about Xist RNA localisation factors and Xist RNA spreading.

1.3.2.1 Known Xist RNA localisation factors

Several Xist tandem repeats and interacting factors have been implicated in Xist localisation. Firstly, it is known that Xist localises to the nuclear matrix facilitated by nuclear matrix scaffold proteins such as scaffold attachment factor A (SAF-A)/ heterogenous nuclear ribonucleoprotein U (hnRNPU), which has been suggested to anchor the Xist RNA within the Xi territory (Helbig and Fackelmayer 2003; Pullirsch et al. 2010; Hasegawa et al. 2010). RNA cross linking studies suggest hnRNPU binds Xist RNA directly, although this appears to occur broadly across the transcript rather than at specific elements or tandem repeats (Hasegawa et al. 2010; Yamada et al. 2015; Cirillo et al. 2016). 3D-SIM analysis demonstrates colocalization of hnRNPU and Xist RNA within interchromatin spaces, spatially separated from chromatin (Smeets et al. 2014).

In other studies YY1 was proposed to have a function in anchoring Xist to chromatin by binding to the YY1 recognition sites present in Xist exon 1 in the Xist C-repeats (Jeon and Lee 2011). The Xist C-repeat had earlier been suggested to facilitate the binding of Xist RNA to chromatin (Figure 3), since locked nucleic acid targeting, as well as peptide nucleic acid treatment of the C-repeat, had been found to lead to the dissociation of Xist from the Xi (Beletskii et al. 2001; Sarma et al. 2010). Recently, the Xist E-repeats in Exon 7 of Xist have been implicated in the recruitment of CIZ-1, a nuclear matrix protein, which has been shown to tether Xist RNA to the chromatin (Ridings-Figueroa et al. 2017) (see section 1.4 and Figure 3). In line with this, deletion of the E-repeats has been found to cause dispersal of Xist in differentiated cells (Yamada et al. 2015; Sunwoo et al. 2017). Exon 7 has also been suggested to interact with hnRNPU (Yamada et al. 2015).

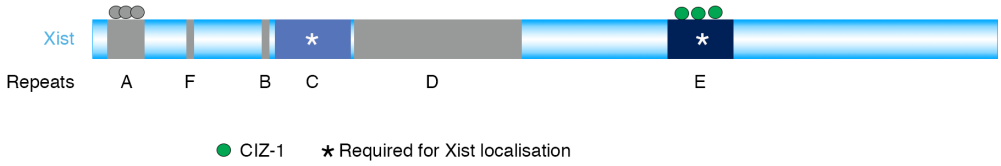

Figure 3: The Xist repeats A-F and *cis*-limited Xist localisation. Scheme illustrating the Xist repeats A-F and indicating repeats required for Xist localisation as well as localisation factor CIZ-1.

Additionally, interaction of Xist with the lamin B receptor (LBR) was implicated in the recruitment of the Xi to the nuclear lamina, modifying chromatin 3D structure in a way that enables the spreading of Xist across actively transcribed genes on the Xi (McHugh et al. 2015; C.-K. Chen et al. 2016). However, deletion of LBR in a different cell line was unable to confirm a role in Xist-mediated gene silencing (Nesterova et al. 2019).

1.3.2.2 Biochemical studies of Xist spreading behaviour

Although experiments using Xist transgenes on autosomes indicate that Xist RNA does not bind to chromatin in an Xi exclusive and sequence specific manner, it has been suggested that Xist RNA binds to high affinity regions with certain properties facilitating the spread across the Xi. Early evidence indicating that the X inactivation signal spreads on autosomes less efficiently than on the Xi led to the proposal that elements on the X chromosome referred to as 'way stations' function to boost the X inactivation signal (Lyon 1998). More recently it has been proposed that long interspersed nuclear elements 1 (LINE1) repeat elements, which are enriched on the X chromosome represent the 'way stations', and that they could function as binding sites for Xist RNA (Lyon 1998). Analysis of active and inactive LINE-1 elements in differentiating mESCs has shown that active LINEs might facilitate local propagation of XCI, while inactive LINEs might aid Xist mediated

heterochromatization (Chow et al. 2010). Related studies by Tang et al. (2010) have shown that gene-rich LINE1 depleted domains on autosomes are more resistant to transcriptional silencing and that gene-poor LINE1 rich domains are more efficiently silenced (Tang et al. 2010). Arguing against LINE1 as Xist RNA binding sites, Xist RNA localisation on the Xi at metaphase specifically excludes LINE1 rich and constitutive heterochromatin regions (Duthie et al. 1999). Additionally, recent biochemical experiments could also not confirm a correlation between Xist binding and LINE1 rich domains (Engreitz et al. 2013).

Whilst evidence shows that LINE1 elements are unlikely to be Xist RNA binding sites, it remains true that autosomes respond to Xist-mediated silencing less efficiently and there is evidence that this can in some cases be due to effects on Xist RNA spreading. Specifically studies examining metaphase chromosomes with X autosome translocations reported attenuated spreading during the initiation of XCI in cells with the T(X;4)37H X;autosome translocation (Popova et al. 2006). Additionally, an insertion of a chromosome 7 region on the Xi chromosome, Is1Ct, results in interruption of Xist RNA coverage of the chromosome (Duthie et al. 1999). These findings suggest that certain autosomal chromatin features may interfere with, or that certain X chromosomal features may facilitate Xist RNA spreading.

Recently, Xist has been suggested to spread across the Xi in 3D following a two-step mechanism, based on capture hybridisation analysis of RNA targets (CHART)-seq data (Simon et al. 2013). Here, Xist spreading targets gene-rich regions first, followed by the spreading of Xist into gene-poor domains (although as discussed above certain LINE1 rich elements are likely to remain free of Xist) (Simon et al.

2013). Furthermore, Xist was found to be depleted from escapees of XCI (Simon et al. 2013). It has also been shown that genes close to the Xic are silenced earlier than more distal genes (Figure 4), and that genes with a lower expression level seemed to be silenced faster than highly expressed genes (Simon et al. 2013). It was therefore proposed that Xist expression related chromatin changes might bring gene-poor regions with genes that are actively transcribed closer to the Xic as XCI progresses, which may in turn actively promote Xist spreading and associated gene silencing. Chromatin immunoprecipitation (ChIP)-seq analysis showed that PRC2 and its associated histone modification H3K27me3 exhibit a very similar pattern to that observed for Xist, since H3K27me3 levels were also higher than average in the gene-rich regions, especially at the promoters and gene bodies of Xi-linked genes (Simon et al. 2013). Hence, PRC2 and Xist RNA might co-migrate across the Xi. These observations do not support a linear spreading model, where Xist RNA and the H3K27me3 mark spread progressively and continuously from the Xic towards both ends of the chromosome. Instead, the CHART-seq results suggest that Xist spreading is a 3D process depending on the chromatin conformation of the Xi (Figure 4). When Xist was stripped off the Xi after XCI had been established, it recovered rapidly in both gene-rich and gene-poor domains within hours (Simon et al. 2013). This result indicates that Xist follows the two step mechanism of spreading only during the initiation of XCI, but spreads rapidly to all regions during the maintenance phase of XCI, likely as a consequence of a more compatible chromatin configuration. This data was based on bulk datasets of mESCs at different stages of differentiation, which are known to display heterogenous dynamics of XCI, raising the question whether similar observations would be made on a single-cell level.

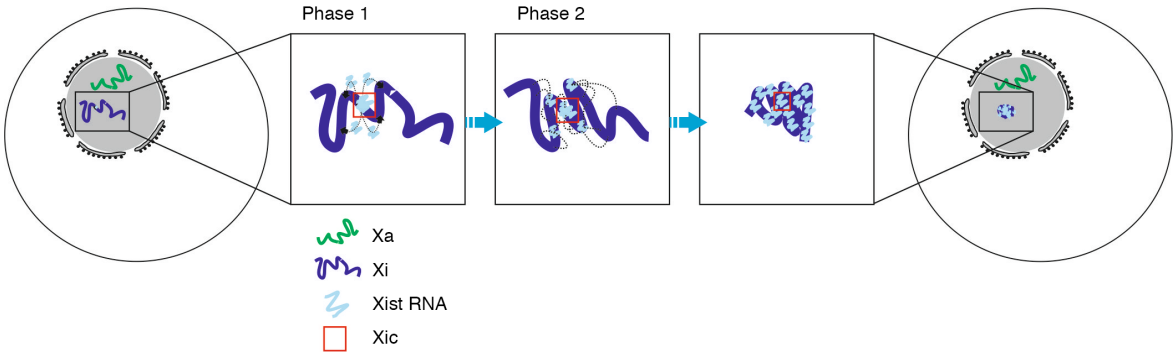

Figure 4: Xist RNA spreading. Schematic illustrating the model of Xist RNA spreading in two phases.

The differentiation time courses conducted in Simon et al 2013 study also did not allow for observation of the very early dynamics of initial Xist spreading across the Xi. This however was addressed in a study that made use of a similar methodology, Xist RNA antisense purification (RAP) (Engreitz et al. 2013). After 1 h of Xist induction in mESCs, a peak of Xist binding was found centred at the locus of Xist transcription (Engreitz et al. 2013). Over time this peak decreased, while Xist levels across the Xi increased and by 6 h the pattern of Xist localisation was similar to that seen in stable XCI (Engreitz et al. 2013). The Xist RAP data also showed that initial Xist binding to these preferred sites strongly correlates with Hi-C data, indicating preferential binding to 3D-proximal sites (Figure 4) (Engreitz et al. 2013). Here, it was suggested that Xist might search for binding sites in 3D, in turn leading to modification of the chromatin structure and making further new regions accessible for Xist to bind (Figure 4). The exact characteristics of Xist binding sites are still not well understood.

In summary, CHART-seq and Xist RAP data suggest a model of Xist spreading in two phases, which involves the localisation of Xist RNA to new sites, potentially through the interaction with nuclear matrix proteins and the chromatin changes connected to Xist-mediated silencing. First, Xist localises to spatially proximal sites

on the periphery of active gene-dense regions, where it establishes Xist-mediated silencing, which relocates these genes into the Xist silenced compartment (Figure 4). This may be achieved through recruitment of proteins such as PRC2. This repositioning brings new regions of active chromatin closer to the Xist transcription locus, which enables Xist RNA to spread to new sites by proximity transfer (Figure 4). Moreover, the biochemical analysis of Xist spreading and binding across the Xi highlights the need for experiments suited to assess the dynamics and spreading of single Xist ribonucleoprotein particles (RNPs) to reveal the fundamental principles of Xist spreading, ideally in single cells.

1.3.2.3 Imaging Xist RNA spreading behaviour

Imaging of Xist RNA in fixed cells has given some insights into how Xist RNA associates with the chromatin of the Xi. During mitosis, mouse Xist RNA dissociates from the Xi and the association is re-established after the restart of transcription during early G1 in the daughter cells (Clemson et al. 1996). Duthie et al (1999) using FISH analysis reported that Xist RNA is retained on Xi at metaphase and that it localises in a banded pattern, which corresponds to gene-rich Giemsa-light chromosome regions (Duthie et al. 1999). The presence of large gaps in these patterns without Xist RNA association already suggested a non-linear spreading model as described above. However, imaging studies of fixed cells, just as well as the above described biochemical studies can only give limited insight into the dynamic behaviour of Xist and its mechanism of spreading, which can only truly be addressed by live cell imaging and studies of single cells.

Initial experiments to assess Xist spreading and dynamics in a live cell setting used GFP-MS2-tagging of an autosomally located Xist transgenes in mouse mESCs and confocal microscopy to image Xist during the cell cycle (Ng et al. 2011). In this autosomal context, Xist was shown to spread from a single point to a steady state, where Xist completely coats the Xi (Ng et al. 2011). Using photobleaching experiments of whole Xist foci, rather than single Xist molecules, Ng et al. observed that the chromosome-bound Xist has a very dynamic turnover with an early recovery already after 30 min if Xist transcription is ongoing (Ng et al. 2011). This points towards an equilibrium of bound Xist lost from the chromatin and new Xist binding in interphase. However, the experiment was conducted after the foci had already stabilized, which does not allow for the assessment of initial Xist spreading, and no interacting proteins were visualised or knocked down. Furthermore, Xist has been shown to spread less efficiently *in cis* on autosomes (Popova et al. 2006), raising the question of how reliably one can draw conclusions about Xist spreading from experiments with inducible Xist transgenes. In addition, the limited resolution of these experiments did not allow for the assessment of single molecule dynamics. Similarly, a recently published paper using the programmable RNA sequence binding domain of the Pumilio protein as RNA tag for live cell imaging could only resolve expansion of entire Xist domains rather than single Xist RNP foci (Ha et al. 2018). Thus, it is important that alternative higher resolution imaging approaches are found or developed to assess Xist dynamics and spreading.

To date, super-resolution studies of Xist have only been conducted in fixed cells. For instance, 3D-SIM has demonstrated that Xist RNA accumulates in the collapsed active nuclear compartment of the Xi in distinct foci which colocalise with SAF-A

(Smeets et al. 2014). The number of Xist foci was found to be variable depending on cell type, but estimated to be less than 100 foci per Xist domain (Smeets et al. 2014), which lies considerably below the estimate of 300 to 1,000 copies of Xist RNA determined by qPCR (Sun, Deaton, and Lee 2006; Buzin, Mann, and Singer-Sam 1994). Equally, stochastic optical reconstruction microscopy (STORM) imaging at 20-nm resolution in individual mouse embryonic fibroblasts (MEFs) has shown that there are only around 50 foci of Xist RNA on the Xi during XCI maintenance, each made up of 1-2 Xist molecules (Sunwoo, Wu, and Lee 2015). Similarly, only around 50 foci of PRC2 were found on the Xi (Sunwoo, Wu, and Lee 2015). Still, application of RNA FISH for these studies has not allowed for the examination of the dynamics of single Xist RNA molecules. Moreover, RNA FISH involves chemical treatment of the cells, which prompts the question as to whether this may affect the chromatin environment and hence the localisation of Xist RNA molecules within it. Thus, high-resolution imaging studies are needed to complement the aforementioned observations in order to obtain a detailed picture of how Xist RNA localises and spreads *in cis*.

1.3.3 Xist mediated silencing of the Xi

Many different proteins involved in chromatin modification, attachment to the nuclear matrix, and RNA remodelling pathways specifically and directly interact with Xist RNA to form a complex RNP, which can initiate XCI. Xist RNA interacts with these different proteins in a developmentally dependent manner to control chromatin changes and silencing. More precisely, it has been suggested that the Xist interacting proteins assemble in a step-wise fashion during differentiation, as

distinct Xist interactors have been identified in pluripotent mESCs as compared to differentiated mESCs (Chu et al. 2015). This might mean that certain proteins representing the ground state Xist-interactome remain associated with Xist during both pluripotency and differentiation, while other proteins associate selectively with Xist upon differentiation.

Xist RNA provides binding sites for its many different interactors through several conserved segments of short tandem repeats, labelled A to F in mouse Xist, each conferring different functions (Brown et al. 1992; Brockdorff et al. 1992; Nesterova et al. 2001; Wutz, Rasmussen, and Jaenisch 2002) (Figure 5). Deletion analysis of different Xist RNA segments has shown that the A-repeats, which interact with the essential silencing factor SPEN (see section 1.5) and the N6-Methyladenosine (m6A) machinery, are necessary for Xist-mediated gene silencing (Wutz, Rasmussen, and Jaenisch 2002; Patil et al. 2016; Lu et al. 2016) (Figure 5).

In addition to the A-repeat, an Xist RNA polycomb interaction domain (XR-PID) has been identified as a region encompassing the Xist B-repeats and at least part of the C-repeats (Pintacuda et al. 2017; Nesterova et al. 2019; Bousard et al. 2019) (Figure 5). When the XR-PID is deleted, no polycomb group proteins are recruited to the Xi by Xist RNA, leading to loss of the repressive histone modifications H2AK119ub and H3K27me3 on the Xi, and hence a silencing defect (Pintacuda et al. 2017; Nesterova et al. 2019; Bousard et al. 2019). These findings built on a report showing that a larger deletion spanning the Xist B and F-repeats abrogates the recruitment of jumonji, AT rich interacting domain (Jarid) 2, a PRC2 co-factor which mediates Xist-induced PRC2 targeting (Rocha et al. 2014). HnrnpK has been

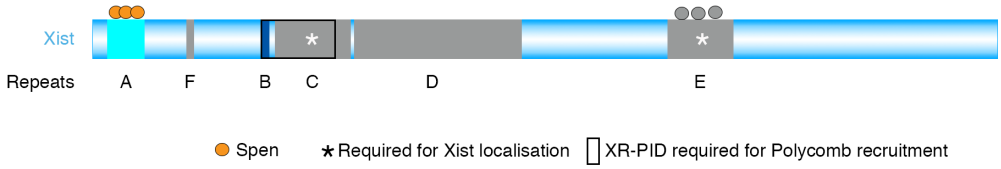

Figure 5: The Xist repeats A-F and Xist-mediated gene silencing. Scheme illustrating the Xist repeats A-F and indicating repeats required for Xist-mediated gene silencing as well as silencing factor SPEN.

identified as the major factor that binds to Xist RNA PID to recruit PRC1 and PRC2 (Chu et al. 2015; Pintacuda et al. 2017). Thus, it has been suggested that Xist is a scaffold for the organization of factors that mediate erasure of histone modification, such as SPEN and associated factors, involved in histone deacetylation, and writers to deposit silencing marks via Polycomb group proteins.

Interestingly, it has been shown that the recruitment of the chromosomal protein structural maintenance of chromosomes flexible hinge domain containing 1 (SmcHD1) is dependent on the earlier activity of PRC1 (Jansz et al. 2018). SmcHD1 is a member of the SMC chromatin remodeller family and has been shown to play a key role in the chromatin organisation of the Xi compartments and the establishment of CpG island promoter DNA methylation and repression of Xi-linked genes (Blewitt et al. 2008; Gendrel et al. 2013; Brideau et al. 2015; Gdula et al. 2019). These links highlight the intricacy of the recruitment cascade initiated by Xist.

While much progress has been made in identifying the different silencing pathways mediated by Xist, there are still many questions left unanswered about their interplay, about some of the mechanistic aspects of Xist mediated silencing, and about how the initiation of XCI links to its maintenance. Historically, pathways involved in Xist mediated silencing and *cis*-limited localisation of Xist RNA were

seen as mechanistically separable (Wutz, Rasmussen, and Jaenisch 2002), but mounting evidence suggests that some factors might in fact play a role in both [reviewed by (Brockdorff, Bowness, and Wei 2020)]. The need for a more holistic analysis of Xist interacting factors, assessing both their role in gene silencing and Xist RNA localisation at high resolution, has therefore become apparent.

1.4 CIZ-1 role in XCI and Xist localisation

Recently the nuclear matrix protein CIZ-1 has been implicated in localisation of Xist RNA to the Xi (Ridings-Figueroa et al. 2017). CIZ-1 was previously found to play a role in the initiation of DNA replication by interaction with CDK2, p21/CIP1 and cyclins, facilitating the recruitment of cyclin to the nuclear matrix, although CIZ-1 can associate with the nuclear matrix with or without bound cyclin (Coverley, Marr, and Ainscough 2005; Mitsui et al. 1999; Copeland et al. 2010, 2015). Interestingly, the Xi is characterised by late replication timing (Gilbert et al. 1962; Takagi, Sugawara, and Sasaki 1982). However, a potential involvement of CIZ-1 has not been explored to date. Nuclear matrix association has been shown to involve the C-terminal domain of CIZ-1 (Ainscough et al. 2007). There are 22 splice variants of CIZ-1 and aberrant splicing has been correlated to paediatric tumours and common adult-onset cancers of the breast and lung as well as neurological abnormalities (Rahman, Aziz, and Coverley 2010; Den Hollander et al. 2006; Higgins et al. 2012; Xiao et al. 2016).

CIZ-1 has been shown to accumulate at the Xi in female cells, as confirmed by the colocalisation of CIZ-1 with Xist by RNA FISH (Ridings-Figueroa et al. 2017). This localisation of CIZ-1 to the Xi was observed to occur very early during ES cell differentiation (day 1) and persisted throughout the time course of the experiment (Ridings-Figueroa et al. 2017). These observations are very similar to those of the dynamics of Xist RNA accumulation during differentiation. CIZ-1 localisation to Xi was also observed in undifferentiated ES cells in response to expression of inducible Xist RNA (Ridings-Figueroa et al. 2017). Like Xist RNA, CIZ-1 is lost from

the Xi in late metaphase in mESCs and differentiated cells, and hence is re-recruited in G1 of each cell cycle (Ridings-Figueroa et al. 2017). Using 3D-SIM, it has been shown that Xist and CIZ-1 colocalise similarly to hnRNPU in female C127 cells (Ridings-Figueroa et al. 2017). However, contrary to hnRNPU and YY1, CIZ-1 at the Xi is part of the RNA fraction of the nuclear matrix confirmed by resistance to high salt and DNase, and subsequent release by RNase (Ridings-Figueroa et al. 2017). The recruitment of CIZ-1 to the Xi is dependent on the C-terminal nuclear matrix anchor domain of CIZ-1, as well as the E repeat region of Xist RNA (Ridings-Figueroa et al. 2017).

Mice deficient in CIZ-1 showed no effects on embryogenesis, early postnatal development, or cell viability *ex vivo* (Ridings-Figueroa et al. 2017). This finding suggests that CIZ-1 is dispensable for the establishment of a transcriptionally silent Xi. Moreover, transcriptional analysis of CIZ-1-null-derived female primary embryonic fibroblasts (PEFs) did not show reactivation of the Xi (Ridings-Figueroa et al. 2017). However, deregulation at the single-gene level was determined for several X-linked genes across the Xi (Ridings-Figueroa et al. 2017). Furthermore, adult female mice deficient in CIZ-1 developed lymphoproliferative disorder, which suggests compromised XCI in lymphoid lineages (Ridings-Figueroa et al. 2017).

Analysis of independently derived CIZ-1 fibroblast cells deficient in CIZ-1 revealed that Xist occupied 40% of the nucleus as compared to less than 5% in WT cells and was correlated to a partial loss of the Xi characteristic enrichment in H3K27me3 (Ridings-Figueroa et al. 2017), which was later confirmed by an independent study (Sunwoo et al. 2017). These results suggest that deficiency in CIZ-1 impairs

Xist localisation in fibroblasts. Moreover, B and T lymphocytes from CIZ-1-null mice fail to properly localise Xist to the Xi (Ridings-Figueroa et al. 2017). Together, these findings suggest that CIZ-1 has an essential role in anchoring Xist RNA to the nuclear matrix in differentiated cells. It has been hypothesized that CIZ-1 functions redundantly with other anchoring factors such as hnRNPU early during development and XCI, and consequently the absence of CIZ-1 only presents with an XCI phenotype in PEFs or lymphocytes. Sunwoo et al (2017) showed that CIZ-1 is essential for Xist localisation to the Xi in MEFs. STORM imaging confirmed the colocalisation of Xist RNA and CIZ-1 and it was demonstrated that CIZ-1 interacts with Xist RNA via the E-repeats in Exon 7 (Sunwoo et al. 2017). KO of CIZ-1, deletion of the E-repeats, or the over expression of CIZ-1, all caused Xist RNA to be dispersed and delocalised from the Xi territory in MEFs, allowing for the conclusion that localisation of Xist RNA to the Xi is highly sensitive to CIZ-1 levels (Sunwoo et al. 2017). This high resolution study also noted a slight dispersal of Xist RNA in Ciz-1 KO mESCs as compared to WT cells. It was established that Xist RNA recruits CIZ-1 to the Xi, since Xist deletion or LNA mediated knock-down, caused the loss of CIZ-1 enrichment on the X (Sunwoo et al. 2017). It was also shown that both CIZ-1 and hnRNPU facilitate Xist localisation to the Xi independently (Sunwoo et al. 2017).

To conclude, CIZ-1 has been implicated in tethering Xist RNA to the nuclear matrix by binding to the E-repeats (Ridings-Figueroa et al. 2017; Sunwoo et al. 2017). There is, however, conflicting evidence as to whether the role of CIZ-1 in Xist localisation is essential during early stages of differentiation. More research is needed to clarify how it functions together with or independently of the different

localisation factors SAF-1 and YY1 at different stages of differentiation in order to guarantee *cis*-limited Xist localisation. It is also unknown to date whether and how CIZ-1 might influence different aspects of Xist RNA behaviour, since its dynamics coincide with those of Xist itself.

1.5 Xist RNA silencing factor SPEN

SPEN, the protein homolog of Drosophila split ends, was first identified as a factor required for silencing by Xist RNA through genetic and biochemical screens (Monfort et al. 2015; Moindrot et al. 2015; Chu et al. 2015; McHugh et al. 2015), and moreover as a factor that interacts with the A-repeat (Monfort et al. 2015; Chu et al. 2015; Lu et al. 2016). SPEN has a SPEN paralog and ortholog C-terminal (SPOC) domain and four RNA binding domains (RRMs), which can bind to long noncoding RNAs such as the steroid receptor RNA activator (SRA) or Xist, and is essential for RNA-directed transcriptional regulation and gene silencing during XCI (McHugh et al. 2015; Żylicz et al. 2019; Nesterova et al. 2019; Dossin et al. 2020). Binding of SPEN to Xist RNA via three of its RRMs has been mapped to single stranded regions upstream of the inter-repeat double-stranded duplexes of the A-repeat by individual-nucleotide resolution cross-linking and immunoprecipitation (iCLIP) (Lu et al. 2016). It has been suggested that clusters of several SPEN proteins bind to Xist (Lu et al. 2016), and SPEN has been shown to colocalise with Xist RNA using 3D-SIM (Moindrot et al. 2015). Due to its large size of 450 kDa, SPEN has been proposed to function as a platform to recruit additional silencing or repressive factors to the Xist coated chromosome (da Rocha and Heard 2017). Moreover, SPEN has been reported to be essential for the exclusion of RNA polymerase II from the Xi (McHugh et al. 2015).

SPEN interacts directly with the silencing mediator of retinoic acid and thyroid hormone receptor (SMRT) subunit of the nuclear co-repressor complex (N-CoR) via its SPOC domain (McHugh et al. 2015). N-CoR has been shown to associate with

HDAC3 and activates its deacetylation activity on chromatin (Guenther, Barak, and Lazar 2001; McHugh et al. 2015). Indeed, the Xi characteristically has high levels of histone deacetylation with SPEN found to act as a bridging factor between Xist and HDAC to facilitate gene silencing in XCI (McHugh et al. 2015; Żylicz et al. 2019; Nesterova et al. 2019; Dossin et al. 2020). Whilst it has been shown that HDAC3 is pre-bound to the Xi chromatin and activated by SPEN (Żylicz et al. 2019), SPEN has also been shown to recruit HDAC3 de novo (Dossin et al. 2020). *In vitro* and structural work by Ariyoshi and Schwabe showed that the amino acid substitutions R3552A and R3554A in the SPOC domain of SPEN abolishes binding of SPEN to N-CoR1 and SMRT co-repressive complexes (Ariyoshi and Schwabe 2003). In line with this, the SPEN SPOC domain was recently confirmed as a major effector of the gene-silencing function of SPEN, and experiments in which a SPOC domain was artificially tethered to Xist RNA through a stem-loop array have demonstrated it to be sufficient to induce Xist-mediated transcriptional silencing (Dossin et al. 2020). Interestingly, this study also found that a HDAC3 KO did not fully recapitulate the same silencing defect seen upon perturbation of the SPOC domain or the SPEN RRM domains (Dossin et al. 2020). This indicates further SPOC domain functions beyond the recruitment of HDAC3 through the N-CoR1 and SMRT co-repressive complexes. Indeed, SPEN has also been shown to associate with the nucleosome remodelling and deacetylase complex (NuRD), which is connected to several gene-silencing pathways, including ATP-dependent nucleosome remodelling, histone deacetylation via HDACs, and modulation of DNA methylation (Dossin et al. 2020). HDACs recruited by SPEN also mediate the deacetylation of several histone tail sites, including H3K27ac, which theoretically could allow for deposition of the

H3K27me3 histone modification by PRC2 to facilitate gene silencing (Reynolds et al. 2012). However, cells with a loss of function or deficiency in SPEN show only a mild effect on the recruitment of PRC1 or PRC2, and associated histone modifications (Monfort et al. 2015). Mass spectrometry analysis of the SPEN SPOC domain found in addition to the NCoR/ SMRT co-repressor complex, the Mettl3/14 m6A methylation complex, the NuRD complex, and RNA polymerase II (Dossin et al. 2020). SPEN has thus been implicated to interact directly with the transcription machinery. Together with the recent finding that perturbation of SPEN affects Xist expression levels (Nesterova et al. 2019), this raises the question whether SPEN might impact Xist transcription and potentially dynamics in an example of autoregulation.

While the RNA binding domains RRM2-4 of SPEN have been found to be essential for SPEN binding to Xist RNA (Monfort et al. 2015; Nesterova et al. 2019), the RRM 1 domain and the nuclear receptor interaction domain (RID) have been shown to be dispensable (Monfort et al. 2015; Dossin et al. 2020). A recent analysis of the effect of deleting RRM2-4 on Xist-mediated silencing in both XY and XX mESCs with doxycycline inducible Xist located on an autosome or the X chromosome respectively confirmed the key role of SPEN in silencing of X-linked genes during XCI (Nesterova et al. 2019). Deletion of RRM2-4 of SPEN, which was achieved by clustered regularly interspaced short palindromic repeats (CRISPR)/Cas9 mutagenesis, demonstrated that both autosomal transgenic and endogenous Xist expression levels are significantly reduced as compared to WT cells after 24 h of induction with doxycycline as described earlier (Nesterova et al. 2019). Moreover, allelic analysis of X-linked gene transcription by chromatin RNA sequencing

demonstrated a dramatic silencing defect in the SPEN mutant cells with only a few weakly expressed genes showing silencing (Nesterova et al. 2019). A recent study by Dossin et al. (2020) utilised an auxin-induced degron system to generate SPEN null cells, and found that while SPEN is essential for initiating transcriptional gene silencing on the Xi, it is dispensable for maintenance of XCI in neural progenitors (Dossin et al. 2020). However, escapees were found to be expressed at a higher level in NPCs deficient in SPEN, pointing towards a potential role of SPEN in dampening of escapees during the later stages of XCI (Dossin et al. 2020). HaloTag labelling of SPEN in combination with Xist RNA FISH, as well as live cell imaging of GFP-tagged SPEN and BglG-mCherry labelled Xist, showed that SPEN is immediately recruited to the Xi when Xist is upregulated (Dossin et al. 2020). Allele-specific cross-linked CUT&RUN experiments on SPEN during Xist induction showed that it is targeted to enhancers and promoters of active genes (Dossin et al. 2020). After 24 h of Xist induction, when gene silencing is initiated, the CUT&RUN experiments showed that SPEN disengages from chromatin (Dossin et al. 2020). Hence, it has been proposed that active transcription is required for SPEN binding to chromatin.

Most studies describe SPEN as dispensable for Xist RNA localisation (Monfort et al. 2015; Dossin et al. 2020), however, Xist localisation upon perturbation of SPEN has not been studied at high resolution. Intriguingly, it was recently noted that SPEN mutant cells show relatively weak or diffuse Xist RNA domains compared to WT cells and that levels of Xist RNA in the chromatin fraction are reduced. Similar results were seen following deletion of the Xist A-repeat to which SPEN binds

(Nesterova et al. 2019). The possible role for SPEN in Xist localisation is explored in chapter 5 of this thesis.

1.6 Imaging RNA

As previously described, it has become clear that the knowledge about Xist RNA is limited by imaging capacity and resolution. Traditionally, visualisation of RNAs, including Xist, in fixed cells has been achieved by FISH. This method has been derived from the earlier developed DNA in situ hybridisation (Gall and Pardue 1969). Here, nucleic acid probes complementary to target denatured DNA sequences were used for detection, often by radiolabelling (Harrison et al. 1973). Fluorescently labelled probes later allowed for detection by microscopy and hence the development of DNA FISH (Bauman et al. 1980), and shortly after RNA FISH (Singer and Ward 1982). Today, FISH probes are routinely generated from cDNA by nick translation with modified bases that enable the conjugation of different fluorophores. However, conventional RNA FISH does not allow for localisation microscopy of RNA molecules at the single molecule level. Hence, different methods for single molecule RNA FISH have been developed in the last two decades (Raj et al. 2008; Taniguchi et al. 2010; Larsson et al. 2010). All of these approaches still require the fixation of cells, however, and so are unsuitable to capture RNA dynamics. Moreover, denaturation of the RNA, often by stringent treatment of the cells with formamide, is thought to lead to alterations of the chromatin environment, potentially affecting RNA localisation, especially in the context of the nucleus. To overcome these limitations ‘molecular beacons’ were developed to label RNA in living cells using short oligonucleotide probes resistant to cellular degradation. These probes have a fluorophore on one end and a quencher on the other, which are only apart far enough to be fluorescent when the probe is bound to the target (Tyagi and Kramer 1996). Unfortunately, molecular

beacons tend to generate false-positive signals, specifically in the nucleus due to nuclease degradation or nonspecific binding of endogenous biomolecules (Chen et al. 2017). To date molecular beacons have not been used successfully to visualise nuclear RNAs in living cells.

A breakthrough for the live cell imaging of RNAs in mammalian cells was the development of the MS2 stem-loop system, which was first used to study mRNAs in yeast (Bertrand et al. 1998; Beach, Salmon, and Bloom 1999). Here, engineered fluorescently labelled MS2 coat protein dimers bind with high affinity to an array of MS2 hairpins (usually present in the MS2 bacteriophage genome). Mutations of the natural loop sequence increased binding of the MS2 coat protein 50-fold (Lowary and Uhlenbeck 1987) and enabled this system to be successfully used to study and image RNA *in vivo* in different cell types, including mammalian cells. Alternative stem-loop based labelling systems such as the λN22, the PP7 and the BglG system with varying affinities and slightly different properties have also been developed (Daigle and Ellenberg 2007; Larson et al. 2011; J. Chen et al. 2009) allowing for simultaneous labelling of different RNAs. These systems allow for great flexibility when choosing fluorescent labels, since the stem-loop binding proteins can be fused to different fluorescent proteins such as GFP and mCherry but also more photostable labels such as the HaloTag or SnapTag. However, said fusion proteins are also fluorescent when not bound to the stem-loops causing some background fluorescence which can be particularly problematic when studying nuclear target RNAs, since the fusion protein carrying a nuclear localisation signal usually accumulates in the nucleus. This problem is routinely solved by using a stem-loop

array with a large number of stem-loops in order to increase the signal to background ratio.

RNA aptamers such as Spinach, Broccoli and Mango, have been developed recently as an alternative (Paige, Wu, and Jaffrey 2011; Filonov et al. 2014; Dolgosheina et al. 2014). Here, RNA aptamer sequences are genetically engineered at either end, or within the target RNA such that they only activate fluorescence in certain ligands, when bound. This system allows for the reduction of background noise, and ligands can be selectively evolved by exponential enrichment (SELEX) (Tuerk and Gold 1990; Ellington and Szostak 1990; Grate and Wilson 1999). However, RNA aptamers need to have matched non-cytotoxic, thermally stable and cell permeable ligands to enable *in vivo* imaging of RNAs, which has proven to be a challenge. The first light up cell permeable aptamer developed, Spinach, was not thermally stable and required extended exposure times (Paige, Wu, and Jaffrey 2011). Although the thermostability and brightness of Spinach was eventually improved (Strack, Disney, and Jaffrey 2013), fluorescent properties and the tendency of modified target RNAs to be readily degraded still hindered regular use of the aptamer to visualise RNAs *in vivo*. Application of combined SELEX-FACs methodology led to the development of Broccoli, which folds more readily, has an increased fluorescence and was found to be more stable in cellular environments than Spinach (Filonov et al. 2014). However, live cell imaging using Spinach or Broccoli, particularly in mammalian cells, still proved challenging due to lower fluorescence intensity in eukaryotic cells leading to poor signal to noise ratio, as well as heterogeneity of cell permeability from cell to cell.

Recently, a promising new fluorescent RNA aptamer system, called Mango, has been developed (Dolgosheina et al. 2014). Continuous development of the Mango aptamers has led to initial results indicating that they may be suitable for RNA imaging not only in fixed, but also in live mammalian cells, without losing the improved signal to noise ratio characteristic for RNA aptamers (Cawte, Unrau, and Rueda 2020). However, stable integration of aptamers into target RNAs has not been possible so far, and experiments rely on transient transfections to date, which is not suitable for the assessment of many RNAs of interest, including Xist RNA.

Considering the aforementioned challenges encountered when labelling RNAs, this thesis details use of the BglG stem-loop system, previously shown to efficiently label Xist RNA (Moindrot et al. 2015; Masui, Heard, and Koseki 2018), to study Xist RNA localisation and dynamics. The BglG system is based on the *E. coli* transcription antitermination protein, which binds to certain hairpins without dimerising (Aymerich and Steinmetz 1992). BglG-mCherry fusion protein has recently been used successfully to label Xist RNA with an array of 18 Bgl-stem-loops (Moindrot et al. 2015). However, visualisation at a super-resolution level using 3D-SIM to study Xist localisation in fixed cells was only possible by antibody detection of mCherry (Moindrot et al. 2015). This was due to the fact that fluorescent proteins such as mCherry and GFP often do not exhibit the fluorescent properties suitable for direct super-resolution imaging. Recently, the BglG system has also been used to label Xist RNA and perform live cell imaging at lower resolution, confirming it to be a suitable system to pursue imaging of Xist RNA *in vivo* (Dossin et al. 2020). In order to improve the brightness and photostability of the BglG fusion protein for the study of Xist dynamics and localisation at a single molecule level the use of HaloTag or

SnapTag labelling technology as described in a number of recent studies was chosen (Grimm et al. 2017).

1.7 Aims

As outlined above, new super-resolution microscopy techniques and RNA labelling approaches could help elucidate how Xist RNA localises and spreads *in cis*, and how different interacting factors affect this unique behaviour. This project aims to comprehensively assess the *in-cis* localisation, spreading behaviour and dynamics of Xist RNA during the early stages of XCI. To achieve this, the super-resolution microscopy technique 3D-SIM will be used in combination with HaloTag technology to study Xist RNA at the level of single foci and in single cells. Optimisation and method development were required to circumvent the challenges associated with live cell imaging of nuclear RNAs using stem-loop systems, specifically the background caused by free diffusing fusion proteins. Comparison of endogenous inducible Xist RNA with autosomal transgenic Xist RNA grants new insights into X chromosome specific behaviour of Xist. Moreover, the project explores the function of the Xist RNA localisation factor CIZ-1 in both mESCs and differentiated cells by perturbation experiments. Finally, the potential role of the above described Xist silencing factor SPEN in Xist RNA localisation and dynamics is thoroughly examined in experiments involving the perturbation of SPEN binding to Xist RNA and mutation of the SPOC domain respectively. To summarise, the development of new techniques has enabled the detailed study of fundamental principles of Xist RNA behaviour, as well as the role of Xist localisation and silencing factors CIZ-1 and SPEN.

CHAPTER II

2 Methods

2.1 Generation of cell lines

During the course of this project, several cell lines were generated for the extensive study of endogenous and autosomal transgenic Xist RNA localisation, dynamics and spreading behaviour using super-resolution microscopy. XX mESCs with doxycycline inducible endogenous Xist have previously been generated in the lab and were used as parental cell line for the analysis of endogenous Xist RNA behaviour (iXist-ChrX) (Nesterova et al. 2019). XY mESCs (C57BL/6JJcl x 129/SvJcl (P4D7)) (Moindrot et al. 2015) were used as parental cell line for the analysis of autosomal transgenic Xist, which was randomly inserted on an autosome, later identified to be chromosome 15. Stem-loop based RNA labelling approaches, such as the MS2 stem-loop system, have frequently been used to facilitate live cell imaging of RNAs in the nucleus (Grünwald, Singer, and Rout 2011). However, previous experience in the lab has suggested that constitutive expression of fluorescently labelled MS2 coat protein binding the MS2 stem-loops could be toxic for mESCs. In contrast, the comparable Bgl-stem-loop labelling system requires expression of a fluorescently labelled BglG fusion protein which has proven to be more tolerable for mESCs (Moindrot et al. 2015). Therefore, the Bgl-stem-loop system was chosen for the labelling of both endogenous and autosomal transgenic Xist RNA in this project. Due to concerns that BglG

expression might be silenced over time in culture, the BglG fusion protein was genetically engineered to be doxycycline inducible.

HaloTag labelling technology was used for fluorescent labelling of the BglG protein, since HaloTag ligands are especially suitable for live cell and super-resolution imaging due to their excellent fluorescent properties (Los et al. 2008). These small organic dyes bind covalently to the Halo protein tag, which is smaller than comparable fluorescent protein tags such as GFP or mCherry. They are more photostable and bright than commonly used fluorescent proteins, different HaloTag ligands with various excitation and emission wavelengths can be used interchangeably, and they are cell permeable making them ideal for time-resolved analysis of the labelled RNA of interest. Alternatively, the conceptually similar SnapTag labelling technology could have been used, but initial experiments showed that the HaloTag performed better in terms of photostability during both 3D-SIM and single particle tracking experiments.

To generate the ChrX mESC line, iXist-ChrX cells were transfected with a vector encoding for doxycycline inducible BglG-Halo fusion protein, followed by insertion of an array of 18 Bgl-stem-loops within Exon 7 of endogenous Xist by CRISPR/Cas9 genome engineering. For the generation of the autosomal transgene mESC line, XY mESCs were co-transfected with vectors encoding for transgenic Xist with an array of 18 Bgl-stem-loops within Exon 7, as well as for doxycycline inducible BglG-Halo fusion protein. After extensive analysis of endogenous and autosomal transgenic Xist RNA behaviour, perturbation experiments of the Xist localisation factor CIZ-1 were carried out by CRISPR/Cas9 mediated genomic KO. Additionally,

ChrX mESCs and the resulting Ciz-1 KO mESCs were differentiated into NPCs to assess Xist RNA behaviour in differentiated cells. Finally, the role of SPEN in Xist localisation and dynamics was examined. For this, SPEN RRM deletion (SPEN RRM del) and SPOC mutant (SPOC mut) cells were generated, where SPEN binding to Xist was abrogated by CRISPR/Cas9 mediated genomic KO of 3 of the 4 SPEN RRM domains in ChrX mESCs, which had previously been identified to be essential for binding of SPEN to Xist, or base pair substitution of the SPOC domain respectively (Figure 30a and 32a).

2.1.1 Tissue culture

mESCs were grown in Dulbecco's modified Eagle's medium (DMEM; Life Technologies). The medium was supplemented with 10% foetal calf serum (Seralab), 0.1 mM non-essential amino acids, 2 mM L-glutamine, 50 μM β-mercaptoethanol and 100 U/ml penicillin/ 100 μg/ml streptomycin (Life Technologies), as well as 1000 U/ml LIF (made in-house). mESCs were grown on gelatine-coated plates with feeder cells at 37 °C with 5% CO_2 in a humid atmosphere. Feeder cells were generated by inactivation of mouse fibroblasts with 10 µg/ml Mitomycin C (Sigma-Aldrich) in DMEM medium supplemented with 10% foetal calf serum (Seralab), 0.1 mM non-essential amino acids, 2 mM L-glutamine, 50 μM β-mercaptoethanol and 100 U/ml penicillin/ 100 μg/ml streptomycin (Life Technologies) for 2 h. mESCs were passaged appropriately after brief treatment with TrypLE Express (ThermoFisher Scientific) every 2-3 days, and discarded after a maximum of 25 passages. Before transfection, cells were grown on gelatine-

coated 6-well plates with feeders. Medium was exchanged for P/S free medium 3-6 h before transfection.

2.1.2 ChrX ES cell line

iXist-ChrX mESCs were used as parental cell line for the generation of the ChrX mESC line (Nesterova et al. 2019). First, a vector encoding for doxycycline inducible BglG-Halo fusion protein was generated by Gibson assembly using the Gibson Assembly® Master Mix (NEB) from different plasmids previously made in the lab containing sequences encoding for the doxycycline inducible promoter, the HaloTag and the BglG protein. The resulting vector also included a Neomycin resistance cassette for selection of clones with successful integration of the construct. Effective cloning of the vector was confirmed by Sanger Sequencing. Cells prepared as described in section 2.1.1 were transfected overnight with 2 μg of the BglG-Halo construct using Lipofectamine 2000 (Life Technologies) according to the manufacturer's instructions. Cells were then passaged to 90 mm gelatine-coated Petri dishes with feeders and grown in medium containing 200 μg/ml neomycin (Geneticin® (G-418); ThermoFisher) for 10 days. Clones were picked and genomic DNA (gDNA) was extracted, before successful insertions were screened by PCR (see 2.1.7). A total of 6 clones were selected for expansion and BglG-Halo expression was assessed by HaloTag ligand staining (see 2.3.2), and subsequent widefield fluorescence microscopy with an inverted fluorescence Axio Observer Z.1 microscope (Zeiss). Additionally, presence of polyploid or XO cells was excluded by Xist RNA FISH (see 2.2.2). One clone was chosen to take forward for the insertion

of the Bgl-stem-loop array based on the comparison of BglG-Halo expression levels and the results of the Xist RNA FISH experiment.

The Bgl-stem-loop array was inserted within Exon 7 of the *Xist* locus by CRISPR/Cas9 mediated genome engineering. Here, a homology construct containing homology regions 1 kb 5′ and 3′ of the targeted insertion site within Exon 7 of Xist was generated using the GeneArt vector synthesis by ThermoFisher Scientific. Targeting was achieved by co-transfection of said construct with a specific sgRNA (Table 1), which was designed using the WGE - CRISPR design tool (Wellcome Sanger Institute) and cloned into a backbone vector encoding for the CRISPR/Cas9 protein (pSpCas9(BB)-2A-Puro, PX459, Addgene). The latter also contained a Puromycin resistance cassette for the selection of successfully targeted clones. For this, pairs of oligos of the single guide RNA (sgRNA) sequence were each phosphorylated and annealed using T4 Polynucleotide Kinase (NEB). The annealed oligos were then diluted 1:250 and added to a digestion-ligation reaction, which was set up with 100 ng of the backbone vector (pSpCas9(BB)-2A-Puro, PX459, Addgene), Fast Digest BbsI (ThermoFisher Fermentas) and T7 DNA ligase (NEB). The ligation reaction was subsequently treated with PlasmidSafe exonuclease (Biosearch Technologies) to prevent unwanted recombination products. Finally, home-made DH5alpha cells were transformed by heat shock, cultured at 37 ^{o}C overnight and plasmids were recovered by using the QIAprep Spin Miniprep Kit (Qiagen). Effective cloning of the sgRNA vector was confirmed by Sanger Sequencing (Source Bioscience). Cells prepared as described in section 2.1.1 were transfected overnight with 2 μg of the sgRNA construct and 1.15 μg of the targeting construct using Lipofectamine 2000 (Life Technologies) according to

the manufacturer's instructions. Then, cells were passaged to 90 mm gelatinised Petri dishes with feeders. After another 24 h, medium containing 1.75 μg/ml puromycin was added and cells were grown under antibiotic selection for 48 h. Colonies were grown for 9 days before being picked. Selected clones with successful insertion were screened for by gDNA extraction followed by PCR analysis (see 2.1.7). Based on this, 6 clones were selected for expansion. Successful labelling of BglG-Halo-Xist was confirmed by HaloTag ligand staining (see 2.3.2) followed by 3D-SIM imaging (see 2.4). Comparison of BglG-Halo-Xist signal intensity to background signal from unbound BglG-Halo allowed for the selection of the most suitable cell line for imaging experiments. This was followed by characterisation of the newly generated ChrX cells by determination of induction efficiency by Xist RNA FISH (see 2.2.2), combined HaloTag staining and Xist RNA FISH, followed by 3D-SIM (see 2.2.3), immunofluorescence staining (see 2.3.1) and chromatin RNA sequencing (see 2.8).

2.1.3 Autosomal transgene ES cell line

XY P4D7 mESCs were used as parental cell line for the generation of the autosomal transgene mESC line (Moindrot et al. 2015). A vector encoding for doxycycline inducible Xist containing an array of 18 Bgl-stem-loops within Exon 7, which had previously been generated in the lab (Moindrot et al. 2015), was used for the generation of the autosomal transgene cell line. Additionally, cells were transfected with the construct encoding for doxycycline inducible BglG-Halo protein described earlier (see 2.1.2). Cells prepared as described in section 2.1.1 were co-transfected overnight with 5 μg of the transgenic Xist and 2.5 μg of the BglG-Halo construct

using TransIT-LT1 transfection reagent (Mirusbio) according to the manufacturer's instructions. Then, cells were passaged to 90 mm gelatine-coated Petri dishes with feeders and grown in medium containing 200 µg/ml neomycin (Geneticin® (G-418); ThermoFisher) for 10 days. Clones were picked and gDNA was extracted, before successful insertions of the BglG-Halo sequence were screened for by PCR (see 2.1.7). A total of 12 clones were selected for expansion, and autosomal transgenic Xist expression was assessed by Xist RNA FISH (see 2.2.2) and subsequent widefield fluorescence microscopy with an inverted fluorescence Axio Observer Z.1 microscope (Zeiss). 3 clones with confirmed Xist expression were chosen to take forward for HaloTag ligand staining (see 2.3.2) and 3D-SIM (see 2.4) to confirm BglG-Halo expression and efficient labelling of autosomal transgenic BglG-Halo-Xist. The final clone to be taken forward for analysis was selected based on suitable BglG-Halo expression levels that allowed for the best ratio of signal from BglG-Halo-Xist to unbound BglG-Halo. This was followed by characterisation of the newly autosomal transgene cells by determination of induction efficiency by Xist RNA FISH (see 2.2.2), combined HaloTag staining and Xist RNA FISH, and chromatin RNA sequencing (see 2.8), which allowed for the determination of the insertion site of autosomal transgenic Xist on chromosome 15.

2.1.4 Ciz-1 KO ES cell line

The previously generated ChrX cell line was used as parental cell line for the generation of the Ciz-1 KO mESCs by CRISPR/Cas9 mediated genome engineering (see 2.1.2). Here, the first sgRNA, which had been previously used to induce a frameshift mutation (Sunwoo et al. 2017), was used in combination with a

second sgRNA designed using the WGE - CRISPR design tool to achieve a genomic deletion of 10.66 kb, resulting in the KO of the majority of *CIZ-1* (Table 1). The sgRNAs were cloned into backbone vectors encoding for the CRISPR/Cas9 protein containing puromycin resistance cassettes for the selection of successfully targeted clones as described in 2.1.2. Effective cloning of the sgRNA vectors was confirmed by restriction enzyme digest and Sanger Sequencing. Cells prepared as described in section 2.1.1 were transfected overnight with 2 μg of each sgRNA construct using Lipofectamine 2000 (Life Technologies) according to the manufacturer's instructions. Then, cells were passaged to 90 mm gelatinised Petri dishes with feeders. After another 24 h, medium containing 2 μg/ml puromycin was added and cells were grown under antibiotic selection for 48 h. Colonies were grown for 8 days before being picked. Selected clones with successful genomic deletion were screened for by gDNA extraction followed by PCR analysis (see 2.1.7). Based on this, 6 clones were selected for expansion. Ciz-1 KO was confirmed on the protein level by Western blot (see 2.9) and immunofluorescence staining for CIZ-1 (see 2.3.1). Presence of polyploid and XO cells was excluded by Xist RNA FISH (see 2.2.2), while successful labelling of BglG-Halo-Xist was confirmed by HaloTag ligand staining (see 2.3.2) followed by 3D-SIM imaging (see 2.4). A final clone for analysis was chosen based on the cumulative results of these assays, as well as the comparison of BglG-Halo-Xist signal intensity to background signal from unbound BglG-Halo. This was followed by characterisation of the newly generated Ciz-1 KO cells by determination of induction efficiency by Xist RNA FISH (see 2.2.2) and chromatin RNA sequencing (see 2.8).

2.1.5 SPEN RRM del ES cell line

The previously generated ChrX cell line was used as parental cell line for the generation of the SPEN RRM del mESCs by CRISPR/Cas9 mediated genome engineering (see 2.1.2). Two sgRNAs, which have first been designed by Monfort et al. in 2015 and have since been used in the lab to generate SPEN KO cells (Monfort et al. 2015), were used to achieve a genomic deletion of 38 kb, resulting in the KO of RRM2-4 of *SPEN* (Table 1). Vectors encoding for the CRISPR/Cas9 protein and either of the sgRNAs, as well as puromycin resistance cassettes for the selection of successfully targeted clones, had been generated in the lab before. Cells prepared as described in section 2.1.1 were transfected overnight with 2 μg of each sgRNA construct using Lipofectamine 2000 (Life Technologies) according to the manufacturer's instructions. Then, cells were passaged to 90 mm gelatinised Petri dishes with feeders. After another 24 h, medium containing 2 μg/ml puromycin was added and cells were grown under antibiotic selection for 48 h. Colonies were grown for 8 days before being picked. Selected clones with successful genomic deletion were screened for by gDNA extraction followed by PCR analysis (see 2.1.7). Based on this, 2 clones with presumed heterozygous deletion and 6 clones with presumed homozygous deletion were selected for expansion. SPEN RRM del was confirmed by Southern blot (see 2.10). Presence of polyploid and XO cells was excluded by Xist RNA FISH (see 2.2.2). Successful labelling of BglG-Halo-Xist was confirmed by HaloTag ligand staining (see 2.3.2) followed by 3D-SIM imaging (see 2.4). A final clone for analysis was chosen based on the cumulative results of these assays, as well as the comparison of BglG-Halo-Xist signal intensity to background

signal from unbound BglG-Halo. This was followed by characterisation of the newly generated SPEN RRM del cells by Southern blot (see 2.10), determination of induction efficiency by Xist RNA FISH (see 2.2.2) and assessment of silencing by chromatin RNA sequencing (see 2.8).

2.1.6 SPOC mut ES cell line

The previously generated ChrX cell line was used as parental cell line for the generation of the SPOC mut mESCs by CRISPR/Cas9 mediated genome engineering (see 2.1.2). A catalytically inactive SPEN mutant was achieved by two amino acid substitution of R3552A and R3554A in the SPOC domain of SPEN, i.e. substitution of 5 nucleotides. This substitution was previously described to abolish binding of SPEN to N-CoR1 and SMRT co-repressive complexes *in vitro* (Ariyoshi and Schwabe 2003), and was thus predicted to disrupt SPEN catalytic activity essential for Xist-mediated silencing without affecting SPEN binding to Xist RNA. Here, a 0.5 kb homology construct containing homology regions within SPEN Exon 14 and said substitutions was designed and cloned in the lab*. The sgRNA (Table 1) was cloned into backbone vectors encoding for the CRISPR/Cas9 protein containing puromycin resistance cassettes for the selection of successfully targeted clones*. Cells were grown on gelatine-coated 6-well plates with feeders before transfection**. Cells were transfected overnight with 1.42 μg of the sgRNA construct and 2.5 μg of the targeting construct using Lipofectamine 2000 (Life Technologies) according to the manufacturer's instructions**. Then, cells were passaged to 90 mm gelatinised Petri dishes with feeders and after another 24 h

*Vectors were designed and cloned by Guifeng Wei and Artun Kadaster

**Tissue culture work was performed by Joseph Bowness

medium containing 3 µg/ml puromycin was added and cells were grown under antibiotic selection for 48 h before colonies were grown for 10 days before being picked**. Selected clones with successful amino acid substitution were screened for by gDNA extraction followed by PCR analysis see 2.1.7)***. 10 potential homozygous clones were selected for expansion. and PCR analysis of gDNA was repeated, followed by Sanger Sequencing of the PCR fragments. Based on this, 4 clones were expanded further for analysis. Presence of polyploid and XO cells was excluded by Xist RNA FISH (see 2.2.2). Successful labelling of BglG-Halo-Xist was confirmed by HaloTag ligand staining (see 2.3.2) followed by 3D-SIM imaging (see 2.4). This was followed by chromatin RNA sequencing (see 2.8) to finally confirm successful amino acid substitution and assess transcriptional silencing of X-linked genes by allelic analysis. A final clone for analysis was chosen based on the cumulative results of these assays, as well as the comparison of BglG-Halo-Xist signal intensity to background signal from unbound BglG-Halo. Lastly, induction efficiency was determined by Xist RNA FISH (see 2.2.2) and the newly generated SPOC mut cells were taken forward for further analysis.

Cell line	sgRNA1 oligo	sgRNA2 oligo
ChrX	CATACGTAGTTCCCCGCTCT	Not applicable
Ciz-1 KO	CAGCCTTACACCACCCCAGA	CAGGGCGTTGCGGGCGTTGA
SPEN RRM del	GGGGTGTCTCCTGCGCATT	CGGACAAGACATTACGATC
SPOC mut	CCCCACTGCGGATCGCCCAG	Not applicable

Table 1: sgRNAs used for the generation of ChrX, Ciz-1 KO, SPEN RRM del and SPOC mutant mESCs.

**Tissue culture work was performed by Joseph Bowness

***PCR screening and restriction digest was performed by Guifeng Wei

2.1.7 PCR screen of gDNA and agarose gel analysis

During the generation of all cell lines for this project, successful genomic modifications were screened for by PCR analysis of extracted gDNA after clonal expansion, followed by visualisation using agarose gels. For extraction of the gDNA, cells were washed with PBS and snap frozen on dry ice. Next, they were incubated with squishing buffer containing 10 mM TrisHCl, pH 8, 1 mM EDTA, 25 mM NaCl and 200 μg/ml fresh Proteinase K at 65 °C for 30 min, before the Proteinase K was inactivated at 95 °C for 2 min.

The extracted gDNA was used as template DNA for PCR analysis with the Mastercycler nexus (Eppendorf). Taq polymerase (Invitrogen) was used routinely to screen for genomic modifications. Here, 1 µl of template DNA was incubated with 0.1 µl 100 µM forward and reverse primer each (Table 2), 0.2 µl Taq polymerase, 5 µl PCR master mix (10x buffer, 50 mM $MgCl_2$ and 10 mM dNTPs in nuclease free water) and 18.6 µl nuclease free water for a total reaction volume of 25 µl. Initial denaturation at 95 °C for 5 min was followed by 37 cycles of denaturation at 95 °C (20 s), annealing at 56 °C (30 s) and extension at 72 °C (40 s), with a final extension of 7 min at 72 °C.

PCR screening of the Bgl-stem-loop inserts and the BglG-Halo was not successful when using Taq DNA polymerase. Therefore, Velocity polymerase (Bioline) was used instead. Here, 1 µl of template DNA was incubated with 0.4 µl 20 µM forward and reverse primer each (Table 2), 0.4 µl Velocity polymerase, 4 µl 5x HiFi reaction buffer, 0.4 µl 10 mM dNTPs, 0.6 µl DMSO (final concentration of 3%) and 12.8 µl nuclease free water for a total reaction volume of 20 µl. Initial denaturation at 98 °C

for 2 min was followed by 35 cycles of denaturation at 98 °C (30 s), annealing at 56 °C (30 s) and extension at 72 °C (30 s), with a final extension of 10 min at 72 °C. All PCR products were run on 1% EtBr Agarose gel at 110 V for 1 h together with the 1 kb+ ladder from New England Biolabs, and visualised with UV-light.

Genetic modification	Forward primer	Reverse Primer	Expected band size for modification
Bgl-stem-loop insert (PCR 1)	AGTGTGTCTTACCTATTCCCAT	GGTAGGGAGGATGGCAGTAT	2.1 kb
Bgl-stem-loop insert (PCR 2)	GATTCAAGTGGCTCTGAAGTGA	GGTAGGGAGGATGGCAGTAT	1.4 kb
BglG-Halo	AAAGAGTATGCCTTGCTACCG	TACAGATCCTCAGTGGTTGGC	950 bps
Ciz-1 KO (PCR 1)	CTCCGTGCTTTCAATGTGAC	ACTACTCACCTTGCGATTGG	230 bps
Ciz-1 KO (PCR 2)	CTCCGTGCTTTCAATGTGAC	TACCATCTCCAGATGCTGGG	1.1 kb
SPEN RRM del	GCGCTCCAGCCGAGCCTTCTC	CAGAAAGAGGCGAGGCGTAAAG	322 bps
SPOC mut (PCR 1)	GGATCGCCCAGGCCATGGCA	CAGCAGCAGGCAGTAGTCGG	365 bps
SPOC mut (PCR 2)	GGGACACCACAACGGCCTGTG	CAGCAGCAGGCAGTAGTCGG	637 bps

Table 2: Primers used for PCR screening for successful genetic modifications during the generation of ChrX, Ciz-1 KO, SPEN RRM del and SPOC mutant mESCs.

2.1.8 NPC derivation

In order to study Xist behaviour in differentiated cells, particularly when CIZ-1 is perturbed, ChrX and Ciz-1 KO mESCs were differentiated into NPCs following a protocol adapted previously in the lab from Conti et al. 2005 and Splinter et al. 2011 (Conti et al. 2005; Splinter et al. 2011)*. Cells were grown in gelatine-coated T25 flasks with feeder cells in DMEM medium as described in 2.1.1. Feeders were removed before differentiation by pre-plating three times for 40 min each on gelatine-coated 90 mm petri dishes. Then, cells were spun down at 1,000 rpm for 3 min and washed twice in PBS, before counting and plating $0.45x10^6$ cells and $0.55x10^6$ cells in a gelatine-coated T25 flasks each. They were grown in N2B27 medium (Table 30) containing 1 µg/ml doxycycline for 7 days changing the medium every other day for the first 3 days of differentiation and then every day. On day 7, the flasks were treated with Accutase (Millipore; diluted 1:2 in PBS) and $3x10^6$ cells were plated each in 90 mm bacterial petri dishes with N2B27 medium containing 1 µg/ml doxycycline and 10 ng/ml EGF and FGF (Peprotech) to prevent cellular attachment. For HaloTag staining (see 2.3.2) and Xist RNA FISH (see 2.2.2) at day 10 of differentiation, cells were plated onto gelatine-coated 18x18 mm No. 1.5H precision coverslips (± 5 μm tol.; Marienfeld Superior) at day 7. At day 10, cell aggregates were collected from the 90 mm petri dishes by mild centrifugation at 800 rpm for 2 min, before being plated onto gelatine-coated 90 mm petri dishes in N2B27 medium containing 1 µg/ml doxycycline and 10 ng/ml EGF and FGF (Peprotech) each. Medium was replaced every other day. When ~80% confluent, cells were split 1:4 by Accutase (Millipore; diluted 1:2 in PBS) treatment at room temperature

*The following NPC differentiation protocol was adapted by Tatyana Nesterova and Mafalda Almeida

followed by collection in PBS in LoBind Falcon tubes and centrifugation at 1,500 rpm for 5 min. For HaloTag staining (see 2.3.2 and 2.6) at day 20 of differentiation, cells were plated onto 18x18 mm No. 1.5H precision coverslips (± 5 μm tol.; Marienfeld Superior) at day 16 of differentiation. For chromatin RNA sequencing (see 2.8) at day 30 of differentiation, cells were expanded onto one 145 mm petri dish per replica on day 25 of differentiation.

Reagent	Volume [ml]	Supplier
DMEM/F12	247	Life Technologies
Neurobasal Medium	247	Life Technologies
N2 (100x)	2.5	Home made
B27 (50x)	2.5	Life Technologies
L-Glutamine (200 mM)	2.5	Life Technologies
2-mercaptoethanol (50mM)	1	Life Technologies
Pen/Strep	2.5	Life Technologies

Table 3: N2B27 medium recipe for 500 ml

2.2 Xist RNA FISH

2.2.1 FISH probe preparation and agarose gel

To generate a labelled Xist RNA FISH probe, 7.5 µl nuclease free water, 1 µg template DNA (full length Xist cDNA), 2.5 µl 0.2 mM Spectrum Texas Red dUTP, 5 µl 0.1 mM dTTP, 10 µl dNTP mix (0.1 mM) and 5 µl 10x nick translation buffer were added on ice. The sample was vortexed before adding 10 µl of the nick translation enzyme (Abbot) followed by a 16 h incubation at 15 °C overnight. Correct probe size of 200 – 500 bps was ensured by running on a 1% EtBr Agarose gel at 110 V for 1 h together with the 1 kb+ ladder from New England Biolabs, and visualised using UV-light. On day 1 of the RNA FISH experiment, the probe was prepared as follows: 3 µl Texas Red labelled Xist RNA FISH probe per hybridisation was added to 1/3 volume 10 mg/mL salmon sperm DNA, then precipitated by addition of 1/10 volume of 3M NaOAc and 3 volumes 100% EtOH. The probe was centrifuged at 16,000 rpm at 4 °C for 20 min, then washed with 70% EtOH. Next, the resulting pellet was resuspended in 70% EtOH and again centrifuged at 16,000 rpm at 4 °C for 10 min. After briefly drying the pellet by speed vacuum, it was resuspended in 6 µl formamide per hybridisation and incubated at 42 °C, 1,400 rpm agitation, for at least 30 min. Next, an equal amount of 2x hybridisation buffer was added (4x SSC, 20% dextran sulphate, 2 mg/ml BSA, 1/10 volume nuclease free water and 1/10 volume VRC pre-warmed at 65 °C for 5 min before use). The probe/ hybridisation buffer mix was denatured at 75 °C for 5 min before being chilled on ice and used for overnight hybridisation (see 2.2.2).

2.2.2 RNA FISH for scoring

All cells were grown on gelatine-coated 18x18 mm No. 1.5H precision coverslips (± 5 μm tol.; Marienfeld Superior) in a 6-well plate. mESCs were grown on a layer of Mitomycin C inactivated feeder cells. When reaching 60-70% confluency, mESCs were induced for 3 h or 24 h with 1 µg/ml doxycycline, reserving one coverslip per experiment without doxycycline induction as a control. After induction, coverslips were washed briefly with PBS twice, before being fixed with 3.7% formaldehyde in PBS at room temperature for 10 min. Cells were rinsed with PBS and then permeabilised with 0.5% Triton X-100 in PBS for 10 min at room temperature, followed by two washes with 70% EtOH. Coverslips were then dehydrated with subsequent washes with 80%, 95%, 100% EtOH for 5 min each, and dried briefly. Each coverslip was hybridised with 15 µl probe/ hybridisation buffer mix, prepared as described in 2.2.1. Finally, coverslips were placed in a very humid chamber overnight at 37 °C. The next day, washes were carried out before mounting the coverslips for imaging. For this, a 50% formamide/ 2x SSC solution in PBST5 (0.05% Tween 20 PBS) and a 2x SSC solution in PBST5 were warmed up at 42 °C in a water bath, and coverslips were gently floated off and placed in an empty 6-well plate. Coverslips were washed 3 times with pre-warmed 50% formamide/ 2x SSC at 42 °C for 5 min each, and subsequently 3 times with 2x SSC at 42 °C for 5 min each. Coverslips were mounted with Vectashield mounting medium (+DAPI) centrally on Superfrost Plus microscopy slides (VWR). Slides were dried, sealed using clear nail polish and cleaned for imaging. Imaging and scoring were carried out using an inverted fluorescence Axio Observer Z.1 microscope (Zeiss) using a

PlanApo ×63/1.4 NA oil-immersion objective. Images were acquired using AxioVision software.

2.2.3 RNA FISH for 3D-SIM

This protocol was adapted from the Stellaris FISH protocol (Biosearch Technologies) for a combination of Xist RNA FISH with HaloTag ligand staining of BglG-Halo-Xist. All cells were grown on gelatine-coated 18x18 mm No. 1.5H precision coverslips (± 5 μm tol.; Marienfeld Superior) in a 6-well plate. mESCs were grown on a layer of Mitomycin C inactivated feeder cells. When reaching 60-70% confluency, mESCs were induced for 3 h or 24 h with 1 µg/ml doxycycline, before being stained with HaloTag ligand as described in 2.3.2. After washout of the ligand, coverslips were washed in the 6-well plate twice with PBS. Fixation was carried out in the 6-well plate by adding 3% formaldehyde (pH7) prepared in fresh PBS for 10 min at room temperature. A stepwise exchange of PBST5 (0.05% Tween 20 PBS) was carried out, then coverslips were carefully transferred to a coverslip rack before being washed twice in 80 mL PBST5 in a small beaker. All further steps were carried out in beakers. Cells were permeabilised in 0.2% Triton X-100 PBS for 10 min at room temperature, before being washed twice with PBST5. Then, coverslips were blocked in 2% BSA/ 0.5% Fish Gelatine/ PBST5 containing freshly added RNAsin Plus (Promega) at a final concentration of 2 U/µl on parafilm in a humid chamber for 30 min. In the meantime, the Xist RNA FISH probe was prepared and precipitated as described in 2.2.1. However, the probe pellet was resuspended in 12 µl Stellaris Hybridisation buffer (Biosearch Technologies) per hybridisation instead of formamide after speed vacuum. The probe/ hybridisation buffer was

prepared as described in 2.2.1, with the exception of that the 2x hybridisation buffer was prepared with 1/10 volume formamide before being added to the probe. After blocking, the cells were washed 3 times with PBST5 and fixed as before. Then, the coverslips were washed twice in PBST5 again, followed by a wash in 2x SSC. Next, the coverslips were incubated with FISH probe/ hybridisation buffer overnight at 37 °C on parafilm in an extra humid chamber. The next day, the coverslips were gently floated off the parafilm using 1x wash buffer (Biosearch Technologies) and transferred to a 6-well plate containing 1 ml Wash buffer A (Biosearch Technologies) per well. After an incubation at 37 °C for 30 min, Wash buffer A was replaced with 1 ml Wash buffer A containing DAPI at 5 ng/mL, and coverslips were incubated at 37 °C for another 30 min. Next, 1 ml of 2x SSC was added to each well, followed by an incubation of 5 min at room temperature. Finally, coverslips were mounted centrally on the unfrosted side of Superfrost Plus microscopy slides (VWR) using Vectashield soft mount media (no DAPI), sealed with clear nail polish and imaged within a week using the DeltaVision OMX V3 Blaze system (GE Healthcare; see 2.4).

2.3 Fluorescence staining

2.3.1 Immunofluorescence staining

All cells were grown on gelatine-coated 18x18 mm No. 1.5H precision coverslips (± 5 μm tol.; Marienfeld Superior) in a 6-well plate. mESCs were grown with Mitomycin C inactivated feeder cells. When reaching 60-70% confluency, mESCs were induced for 3 h or 24 h with 1 µg/ml doxycycline. Optionally, cells were stained with HaloTag ligand at this stage as described in 2.3.2 for a combination of HaloTag ligand and immunofluorescence staining. Coverslips were washed twice with PBS in the 6-well plate. Fixation was carried out in the 6-well plate, adding 2% formaldehyde (pH7) prepared in fresh PBS for 10 min at room temperature. A stepwise exchange of PBST5 was carried out, then coverslips were carefully transferred to a coverslip rack before being washed twice in 80 mL PBS in a small beaker. All further steps were carried out in beakers. Cells were permeabilised with 0.2% Triton X-100 in PBS for 10 min at room temperature, followed by a wash with PBST5. Coverslips were then blocked using 3% BSA/ 5% normal goat serum/ PBST5 on parafilm in a humid chamber for 30 min at room temperature. Next, coverslips were incubated with primary antibody (Table 4) diluted in block buffer for 1 h in a humidified chamber at 37 °C. After 3 washes in PBST5, coverslips were incubated with the Alexa fluorophore conjugated secondary antibody (Table 4) diluted 1:1000 in block buffer for 30 min in a humidified chamber at 37 °C. After another 4 washes with PBST5, the cells were fixed as before, followed by a final wash in PBST5. Lastly, coverslips were incubated with 2 µg/mL DAPI in PBS for 10 min, before being washed briefly with ddH_2O to remove salt and equilibrated with

Vectashield mounting medium. The coverslips were mounted centrally on the unfrosted side of Superfrost Plus microscopy slides (VWR) using Vectashield soft mount media (no DAPI), sealed with clear nail polish and imaged within a week using the DeltaVision OMX V3 Blaze system (GE Healthcare; see 2.4).

	Primary Antibody	Primary antibody dilution	Secondary Antibody
H3K27me3	Anti-mouse, monoclonal, Actif motive (ab61017)	1:500	Anti-mouse Alexa Fluor 594, Thermofisher Scientific
uH2AK119	Anti-rabbit, monoclonal, Cell Signalling (Cat. No 8240S)	1:500	Anti-rabbit Alexa Fluor 594, Thermofisher Scientific
CIZ-1	Anti-rabbit, polyclonal, received from the Dawn Coverley lab; purified version used for 3D-SIM	1:1000	Anti-rabbit Alexa Fluor 594, Thermofisher Scientific
RNA polymerase II	Anti-mouse, monoclonal, Milipore 05-623	1:300	Anti-mouse Alexa Fluor 594, Thermofisher Scientific

Table 4: Primary and according secondary antibodies used for different immunofluorescence staining

2.3.2 HaloTag staining

All cells were grown on gelatine-coated 18x18 mm No. 1.5H precision coverslips (± 5 μm tol.; Marienfeld Superior) in a 6-well plate. mESCs were grown with Mitomycin C inactivated feeder cells. When reaching 60-70% confluency, mESCs were induced for 3 h or 24 h with 1 µg/ml doxycycline. Then, cells were incubated with medium containing 50 nM diAcFAM HaloTag ligand (488 nm, Promega) and 1 µg/ml

doxycycline for 45 min, before being washed with medium containing 1 µg/ml doxycycline for 15 min. After a brief wash with PBS, cells were fixed for 10 min at room temperature with 2% formaldehyde prepared fresh in PBS (pH 7). A stepwise exchange of PBST5 was carried out, and cells were permeabilised with 0.2% Triton X-100 for 10 min at room temperature, followed by two washes with PBST5. Next, cells were incubated with 2 µg/ml DAPI in PBST5 for 10 min, before being washed briefly with PBS and, subsequently with ddH_2O to remove salt, and equilibrated with Vectashield mounting medium. The coverslips were mounted centrally on the unfrosted side of Superfrost Plus microscopy slides (VWR) using Vectashield soft mount media (no DAPI), sealed with clear nail polish and imaged within a week using the DeltaVision OMX V3 Blaze system (GE Healthcare; see 2.4).

2.4 3D-SIM

2.4.1 Acquisition

3D-SIM imaging of fixed samples was performed on a DeltaVision OMX V3 Blaze system (Applied Precision, GE Healthcare) equipped with a 60 ×/1.42 NA Plan Apo oil immersion objective (Olympus), pco.edge 5.5 sCMOS cameras (PCO), and 405, 488, 593 and 640 nm diode lasers. Image stacks were acquired with a z-distance of 125 nm and with 15 raw images per plane (5 phases, 3 angles). Spherical aberration after reconstruction was reduced by using immersion oil of different refractive indices (RIs) matched to respective optical transfer functions (OTFs). Here, immersion oil with an RI of 1.514 was used for the sample acquisition and matched to OTFs generated using immersion oil of RI 1.512 for the blue and green, and 1.514 for the red channel. OTFs were acquired using 170 nm diameter blue PS-Speck beads and 100 nm diameter green and red FluoSphere beads (ThermoFisher Scientific).

2.4.2 Reconstruction

The raw data was computationally reconstructed with softWoRx 6.5.2 (GE Healthcare) using the channel-specific OTFs acquired previously and Wiener filter settings of 0.005 (see 2.4.1). A lateral (x-y) resolution of approximately 120 nm and an axial (z) resolution of approximately 320 nm was achieved. All reconstructed 32-bit 3D-SIM datasets were thresholded to the stack modal intensity value and converted to 16-bit composite z-stacks to discard negative intensity values, and modulation contrast-to-noise ratio (MCNR) maps were generated by an adapted in-

house ImageJ script. Moreover, all data underwent assessment via SIMcheck (Ball et al. 2015) to determine image quality via MCNR, spherical aberration mismatch, reconstructed Fourier plot and reconstructed intensity histogram values.

2.4.3 Alignment

Colour channels were aligned laterally using the open-source software package Chromagnon (Matsuda et al. 2018) and EdU calibration data acquired on the date of image acquisition. Here, female mouse epithelial C127 cells were 15 min pulse replication labelled with 5-ethynyl-2'-deoxyuridine (EdU) and incorporated EdU was detected by a simultaneous three-colour click reaction at a 7:2:1 ratio of azide-tagged CF405M (blue), Alexa Fluor 594 (red) and Alexa Fluor 488 (green), respectively, as previously described in a published protocol (Kraus et al. 2017).

2.5 Live cell imaging

2.5.1 3D-SIM live cell imaging

Cells were grown on gelatine-coated 35 mm No. 1.5H glass bottom imaging dishes (Ibidi) with Mitomycin C inactivated feeder cells. When reaching 50% confluency, mESCs were induced for 24 h with 1 µg/ml doxycycline. Then, cells were incubated with medium containing 50 nM JF-646 HaloTag ligand (Janelia Fluor 646, kindly gifted to us by Luke Lavis at HHMI Janelia, US) and 1 µg/ml doxycycline for 45 min, before being washed with medium containing 1 µg/ml doxycycline for 15 min. Before imaging, cells were washed briefly with PBS and medium was replaced with phenol red free medium with 1 µg/ml doxycycline. Live cell 3D-SIM was performed with a DeltaVision OMX V3 Blaze system (Applied Precision, GE Healthcare), equipped with a 60 ×/1.42 NA Plan Apo oil objective, Olympus and sCMOS cameras (PCO), and a 633 nm diode laser. Image stacks with a z-distance of 125 nm and with 15 raw images per plane (5 phases, 3 angles) were acquired in 10 s intervals for up to 10 min. Image acquisition was performed at 37 °C with 5% CO2. To adapt for the temperature increase, immersion oil with an RI of 1.520 was used for the sample acquisition and matched to OTFs generated. Images were then processed as described above, with the exception that bleach correction was carried out. Image reconstruction was performed as described in 2.4.2.

2.5.2 PALM-TIRF single particle tracking

Cells were grown on gelatine-coated 35 mm No. 1.5H glass bottom imaging dishes (Ibidi) with Mitomycin C inactivated feeder cells. When reaching 50% confluency,

mESCs were induced for 24 h with 1 µg/ml doxycycline. Then, cells were incubated with medium containing 50 nM diAcFAM HaloTag ligand (488 nm, Promega) and 1 µg/ml doxycycline for 45 min, before being washed with medium containing 1 µg/ml doxycycline for 15 min. Subsequently, medium containing 50 nM photo-activatable JF-549 HaloTag ligand (kindly gifted to us by Luke Lavis at HHMI Janelia, US) and 1 µg/ml doxycycline was added for 45 min, followed by another wash with medium containing 1 µg/ml doxycycline. Before imaging, cells were washed briefly with PBS and medium was replaced with phenol red free medium. Single particle tracking was performed with the photoactivated localisation microscopy/total internal reflection fluorescence (PALM/TIRF) super-resolution localisation microscope build by the Kapanidis lab (Department of Physics, Oxford University), with a Toptica Multi Laser Engine with 405 nm, 488 nm, 561 nm, 640 nm lasers. Fluorescence emission was recorded on an Andor iXon 897 ultra electron multiplying CCD (EMCCD) camera at a magnification resulting in a pixel length of 96 nm/pixel. The photo-activatable ligand was activated using the 405 nm laser. Images were acquired with an exposure of 200 ms/frame. Molecule tracks were determined by an in-house MATLAB script*. Data analysis and modelling was performed using the Spot-on tool developed by Berkley. A bin width of 0.01, 8 time points and 4 jumps to consider, with a maximum jump distance of 5.05 µm and a maximum of one allowed gap were set as parameters for the kinetic model fitting.

*The script was adapted and kindly shared by Miles Huseyin

2.6 RNA-SPLIT (Sequential Pulse Localisation Imaging over Time)

2.6.1 Sample preparation

All cells were grown on gelatine-coated 18x18 mm No. 1.5H precision coverslips (± 5 μm tol.; Marienfeld Superior) in a 6-well plate. mESCs were grown with Mitomycin C inactivated feeder cells. When reaching 60-70% confluency, mESCs were induced for different times with 1 µg/ml doxycycline (see 2.6.2-2.6.6). Then, cells were stained according to a variation of RNA-SPLIT as described in sections 2.6.2 - 2.6.6 with HaloTag ligands carefully selected by conducting pilot experiments. RNA-SPLIT was determined to achieve optimal results when using the diAcFAM HaloTag ligand from Promega as HaloTag ligand 1 and the JF-585 HaloTag ligand (kindly gifted to us by Luke Lavis at HHMI Janelia, US) as HaloTag ligand 2. Initial experiments with different dye concentrations showed that a concentration of 50 nm for each of the ligands lead to optimal results. After a wash with PBS, cells were fixed for 10 min at room temperature with 2% formaldehyde prepared fresh in PBS (pH 7). A stepwise exchange of PBST5 was carried out, and cells were permeabilised with 0.2% Triton X-100 for 10 min at room temperature, followed by two washes with PBST5. Next, cells were incubated with 2 µg/ml DAPI in PBST5 for 10 min, before being washed briefly with PBS and, subsequently with ddH_2O to remove salt, and equilibrated with Vectashield mounting medium. The coverslips were mounted centrally on the unfrosted side of Superfrost Plus microscopy slides (VWR) using Vectashield soft mount media (no DAPI), sealed with clear nail polish

and imaged within a week using the DeltaVision OMX V3 Blaze system (GE Healthcare; see 2.4).

2.6.2 Nascent Xist RNA dynamics

In order to assess the transcription dynamics of Xist RNA, a total of 6 coverslips with cells were sequentially stained with two different HaloTag ligands in each experiment. For analysis of expansion, cells were induced for 1.5 h with 1 µg/ml doxycycline, while cells were induced for 24 h to study the steady state phase. Then, cells were incubated with medium containing 50 nM diAcFAM HaloTag ligand (488 nm, Promega) and 1 µg/ml doxycycline for 45 min to label pre-synthesised Xist RNA molecules, before they were washed with medium containing 1 µg/ml doxycycline for 15 min. Next, the different coverslips were incubated with 50 nM JF-585 HaloTag ligand and 1 µg/ml doxycycline for 10 min, 20 min, 30 min, 40 min, 50 min and 60 min respectively to label newly synthesised Xist RNA molecules, before being washed with PBS, and samples were prepared for imaging as described in 2.6.1. Induction and staining times with the first HaloTag ligand were staggered, such that all coverslips could be fixed at the same time despite the different staining times with the second HaloTag ligand.

2.6.3 Xist turnover on chromatin

In order to assess the turnover on chromatin of Xist RNA, 10 coverslips with cells were sequentially stained with two different HaloTag ligands for each experiment. For analysis of expansion, cells were induced for 1.5 h with 1 µg/ml doxycycline, while cells were induced for 24 h to study the steady state phase. Then, cells were

incubated with medium containing 50 nM diAcFAM HaloTag ligand (488 nm, Promega) and 1 µg/ml doxycycline for 45 min to label pre-synthesised Xist RNA molecules, before they were washed with medium containing 1 µg/ml doxycycline for 15 min. Next, the different coverslips were incubated with 50 nM JF-585 HaloTag ligand and 1 µg/ml doxycycline for 60 min, 80 min, 100 min, 120 min, 140 min, 160 min, 180 min, 200 min and 220 min respectively to label newly synthesised Xist RNA molecules, while one coverslip per experiment was not stained with the second HaloTag ligand at all and served as 0 min time point. Coverslips were washed with PBS and samples were prepared for imaging as described in 2.6.1. Induction and staining times with the first HaloTag ligand were staggered, such that all coverslips could be fixed at the same time despite the different staining times with the second HaloTag ligand. For each experiment, image acquisition was stopped once no more signal from the first HaloTag ligand could be detected in the cells for two samples in a row to minimise work load, e.g. for ChrX cells during expansion complete turnover was achieved after 140 min, and hence image acquisition was stopped after the 160 min time point.

2.6.4 Image analysis workflow

After image acquisition, reconstruction and pre-processing as described in section 2.4, images were further processed and subsequently analysed. It has to be noted that, in contrast to all other images acquired in this project, RNA-SPLIT images were only aligned later during the imaging process. First, signal with low modulation contrast (MCN) was discarded by an adapted in-house ImageJ script* based on the MCNR maps and thresholded files generated as described in 2.4.2. The MCN

*The script was adapted by Roel Oldenkamp

threshold was set at 4 with a Gaussian blur of 0.8. Next, manual thresholding of the red and green channel was performed in order to discard signal stemming from free floating BglG-Halo. Here, low intensity signal was discarded according to the fluorescence intensity histogram by eye. Usually, a clear cut off between low and high intensity signal of BglG-Halo and BglG-Halo-Xist respectively could be identified easily. However, thresholding was performed stringently with a preference for under sampling to avoid inclusion of false signal. Images, where fluorescence intensity histograms did not allow for clear distinction, were discarded and not used for analysis. Next, lateral colour channel alignment was performed as described in 2.4.3. The resulting images were used as representative images of whole nuclei throughout the project. For further analysis however, the blue channel (DAPI) was discarded, and Xist territories were cropped manually using ImageJ to exclude signal from BglG-Halo accumulation in the nucleoli or signal from other cells. The cropped dimensions were later used to define Xist territory volume during expansion and steady state in all different cell types. Representative images were selected at this stage. Maximum intensity projections were generated with ImageJ using the entire z-stack of each Xist territory for maximum intensity projection.

The resulting image files were subsequently analysed using an in-house adapted makefile script for masking of the signal and centroid determination by watershed algorithm**. The output data was used to determine the molecule numbers during expansion and steady state in all different cell types. Moreover, it was used to determine the transcription rates based on the centroid count of the HaloTag ligand labelling newly synthesised Xist RNA molecules for samples prepared according to 2.6.2, as well as the turnover of Xist RNA based on the count of the HaloTag ligand

**The script was created by David Pinto and Ezequiel Miron, and adapted by Roel Oldenkamp

labelling pre-synthesised Xist RNA molecules for samples prepared according to 2.6.3. Then, nearest neighbour analysis (NNA) and variations thereof were conducted based on the x, y and z coordinates of centroids determined previously using another in-house adapted makefile script**. Distances determined from HaloTag ligand labelling newly synthesised RNA to the HaloTag ligand labelling pre-synthesised RNA in samples prepared as described in 2.6.2 were used to assess coupling behaviour of Xist RNA during expansion and steady state in all cell types. Data from female C127 cells pulsed with EdU used previously for alignment (see 2.4.3) was used as a technical control to determine nearest neighbour distances of molecules labelled with different ligands at the same time. Here, only EdU files acquired on the days of corresponding RNA-SPLIT data acquisition were used, allowing for sample-specific matched technical controls. Additionally, 'Random' sample controls were generated in a sample-specific manner as well, by scrambling of the x, y and z coordinates of the centroids determined for newly synthesised RNA of each specific sample using Microsoft Excel. Distance distribution of this control therefore indicated, what a result obtained by random localisation of newly synthesised RNA across the Xist territory would look like.

Using a variation of the aforementioned NNA, median distances between each molecule and its ten nearest neighbouring molecules in the same channel were determined as a measure of Xist RNA density for all samples prepared as described in 2.6.2. Combined densities of newly synthesised and pre-synthesised RNA in expansion and steady state were used for comparison of Xist RNA densities in different cell types. For NPCs in particular, median distances between each molecule and all other molecules were determined as measure of Xist RNA density

**The script was created by David Pinto and Ezequiel Miron, and adapted by Roel Oldenkamp

in order to account for clustering of Xist RNA at different sites throughout the nucleus in Ciz-1 KO NPCs. For this reason, no direct comparisons were made between Xist RNA density in mESCs and NPCs.

Finally, approximate localisations of the Xist transcription site were determined for each Xist territory based on fluorescence intensity and density of the newly synthesised Xist RNA signal of ChrX mESC samples prepared as described in 2.6.2. A variation of NNA was used to measure the distance of said approximate transcription sites to all newly synthesised Xist molecules and to all pre-synthesised Xist molecules separately. In order to account for variability in Xist territory size, distances were normalised to the maximum distance measured for each territory, which was set to 1. This was then used to characterise the spreading behaviour of newly synthesised Xist RNA molecules by comparing distance distributions in relation to the transcription site over time. Here, the Xist territory was divided into 3 zones, with zone 1, 2 and 3 extending 0-50%, 50-75% and 75-100% of the maximum distance from the transcription site respectively. Then, the proportion of newly synthesised or pre-synthesised Xist RNA molecules in each zone over time was quantified. This approach allowed for the time-resolved comparison of newly synthesised Xist RNA molecule and pre-synthesised Xist RNA molecule distributions during both expansion and steady state in ChrX mESCs. Furthermore, the localisations of transcription sites could be used to assess their distribution during expansion as compared to the steady state phase. Similarly to the previous analysis, 3D coordinates of Xist transcription sites were normalised to Xist territory dimensions and Xist territories were divided into 3 zones to account for variability in

Xist territory size. The latter analysis was conducted for both ChrX and autosomal transgene mESCs.

2.6.5 Dual colour control

In order to exclude that the results obtained by NNA are not due to coupling of Xist but due to simultaneous labelling of Xist RNA molecules with BglG-Halo fusion proteins labelled with the two different HaloTag ligands, a dual colour control was performed. Here, a total of 6 coverslips with cells were stained simultaneously with the two different HaloTag ligands. ChrX mESCs were induced for 24 h with 1 µg/ml doxycycline, before being incubated with medium containing 50 nM diAcFAM HaloTag ligand (488 nm, Promega), 50 nM JF-585 HaloTag ligand and 1 µg/ml doxycycline for 45 min to label pre-synthesised Xist RNA molecules. Then, coverslips were washed with medium containing 1 µg/ml doxycycline for 15 min, followed by a wash with PBS. The samples were prepared for imaging as described in 2.6.1.

2.6.6 Dox washout experiment

In order to assess the turnover on chromatin of Xist RNA when Xist transcription is reduced, a washout of doxycycline was performed. Here, 10 coverslips with cells were sequentially stained with two different HaloTag ligands. ChrX mESCs were induced for 1.5 h with 1 µg/ml doxycycline. Then, cells were incubated with medium containing 50 nM diAcFAM HaloTag ligand (488 nm, Promega) but without doxycycline for 45 min to label pre-synthesised Xist RNA molecules, before they were washed just with medium for 15 min. Next, the different coverslips were

incubated with 50 nM JF-585 HaloTag ligand but without doxycycline for 60 min, 80 min, 100 min, 120 min, 140 min, 160 min, 180 min, 200 min and 220 min respectively to label newly synthesised Xist RNA molecules, while one coverslip was not stained with the second HaloTag ligand and served as the 0 min time point. Coverslips were washed with PBS and samples were prepared for imaging as described in 2.6.1. Induction and staining times with the first HaloTag ligand were staggered, such that all coverslips could be fixed at the same time despite the different staining times with the second HaloTag ligand. Successful reduction of Xist transcription was determined by comparison of the newly synthesised Xist RNA molecule count determined for the doxycycline washout experiment to that determined for ChrX mESCs during expansion.

2.7 SLAM-seq

2.7.1 Sample preparation

SLAM-seq of ChrX cells, as well as the corresponding parental cell line with untagged Xist, was performed using the SLAMSeq Kinetics Kit, Catabolic Kinetics Module (Cat. No. 062.24, Lexogen). Cells were grown in gelatine-coated 6-well plates after pre-plating to discard feeder cells, with 6 wells needed for each experimental replica. When reaching 60-70% confluency, cells were induced with 1 µg/ml doxycycline for 17.5 - 20 h depending on the length of the subsequent washout times. Then, transcribed RNA was labelled with 4SU by incubation with medium containing 500 µM 4SU (Lexogen) and 1 µg/ml doxycycline for 4 h. Next, 4SU was withdrawn by washout for all samples except the 0 min sample. Different samples were washed with medium containing 1 µg/ml doxycycline and 50 mM uridine (in excess, Lexogen) for 30 min, 60 min, 90 min, 120 min and 150 min respectively. Induction, 4SU labelling and withdrawal times were staggered, such that all samples could be harvested at the same time despite the different washout times. Cells were washed twice with PBS, before being scraped into 1 ml PBS with the aid of a rubber policeman. 4SU treated samples are light sensitive, hence, the next steps were carried out in amber coloured screw cap microcentrifuge tubes (ThermoFisher Scientific) to protect samples from light exposure. After cells were collected by centrifugation at 1,500 g for 5 min at room temperature, nuclear extracts were obtained as follows: Cells were washed again with PBS and resuspended in 10 volumes buffer A (10 mM HEPES pH 7.9, 1.5 mM $MgCl_2$, 10 mM KCl, 0.5 mM DTT and complete protease inhibitors in RNase free water).

Subsequently cells were incubated on ice for 10 min and recovered by centrifugation at 1,500 g for 5 min, followed by resuspension in 3 volumes buffer A with 0.1% NP-40 for 10 min with some gentle inversions. Nuclei were recovered by centrifugation at 1,500 g for 5 min. Next, an RNA extraction was performed. Here, 200 µl TRIzol were added to each pellet, followed by incubation at room temperature for 5 min. Samples were stored at -80 °C for continuation the next day. The following day, the lysate was thawed and incubated at room temperature for 5 min, before 40 µl chloroform:isoamyl alcohol mix (24:1) were added to every 200 µl of TRIzol lysate. Samples were shaken vigorously for 15 s and then incubated at room temperature for 3 min. Phases were separated by centrifugation at 16,000 g for 15 min at 4 °C and the colourless upper aqueous phase of each sample was transferred to a new tube each. Next, 1 µl of Carrier Substance (Lexogen), 1/1000th volume of Reducing Agent (Lexogen), and 1 volume of 2-propanol were added to each aqueous phase, and samples vortexed well. After an incubation of 10 min at room temperature, RNA containing pellets were obtained by centrifugation at 16,000 g for 20 min at 4 °C and the supernatant was removed. The pellets were washed with 500 µl EtOH and 0.5 µl of Reducing Agent (Lexogen) each. Samples were vortexed well and then centrifuged at 7,500 g for 5 min at 4 °C. After removal of the supernatant, pellets were air dried for 5-10 min and resuspend in 16 µl of Elution Buffer (Lexogen). Resuspended RNA samples were incubated for 10 min at 55 °C shaking, before the RNA concentration was measured by nanodrop. Based on this, RNA was diluted with nuclease free water to achieve a final amount of 5 µg of RNA in 15 µl water. Finally, samples were treated with iodoacetamide to modify the 4-thiol group of S4U-containing nucleotides via the addition of a

carboxyamidomethyl group. For this, 1 tube of Iodoacetamide (Lexogen) was dissolved in 500 µl of 100% EtOH to give 100 mM final concentration. A mastermix containing 5 µl of the freshly prepared iodoacetamide (Lexogen), 25 µl Organic Solvent (Lexogen), and 5 µl of sodium phosphate (Lexogen) per sample. The previously prepared RNA samples were then incubated with 35 µl of the master mix each at 50 °C for 15 min. The reaction was stopped by addition of 1 µl Stopping Reagent (Lexogen) and thorough mixing. At this stage, samples were no longer light sensitive, and therefore all samples were transferred to clear tubes. Then, 1 µl of Carrier Substance (Lexogen), 5 µl of sodium acetate (Lexogen), and 125 µl of 100% EtOH were added to each sample. Samples were vortexed and the RNA was precipitated for 30 min at -80 °C. RNA pellets were obtained by centrifugation at 16,000 g for 30 min at 4 °C and the supernatant was removed. Subsequently, the pellets were washed with 1 ml 75% EtOH and vortexed again, before being centrifuged at 16,000 g for 10 min at 4 °C to recover the pellets. The supernatant was removed and the pellets were dried for 5-10 min. Pellets were resuspended in 10 µl nuclease free water each, and 1 ng RNA of each sample were run on the bioanalyzer to determine the exact RNA concentration and RNA integrity of all samples. Based on this, 1 µg RNA of each sample was then taken forward for library preparation using the Illumina TruSeq stranded total RNA kit (RS-122-2301). Quantification of the libraries was performed by qPCR using KAPA Library Quantification DNA standards (Kapa Biosystems, KK4903). Finally, the libraries were pooled and 2×81 e-end sequencing was performed using Illumina NextSeq500 (FC-404-2002).

2.7.2 Data Analysis

Estimation of nuclear RNA half-life was performed using GRAND-SLAM (Jürges, Dölken, and Erhard 2018). Briefly, the paired-end sequencing reads were mapped to mouse genome mm10 by STAR (v2.5.2b) (Dobin et al. 2013) with the key parameters (--outFilterMultimapNmax 1 --outFilterMismatchNmax 999 --alignEndsType EndToEnd). Given that T to C conversion is the signature of SLAM-seq, the T to C conversion rate was calculated as 4SU incorporation and the average of all the rest conversions was calculated as background due to errors from sequencing or library preparation. The T to C conversion rate and background rate were calculated accordingly for each sample. The nuclear RNA decay was assumed to follow an exponential model, so the T2C conversion rate (or T2C conversion rate -corresponding background rate) was fitted to the exponential model to estimate RNA's half-life in nucleus. In addition, the sample (Dox-treated A11B2 cells, ChrRNA-seq) (Nesterova et al. 2019) without 4SU incorporation was used to estimate the background mutation rate for all 12 potential mismatches. Half-life of Xist RNA and other nuclear RNAs were plotted.

*Analysis of all SLAM-seq data was performed by Guifeng Wei

2.8 Chromatin RNA sequencing to assess silencing

2.8.1 Sample preparation

For chromatin RNA sequencing experiments, cells were grown in gelatine-coated T25 flasks with Mitomycin C inactivated feeder cells. When confluent, cells were pre-plated for 40 min twice to discard the feeder cells, and expanded to gelatine-coated 15 cm dishes. Before chromatin RNA extraction, cells were induced for 3 h or 24 h with 1 µg/ml doxycycline to study expansion and steady state respectively. A control sample comprising cells without addition of doxycycline was included with the analysis of each cell line. Chromatin RNA for each sequencing replica was extracted from one confluent 15 cm dish of cells. Cells were detached by addition of 5 ml PBS to each plate and scraping off with rubber policemen. Then, cells were transferred to a 15 ml Falcon tube each and the remaining cells on each plate were retrieved by washing with PBS. Pellets were obtained by centrifugation at 1,000 rpm for 3 min at room temperature, and were snap frozen on dry ice (pellets could be stored at -80 °C at this point). Next, pellets were resuspended in RLB (10 mM Tris pH 7.5, 10 mM KCl, 1.5 mM $MgCl_2$, and 0.1% NP40) and incubated on ice for 5 min to lyse the cells. Nuclei were purified by centrifugation through a sucrose cushion (24% sucrose in RLB) at 2,800 g for 10 min at 4 °C. The pellets were resuspended in NUN1 (20 mM Tris pH 7.5, 75 mM NaCl, 0.5 mM EDTA, 50% glycerol), and subsequently lysed with NUN2 (20 mM HEPES pH 7.9, 300 mM, 7.5 mM $MgCl_2$, 0.2 mM EDTA, 1 M urea). Samples were incubated for 15 min on ice, vortexing occasionally, before being centrifuged at 2,800 g for 10 min at 4 °C to isolate the

insoluble chromatin fraction. TRIzol/chloroform RNA extraction was performed to extract the chromatin-associated RNA from the pellets. Here, the pellets were resuspended in 750 µl TRIzol each and homogenised by passing multiple times through a 23 gauge needle. Then, 150 µl chloroform: isoamyl was added to each sample, before vortexing and inversion of the samples. After an incubation of 3 min at room temperature, samples were centrifuged at 12,000 g for 15 min at 4 °C. The upper aqueous phase was transferred to RNase free tubes and 375 µl isopropanol was added to each sample. Samples were mixed well and incubated for 10 min at room temperature, followed by centrifugation at 12,000 g for 10 min at 4 °C. Resulting pellets were washed with 750 µl 75% EtOH each and recovered by centrifugation at 9,500 rpm for 5 min at 4 °C. Finally, pellets were air dried and dissolved in 100 µl ddH_2O each. Samples were then treated with Turbo DNase and the RNA was purified by RNeasy column cleanup (Qiagen). 100 ng - 1 µg RNA of each sample were taken forward for library preparation using the Illumina TruSeq stranded total RNA kit (RS-122-2301). Quantification of the libraries was performed by qPCR with KAPA Library Quantification DNA standards (Kapa Biosystems, KK4903). Finally, the libraries were pooled and 2×81 paired-end sequencing was performed using Illumina NextSeq500 (FC-404-2002).

2.8.2 Data analysis

The analysis strategy that was used for chromatin RNA sequencing has been described in detail in a recent paper published by the lab (Nesterova et al. 2019)*. In summary, raw fastq files of read pairs were mapped to an rRNA build by bowtie2 (v2.3.2), while rRNA-mapped reads were discarded. Remaining unmapped reads

*Analysis of all chromatin RNA sequencing data was performed by Guifeng Wei

were aligned to the “N-masked” genome (from mm10 coordinates) with STAR (v2.4.2a) using parameters “–outFilterMultimapNmax 1 –outFilterMismatchNmax 4 –alignEndsType EndToEnd”. Unique alignments were retained for further analysis. 23,005,850 single nucleotide polymorphisms (SNPs) between Cast and 129S genomes were identified. These were used to split the alignment into distinct alleles (Cast and 129S) with the help of SNPsplit (v0.2.0; Babraham Institute, Cambridge, UK). The allelic read numbers were counted using the program featureCounts (-t transcript -g gene_id -s 2; Liao et al. 2014), while the alignments were sorted by Samtools (Li et al. 2009). For bi-allelic analysis, counts were normalised to one million mapped read pairs using the edgeR R package. Genes with a minimum of 10 SNP-covering reads across all the samples were further taken to calculate the allelic ratio of Xi/(Xi+Xa). Here, Xi and Xa indicate the inactive and active allele, respectively. Xist mediated gene silencing during expansion and steady state was determined by the difference in the aforementioned allelic ratios between uninduced and doxycycline induced samples, as well as the different time points. This analysis also allowed for the comparison of Xist mediated gene silencing in ChrX mESCs and the CIZ-KO, SPEN RRM del and SPOC mut cell lines generated as described in 2.1.

2.9 Western blot

For the Western blot experiment, the different potential Ciz-1 KO clones, and WT cells serving as control, were grown in gelatine-coated T25 flasks each with Mitomycin C inactivated feeder cells. When confluent, cells were pre-plated for 40 min twice to discard the feeder cells, and subsequently plated in a well of a gelatine-coated 6-well plate each. When confluent, cells were washed with PBS and detached using TrypLE Express (ThermoFisher Scientific). Cells were resuspended in medium and transferred to a 15 ml Falcon tube each, before centrifugation at 1,000 rpm for 3 min at room temperature. Resulting pellets were resuspended in 5 ml medium each and cells in each sample were counted using a Neubauer chamber. Based on this, $3x10^6$ cells of each clone were pelleted. The pellets were washed with PBS and spun down again at 1,000 rpm for 3 min at room temperature, before the supernatant was removed. Each pellet was then dissolved in 200 µl 2x SMASH buffer (33 mM TrisHCl (pH 6.8), 11% glycerol, 40 mg/ml SDS, 200 µg/ml bromophenol blue and 10% β-mercaptoethanol in nuclease free water) and transferred to a microcentrifuge tube each. Samples were left shaking for 20 min, and then snap frozen on dry ice for 30 min. Samples were thawed once, before being stored at -80 °C.

Samples were then separated by sodium dodecyl sulphate (SDS) polyacrylamide gel electrophoresis (8% separating gel and 5% stacking gel) at 80 V for 15 min, and then at 180 V for another 70 min. Next, samples were transferred onto a polyvinylidene difluoride (PVDF) membrane by semi-dry transfer at 15 V for 1 h. The membrane was blocked by incubation with 10 ml PBS, 0.1% Tween (PBST) with 5%

w/v Marvel milk powder for 1 h at room temperature. The blot was cut in half to allow for detection of tubulin as a control. Then, the two halves were incubated with the corresponding primary antibody each (CIZ-1, anti-rabbit, affinity purified, polyclonal (a kind gift from the Coverley lab, University of York); and tubulin, anti-rabbit, Cell Signaling, Cat. No 2144) diluted 1:1000 in PBST with 5% w/v Marvel milk powder at 4 °C overnight. The membrane was washed 3 times in PBST with 5% w/v Marvel milk powder for 10 min each, before being incubated with secondary antibody conjugated to horseradish peroxidase (anti-rabbit, HRP linked, Amersham) diluted 1:1000 in PBST with 5% w/v Marvel milk powder for 1 h. Next, the membrane was washed with PBST with 5% w/v Marvel milk powder once to rinse and then twice shaking for 15 min each. After a wash with PBST only, shaking for 15 min, the membrane was rinsed with PBS once and then washed shaking for 5 min. Bands were visualised using ECL (GE Healthcare) for antibody detection.

2.10 Southern blot

For the Southern blot experiment*, the different potential SPEN RRM del clones, and WT cells serving as control, were grown in gelatine-coated T25 flasks each with Mitomycin C inactivated feeder cells. When confluent, cells were pre-plated for 40 min twice to discard the feeder cells, and subsequently plated in a well of a gelatine-coated 6-well plate each. After passaging the cells once, they were grown until confluent. Then, cells were washed 3 times with PBS, before 1 ml Lysis Buffer (10 mM NaCl, 10 mM Tris pH 7.5, 10 mM EDTA pH 8, 0.5% Sarcosyl; filter sterilised; 1 mg/ml Proteinase K added fresh) was added directly to each well to lyse the cells completely. Each lysate was transferred to a 2 ml Eppendorf tube and incubated at 55 °C shaking at 300 rpm overnight.

To extract the DNA, 1 ml of phenol chloroform (pH 8) was added to each sample and samples were mixed by inverting manually until a transiently homogenous suspension was formed. Then, samples were rocked at room temperature for ~1 h, before the total volume of each sample was transferred to a MaXtract High Density tube (Qiagen) each. After centrifugation at 1,500 g for 5 min to separate the phases, each upper, nucleic acid containing, aqueous phase was carefully removed by decanting into a fresh 50 ml Falcon tube. 1/25 5M NaCl was added to each tube and samples were mixed by inversion. Next, 2.5 volumes of 100% cold EtOH were added to precipitate the DNA and the tubes were inverted gently. Using a pre-wet 1 ml cut tip the DNA was spooled into 1 ml 70% EtOH in an Eppendorf tube. Then, samples were centrifuged for 5 min at maximum speed and the EtOH was removed.

*The Southern blot protocol was kindly shared and all hot lab work was performed by Tatyana Nesterova

The pellets were dried at room temperature for 10 - 15 min and finally DNA of previously confirmed SPEN RRM del cells were received and used as a control**.

Next, an EcoRV restriction digest of the samples was performed. Here, 6 µg of DNA each were incubated with 10x Cutsmart Buffer (NEB) and 1.5 µl EcoRV HF (NEB) at 37 °C overnight. Then, concentrations were measured using the nanodrop and samples were diluted such as to contain 5 µg DNA each for loading on a 1% EtBr agarose gel. The gel was run for ~4 h at 50 V, before it was transferred to a tray with depurination solution (0.125 M HCl in MiliQ water) and rotated gently for 15 min. The gel was then rinsed in ddH_2O. The denaturation buffer (0.5 M NaOH, 1.5 M NaCl in Milli-Q water) was added and the gel was rotated gently for 45 min. The gel was again rinsed with water, before neutralisation buffer (0.5 M Tris, 1.5 M NaCl in Milli-Q water, pH 8) was added and the gel was rotated gently for 30 min.

Subsequently, the capillary transfer was assembled as follows: A tray was filled with 10x SSC and a glass plate on top. A wick was made from 3 sheets of Whatman 3MM paper over the glass plate and wet with 10x SSC. An Immobilon NY+ membrane (Millipore) was cut to the same size as the gel and pre-wet in 2x SSC. Then, the gel was placed upside down onto the wick and air bubbles were removed. Parafilm was used to stick around the gel and the Immobilon membrane was placed on the gel avoiding air bubbles. 3 sheets of Whatman 3MM paper were placed over the Immobilon membrane and bubbles were removed once more. Stacks of paper towels were placed on top, followed by a plate with about 500 g weight.

After capillary transfer overnight for at least 18 h, the assembly was dismantled and

**The control samples were kindly provided by Tatyana Nesterova

the Whatman paper-gel-membrane-Whatman sandwich was flipped upside down. Positions of the wells were gently marked on the membrane with a pencil. Then, the membrane was rinsed briefly in 2x SSC to remove any pieces of agarose and excess of salts. The blot was air dried for 15 - 20 min, before it was UV crosslinked using the optimal crosslink button on the Stratalinker. The membrane was placed in a hybridisation tube with the DNA side facing the interior and ~20 mL of Dextran - SLS - SCC hybridisation solution pre-warmed to 65 °C (83 mg/ml Dextran Sulphate, 5x SSC and 0.875% N-Lauryl sarcosine Sodium Salt solution in MiliQ water filtered through a 0.8 µM membrane before addition of 48 µg/ml denatured sheared salmon sperm DNA just before use) was added to the tube. Pre-hybridisation was carried out for ~1 h at 65 °C. In the meantime, the probe was prepared using the prime-H II kit (Stratagene) as follows: A 626 bp fragment downstream of the sgRNA used for the SPEN RRM del in exon 12 (Table 1) was excised from a template plasmid by restriction digest and gel purified. 25 - 30 ng of this probe DNA was mixed with 10 µl of 9-mer primer (final volume 34 µl). The probe was boiled at 95 °C for 5 min and spun briefly, before being placed on ice. Then, 10 µl of 5x dATP buffer were added. In the hot lab, 5 µl alpha -32 ATP and 1 µl exo(-) Klenow (5 U/µl) were added. The probe was mixed well and kept at 37 °C for 10 min. 2 µl STOP buffer was added, the probe was mixed and quickly placed on ice. Finally, the probe was purified using a G50 Micro column (GE Healthcare): The column was vortexed, the cap was loosened one quarter turn and the column was placed in the collection tube. The column was spun at 735 g for 1 min, before it was placed in a screw top Eppendorf tube and the hot probe was added. The cap was then loosened another quarter turn, before the column was spun at 735 g for 2 min. The column was discarded,

and the probe was boiled in the capped Eppendorf tube for 5 min at 95 °C. The denatured probe was placed on ice for at least 1 min. Radioactivity of the probe before and after the purification was compared to determine an incorporation yield of ~70.5%, which was deemed sufficient for the experiment. The probe was added to the hybridisation mixture and membrane in the hybridisation bottle, and was hybridised overnight at 65 – 67 °C.

The next day, the membrane was washed twice with low stringency at 65 °C for 15 min each. It was subsequently removed, wrapped in Saran wrap and exposed in a Fuji cassette overnight, before it was scanned on a FLA-7000 (Fujifilm). Mutant bands were detectable at 2.64 kb, while WT bands were detectable at 4 kb.

2.11 Statistical analysis

For the comparison of two independent large datasets throughout the project, statistical significance was determined by conducting an unpaired two-sample Wilcoxon test using R. This statistical test determines whether it is equally likely that a randomly selected value from one dataset will be less than or greater than a randomly chosen value from another population, making it ideal to determine whether two large datasets have the same distribution. Hence, the unpaired two-sample Wilcoxon test was used as a non-parametric alternative to the unpaired t-test to determine statistical significance.

CHAPTER III

3 Super-resolution RNA-SPLIT – a new method to assess RNA dynamics and localisation

3.1 BglI-stem-loop tagging of Xist RNA in combination with HaloTag technology and 3D-SIM allows for detection of individual Xist foci

3.1.1 Generation and characterisation of the ChrX ES cell line

The mESC model system with doxycycline inducible Xist RNA is one of the most widely used and practical tools to study XCI. Controlled doxycycline induction of Xist allows for a more homogenous induction than is seen with expression from the natural promoter during differentiation, where commencement of Xist transcription occurs progressively over several days. Therefore, the results obtained using the inducible system are more reliable and easier to interpret.

XX mESC lines tend to be unstable in culture, often losing one of their X chromosomes over time. As an alternative, genetically engineered inducible Xist inserted on an autosome can establish transcriptional silencing *in cis*. Despite the many striking discoveries made using this model system, it is evident that autosomal Xist does not silence as efficiently as endogenous Xist, attributed at least in some cases to attenuated spreading (Popova et al. 2006). This highlights the importance of stable XX mESC lines with inducible endogenous Xist to study Xist RNA dynamics and spreading behaviour. Recently, our lab has generated such a line (iXist-ChrX) (Nesterova et al. 2019), where the endogenous Xist promoter has been

replaced by a doxycycline inducible promoter using CRISPR/Cas9 genome engineering (Figure 6a). Moreover, the line is interspecific allowing for allelic analysis of transcriptional silencing and making it a useful tool to study XCI (Figure 6a). Chromosomal rearrangement during derivation, however, means that informative single nucleotide polymorphisms (SNPs) are present only for 103 Mb proximal to Xist (Nesterova et al. 2019) (Figure 6a). In this project, XX mESCs with inducible endogenous Xist RNA, as well as XY mESCs with inducible autosomal transgenic Xist RNA, were used to study the localisation, dynamics and spreading behaviour of Xist RNA during the early phases of XCI. Comparison of Xist RNA behaviour in the context of autosomal transgenes and that of the Xi will yield important insights into Xi specific behaviour of Xist (discussed in detail in Chapter 3.1.2).

The MS2 system, as well as other stem-loop based RNA labelling systems, have allowed for *in vivo* analysis of RNA dynamics by live imaging. In this system, an array of RNA stem-loops is inserted into the genomic sequence of the RNA of interest (Figure 6b). Furthermore, the cells are genetically engineered to express a fluorescently labelled protein that binds the aforementioned loops with high affinity (Figure 6b). The comparable BgI-stem-loop labelling system used in this project has been shown to be suitable for use in mESCs (Moindrot et al. 2015). In previous work in the lab, BgIG expression was found to reduce over time in culture. To overcome this the transgene encoding the BgIG fusion protein was engineered to be doxycycline inducible.

The inducible BglG protein was labelled with HaloTag technology (Figure 6b). Here, addition of small organic dyes, the HaloTag ligands, to live cells allows for visualisation of the RNA (Figure 6b). Specific HaloTag ligands used in this work have high photostability and brightness having been developed for live and super-resolution imaging (Grimm et al. 2017). Moreover, different ligands can be used interchangeably allowing for the use of different wavelengths. Cells were first transfected with a vector encoding the doxycycline inducible BglG-Halo protein, and clones with successful integration were selected by PCR analysis of the gDNA (Figure 6c). Then, an array of Bgl-stem-loops was inserted towards the 3' end of the endogenous Xist locus within exon 7 using CRISPR/Cas9 genome engineering and a homology vector (Figure 6b). Specifically, an array of 18 stem-loops was used, as it was predicted to provide a sufficient signal to noise ratio of stem-loop-bound to unbound BglG-Halo (Moindrot et al. 2015) (Figure 6b). Successful insertion was screened for by PCR analysis of the gDNA (Figure 6d). Xist RNA FISH was then performed to ensure there was no polyploidy or X chromosome aneuploidy (Figure 6e). Finally, HaloTag staining was conducted to identify the clone with the most suitable BglG-Halo expression levels to take forward (Figure 6f).

Traditionally, RNA FISH has been used to visualise Xist RNA. Full length Xist RNA FISH in combination with HaloTag ligand staining in the ChrX cells showed successful labelling of distinct Xist particles using the Bgl-stem-loop system in combination with HaloTag technology (Figure 7a). Noticeably, most Xist RNA FISH domains were associated with two to three BglG-Halo-Xist foci (Figure 7a). This suggests that the BglG-stem-loop labelling system better resolves individual Xist

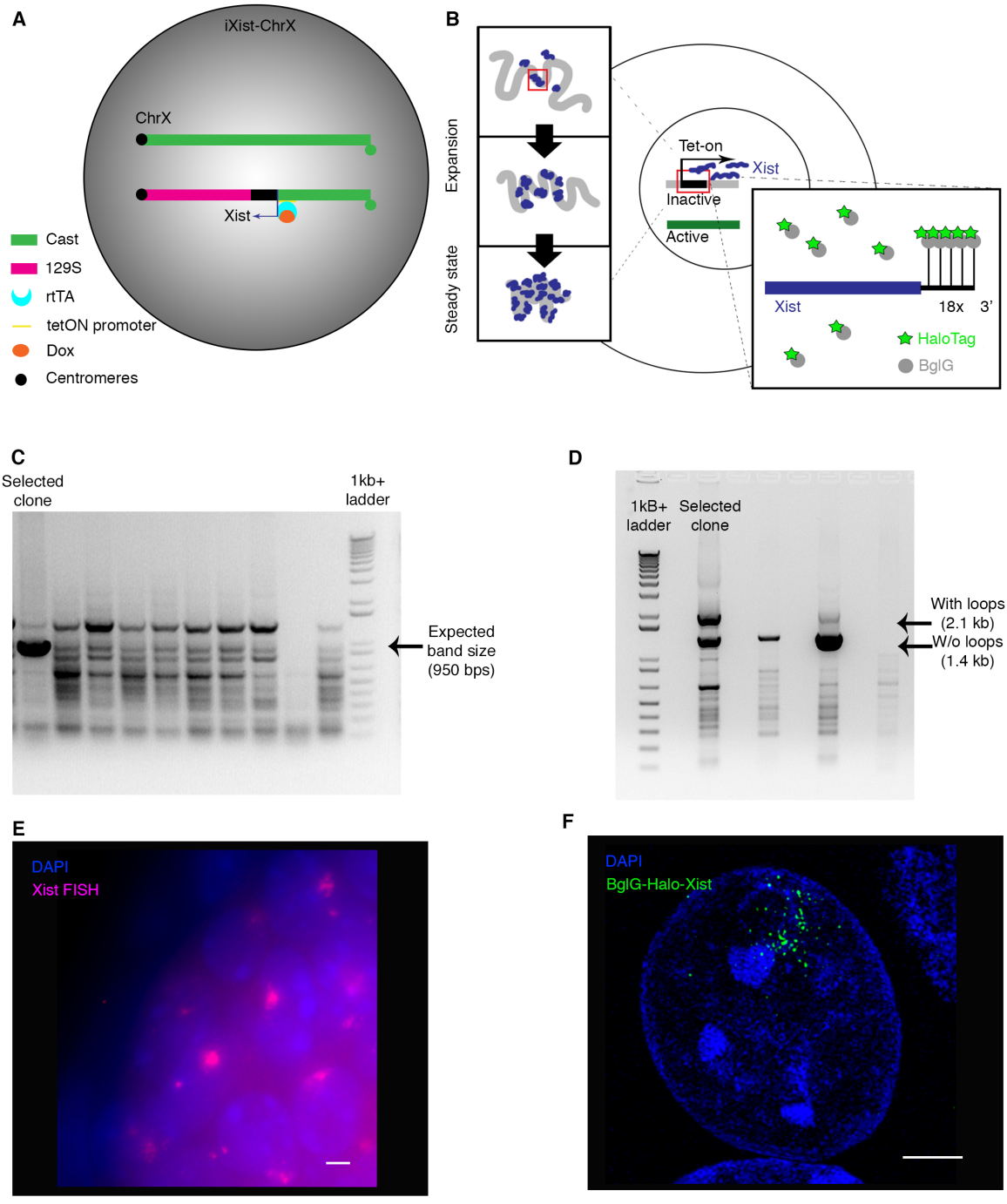

Figure 6: Generation of XX mESCs with inducible endogenous BglG-Halo-Xist. A) Schematic drawing describing the interspecific iXist-ChrX XX mESC line used as parental cell line in this project, including the doxycycline inducible Xist promoter. B) Schematic drawing illustrating the use of the Bgl-stem-loop system in combination with HaloTag technology to assess Xist RNA dynamics at different stages of XCI. C) PCR screen of gDNA for insertion of the BglG-Halo genomic sequence run on an EtBr Agarose gel, including 1kb+ ladder. Expected band size for successful insertion is 950 bps. D) PCR screen of gDNA for insertion of the Bgl-stem-loop sequence run on an EtBr Agarose gel, including 1kb+ ladder. Expected band size for insertion is 2.1 kb, while a band at 1.4 kb indicates the presence of one or more alleles without insertion. E) Representative image of Xist RNA FISH with DAPI counter stain of ChrX cells 3 h post-induction, visualised with a Zeiss fluorescence microscope. Maximum intensity projection. Scale bar corresponds to 5 μm. F) Representative image of HaloTag staining and DAPI counter stain of ChrX cells in expansion, visualised by 3D-SIM. Maximum intensity projections. Scale bar corresponds to 5 μm.

foci, and that Xist foci tend to accumulate in pairs or triplets. Visualisation of single Xist foci was confirmed by the observation of similar intensity profiles and similar sizes of BglG-Halo-Xist foci. Centroid determination by watershed algorithm showed that, while two or more centroids can often be assigned to each Xist RNA FISH signal, just one centroid can be assigned to each BglG-Halo-Xist signal. Additionally, comparison of the same sample acquired with widefield microscopy and 3D-SIM convincingly underlines the importance of using super-resolution microscopy to study Xist localisation and dynamics (Figure 7a).

Identification of Xist RNA FISH domains associated with only one BglG-Halo-Xist signal allowed for an estimate of Xist foci size and shape based on the full-length labelling of Xist with RNA FISH (Figure 7b). Xist foci were found to be of globular shape and measure approximately 200 nm across all three dimensions (Figure 7b). Moreover, it can be noted that the BglG-Halo-Xist foci were located predominantly at the chromatin boundaries, while the Xist RNA FISH signal extended throughout the inter-chromatin space (Figure 7b). This hints at a potential anchoring of Xist to the chromatin through its 3' end.

Since the BglG fusion protein was engineered to be inducible and the project aims to assess Xist RNA behaviour during early stages of spreading, it is of utmost importance that labelling of Xist RNA occurs at or immediately after transcriptional induction with doxycycline. To ensure that this was the case, Xist RNA was visualised using RNA FISH and HaloTag staining in parallel at different time points post-induction starting at 1 h 45 min (Figure 7c). Labelling of Xist RNA with BglG-Halo could be detected even at the earliest time point and BglG-Halo-Xist co-

localised with the Xist RNA FISH signal as the Xist territory expanded in size over the first 5 h of induction (Figure 7c).

Using the BglG-stem-loop system allowed for the quantification of the increase of Xist molecules over time by centroid counting after image reconstruction and thresholding (Figure 7d). A gradual increase in the number of Xist molecules could be seen in the first 5 h of induction, which makes this the ideal time window to study the initial spreading of Xist across the Xi territory (Figure 7d). This is in line with a previous study by Engreitz et al., where Xist binding to the chromatin was assessed by Xist RAP during the first 6 hours of Xist induction (Engreitz et al. 2013). Hence, the matched time window will allow for the direct comparison of the acquired data with the aforementioned study. It has been suggested that Xist spreads to sites in close spatial proximity to the XIC, before new sites become accessible through silencing induced chromatin changes (Engreitz et al. 2013; Simon et al. 2013) (Figure 6b). This phase will be referred to as 'expansion' (Figure 6b). Once Xist has expanded across the chromosome and all sites have become accessible, Xist is maintained on the Xi through constant transcription in a phase that will be referred to as 'steady state' (Figure 6b). Based on the observations from the time course experiments, Xist will be induced for 3 h and 24 h as representative of behaviour in expansion and steady state respectively in all further experiments (Figure 6b).

Molecule number and thus volume of Xist RNA clouds can vary a lot, even within a given time point and especially in expansion when cells are first induced (Figure 7d). Therefore, it is necessary to quantify the colocalisation of Xist RNA FISH with BglG-Halo Xist signal across a number of cells to validate efficient labelling. For this

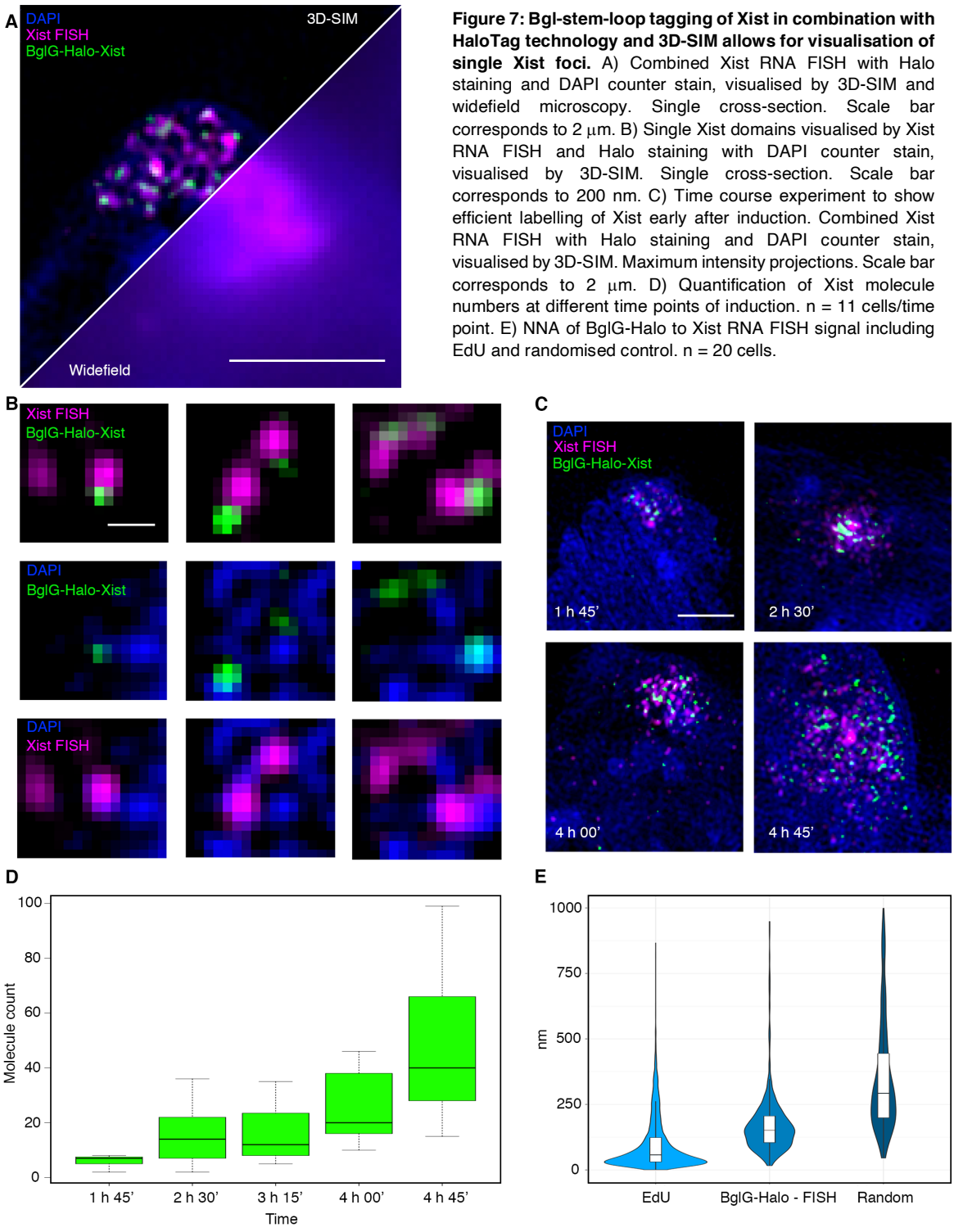

Figure 7: Bgl-stem-loop tagging of Xist in combination with HaloTag technology and 3D-SIM allows for visualisation of single Xist foci. A) Combined Xist RNA FISH with Halo staining and DAPI counter stain, visualised by 3D-SIM and widefield microscopy. Single cross-section. Scale bar corresponds to 2 μm. B) Single Xist domains visualised by Xist RNA FISH and Halo staining with DAPI counter stain, visualised by 3D-SIM. Single cross-section. Scale bar corresponds to 200 nm. C) Time course experiment to show efficient labelling of Xist early after induction. Combined Xist RNA FISH with Halo staining and DAPI counter stain, visualised by 3D-SIM. Maximum intensity projections. Scale bar corresponds to 2 μm. D) Quantification of Xist molecule numbers at different time points of induction. n = 11 cells/time point. E) NNA of BglG-Halo to Xist RNA FISH signal including EdU and randomised control. n = 20 cells.

purpose nearest neighbour analysis (NNA) was applied, where the distance from each BglG-Halo-Xist signal to the nearest Xist RNA FISH signal was measured (Figure 7e). Female mouse epithelial C127 cells, pulsed with EdU such that each

RNA molecule was stained in two different colours, were used as technical control and showed a median NNA distance of 57 nm (Figure 7e). BglG-Halo-Xist showed clear colocalisation with Xist RNA FISH at a median NNA distance of 152 nm as compared to the randomised control with a median NNA distance of 300 nm (Figure 7e). To conclude, labelling of Xist RNA was found to be efficient across different cells and time points.

A potential concern with this approach is that steric hindrance of BglG fusion proteins binding to the loop array, as well as imperfect labelling efficiency of the Halo ligand, might significantly reduce the number of bound and fluorescent BglG fusion proteins. In order to assess this, the mean fluorescence intensity of detected molecules within the Xist territory was compared with that of molecules detected in other areas of the nucleus, where only free floating BglG fusion proteins should be present (Figure 8a). The intensity fold change, which is sufficient for confident thresholding, indicates that between 2-4 labelled BglG-molecules are bound to one Xist molecule at any given time (Figure 8a).

To address concerns that insertion of Bgl-stem-loops could alter the functionality of Xist, chromatin RNA sequencing after 24 h of doxycycline induction was performed for the BglG-Halo-Xist cell line and the corresponding parental cell line (Figure 8b). No significant difference could be detected, confirming that addition of the Bgl-stem-loops does not alter Xist RNA function in relation to transcriptional silencing in *cis* (Figure 8b).

To further confirm that BglG-Halo-Xist is fully functional, recruitment of the localisation factor CIZ-1, induction of Xist-dependent Polycomb-mediated histone

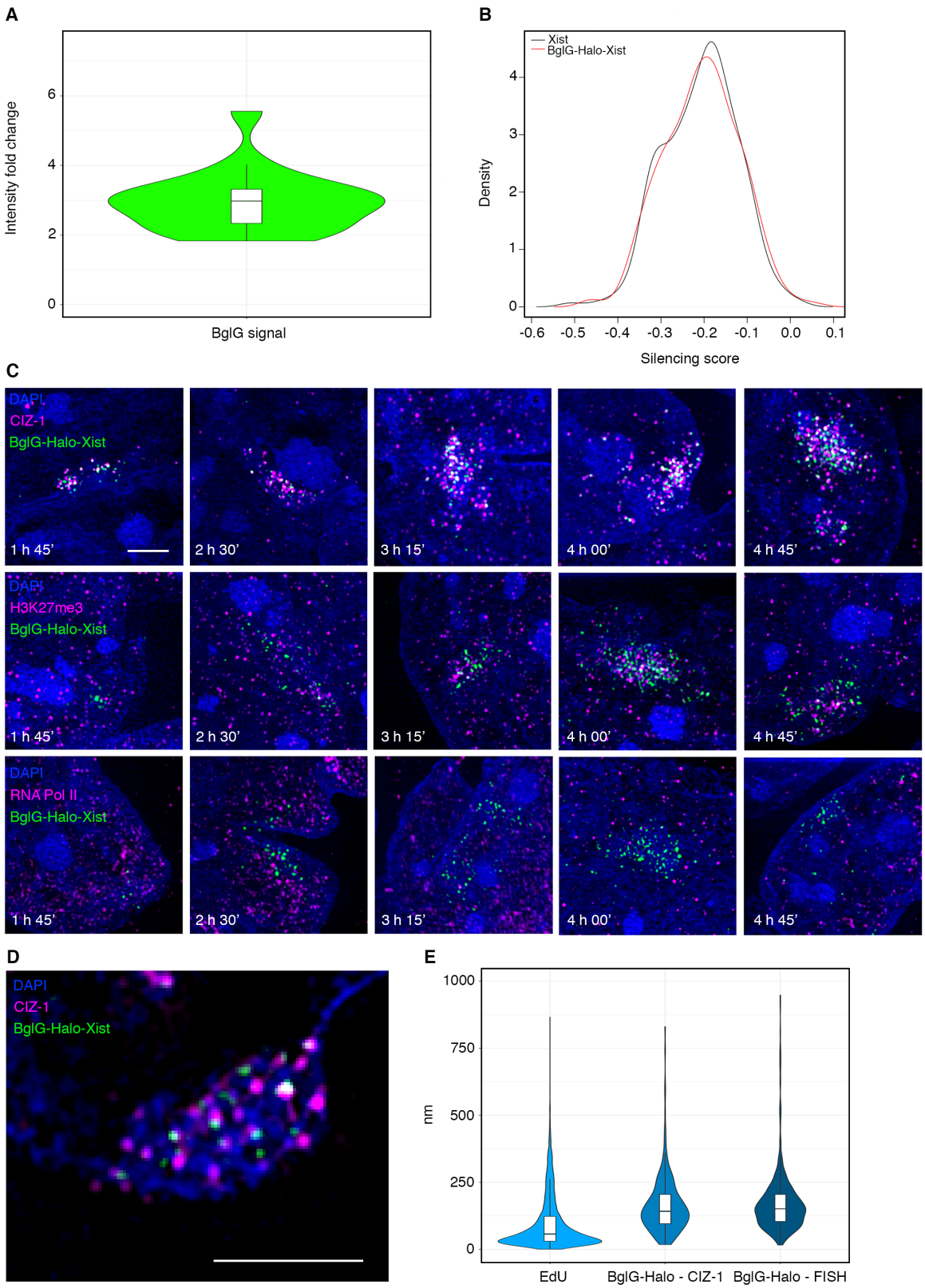

Figure 8: Insertion of the bgl-stem-loop array does not alter Xist functionality. A) Intensity fold change of fluorescence detected within the Xist territory vs the rest of the nucleus. n = 10 cells. B) Comparison of Xist RNA induced silencing 24 h post-induction in the BglG-Halo-Xist (red) and corresponding parental line (black). Silencing scores were obtained by comparing transcription of X-linked genes from both alleles after chromatin RNA sequencing. n = 242, bandwidth = 0.02581. C) Time course of immunostaining of CIZ-1 (top), H3K27me3 (middle) and RNA Pol II (bottom) in combination with HaloTag and DAPI staining, visualised by 3D-SIM. Maximum intensity projection. Scale bar corresponds to 2 μm. D) Close up of Immunostaining of CIZ-1 in combination with Halo staining and DAPI counter stain, visualised by 3D-SIM. Single cross-section. Scale bar corresponds to 2 μm. E) NNA of BglG-Halo to CIZ-1 signal, as well as BglG-Halo to Xist RNA FISH signal including EdU control. n = 20 cells

modifications (H3K27me3) and exclusion of RNA polymerase II from the Xi, were all assessed (Figure 8c). CIZ-1 was observed to be closely associated with Xist from as early as 1 h 45 min post-induction and throughout the expansion phase, while H3K27me3 enrichment could be seen from 4 h post-induction (Figure 8c). The exclusion of Pol II coincides with this time line, with exclusion detected as early as 3 h 15 min post-induction in some cells (Figure 8c). Considering these observations and the normal X chromosome silencing profile confirmed by chromatin RNA sequencing (Figure 8a and 8c), it can be concluded that BglG-Halo-Xist behaviour, localisation and dynamics reflect that of unmodified Xist and therefore validate that this is an appropriate system to take forward for further analysis.

When performing the immunostaining for CIZ-1, it was noticeable that the signal is very closely associated with each single BglG-Halo-Xist signal (Figure 8d). Remarkably, NNA showed a median distance of 140 nm from BglG-Halo-Xist to CIZ-1, which is even lower than the measurement of BglG-Halo-Xist to Xist RNA FISH signals. This observation is consistent with data showing that CIZ-1 interacts with Xist RNA towards the 3' end (Ridings-Figueroa et al. 2017; Sunwoo et al. 2017), where the Bgl stem loops are also located (Figure 8e).

3.1.2 Generation and characterisation of the autosomal transgene ES cell line

Comparison of endogenous with autosomal transgenic Xist could potentially allow for more insight into how Xist localisation and spreading depends on chromosomal context. Although the results might differ from one autosomal transgene line to another and therefore have to be interpreted with caution, this could help explain why autosomal transgenic Xist does not silence as efficiently as endogenous Xist.

Hence, an XY mESC line with inducible autosomal transgenic BglG-Halo-Xist was generated by co-transfection of male P4D7 mESCs with a vector encoding the doxycycline inducible BglG-Halo protein and a vector encoding doxycycline inducible Xist with Bgl-stem-loops. As previously described for the ChrX cell line, an array of 18 Bgl-stem-loops was placed within Exon 7 of the autosomal transgenic Xist. Positive clones were selected by PCR analysis of the gDNA and Xist RNA FISH was carried out to identify clones with autosomal transgenic Xist expression (Figure 9a and 9b). A cell line suitable for further analysis was selected based on BglG-Halo expression levels after HaloTag staining. Chromatin RNA sequencing was performed to assess silencing after 24 h doxycycline induction and determine the location of integration (Figure 9c). A reduction of transcription was detected on one allele of chromosome 15, although the silencing effect was relatively weak, as expected for autosomal transgenic Xist (Figure 9c and 9d).

Due to possible multi-copy insertion Xist expression can vary largely between different autosomal transgene Xist cell lines. Quantification of the number of Xist molecules in expansion and steady state in both the ChrX and autosomal transgene cell line showed that Xist molecule numbers decrease significantly from expansion to steady state (Figure 10a). Because of the need to compare two independent large datasets, statistical significance was determined by conducting an unpaired two-sample Wilcoxon test using R. This statistical test determines whether it is equally likely that a randomly selected value from one dataset will be less than or greater than a randomly chosen value from another population, making it ideal to determine whether two large datasets have the same distribution. Hence, the unpaired two-

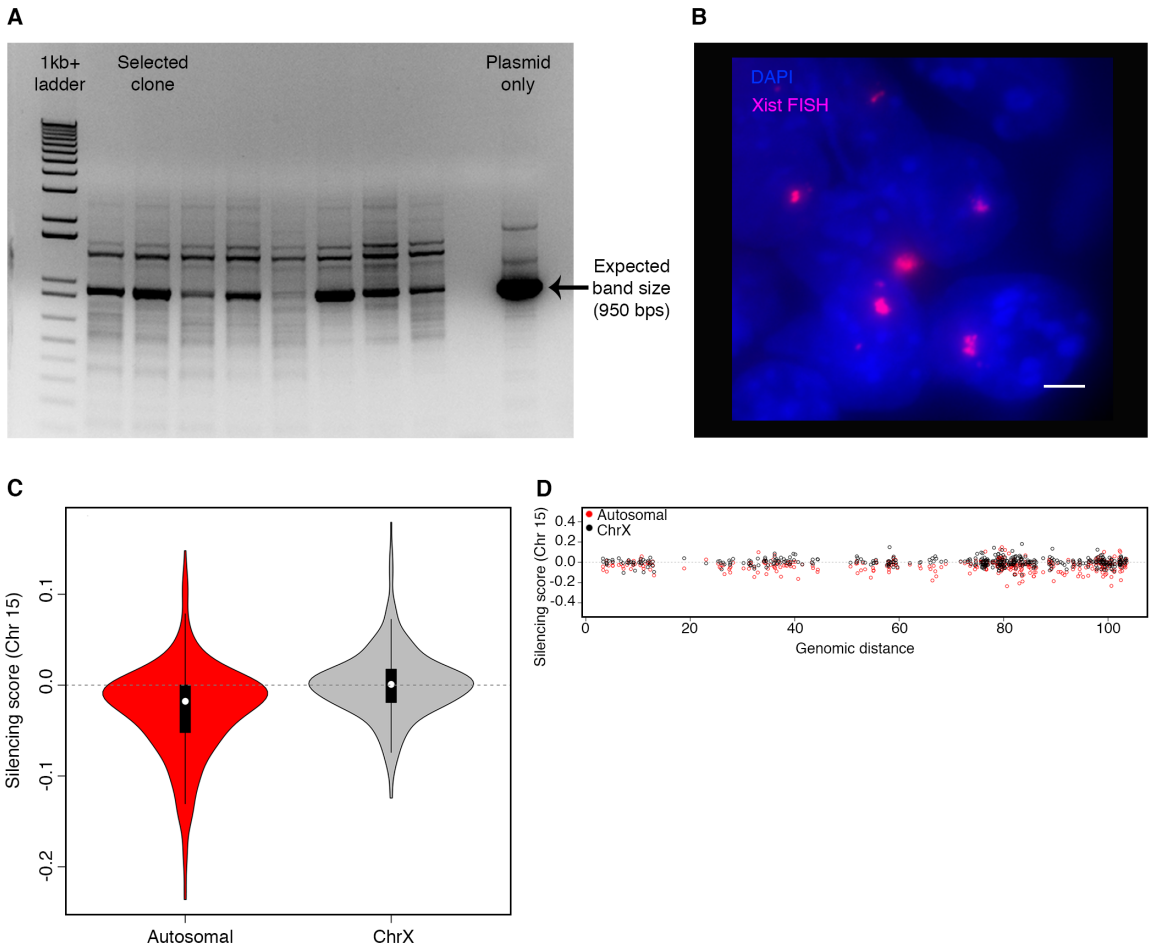

Figure 9: Generation of XY mESCs with inducible autosomal transgenic BglG-Halo-Xist on chromosome 15. A) PCR screen of gDNA for insertion of the BglG-Halo genomic sequence run on an EtBr Agarose gel, including 1kb+ ladder. Expected band size for successful integration is 950 bps. B) Representative image of Xist RNA FISH with DAPI counter stain of autosomal transgene cells 3 h post-induction, visualised with a Zeiss fluorescence microscope. Scale bar corresponds to 5 μm. C) Transcriptional silencing induced by autosomal transgenic Xist on chromosome 15. Silencing scores were obtained by comparing transcription of both alleles of chromosome 15 genes in the ChrX and the autosomal transgene line after chromatin RNA sequencing. D) Transcriptional silencing of single genes induced by autosomal transgenic Xist on chromosome 15 (red circles) compared with ChrX (black circles). Silencing scores were obtained by comparing transcription from both alleles of chromosome 15 in the ChrX and the autosomal transgene line after chromatin RNA sequencing.

sample Wilcoxon test was used as a non-parametric alternative to the unpaired t-test to determine statistical significance throughout this project, unless stated otherwise. Xist levels were slightly reduced in the in the autosomal transgene line compared to the ChrX line in both expansion and steady state (Figure 10a). To get an idea of the doxycycline induction efficiency of both the ChrX and autosomal transgene line, Xist RNA FISH was performed and cells with and without Xist territory formation were scored (Figure 10b). ChrX cells showed an induction

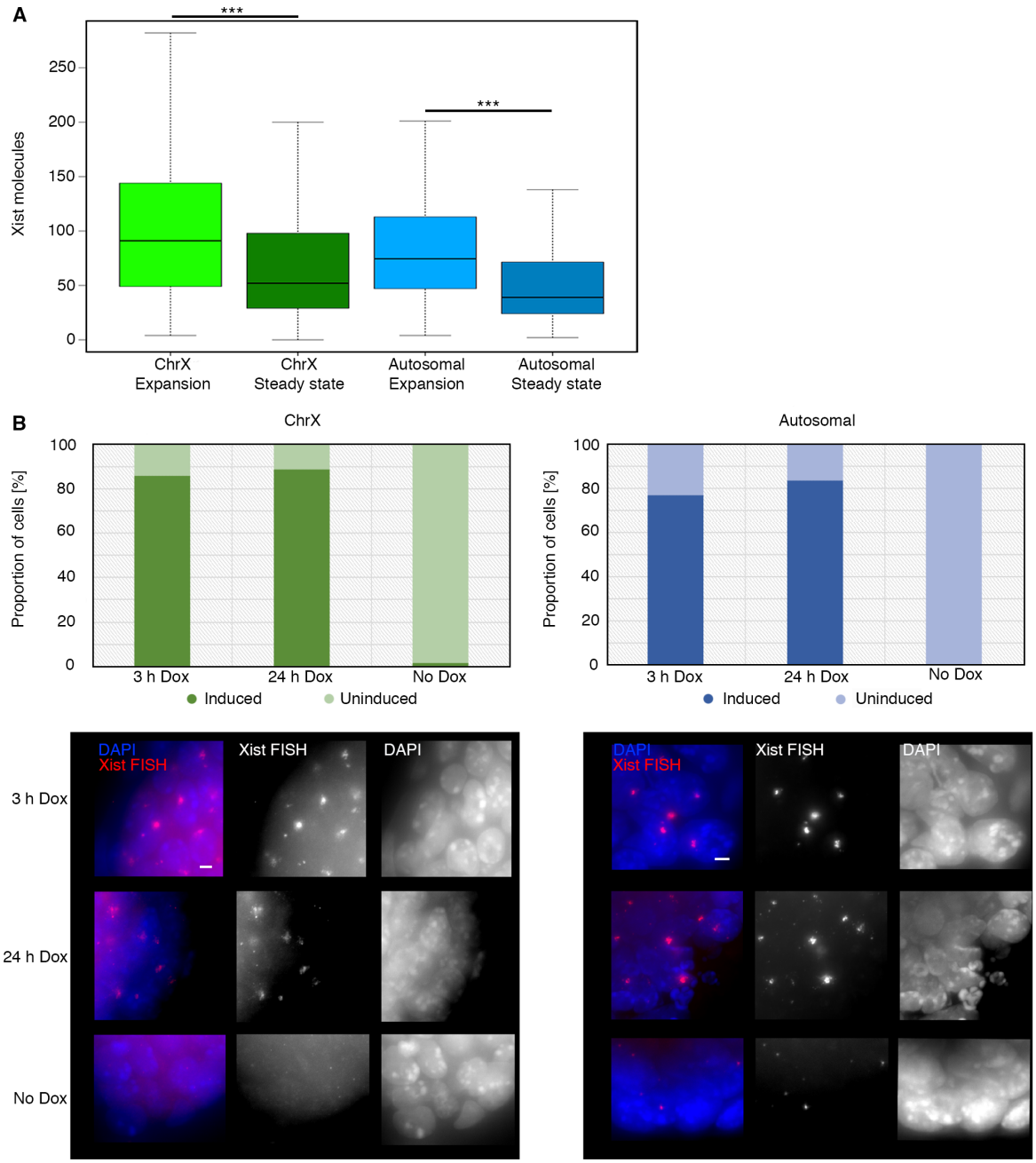

Figure 10: Xist molecule number and induction efficiency of ChrX and autosomal transgene cells during expansion and steady state. A) Quantification of Xist molecules in ChrX and autosomal transgene line, in expansion and steady state. n = 200 cells. B) Scoring of induction efficiency of the ChrX and autosomal transgene line after none, 3 h and 24 h doxycycline induction. n = 200 cells. Including representative images of Xist RNA FISH with DAPI counter stain, visualised with a Zeiss fluorescence microscope. Maximum intensity projections. Scale bars correspond to 5 μm.

efficiency of 86% in expansion, which increased to 89% in steady state (Figure 10b). Induction efficiency was slightly lower in the autosomal transgene line with 77% of the cells in expansion and 83.5% of the cells in steady state showing Xist territory formation (Figure 10b). Importantly, there was little to no Xist expression detected

before doxycycline addition, suggesting that there is no leakiness of the promoter (Figure 10b). The ChrX line did not show any XO cells, and both lines showed no polyploidy as indicated by the presence of one Xist territory and one pin-prick signal corresponding to antisense transcripts from the Tsix gene (Sheardown et al. 1997; Sado, Li, and Sasaki 2002) (Figure 10b).

In conclusion, both XX mESCs with endogenous inducible BglG-Halo-Xist and XY mESCs with autosomal transgenic inducible BglG-Halo-Xist have been successfully generated. Since it was validated that Bgl-stem-loop tagging of Xist is efficient, allows for the detection of distinct Xist foci, and does not alter Xist function, these cell lines can be taken forward for the analysis of Xist RNA dynamics and spreading.

3.2 Live imaging to investigate Xist RNA dynamics

Initially, we set out to assess Xist dynamics by live cell imaging, as this would give valuable insight into its spreading behaviour and mechanism in expansion and steady state. Live imaging of BglG-Halo-Xist in widefield mode (OMX V3) showed fairly static behaviour of the Xist territory over time, but lacked the necessary resolution to observe the dynamics of distinct Xist foci, even when using deconvolution (Figure 11a). 3D-SIM, however, yielded the necessary increase in resolution (Figure 11a). Due to cellular movement over time, a z-stack of considerable size had to be acquired to prevent the Xist territory from moving out of focus. This limited the fastest acquisition speed to 10 s intervals. At this acquisition speed, bleaching of the HaloTag ligand restricted the acquisition time to 5-10 min, despite using the brightest and most photostable HaloTag Ligand available for live imaging (Janelia Fluor 646, kindly gifted by Luke Lavis at HHMI Janelia, US). Under these conditions, BglG-Halo-Xist also appeared largely static (Figure 11a). Hence, it can be concluded that the limited acquisition speed might not be fast enough or that the acquisition time may not be long enough to successfully observe dynamic Xist particles.

Single particle photoactivated localisation microscopy/ total internal reflection fluorescence (spt PALM/TIRF) microscopy allows for single molecule tracking of highly dynamic molecules using photoactivatable fluorophores. Since many different photoactivatable HaloTag ligands are available, using this method to track BglG-Halo in our system could potentially help overcome the limitations of 3D-SIM.

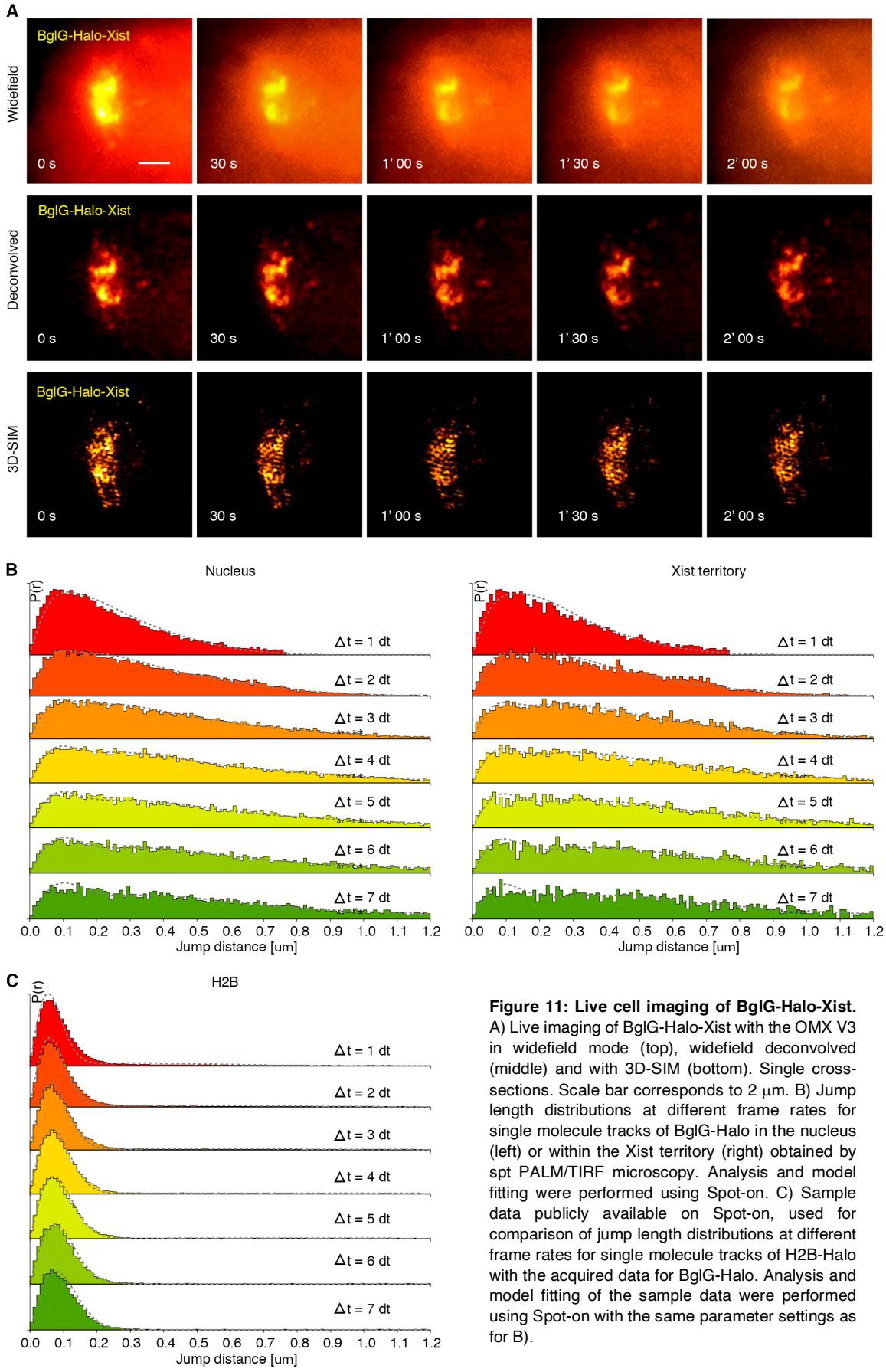

Figure 11: Live cell imaging of BglG-Halo-Xist. A) Live imaging of BglG-Halo-Xist with the OMX V3 in widefield mode (top), widefield deconvolved (middle) and with 3D-SIM (bottom). Single cross-sections. Scale bar corresponds to 2 μm. B) Jump length distributions at different frame rates for single molecule tracks of BglG-Halo in the nucleus (left) or within the Xist territory (right) obtained by spt PALM/TIRF microscopy. Analysis and model fitting were performed using Spot-on. C) Sample data publicly available on Spot-on, used for comparison of jump length distributions at different frame rates for single molecule tracks of H2B-Halo with the acquired data for BglG-Halo. Analysis and model fitting of the sample data were performed using Spot-on with the same parameter settings as for B).

However, using photoactivatable ligands in the context of a stem-loop based system results in the loss of the fluorescence intensity fold change of stem-loop bound over unbound fusion proteins, disallowing discrimination of the molecule of interest (Figure 8a). In this context, single BglG-Halo molecules representing both freely diffusing BglG-Halo and BglG-Halo bound to Xist would be photo-activated and tracked. As little is known about Xist dynamics it is not possible to reliably exclude tracks of free diffusing BglG-Halo using prior knowledge. In an attempt to distinguish the two populations, the cells were stained with photo-activatable and conventional HaloTag ligands in parallel. A snapshot of the cell was acquired using the conventional HaloTag ligand at the beginning of each acquisition. Subsequently, single molecule tracks were acquired. Later, the snapshot was used as a reference image to identify the Xist territory and analyse tracks of BglG-Halo from the entire nucleus as compared to tracks from the Xist territory only (Figure 11b).

Spot-on analysis of the jump distance distribution of nuclear tracks revealed that BglG-Halo is highly dynamic, and the data could not be fitted to a two-state or three-state model (Figure 11b). For comparison, publicly available data on H2B-Halo was analysed using the same parameters (Figure 11c). The jump distance distribution for H2B-Halo could be fitted to a two-state model illustrative for proteins with a large bound fraction (Figure 11c). Jump distances were dramatically shorter for H2B-Halo as compared to BglG-Halo underlining that most BglG-Halo molecules were unbound (Figure 11b and 11c). This observation is in line with the assumption that nuclear tracks would largely stem from unbound BglG-Halo. However, there was no major difference in jump distance distribution between the nuclear tracks and those

from the Xist territory (Figure 11b). Shorter jump distances were found to be slightly more common at higher frame rates, and longer distances less represented at lower frame rates in the Xist territory as compared to the nucleus (Figure 11b). These very subtle changes suggest that BglG-Halo is more often bound in the Xist territory than in rest of the nucleus (Figure 11b). However, the differences are too minor to confidently discriminate free floating BglG-Halo and Xist-BglG-Halo and thus draw conclusions about Xist dynamics and behaviour. While the heterochromatin of the Xi might reduce the number of unbound BglG-Halo slightly, efficient labelling of Xist with BglG-Halo suggests that unbound BglG-Halo must be present in the Xist territory. Considering the relatively low number of 50 – 150 Xist foci present on the Xi at any given time (Figure 10a), tracks from BglG-Halo-Xist might be swamped by the abundance of tracks of unbound BglG-Halo, even when looking at the Xist territory in isolation. In summary, the aforementioned technical challenges rule out the use of single molecule tracking in this system, at least without further developments.

One approach to overcome these challenges would be a system where ligands are only fluorescent when bound to the RNA of interest. RNA aptamers, such as Mango, fulfil the aforementioned criteria and have recently been used for single molecule detection in living cells (Cawte, Unrau, and Rueda 2020). However, generation of a cell line with inducible endogenous Xist containing an array of Mango aptamer sequences proved difficult, because the Mango aptamer sequence seemed to be unstable during replication and was lost after a small number of cell divisions. As a stable cell line is essential for the study of endogenous Xist dynamics and

behaviour, aptamer technology will have to be significantly improved before it can be applied to study endogenous Xist.

To conclude, whilst BglG can be used to efficiently label Xist in fixed cells, technical limitations currently prevent the use of this system to image Xist in living cells at high-resolution.

3.3 Development of RNA-SPLIT as an alternative approach to live imaging

Considering the technical difficulties associated with live imaging of Xist foci, a different approach to studying Xist RNA dynamics was implemented. The use of HaloTag technology is one of the major strengths of this system allowing for the performance of localisation microscopy at super-resolution level. In order to add temporal information one can make use of the fact that HaloTag technology enables addition of cell permeable ligands with different properties to cells, with excess ligand being washed out prior to fixation. Specifically, instead of a single HaloTag ligand, two different wavelength emitting HaloTag ligands were added sequentially after induction with doxycycline (Figure 12a). It has to be noted that the binding kinetics of BglG-Halo fusion protein to the Bgl-stem-loops, as well as BglG-Halo fusion protein stability are key factors for the feasibility of such an experiment. Unfortunately, it was technically not possible to measure the binding kinetics of BglG-Halo to the Bgl-stem-loops *in vivo*. FRAP experiments were unsuccessful due to high intensity background signal and imaging times being limited by increased mobility of mESCs. Therefore, carefully designed controls have been introduced throughout the course of this study to exclude exchange of the differently labelled BglG-Halo fusion proteins on the Bgl-stem-loops, such as a Dox washout experiment and a dual colour control, which are detailed in Chapter 3.4 and 3.7 respectively. Cells were induced for 1.5 h and 24 h before the start of the experiment to assess Xist localisation and dynamics in expansion and steady state respectively (Figure 12a). Subsequent addition of the HaloTag ligands allowed for splitting the

RNA into two differently labelled pools, pre-synthesised RNA labelled with Halo ligand 1 and newly synthesised RNA labelled with Halo ligand 2 (Figure 12a and 12b). Hence, the new method was named sequential pulse localisation imaging over time (RNA-SPLIT). This novel technique is especially powerful because variations of the set up can be used to study different aspects of RNA dynamics and localisation, and it can potentially be applied to any RNA and any stem-loop labelling system.

Figure 12a summarises the main variations used in this work. Firstly, localisation of Xist to the X chromosome territory at the different stages of XCI and in different cellular backgrounds can be assessed by measuring the molecule density and volume of spread. Moreover, one can determine RNA turnover by scoring the number of pre-synthesised RNA molecules over time, while gradually increasing the staining time of newly synthesised RNA molecules for up to 4 h. Full turnover of the RNA can be assumed when no pre-synthesised RNA signal can be detected anymore. Turnover rates can be complemented by analysis of RNA transcription dynamics, quantified by scoring the number of newly synthesised RNA molecules while gradually increasing the staining time of newly synthesised RNA in 10 min intervals. Using those short intervals of newly synthesised RNA staining also allows for definition of the approximate location of the RNA transcription site based on density and fluorescence intensity of the newly synthesized RNA. This can be used to examine the distribution of newly synthesised and pre-synthesised RNA molecules with respect to the transcription site over time, giving insight into the spreading behaviour of the RNA. Here, distances of RNA molecules from the

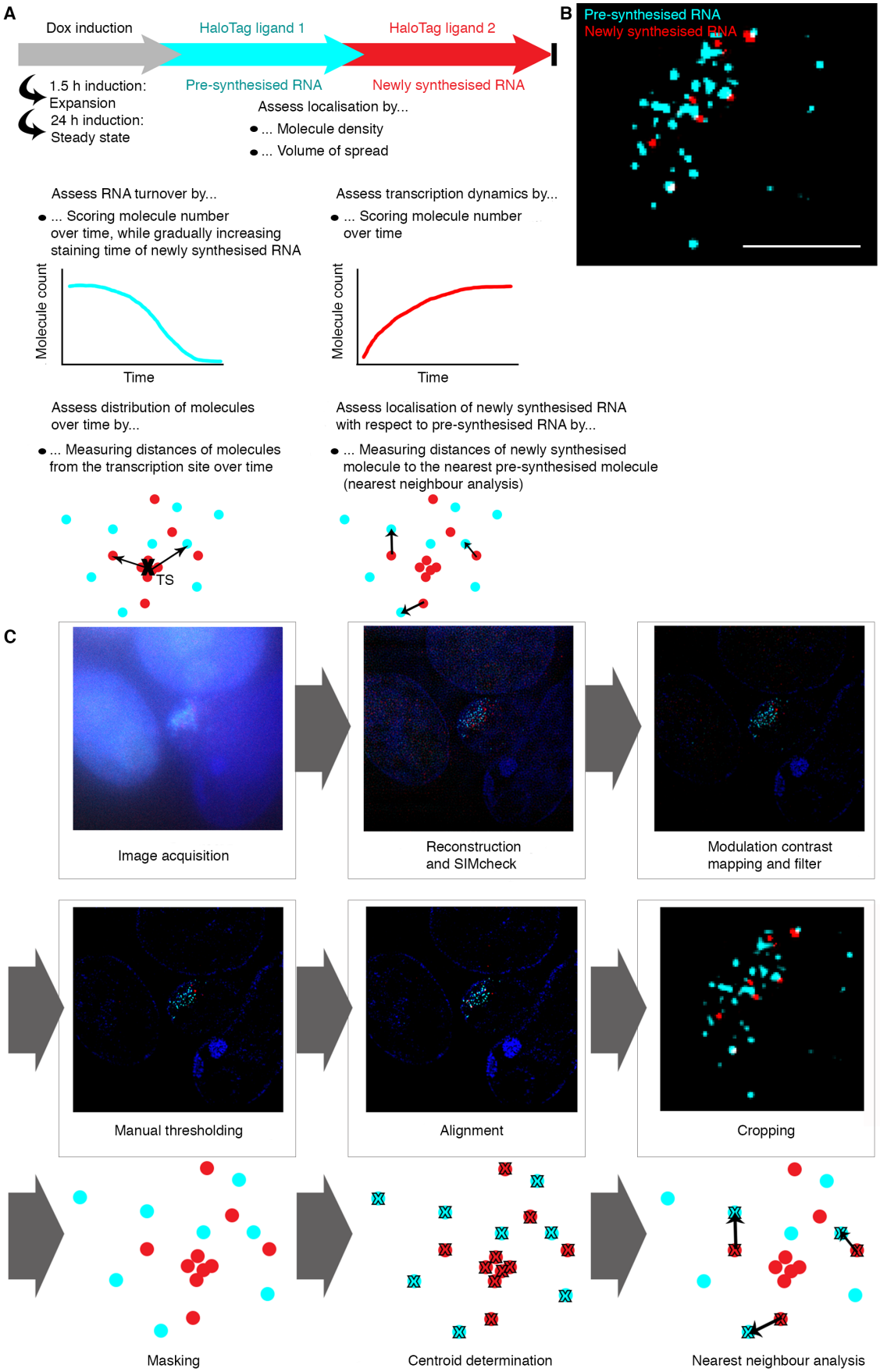

Figure 12: RNA-SPLIT – a new method to assess RNA localisation and dynamics. A) Schematic illustrating experimental set up and different applications of RNA-SPLIT. B) Example image of pre-synthesised and newly synthesised Xist in Expansion labelled by RNA-SPLIT visualised using 3D-SIM. Single cross-section. Scale bar corresponds to 2 μm. C) Image processing and analysis workflow of RNA-SPLIT samples.

approximate transcription site can be measured and compared between different time points. Finally, RNA-SPLIT can be used to assess the localisation of newly synthesised RNA with respect to pre-synthesised RNA by measuring the distance of each newly synthesised molecule to the nearest pre-synthesised molecule.

Image processing and analysis is critical for successful RNA-SPLIT experiments. After image acquisition with 3D-SIM, the data is reconstructed and undergoes quality checks through the SIMcheck plugin (Ball et al. 2015) (Figure 12c). Artefacts are reduced by generating modulation contrast maps and applying suitable and consistent filters to discard low modulation contrast signal (Figure 12c). Then, background stemming from free diffusing BglG-Halo is discarded by manual

thresholding (Figure 12c). Channels are aligned using the open-source software package Chromagnon and EdU calibration data acquired on the date of image acquisition (Figure 12c). In the final step of image processing, Xist territories are manually cropped (Figure 12c). The DAPI counter stain is currently only used for reference in representative images and the information is discarded at the stage of cropping (Figure 12c). The volume of the cropped Xist territory gives first insights into the spreading volume of the RNA (Figure 12a). To analyse the fully processed images, the signal is masked and the centroids of each molecule are determined by a Watershed algorithm (Figure 12c). This allows for the counting of pre-synthesised and newly synthesised molecules at different time points and under various experimental conditions. RNA turnover and transcription dynamics can be deduced from this information (Figure 12a). The localisation of each molecule in 3D determined by the Watershed algorithm can then be used to conduct NNA, where

the distance of each newly synthesised molecule to its nearest neighbouring pre-synthesised molecule is measured (Figure 12a and 12c). Variations of NNA, where distances between all RNA molecules or between the approximate transcription site and newly synthesised RNA are determined, can be used to examine RNA density and spreading behaviour (Figure 12a and 12c). The development of this new tool for studying RNA localisation and dynamics allows for the addition of temporal resolution to super-resolved localisation microscopy data without the need for live cell imaging. Therefore, this powerful technique was utilised to further investigate Xist RNA dynamics, localisation and spreading behaviour.

3.4 Xist RNA stability is defined by its chromatin environment and rate of transcription

Xist RNA stability was assessed using RNA-SPLIT. The experiment was conducted in expansion and steady state phase, as well as in the ChrX and autosomal transgene cell line, allowing measurement of Xist stability changes with phase of XCI or chromatin environment (Figure 13a). After induction with doxycycline for 1.5 h and 24 h for the analysis of expansion and steady state respectively, cells were incubated with HaloTag ligand 1, a green ligand with excitation at a wavelength of 488 nm, for 60 min (Figure 13a). A washout of 15 min ensured that any unbound BglG was removed from the cells. The second HaloTag ligand, a red ligand with excitation at a wavelength of 585 nm, was then added to differentially label all newly synthesised RNA molecules for different time periods starting with 60 min and then increasing in 20 min intervals until no more pre-synthesised RNA molecules labelled by HaloTag ligand 1 could be detected (Figure 13a). Labelling time of newly synthesised RNA molecules did not exceed 4 h due to concerns that the BglG-Halo might unbind and exchange at later time points. Using these parameters a visible reduction in pre-synthesised RNA molecules could be observed over time until complete turnover occurred (Figure 13b). Interestingly, pre-synthesised RNA signal was seen to be lost from the periphery of the Xist territory first, before being lost from more central locations (Figure 13b). This observation could be explained if Xist gradually spreads in 3D through consecutive binding and unbinding events, effectively ‘hopping’ towards the periphery of the Xist territory, before being degraded when reaching the peripheral boundaries of the Xi.

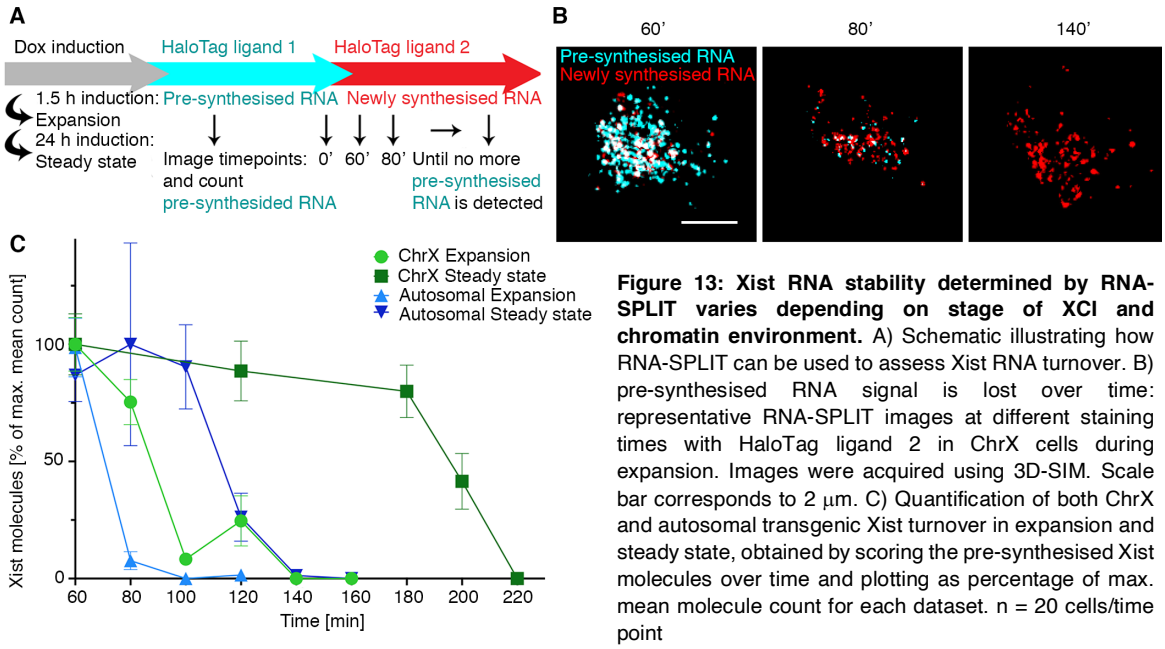

Figure 13: Xist RNA stability determined by RNA-SPLIT varies depending on stage of XCI and chromatin environment. A) Schematic illustrating how RNA-SPLIT can be used to assess Xist RNA turnover. B) pre-synthesised RNA signal is lost over time: representative RNA-SPLIT images at different staining times with HaloTag ligand 2 in ChrX cells during expansion. Images were acquired using 3D-SIM. Scale bar corresponds to 2 μm. C) Quantification of both ChrX and autosomal transgenic Xist turnover in expansion and steady state, obtained by scoring the pre-synthesised Xist molecules over time and plotting as percentage of max. mean molecule count for each dataset. n = 20 cells/time point

Quantification of the pre-synthesised RNA molecule count over time in the ChrX cell line during expansion showed a gradual reduction of Xist starting at 60 min with a complete turnover at 140 min (Figure 13c). Strikingly, Xist was found to be almost 2-fold more stable in ChrX cells during steady state, where a significant reduction of pre-synthesised RNA molecules could only be seen after 180 min and complete turnover occurred after 220 min (Figure 13c). The results suggest that Xist stability increases with the progression of XCI. This could be due to physical changes in the chromatin environment and transcriptional activity of the X chromosome over time. Alternatively, a factor(s) absent up to 3 h and present by 24 h of induction could increase Xist RNA stability.

Interestingly, it could be seen that Xist stability is similarly increased by almost 2-fold in steady state as compared to expansion in the autosomal transgene line, where Xist is expressed from and spreads in *cis* on chromosome 15 (Figure 13c). However, Xist stability was significantly lower compared to the ChrX cell line (Figure

13c). In expansion, complete turnover was already reached after 100 min, which is 40 min earlier than in the ChrX cells (Figure 13c). Furthermore, Xist turnover was reduced from 220 min in the ChrX cells to 140 min in the autosomal transgene cells during steady state (Figure 13c). In summary these observations indicate that the increase of Xist RNA stability with progression of XCI is a general phenomenon (occurring for endogenous Xist as well as autosomal transgenic Xist), but that Xist stability can nevertheless be modulated by chromosome environment.

To validate this result and the accuracy of RNA-SPLIT a different experimental method, SLAM-seq was applied (Herzog et al. 2017). SLAM-seq enables the analysis of RNA kinetics by using a modified methodology developed from S4U pulse-chase experiments. S4U was added to the ChrX cells with Bgl-stem-loop tagged Xist, as well as to the parental cell line with untagged Xist, after 24 h of doxycycline induction (Figure 14a). After S4U labelling and at the beginning of the washout step, t0 cells were collected (Figure 14a). Then, cells were collected in 30 min intervals of the washout until the 150 min time point (Figure 14a). Here, cells at later time points should contain a decreasing proportion of Xist RNA with S4U due to Xist RNA degradation (Figure 14a). After sample collection and nuclear RNA extraction, alkylation of the incorporated S4U was performed (Figure 14a). Reverse transcription was used to convert the modified S4U (*S4U) to G instead of A, which was then converted to a C instead of a T by PCR (Figure 14a). This T to C conversion ratio was quantified by chromatin RNA sequencing, and degradation kinetics of different RNAs were inferred from the decrease of the ratio over time (Figure 14a).

T to C conversion rates were significantly higher than background at all time points for both BglG-Halo-Xist and untagged Xist suggesting that S4U incorporation and sample preparation were successful (Figure 14b). Moreover, overall T to C conversion rates showed the expected significant and gradual decline over time with the exception of a slightly reduced rate at the 90 min time point for untagged Xist (Figure 14b). In line with the cumulative results, BglG-Halo-Xist showed a gradually decreasing T to C conversion rate, which could be used to fit an exponential decay curve, and to determine a half-life of 63 min and 58 min for each biological replica respectively (Figure 14c). The microscopy data does not allow for the determination of a half-life, because it is based on the selection of visible Xist territories by eye biasing towards cells with Xist expression. Therefore, it is more reliable to use the time point of complete Xist turnover for comparison, i.e. the time point at which no more pre-synthesised RNA could be detected by RNA-SPLIT. It was determined that Xist molecule numbers of less than 10 could no longer be confidently recognised as Xist territories during image acquisition and before reconstruction of the data, and are hence selected against. Considering that previous experiments showed Xist territories were comprised of approximately 100 BglG-Halo-Xist molecules per cell, the threshold for complete Xist turnover determined by SLAM-seq was set at 10% of the original T to C conversion rate (Figure 10a and 14c). Complete turnover of BglG-Halo-Xist occurred after 193 min according to the SLAM-seq data as compared to 220 min according to RNA-SPLIT (Figure 13c and 14c). Taking into consideration how different the two technologies are, the predicted turnover rates are very similar. This provides confirmation that RNA-SPLIT is a robust method to assess RNA dynamics.

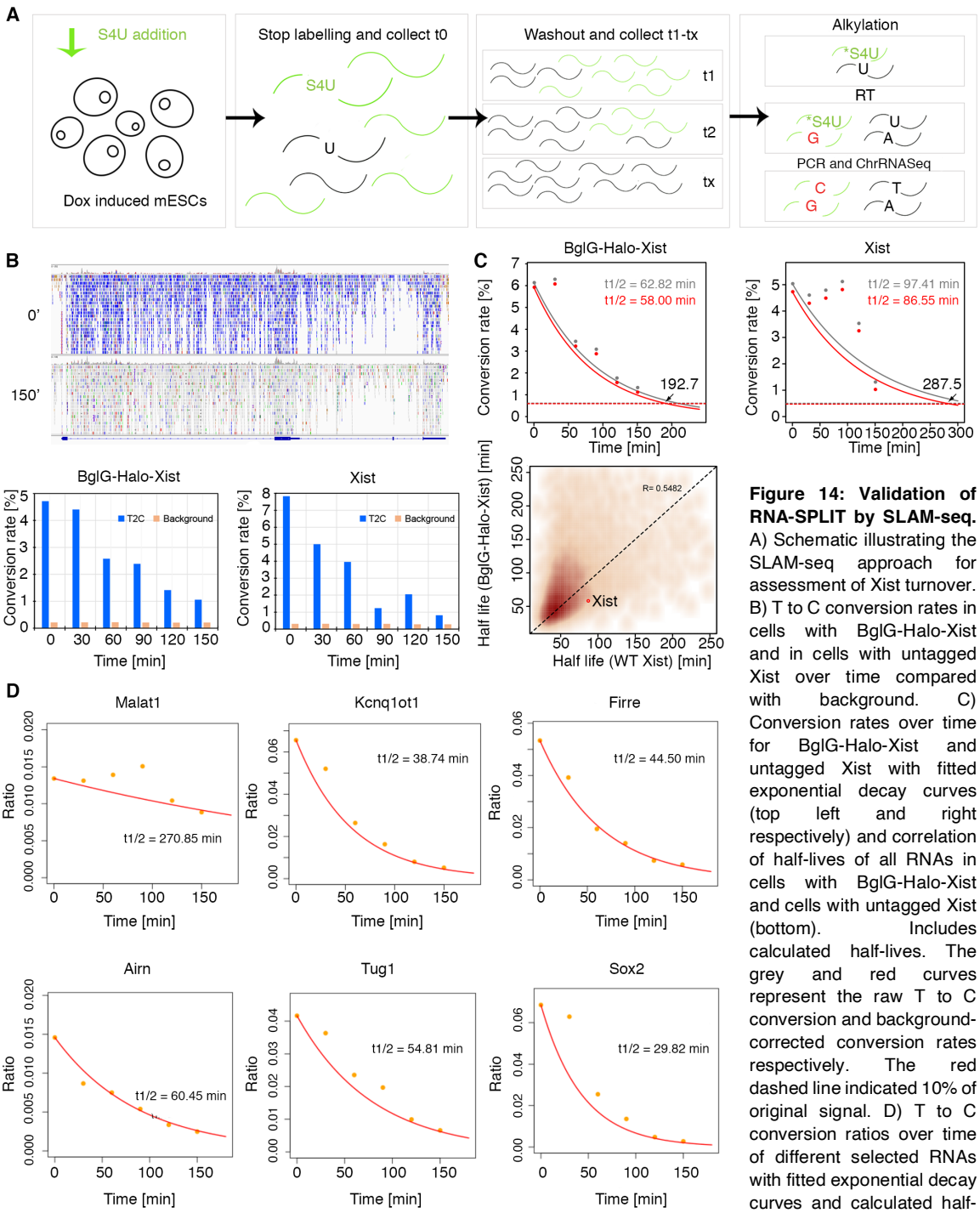

Figure 14: Validation of RNA-SPLIT by SLAM-seq. A) Schematic illustrating the SLAM-seq approach for assessment of Xist turnover. B) T to C conversion rates in cells with BglG-Halo-Xist and in cells with untagged Xist over time compared with background. C) Conversion rates over time for BglG-Halo-Xist and untagged Xist with fitted exponential decay curves (top left and right respectively) and correlation of half-lives of all RNAs in cells with BglG-Halo-Xist and cells with untagged Xist (bottom). Includes calculated half-lives. The grey and red curves represent the raw T to C conversion and background-corrected conversion rates respectively. The red dashed line indicated 10% of original signal. D) T to C conversion ratios over time of different selected RNAs with fitted exponential decay curves and calculated half-lives.

As an aside, allelic analysis of X-linked transcription using the chromatin RNA sequencing data obtained through the SLAM-Seq experiment allowed for the comparison of Xist mediated silencing of S4U treated and untreated cells 24 h post-induction. Interestingly, the analysis showed that Xist silencing was impaired by

S4U addition. This might be due to the accumulation of mutations in the Xist RNA sequence leading to interruption of binding of important secondary factors, or potentially changes in the RNA structure that impair its function. These observations highlight the importance of RNA-SPLIT for a native assessment of Xist RNA turnover without interfering with Xist function.

It is possible that insertion of stem-loop arrays might have an impact on Xist RNA stability. Although there were no observable differences in silencing ability between BglG-Halo-Xist and untagged Xist according to the chromatin RNA sequencing data (Figure 8b), SLAM-seq allowed for this to be determined directly. Untagged Xist was found to be more stable than BglG-Halo-Xist with a derived half-life of 97 min and 87 min for each biological replica respectively, and a complete turnover after 287 min (Figure 14c). The latter is roughly 1 h longer than that measured by RNA-SPLIT, suggesting that the insertion of the Bgl-stem-loop array may indeed have made Xist slightly less stable (Figure 13c and 14c). This is not surprising, since stem-loop insertions have been implicated in RNA stability before (Heinrich et al. 2017; Garcia and Parker 2016). However, it is important to interpret this result with caution, since the exponential decay curve could not be as well fitted to the untagged Xist data compared to the BglG-Halo-Xist data, suggesting some technical variation (Figure 14c).

Variability in SLAM-seq data was highlighted by comparison of the half-live of all RNAs, which, with the exception of Xist, were untagged in both cell lines (Figure 14c). The correlation coefficient of 0.55 indicates that there was a high technical variation between samples (Figure 14c). Indeed, this was a particular difficulty

experienced with SLAM-seq, even with specific attention being paid to meticulous experimental procedure. The SLAM-seq analysis showed that, while Xist is highly dynamic, many other RNAs have similar half-lives in the nucleus (Figure 14c and 14d). For instance for other lncRNAs like Kcnq1ot1, Firre, Airn and Tug1, half-lives of 39 min, 45 min, 60 min and 55 min were determined as compared to 60 min for BglG-Halo-Xist (Figure 14c and 14d). Other lncRNAs such as Malat1 showed significantly longer half-lives of many h (Figure 14d).

In summary, the SLAM-seq experiments confirmed that RNA-SPLIT is a reliable method to examine RNA dynamics because of the similarity of Xist RNA turnover rates determined by each method. This supports the use of RNA-SPLIT which has greater technical reliability and also provides 3D localisation data of single Xist foci. The SLAM-seq data did, however, suggest that Bgl-stem-loop insertion might slightly reduce Xist RNA stability, but as long as experiments use similarly tagged lines, valid comparisons, in a mutant cell line for example, can be made.

Despite a reduced total Xist molecule count, Xist stability increased in steady state as compared to expansion (Figure 10a and 13c). This raises the question whether Xist transcription is decreased in steady state to maintain similar levels of Xist RNA. To investigate this point, RNA-SPLIT was used to examine Xist transcription dynamics. Cells were induced for 1.5 h and 24 h with doxycycline to study expansion and steady state respectively, before being incubated with HaloTag ligand 1 to label pre-synthesised RNA molecules for 60 min (Figure 15a). Next, cells were incubated with HaloTag ligand 2 for short time periods gradually increasing by 10 min to label the nascent newly synthesised RNA molecules (Figure 15a). Scoring of the newly

synthesised RNA molecules over time was used to examine Xist transcription rates (Figure 15a). newly synthesised Xist molecules were indeed found to gradually increase over time in both expansion and steady state in ChrX cells (Figure 15b). As anticipated, Xist transcription was significantly reduced in steady state as compared to expansion with average molecule numbers consistently at least 2-fold lower in steady state (Figure 15b). This decrease of Xist transcription over time could also be observed in the autosomal transgene cells (Figure 15b). As described previously, Xist molecule numbers were only slightly reduced in autosomal transgene compared to ChrX cells (Figure 10a), although Xist stability was dramatically decreased in autosomal transgene cells (Figure 13c). However, the observed overall increase in Xist transcription in autosomal transgene as compared to ChrX cells can account for this discrepancy (Figure 15b).

Overall, these results suggest that a lower transcription rate in steady state could be linked to increased Xist stability. This observation is in line with previous research suggesting that halting Xist transcription by Actinomycin D treatment increases the stability of previously transcribed Xist (Ng et al. 2011). Because Actinomycin D treatment is highly disruptive to cells, it is important to test this hypothesis using a different approach. Here, Xist expression was decreased by washout of doxycycline 1.5 h post- induction, followed by RNA-SPLIT to examine Xist RNA turnover, comparing with the results obtained in untreated ChrX cells during expansion. A significant reduction of Xist transcription following doxycycline washout could be confirmed (Figure 15c). Xist stability was found to be dramatically increased in the doxycycline washout condition as compared to the ChrX cells with pre-synthesised

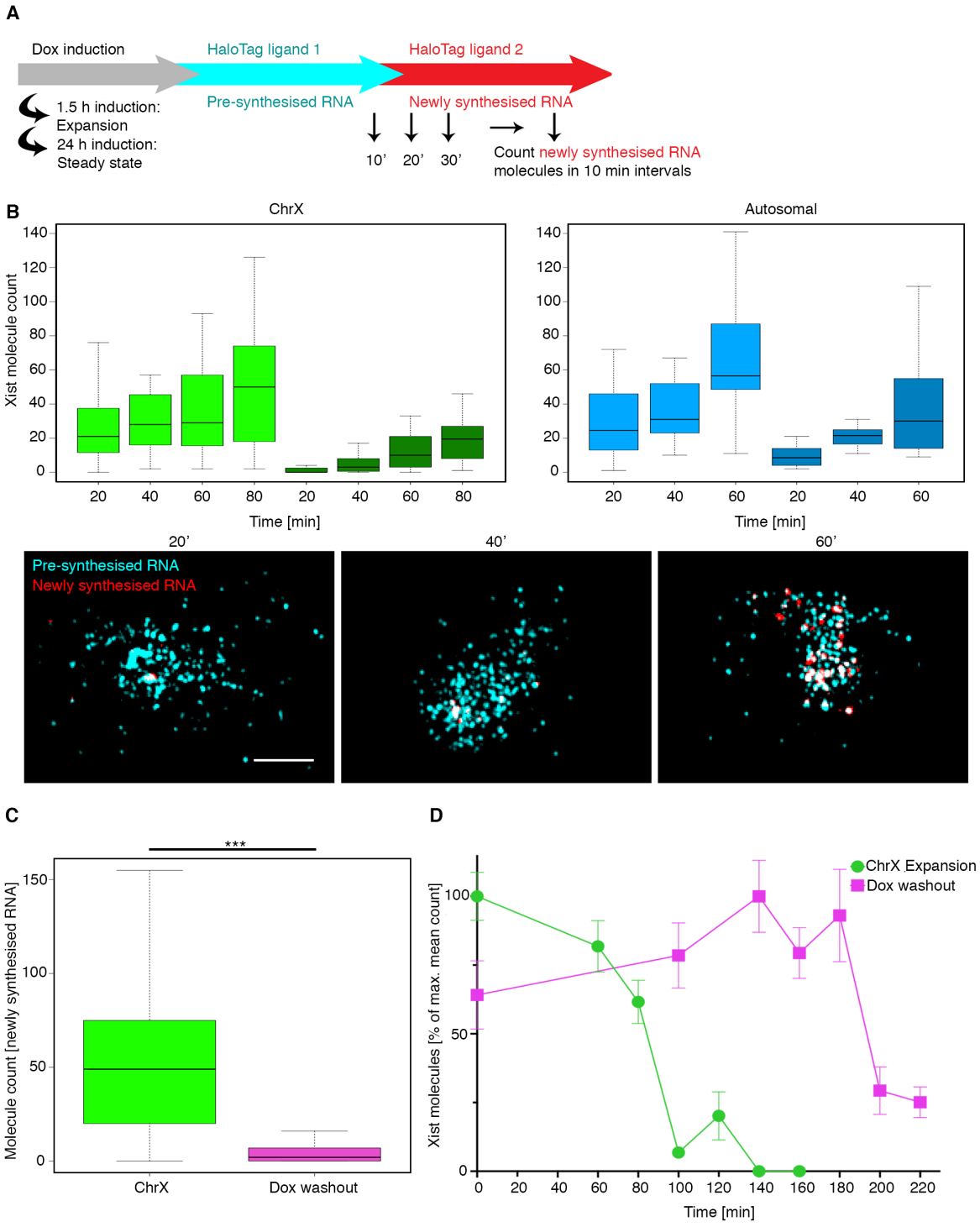

Figure 15: Xist RNA stability is defined by its rate of transcription. A) Schematic illustrating how RNA-SPLIT can be used to assess Xist RNA transcription. B) Quantification of Xist RNA transcription in ChrX and autosomal transgene cells during expansion and steady state, obtained by scoring the number of newly synthesised Xist molecules over time. n = 20 cells/ time point. Including representative RNA-SPLIT images of ChrX cells during Expansion acquired by 3D-SIM. Maximum intensity projections. Scale bar corresponds to 2 μm. C) Quantification of Xist RNA transcription in ChrX cells during Expansion as compared to washout of doxycycline, obtained by scoring the number of newly synthesised Xist molecules. n = 100 cells/ time point. D) Quantification of Xist turnover in ChrX and doxycycline washout cells during Expansion, obtained by scoring the pre-synthesised Xist molecules over time and plotting as percentage of max. mean molecule count for each dataset. n = 20 cells/time point.

Xist RNA still present at 220 min (Figure 15d). This result definitively proves that Xist stability is defined by its rate of transcription. As an aside, this experiment illustrates that eventual turnover of Xist in steady state is not due to unbinding of BglG-Halo from the stem-loops.

3.5 Newly transcribed Xist spreads in 3D from the transcription site towards the periphery of the Xi territory

When studying Xist RNA transcription using RNA-SPLIT, it became apparent that newly synthesised RNA displays a distinct spreading behaviour towards the periphery of the Xist territory (Figure 15b and 16a). Re-evaluation of the data previously acquired in section 3.4 allowed for the quantification of this effect. Since only Xist RNA transcribed for 10 to 60 min was labelled with HaloTag ligand 2 in this experimental set up, the location of the Xist transcription site (TS) could be extrapolated based on density and intensity of the nascent RNA signal (Figure 16a). NNA enabled measurement of the distance of each newly synthesised and pre-synthesised RNA molecule from the transcription site at every time point. The change in distances over time indicates how nascent Xist spreads across the Xist territory. However, Xist territories are highly variable in size, which makes it difficult to compare absolute distances. Therefore, one can instead express the distances as percentage of the maximum distance detected for each Xist territory. In order to quantify the distribution of Xist RNA over time, the Xist territory was divided into 3 zones, with zone 1, 2 and 3 extending 0-50%, 50-75% and 75-100% of the maximum distance from the transcription site respectively (Figure 16b). Then, the proportion of newly synthesised or pre-synthesised molecules in each zone over time was quantified (Figure 16b). In expansion, a significant and gradual re-distribution of newly synthesised Xist from the inner zone to the outer zones over time could be observed, confirming 3D spreading of Xist from the transcription site towards the periphery of the Xist territory (Figure 16b). Noticeably, the distribution

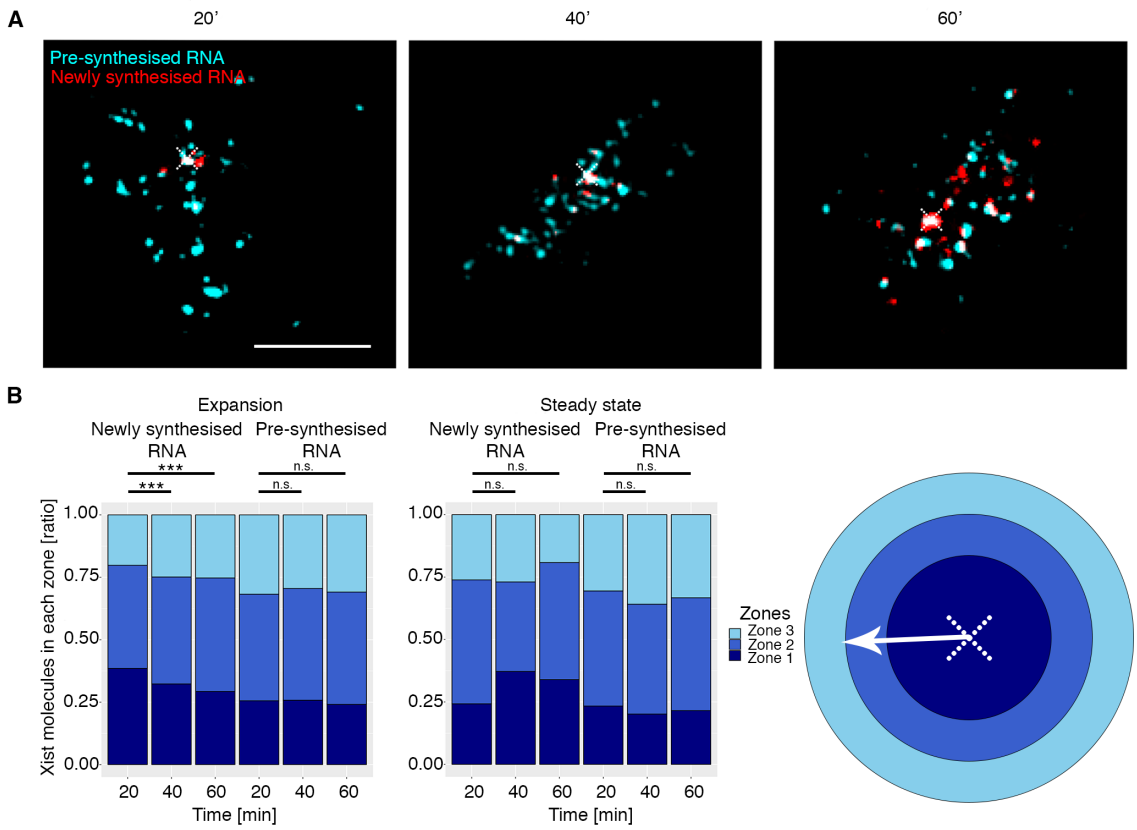

Figure 16: RNA-SPLIT reveals 3D spreading behaviour of Xist during expansion. A) Representative RNA-SPLIT images of newly synthesised and pre-synthesised Xist RNA distribution over time in ChrX cells during Expansion. Images were acquired by 3D-SIM. Maximum intensity projections. Approximate transcription site locations are indicated (white cross). Single cross=sections. Scale bar corresponds to 2 μm. B) Bar chart showing the proportion of newly synthesised and pre-synthesised Xist molecules found in zone 1, 2 and 3 over time. Quantification based on RNA-SPLIT data of ChrX cells during expansion and steady state. Includes schematic illustrating of division of the Xist territory into 3 zones according distance from the Xist transcription site.

of newly synthesised RNA in expansion seems to gradually approach that of pre-synthesised RNA and nearly equals it after 60 min (Figure 16b). A rate of expansion could be calculated, since NNA distances were measured in 3D and the 3D volumes of the clouds were already known. On average, Xist territories had a size of 98.9 μm^3 in expansion, which when set equal to 100% of the normalised volume, can be used to determine previous Xist spreading. On average, newly synthesised Xist extends across 29.9% of this volume after 20 min and 35.2% after 60 min, meaning that there is an increase of 5.3% of the Xist expansion volume within 40 min. 5.3% of the average Xist territory volume of 98.9 μm^3 corresponds to 5.11 μm^3. Based on

this, the expansion rate of newly synthesised Xist RNA can be approximated as 7.67 μm^3/h.

However, 3D spreading behaviour of Xist could not be shown in steady state phase, where the distribution of newly synthesised Xist RNA molecules over time seems more random and any apparent changes are not significant (Figure 16b). This is in line with Xist RAP and CHART-seq data, suggesting Xist preferentially spreads to 3D proximal sites at early time points post induction, but seems to lose this preference at later stages (Engreitz et al. 2013; Simon et al. 2013). It is noteworthy that the distribution of pre-synthesised RNA in both expansion and steady state remains stable over time. A control experiment using intronic Xist FISH probes in combination with HaloTag staining was planned to confirm accurate determination of transcription site localisation. Unfortunately, this had to be postponed due to the ongoing COVID-19 pandemic.

3.6 The Xist transcription site relocates from the centre of the Xi territory towards the periphery over time

Besides the assessment of Xist spreading behaviour, determination of the Xist transcription site localisation at different time points can also give insight into changes in spatial organisation of the chromatin as XCI progresses. Here, normalised x, y and z coordinates of each transcription site were obtained by expressing them as proportion of the corresponding cloud dimension in x, y and z. This enabled accounting for the variation in Xist territory size, and the display of all transcription sites in expansion together in 3D (Figure 17a). The transcription site seemed to be preferentially located at the centre of the Xist territory (Figure 17a). It becomes even more evident when looking at transcription site distribution in 2D from three angles (Figure 17b). This observation raises the question whether the distribution might change when XCI progresses to steady state. Indeed, the Xist transcription sites seemed to show more peripheral distribution in steady state than in expansion (Figure 17b).

In order to quantify this apparent relocation of the Xist transcription site over time, the territories were divided into 3 zones with inner zone 1 at the centre of the Xist territory and outer zone 3 at the periphery of the Xist territory. The results showed that approximately 60% of the transcription sites are found in the inner zones 1 and 2 in expansion (Figure 17c). Strikingly, in steady state this was significantly reduced to approximately 40%, with 60% of the transcription sites now found in the outer zone 3 (Figure 17c). This observation confirms that the Xist transcription site relocates from the centre of the Xi territory towards the periphery over time as XCI

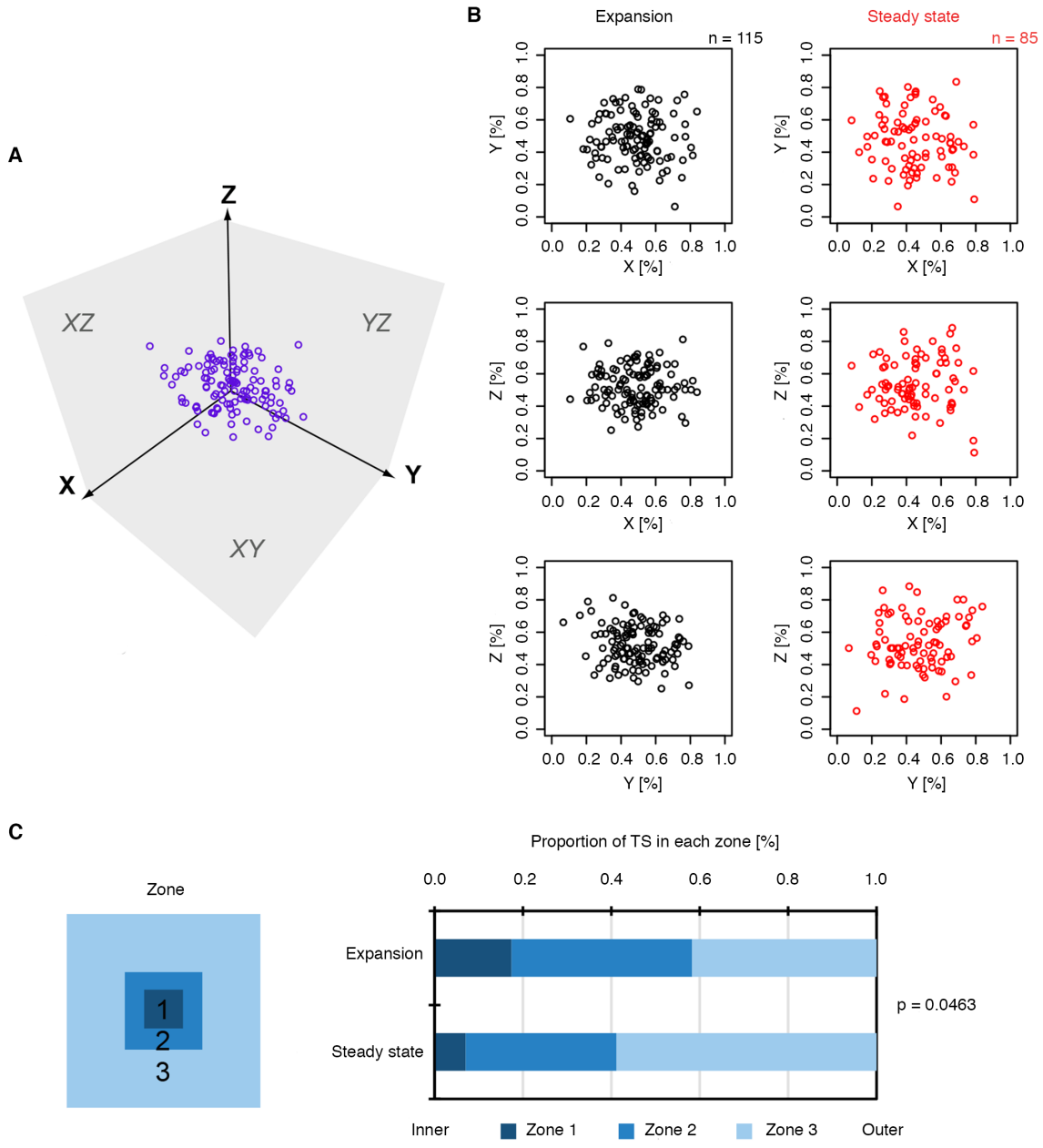

Figure 17: The Xist TS relocates towards the periphery of the Xi territory over time in ChrX cells. A) 3D distribution of approximated Xist transcription sites localisation in expansion based on RNA-SPLIT data. X, y and z coordinates are expressed as proportion of absolute dimensions in x, y and z of each Xist territory respectively to normalise for variation in Xist territory size. B) Comparison of normalised localisations of Xist transcription sites in expansion (black) and steady state (red) in 2D from 3 different angles: Y/X, Z/X and Z/Y. C) Proportion of Xist transcription sites found in inner zone 1 to outer zone 3 of the Xist chromosome territory in expansion as compared with steady state. Includes schematic illustrating division of the Xist territories into the three zones.

progresses from expansion to steady state (Figure 17c). Since the Xist locus is one of the few X-linked genes that remain active throughout XCI, it can be suggested that relocation towards the periphery might help ensure accessibility of the Xist

locus for RNA polymerases as the X chromosome progressively compacted during XCI advancement. Such a process could help guarantee reliable and constant Xist expression even as most genes on the X chromosome undergo transcriptional silencing.

To determine if the same effect can also be seen in the autosomal transgene context, Xist transcription site localisations were determined in expansion and steady state based on the RNA-SPLIT data as described previously. Interestingly, it could be observed that the transcription sites in autosomal transgene cells are more often localised at the periphery of the Xist territory than in ChrX cells during expansion (Figure 18a). Surprisingly, the distribution of Xist transcription sites seemed more central in steady state as compared to expansion in autosomal transgene cells, instead of transcription sites relocating further to the periphery as we expected based on the results in the ChrX cells (Figure 17b and 18a). This relocation of the autosomal transgenic Xist transcription sites could be confirmed by comparing the cumulative distribution of localisations in expansion and steady state (Figure 18b). The endogenous Xist locus is located fairly centrally on the X chromosome. Because it is not known where exactly the transgene has been inserted on chromosome 15, it cannot be excluded that the different relocation behaviour of transcription sites could be due to the genomic location of the transgene on the chromosome itself. Moreover, the chromatin RNA sequencing assay showed that autosomal transgenic Xist on chromosome 15 does not silence as efficiently as endogenous Xist on the Xi (Figure 9c and 9d). Hence, there is reason to assume that this could lead to differences in compaction and chromatin

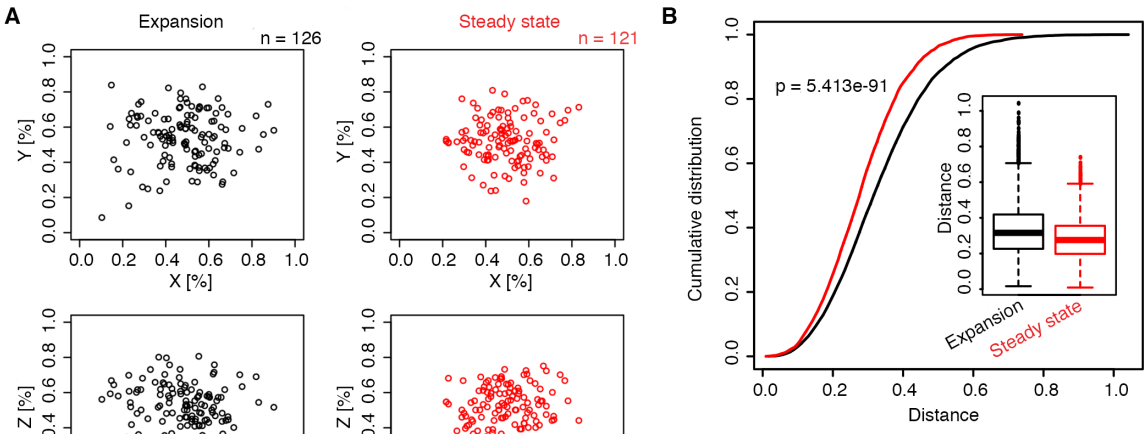

Figure 18: The Xist TS relocates towards the centre of the Xi territory over time in autosomal transgene cells. A) Comparison of the distribution of approximated Xist transcription site localisations during expansion (black) and steady state (red) in autosomal transgene cells based on RNA-SPLIT data. X, y and z coordinates are expressed as proportion of absolute dimensions in x, y and z of each Xist territory respectively to normalise for variation in Xist territory size. Localisations are shown in 2D from 3 different angles: Y/X, Z/X and Z/Y. B) Comparison of cumulative distribution of Xist transcription site localisations during expansion (black) and steady state (red), including boxplot diagram.

changes during the progression from expansion to steady state, and ultimately to differences in transcription site relocation. Finally, one has to take into consideration that only one autosomal transgene and one ChrX cell line were analysed in this project, and that there might be variation between cell lines, especially between those with different autosomal transgenic Xist integration sites.

3.7 Coupling of newly transcribed Xist with previously bound Xist

When confirming efficient labelling of Xist with BglG-Halo by combining Xist RNA FISH with HaloTag staining of BglG-Halo-Xist, it was noticeable that each distinct Xist RNA FISH domain was usually associated with two BglG-Halo foci (Figure 19a). Examination of different domains across the Xist territory indicated that Xist RNA accumulates in couplets, a phenomenon which could only be observed due to the increased resolution and sensitivity provided by the BglG-Halo system (Figure 19a). Fascinatingly, the images acquired using RNA-SPLIT overwhelmingly showed that couplets comprise single newly synthesised and pre-synthesised molecules (Figure 19a).

The above observations prompted the hypothesis that newly synthesised Xist RNA molecules couple with pre-synthesised Xist RNA when spreading across the X chromosome territory. To investigate this idea and to examine whether coupling is seen both in expansion and steady state, a variation of RNA-SPLIT combined with NNA was set up (Figure 19b). Here, cells were labelled with HaloTag ligand 1 for 60 min after 1.5 h or 24 h induction with doxycycline to study coupling during expansion and steady state respectively (Figure 19b). Then, HaloTag ligand 2 was added for up to 60 min in 10 min time intervals (Figure 19b). After determination of the localisations of both newly synthesised and pre-synthesised RNA molecules, NNA was conducted to measure the distance of each newly synthesised RNA molecule to the nearest pre-synthesised RNA molecule (Figure 19b). As in previous NNA experiments, C127 cells pulsed with EdU, where each RNA molecule was stained in two different colours, were used as a technical control. Additionally, a

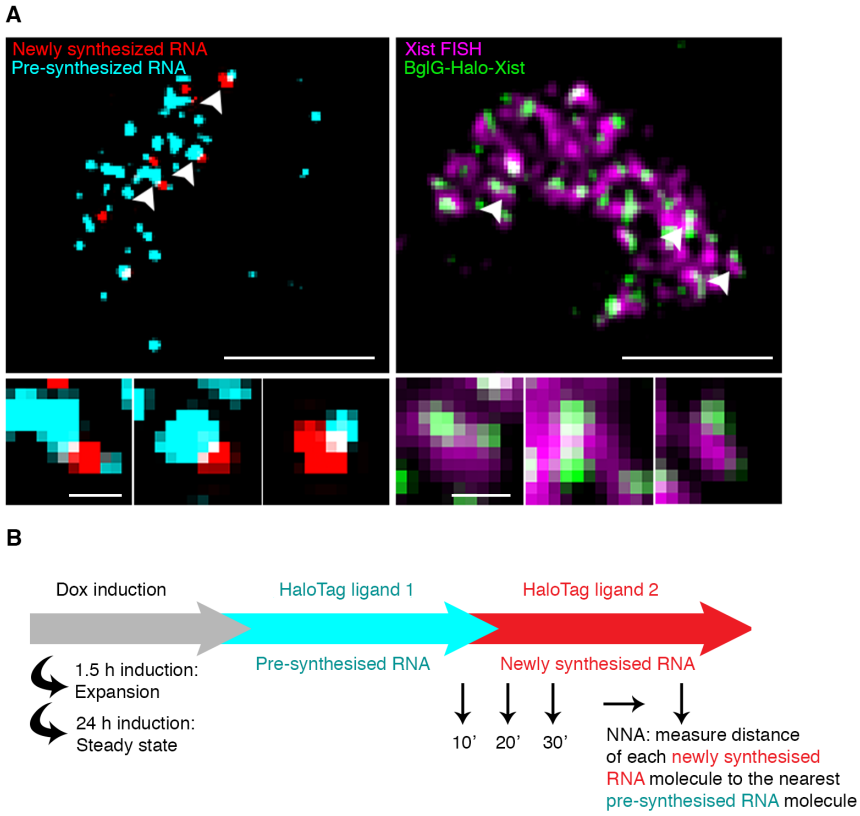

Figure 19: RNA-SPLIT shows that newly synthesised Xist couples with pre-synthesised Xist. A) Example image of pre-synthesised and newly synthesised Xist in expansion labelled by RNA-SPLIT (left) and combined Xist RNA FISH with Halo staining (right), visualised by 3D-SIM. Single cross-sections. Scale bars correspond to 2 μm in the main image and 200 nm in the small inserts. Arrows indicate 'coupled' Xist that are enlarged in the lower panels. B) Schematic illustrating experimental set up of RNA-SPLIT in combination with NNA. C) NNA of newly synthesised RNA to pre-synthesised RNA signal obtained by RNA-SPLIT during expansion and steady state in ChrX cells, including EdU and randomised control. n = 200 cells. D) NNA of RNA labelled with HaloTag ligand 2 to RNA labelled with HaloTag ligand obtained by dual-colour labelling, including NNA data of expansion in ChrX cells, EdU and randomised control for comparison. n = 20 cells (dual-colour control). E) NNA of newly synthesised RNA to pre-synthesised RNA signal obtained by RNA-SPLIT during expansion and steady state in autosomal transgene cells, including EdU and randomised control. n = 200 cells.

‘Random’ control was included, where the x, y and z coordinates determined for the newly synthesised RNA molecules were scrambled. This was done separately for each Xist territory to account for variation in Xist territory dimensions. The result from NNA of the ‘Random’ control illustrates the distribution of distances that would be obtained, if newly synthesised Xist RNA molecules would spread randomly across the Xist territory after transcription, while the result from the ‘EdU’ control shows the distribution that would be expected from perfectly co-localised newly synthesised and pre-synthesised Xist RNA molecules (Figure 19c). The latter distribution would suggest possible double-labelling of Xist molecules with the different HaloTag ligands.

Analysis of endogenous Xist in ChrX cells showed a median distance of 164 nm between newly synthesised Xist RNA molecules and pre-synthesised Xist RNA molecules during expansion (Figure 19c). These distances were significantly longer than in the EdU control (63 nm), thereby excluding prevalent double-labelling of the same Xist molecule, but were significantly shorter than in the ‘Random’ control (307 nm, Figure 19c). In fact, the distribution of NNA distances for couplets looked very similar to those obtained from measuring distances between BglG-Halo-Xist and Xist RNA FISH, where a median of 152 nm was determined (Figure 7e and 19c). These results suggest that newly synthesised Xist RNA molecules preferentially localise to previously occupied sites, coupling with pre-synthesised Xist RNA molecules (Figure 19c). Additionally, analysis of the RNA-SPLIT data obtained during steady state showed a median distance of 178 nm, significantly lower than the ‘Random’ control (Figure 19c), demonstrating that the phenomenon of Xist

coupling persists with progression of XCI. The proportion of newly synthesised Xist RNA molecules coupled with pre-synthesised Xist RNA molecules was slightly reduced in steady state as compared with expansion (Figure 19c).

In order to eliminate the possibility that turnover of BglG-Halo bound to Xist results in double-labelling of Xist molecules with the two different HaloTag ligands during RNA-SPLIT, a dual-colour control was set up (Figure 19d). Here, cells were incubated with an identical concentration of HaloTag ligand 1 and HaloTag ligand 2 at the same time instead of the sequential labelling approach of RNA-SPLIT. This should result in binding of BglG-Halo labelled with HaloTag ligand 1 and BglG-Halo labelled with HaloTag ligand 2 to the same Bgl-stem-loop array, at least in some instances. In fact, there was separate labelling of single foci either with ligand 1 or ligand 2 in most instances. This is most likely due to the fact that on average only 3 fluorescent BglG-Halo molecules bind to one Xist molecule (Figure 8a). Hence, only Xist molecules with 2 or more BglG-Halo molecules labelled with the same HaloTag ligand would have a sufficient signal to background ratio for confident thresholding and identification of Xist molecules. It follows that binding of BglG-Halo labelled with HaloTag ligand 1 and 2 at the same time would lead to a loss of increased intensity over background of free diffusing BglG-Halo in at least one of the channels. Importantly, the absence of co-labelled Xist molecules effectively rules out that the coupling observed in RNA SPLIT experiments is attributable to both ligands binding to the same stem-loop array.

In the dual labelling experiment the median distance was 514 nm, which is significantly higher than the median distance determined for the EdU control or the expansion phase in ChrX cells (Figure 19d). Distances were also significantly larger than in the 'Random' control, which was generated by randomisation of x/y/z coordinates after RNA-SPLIT was performed in ChrX cells (Figure 19d). This is most likely due to Xist molecules that bind a combination of one of each fluorescent fusion protein going entirely undetected, with the resulting loss of signal expected to lead to larger distances in the dual-colour control as compared to 'Random' RNA-SPLIT control (Figure 19d).

RNA-SPLIT followed by NNA was repeated for the autosomal transgene cell line to determine whether coupling of Xist could be a phenomenon specific to the X chromosome territory (Figure 19e). In expansion, a median distance of 186 nm from newly synthesised Xist RNA molecules to the nearest pre-synthesised Xist RNA molecule was detected, which is significantly higher than the EdU control at 77 nm and significantly lower than the 'Random' control at 410 nm (Figure 19e). While distances were slightly longer than in the ChrX cells, those of both controls were similarly longer. In fact, the median NNA distance was 2.4-fold higher than the EdU control in expansion in autosomal transgene cells, while it was 2.6-fold higher in ChrX cells, indicating that there is no significant difference in coupling in endogenous and autosomal transgenic Xist during expansion (Figure 19c and 19e). Similarly, coupling was also evident during steady state with a median distance of 245 nm from newly synthesised Xist RNA molecules to the nearest pre-synthesised Xist RNA molecule (Figure 19e). Thus, similar to Xist on the X chromosome,

autosomal transgenic Xist shows slightly reduced coupling in steady state compared to expansion (Figure 19c and 19e). Overall, coupling does not seem to be dependent on the X chromosomal context or the stage of XCI.

3.8 Summary: Fundamental principles of Xist spreading revealed

This chapter describes the generation of XX mESCs with doxycycline inducible endogenous Xist containing a Bgl-stem-loop array, as well as BglG-Halo fusion protein (Figure 6). For comparison, XY mESCs with doxycycline inducible autosomal transgenic Xist containing a Bgl-stem-loop array, as well as BglG-Halo fusion protein were also generated (Figure 9). Initial experiments showed that the Bgl-stem-loop system allows for efficient labelling of inducible endogenous Xist RNA on the X chromosome and autosomal transgenic Xist RNA on chromosome 15 to study Xist behaviour (Figure 7). Combining the BglG system with HaloTag technology, allowed exploitation of ligands with increased photostability and brightness to use 3D-SIM, which in turn yielded an increase in resolution sufficient for the detection of distinct Xist foci. Chromatin RNA sequencing confirmed that Xist mediated transcriptional silencing is achieved at WT levels after insertion of the Bgl-stem-loop array, and immunostaining showed that tagged Xist recruits secondary factors and brings about histone modification and chromatin changes as expected (Figure 8b and 8c). Moreover, the time window from 1.5 h until 5 h post-induction was identified for the assessment of initial Xist spreading across the chromosome territory (expansion), while experiments starting 24 h post-induction would be conducted to assess the maintenance of Xist on the chromosome territory in *cis* (steady state) (Figure 7c and 7d).

Combination of HaloTag ligand staining in ChrX cells with traditional Xist RNA FISH revealed that Xist foci appear globular with dimensions of approximately 200 nm in 3D and that Xist foci generally occur as couplets (Figure 7b). Furthermore, the 3’

end of Xist was found to be more closely associated with the chromatin boundary, while Xist in general was mostly located in the interchromatin space (Figure 7b), in line with previous 3D-SIM studies (Smeets et al. 2014). Furthermore, HaloTag ligand staining combined with immunostaining of the Xist localisation factor CIZ-1 and subsequent NNA indicated that CIZ-1 binds towards the 3' end of Xist, and does so very early after Xist induction (Figure 8d and 8e). This agrees with previous research, which established that CIZ-1 binds to Xist at the E-repeats (Ridings-Figueroa et al. 2017; Sunwoo et al. 2017). Based on these observations and the knowledge that CIZ-1 is a nuclear matrix protein and has been implicated in Xist localisation to the X chromosome territory (Ridings-Figueroa et al. 2017), one can suggest that globular Xist RNPs are tethered to the chromatin through CIZ-1 at their 3' end.

Originally, the aim of the project was to study Xist dynamics by live cell imaging of BglG-Halo-Xist, but as discussed technical limitations barred achieving this goal. 3D-SIM live cell imaging allowed for the detection of distinct Xist foci over time (Figure 11a). However, Xist was largely static. The most likely explanation is that the acquisition rate of 10 seconds/frame is too slow to observe Xist foci movements (Figure 11a). Fluorescence recovery after photobleaching (FRAP) experiments have previously shown that Xist is very dynamic with recovery times of approximately 30 min (Ng et al. 2011). Based on this and the aforementioned observations, Xist might be highly dynamic when finding binding sites across the chromosome territory, but might remain static for extended time periods once bound. The application of spt PALM/ TIRF could potentially have overcome the

issues of slow acquisition rates, but it was found that using photoactivatable ligands precludes using the increase in intensity of multiple BglG-Halo molecules binding to the stem-loop array to discriminate bound and unbound BglG-Halo proteins. Comparison of tracks from the nucleus and the Xist territory only was attempted to counter this, but significant differences were not apparent, and it was therefore not possible to confidently discriminate tracks for unbound and bound BglG-Halo (Figure 11b). The option of using the Mango RNA aptamer was also investigated but here mESC lines with stably integrated arrays could not be generated.

The limits of currently available live cell imaging approaches necessitated the development of RNA-SPLIT, a new method to study Xist dynamics and spreading behaviour. Here, sequential addition of different HaloTag ligands to live cells before fixation enables distinction of existing pre-synthesised RNA molecules from recently transcribed newly synthesised RNA molecules (Figure 12a and 12b). In addition, combination of this labelling approach with 3D-SIM results in high spatial and temporal resolution. Variations of staining times together with a sophisticated image processing workflow and different computational image analysis tools, such as centroid determination by Watershed algorithm and NNA, make RNA-SPLIT a powerful tool to assess many different aspects of RNA dynamics and localisation, such as molecule density and spreading behaviour, as well as RNA turnover and transcription dynamics (Figure 12c).

Initially, RNA-SPLIT was applied to assess RNA turnover. Both endogenous and autosomal transgenic Xist RNA were found to have 2-fold increased stability in expansion as compared to steady state (Figure 13c). This suggests that Xist stability

increases with progression of transcriptional silencing and associated chromatin changes independently of the chromosomal context. However, stability was found to be significantly decreased in the autosomal transgene cells as compared to the ChrX cells, with complete turnover of endogenous Xist at 140 and 220 min in expansion and steady state versus complete turnover of autosomal transgenic Xist at 80 and 140 min in expansion and steady state respectively (Figure 13c). This indicates that Xist RNA may be more stable in the X chromosome context, although further analysis of multiple autosomal transgene cell lines would be needed to confirm this. Assuming this is generally the case, increased stability of Xist RNA on the X chromosome could be due to the different chromatin environment compared to chromosome 15 and/or X chromosome specific factors. An example would be the differences seen in abundance and distribution of LINE1 elements reported previously (Lyon 1998; Tang et al. 2010; Chow et al. 2010). Effects on Xist RNA stability may contribute to the reduced silencing abilities of autosomally located Xist. Equally, the increase in stability over time could be caused by physical changes to the chromatin environment linked to chromosome silencing or by secondary factor(s) present only in the steady state phase of XCI. SLAM-seq analysis of the degradation kinetics of Xist was successfully used to cross-validate the RNA-SPLIT results, and showed that Xist stability does not change dramatically after insertion of the Bgl-stem-loop array (Figure 14).

Increased stability of Xist RNA in steady state compared to expansion is apparently at odds with the observation of a general decrease in Xist molecule number. A change in transcription dynamics was hypothesised to account for this and indeed,

RNA-SPLIT revealed that both endogenous and autosomal transgenic Xist transcription is significantly decreased in steady state as compared to expansion (Figure 15b). Moreover, Xist transcription was found to be generally increased in the autosomal transgene compared to the ChrX cell line (Figure 15b). These observations are surprising considering that both endogenous and autosomal transgenic Xist are controlled by a doxycycline inducible promoter. However, it is feasible to think that chromosome wide transcriptional silencing and chromatin changes might impact on accessibility of the Xist promoter for RNA polymerases and thereby decrease transcription as XCI progresses. Hence, there might be a feedback mechanism controlling Xist stability depending on transcription rates.

Previous studies suggest that interruption of transcription by Actinomycin D treatment leads to an increase in Xist stability (Ng et al. 2011). This finding was reinvestigated using doxycycline washout, negating effects of halting DNA-dependent RNA polymerase mediated transcription on the full range of cellular processes. The results showed that Xist stability is dramatically increased in the washout condition, confirming that Xist stability must be linked to Xist transcription through some sort of feedback mechanism (Figure 15d).

RNA-SPLIT was also used to investigate Xist RNA spreading. In previous work Xist RAP experiments revealed that Xist spreading across the X chromosome correlates to Hi-C data, indicating that Xist spreads from its transcription site to 3D proximal sites first (Engreitz et al. 2013). However, this was based on the correlation of bulk Xist RAP data with a different publicly available Hi-C dataset obtained from male XY mESCs. RNA-SPLIT on the other hand provides temporally resolved 3D

localisation information. Approximate Xist transcription site localisation was determined based on the density and fluorescence intensity of the signal from newly transcribed Xist RNA, which enabled comparison of the distances of RNA molecules from the transcription site in 3D over time. Indeed, newly transcribed Xist was found to spread in 3D from the transcription site towards the periphery of the Xi territory with an expansion rate of 7.67 $\mu m^3/h$ during the expansion phase. No significant redistribution of pre-synthesised Xist could be detected over this time course (Figure 16b). Taken together with the observation of more rapid turnover of peripheral compared to centrally located Xist RNA (Figure 13b), it seems likely that newly transcribed Xist molecules find 3D proximal binding sites before gradually spreading towards the periphery of the Xi in a series of binding and unbinding steps. RNA-SPLIT did not show said 3D spreading behaviour of Xist in steady state (Figure 16b), in line with CHART-seq experiments showing that Xist RNA spreads to all regions without preference after locked nucleic acids knockoff at later stages of XCI (Simon et al. 2013).

Determination of Xist transcription site localisations and comparison of their distribution in expansion and steady state revealed that the Xist transcription site relocates from the centre of the Xi territory towards the periphery over time in ChrX cells (Figure 17b and 17c). This might help to maintain accessibility of the Xist promoter for RNA polymerases as chromatin is compacted throughout XCI.

Xist RNA labelling using RNA-SPLIT also allowed for the observation of accumulation of Xist in couplets. This phenomenon had not previously been described, because such an accumulation would show as one single Xist RNA FISH

domain, even when detected by 3D-SIM. Upon close examination of the RNA-SPLIT data newly synthesised Xist RNA molecules were found to be overwhelmingly associated with pre-synthesised Xist RNA molecules (Figure 19a). Quantification by NNA confirmed this phenomena, with newly transcribed Xist coupling with previously bound Xist (Figure 19c). Detection of double-labelling of Xist with the different HaloTag ligands was ruled out by a dual-colour control (Figure 19d). Coupling was observed in both expansion and steady state, as well as in the endogenous and autosomal transgenic context (Figure 19c and 19e), suggesting that it is independent of the stage of XCI, chromosomal context, as well as accompanying changes in Xist stability and transcription rate. Overwhelmingly, coupling was observed as one newly synthesised and one pre-synthesised Xist RNA molecule, as opposed to two newly synthesised or two pre-synthesised molecules. This implies that newly synthesised molecules do not usually pair up or travel in pairs, but rather that coupling happens at the binding site marked by an existing molecule. An important consideration is whether or not coupling facilitates Xist RNA spreading. This point is discussed further in chapters below.

In summary, RNA-SPLIT, a powerful method to assess RNA dynamics and behaviour, was developed. Careful time-resolved analysis of endogenous and autosomal transgenic Xist RNA localisation, turnover and transcription during expansion and steady state revealed fundamental principles of Xist spreading. Cumulatively, the results allow for the proposal of a new model of Xist behaviour, where its stability is dependent on the chromatin environment, and Xist transcription rates define Xist stability through an unknown feedback mechanism. Here, highly

dynamic newly transcribed Xist RNA molecules gradually spread in 3D across the Xi territory during expansion, localising to previously occupied sites by coupling, before being preferentially degraded when reaching the periphery of the Xi.

CHAPTER IV

4 Application of RNA-SPLIT to investigate Xist dynamics and behaviour in Ciz-1 knockout cells

4.1 CRISPR mediated knockout of CIZ-1 in BglG-Halo-Xist mESCs

In addition to the previously described assessment of Xist RNA dynamics, localisation and spreading behaviour in ChrX and autosomal transgene cells, the newly developed RNA-SPLIT methodology allows quantitative analysis of Xist RNA behaviour following perturbation of factors implicated in Xist localisation/spreading. A prime candidate for such experiments is the nuclear matrix protein CIZ1, which has recently been implicated in Xist localisation to the Xi (Ridings-Figueroa et al. 2017; Sunwoo et al. 2017). KO of CIZ-1 has been shown to lead to Xist RNA dispersal in mouse fibroblasts as well as B- and T-lymphocytes (Ridings-Figueroa et al. 2017). Hence, the next aim of this study was to perturb CIZ-1 function in XX mESCs and study its effect on Xist localisation and dynamics before and after differentiation.

Ciz-1 KO cells were generated by CRISPR/Cas9 mediated genome engineering (Figure 20a). The first guide RNA (gRNA1) was used previously used to induce a frameshift mutation (Sunwoo et al. 2017) (Figure 20a). Here, it was used in combination with a second guide RNA (gRNA2) to achieve a genomic deletion of 10.66 kb, resulting in the KO of the gene encoding CIZ-1 in the parental XX mESC line used previously to enable both RNA-SPLIT and allele-specific analysis as

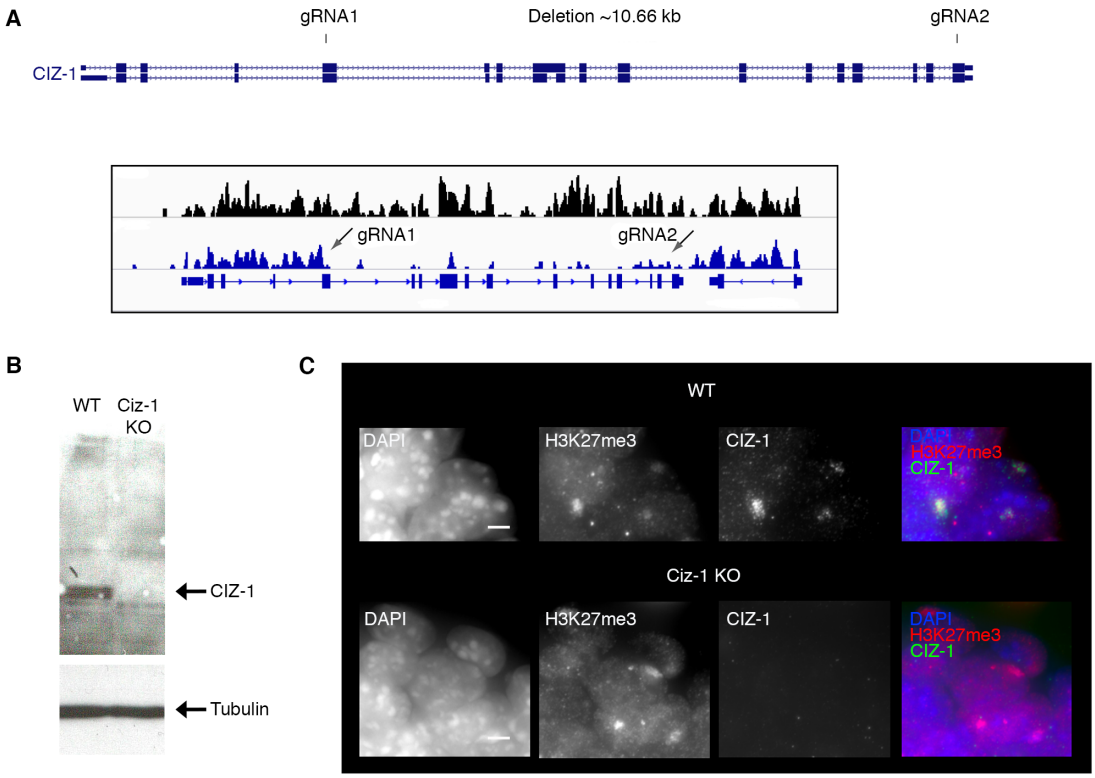

Figure 20: Generation of Ciz-1 KO mESCs. A) Schematic illustrating the strategy to achieve Ciz-1 KO in XX mESCs by CRISPR/Cas9 mediated genome engineering. Includes chromatin RNA sequencing results of CIZ-1 transcripts in WT (black) and Ciz-1 KO cells (blue). B) Western blot for CIZ-1 in WT and Ciz-1 KO cells, confirming successful depletion of CIZ-1 on the protein level. Includes α-tubulin loading control. C) Representative images of combined immunostaining for H3K27me3 and CIZ-1 with DAPI counter stain of WT cells and Ciz-1 KO cells 24 h post-induction, visualised with a Zeiss fluorescence microscope. Maximum intensity projections. Scale bars correspond to 5 μm.

described in chapter 3 (Figure 20a). This KO strategy includes the removal of a major part of both common CIZ-1 splice variants (Figure 20a). As expected, chromatin RNA sequencing showed a dramatic reduction of transcripts from the genomic region between gRNA1 and gRNA2, confirming successful deletion of the majority of *CIZ-1* (Figure 20a). Western blot analysis of CIZ-1 was performed, comparing ChrX cells (henceforth referred to as WT for comparison with mutant cell lines) and Ciz-1 KO cells to confirm depletion of CIZ-1 at the protein level and indeed, no CIZ-1 protein could be found in the Ciz-1 KO cell line (Figure 20b). It is noteworthy that the CIZ-1 band appeared as a doublet, which agrees with the presence of CIZ-1 splice variants with a difference of only 50 amino acids (Figure

20a and 20b). Importantly, neither isoforms of CIZ-1 could be detected in Ciz-1 KO cells (Figure 20b). To further validate the KO, combined immunostaining for the Xi mark H3K27me3 and CIZ-1 was carried out (Figure 20c). H3K27me3 enrichment could be observed in both WT and Ciz-1 KO cells, indicating successful deposition of the PRC-mediated histone modification on the Xi (Figure 20c). In contrast, CIZ-1 enrichment on the Xi was only found in the WT cells, confirming successful KO of CIZ-1 (Figure 20c).

Xist RNA FISH was conducted to eliminate the potential presence of polyploid or XO cells in the Ciz-1 KO cell line (Figure 21a): Scoring of Xist territories after doxycycline treatment of Xist demonstrated a high induction efficiency of Ciz-1 KO cells (84.5% after 3 h, which increased to 90% after 24 h), similar to WT (Figure 21a). Only 2% of cells showed Xist territory formation without doxycycline induction, suggesting negligible leakiness of the inducible promoter (Figure 21a). As expected considering previous research (Ridings-Figueroa et al. 2017), Xist localisation seemed to be unaffected in Ciz-1 KO mESCs at this resolution (Figure 21a).

Finally, chromatin RNA sequencing and allelic analysis showed that Xist-mediated silencing of X-linked genes after 24 h of doxycycline induction was unaffected upon perturbation of CIZ-1 (Figure 21b). Even when examining the transcription of different genes separately, no significant changes could be detected (Figure 21b).

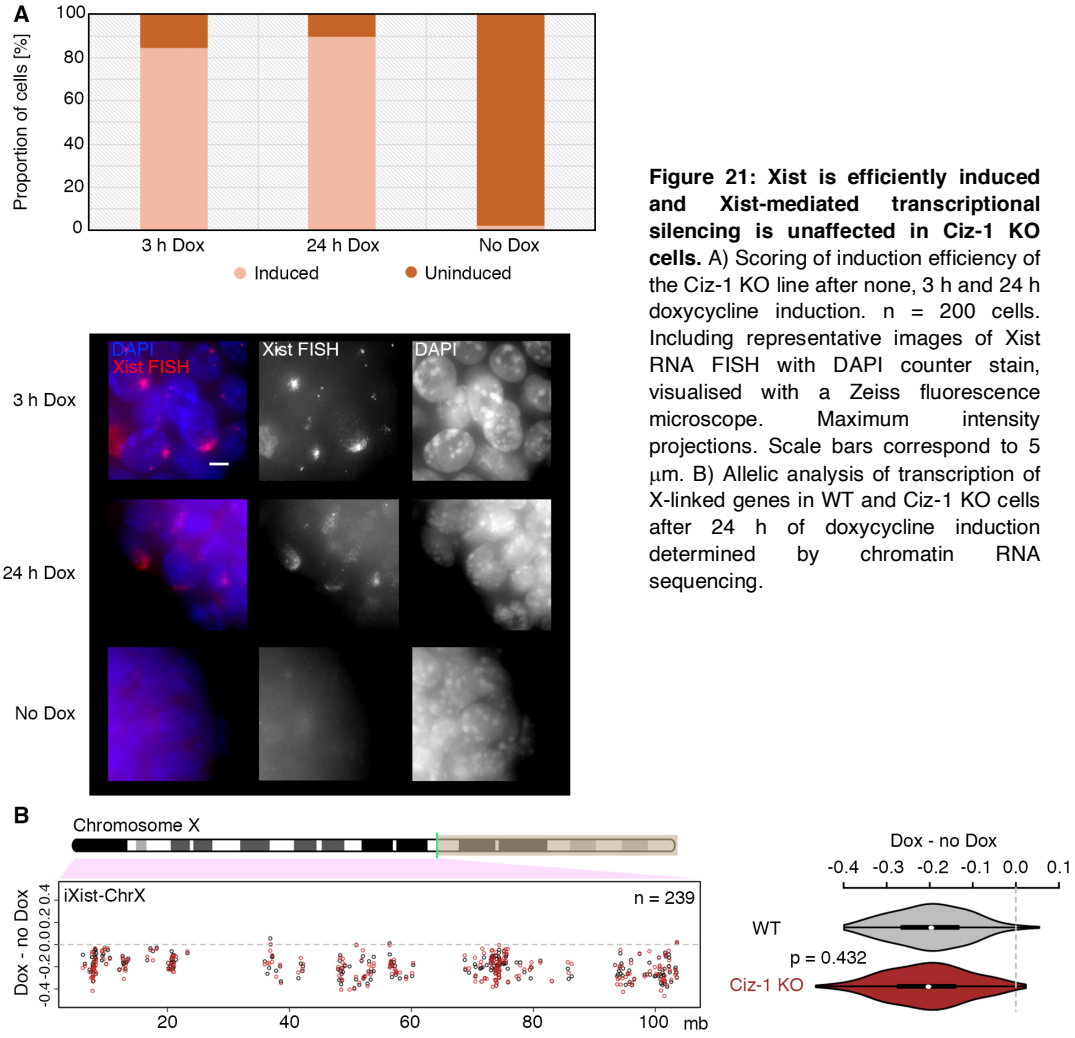

Figure 21: Xist is efficiently induced and Xist-mediated transcriptional silencing is unaffected in Ciz-1 KO cells. A) Scoring of induction efficiency of the Ciz-1 KO line after none, 3 h and 24 h doxycycline induction. n = 200 cells. Including representative images of Xist RNA FISH with DAPI counter stain, visualised with a Zeiss fluorescence microscope. Maximum intensity projections. Scale bars correspond to 5 μm. B) Allelic analysis of transcription of X-linked genes in WT and Ciz-1 KO cells after 24 h of doxycycline induction determined by chromatin RNA sequencing.

4.2 KO of CIZ-1 has a minor effect on Xist localisation in mESCs

Although no localisation defect was observed in Ciz-1 KO mESCs using a widefield fluorescence microscope, more subtle effects might have been overlooked due to the low resolution (Figure 21a). Therefore, single-colour HaloTag staining was performed 3 h and 24 h post-induction and Xist territories were visualised using 3D-SIM (Figure 22a). No significant differences in Xist localisation between WT and Ciz-1 KO cells could be seen by eye, both in expansion and steady state (Figure 22a). However, quantification of different parameters showed that KO of CIZ-1 in mESCs in fact has a minor effect on Xist localisation. Specifically, measurement of the volume of the Xist territory as obtained during the cropping stage of image processing showed a significant decrease in steady state as compared to expansion in both WT and Ciz-1 KO cells (Figure 12c and 22b). In expansion, Xist territories were determined to be of similar volume in WT and Ciz-1 KO cells (Figure 22b). These results indicate that Xist territory compaction and a resulting reduction of Xist transcription is unaffected in Ciz-1 KO cells. However, a significant decrease of Xist territory volume in Ciz-1 KO as compared to WT cells was shown in steady state (Figure 22b). A possible explanation is that the number of Xist molecules is reduced upon perturbation of CIZ-1, and indeed, this was found to be the case both in expansion and steady state. Presumably this effect is linked to differences in Xist transcription and/or stability (Figure 22c). Xist molecule number decreased from expansion to steady state in Ciz-1 KO cells, which points towards a potential reduction of Xist transcription over time, as previously described in WT and autosomal transgene cells (Figure 22c).

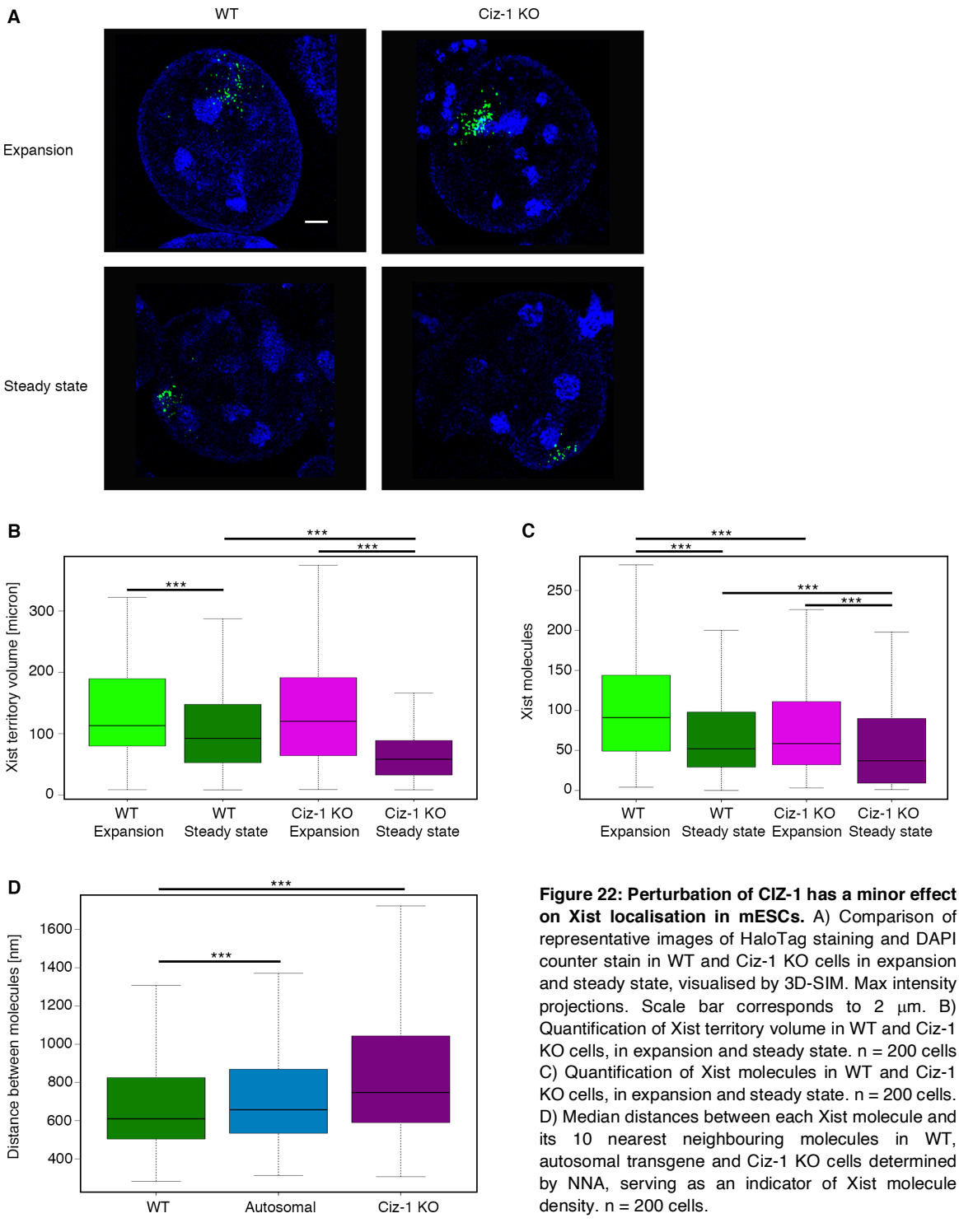

Figure 22: Perturbation of CIZ-1 has a minor effect on Xist localisation in mESCs. A) Comparison of representative images of HaloTag staining and DAPI counter stain in WT and Ciz-1 KO cells in expansion and steady state, visualised by 3D-SIM. Max intensity projections. Scale bar corresponds to 2 μm. B) Quantification of Xist territory volume in WT and Ciz-1 KO cells, in expansion and steady state. n = 200 cells C) Quantification of Xist molecules in WT and Ciz-1 KO cells, in expansion and steady state. n = 200 cells. D) Median distances between each Xist molecule and its 10 nearest neighbouring molecules in WT, autosomal transgene and Ciz-1 KO cells determined by NNA, serving as an indicator of Xist molecule density. n = 200 cells.

To confirm the apparent difference in Xist domain volume in Ciz-1 KO cells NNA of BglG-Halo-Xist was used to quantify the density of Xist molecules in different cellular backgrounds. Here, the median distance of each Xist molecule to the 10

nearest neighbouring Xist molecules was determined in WT and Ciz-1 KO cells in order to assess Xist molecule density and chromosome coverage (Figure 22d). As an additional control Xist density was also measured for the autosomal transgene mESCs described above. The results show a significant increase in median distances between Xist molecules in Ciz-1 KO as compared to WT cells, i.e. a significant decrease in Xist molecule density (Figure 22d). Considering that there is no change in the size of the Xist territory volume, perturbation of CIZ-1 does not seem to cause delocalisation of Xist from the Xi, but instead leads to a less dense coverage of Xist RNA molecules (Figure 22b and 22d). A similar but less pronounced effect on Xist density could also be observed in the autosomal transgene cells (Figure 22d). This is in line with the suggestion that transgenic Xist spreading on autosomes may be attenuated and that Xist coverage of autosomes might not be as efficient as in WT (Popova et al. 2006). That the density defect seems to be even more pronounced in Ciz-1 KO cells indicates that perturbation of CIZ-1 might lead to a similar defect in Xist spreading and/or coverage of the chromosome *in cis* (Figure 22d).

Considering the suggested role of CIZ-1 in anchoring Xist to the chromatin (Sunwoo et al. 2017), reduced density of Xist RNA molecules could indicate that less Xist molecules are bound to chromatin in Ciz-1 KO than in WT cells, and that unbound molecules are rapidly degraded. Less efficient compaction of the Xi could be ruled out as a reason, since Xist territory volumes were found to be significantly reduced with progression of XCI similar to WT cells (Figure 22b). Alternatively, the density defect could be an indirect result of a reduction in Xist transcription or stability, which

would agree with the general reduction in Xist molecule numbers (Figure 22c). RNA-SPLIT and subsequent analysis of Xist transcription and degradation dynamics were therefore used to investigate this further.

4.3 Xist dynamics are largely unaffected in Ciz-1 KO mESCs

Development of RNA-SPLIT has enabled the distinction of pools of newly synthesised and pre-synthesised RNA and their observation over time. This allows for a unique insight into Xist RNA dynamics. As described in chapter 3 section 3, one can detect the number of pre-synthesised RNA molecules while increasing the staining time for newly synthesised RNA until no more pre-synthesised RNA is present (Figure 23a). This can then be used to derive the turnover time of Xist RNA on chromatin, and comparison of different cell lines can reveal the potential impact of perturbation of Xist silencing and localisation factors on Xist RNA stability. Here, Xist turnover was assessed in Ciz-1 KO cells in expansion and steady state.

Xist RNA stability was found to increase almost 2-fold from expansion to steady state in Ciz-1 KO cells, confirming the same observation made in the WT context previously (Figure 23b). Strikingly, complete turnover times of Xist in Ciz-1 KO cells were exactly the same as in WT cells, with 140 min in expansion and 220 min in steady state (Figure 23b). However, the decrease of Xist molecule numbers commenced slightly earlier in steady state in the Ciz-1 KO cells as compared to WT cells (Figure 23b). Hence, a minor decrease in Xist stability could possibly account for the slightly reduced Xist molecule number in steady state in Ciz-1 KO cells compared to WT cells (Figure 22c and 23b).

RNA-SPLIT not only allows for the assessment of Xist RNA stability, but also for the determination of Xist RNA transcription rates. Here, the gradual increase of newly synthesised RNA molecules was counted in short time intervals in order to examine Xist RNA transcription in expansion and steady state in Ciz-1 KO cells and

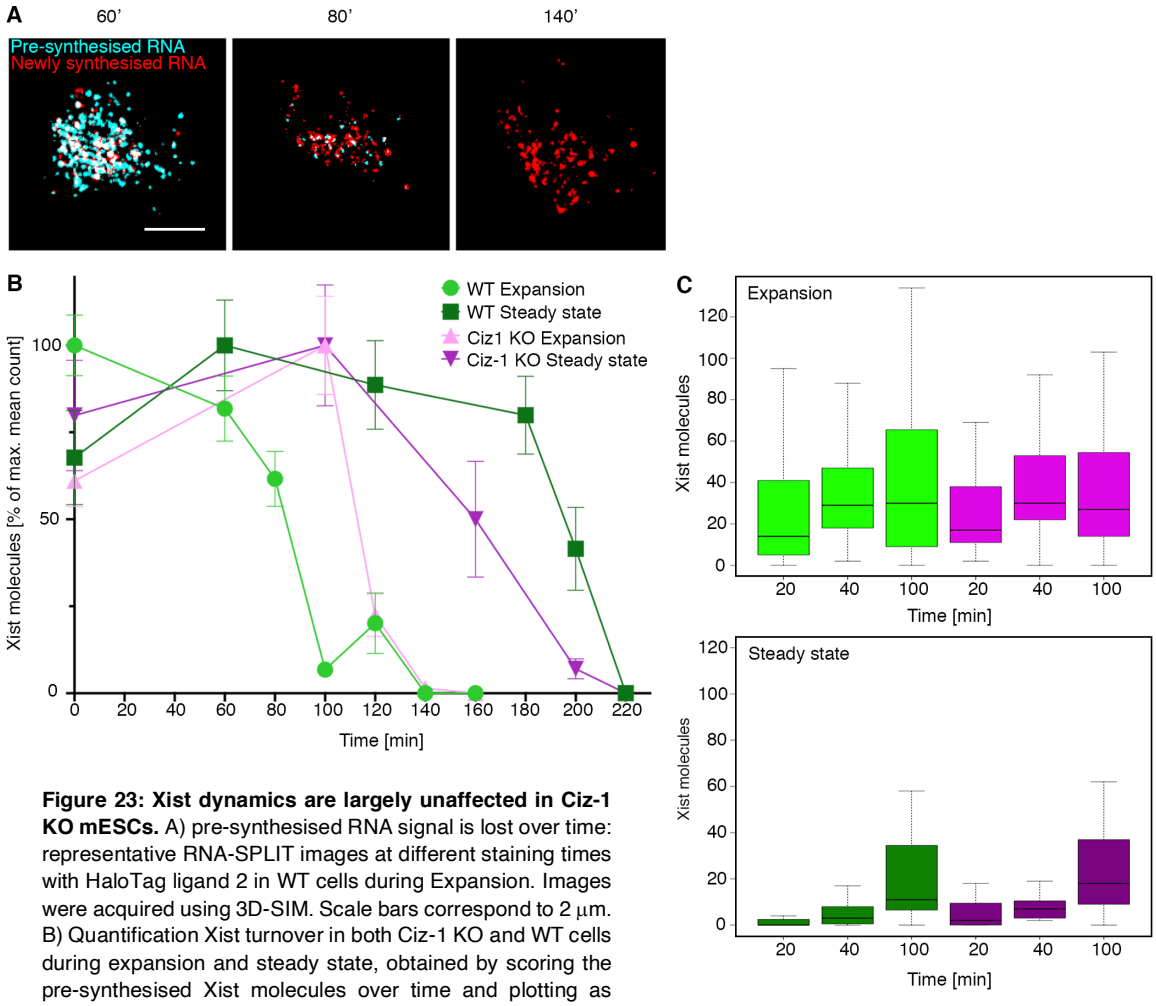

Figure 23: Xist dynamics are largely unaffected in Ciz-1 KO mESCs. A) pre-synthesised RNA signal is lost over time: representative RNA-SPLIT images at different staining times with HaloTag ligand 2 in WT cells during Expansion. Images were acquired using 3D-SIM. Scale bars correspond to 2 μm. B) Quantification Xist turnover in both Ciz-1 KO and WT cells during expansion and steady state, obtained by scoring the pre-synthesised Xist molecules over time and plotting as percentage of max. mean molecule count for each dataset. n = 20 cells/time point. C) Quantification of Xist RNA transcription in Ciz-1 KO and WT cells during expansion and steady state, obtained by scoring the number of newly synthesised Xist molecules over time. n = 20 cells/ time point.

compared to Xist transcription in WT cells (Figure 23c). A general reduction of Xist transcription with progression of XCI from expansion to steady state could be observed in Ciz-1 KO cells similar to WT cells (Figure 23c). This agrees with a reduction of Xist molecule numbers in steady state as compared to expansion in both Ciz-1 KO and WT cells (Figure 22c and 23c). Additionally, comparison of Xist transcription in Ciz-1 KO and WT showed a slight decrease of transcription in Ciz-1 KO cells during expansion, but not during steady state (Figure 23c). Together with the minor decrease in Xist stability in Ciz-1 KO cells during steady state, these

findings might account for the generally reduced number of Xist molecules in Ciz-1 KO cells (Figure 22c, 23b and 23c). However, it cannot be excluded that technical variations could be the cause of these minor differences, since only one WT line has been assessed due to time restrictions. To conclude, RNA-SPLIT analysis indicates that perturbation of CIZ-1 has no major effect on Xist RNA dynamics in mESCs.

4.4 Xist coupling is unaffected in Ciz-1 KO mESCs

RNA-SPLIT revealed the fascinating phenomenon of Xist 'coupling' at different stages of XCI, as well as in the context of the X chromosome and chromosome 15 (Figure 19). To determine if this phenomenon is affected in Ciz-1 KO mESCs RNA-SPLIT images of Ciz-1 KO mESCs were examined and found to have seemingly undisrupted Xist coupling (Figure 24). To quantify this result NNA was used to measure the distances between newly synthesised Xist RNA molecules and their respective nearest neighbouring pre-synthesised Xist RNA molecules. As previously described, female C127 cells pulsed with EdU were used for alignment and as technical control, while x, y, and z coordinates of newly synthesised mESC Xist RNA molecule localisations were scrambled before NNA to serve as 'Random' control (Figure 24).

NNA showed a median distance of 166 nm between newly synthesised Xist RNA molecules and pre-synthesised Xist RNA molecules during expansion in Ciz-1 KO cells as compared to 164 nm in WT cells, indicating that Xist coupling is indeed unaffected (Figure 19c and 24). The distance recorded is 3.3-fold higher than the EdU control, similar to the fold change of 2.6 seen in WT cells (Figure 19c and 24). Moreover, the median distance between newly synthesised Xist RNA molecules and pre-synthesised Xist RNA molecules was significantly shorter than in the 'Random' control, which showed a median distance of 720 nm (Figure 24). It is worth mentioning that the latter control is more than two times higher than the median distance of 302 nm measured in WT cells (Figure 19c and 24). This is explained by the lower density of Xist molecules in Ciz-1 KO leading to increased

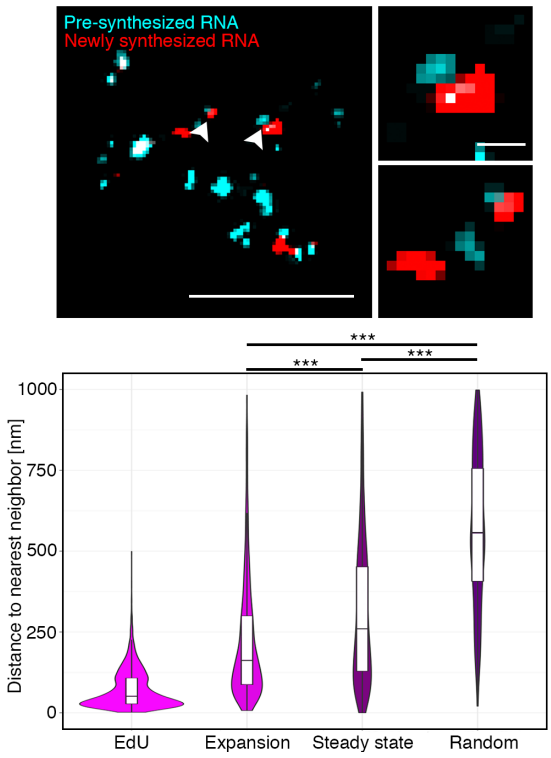

Figure 24: Xist coupling is unaffected in Ciz-1 KO mESCs. Example image of pre-synthesised and newly synthesised Xist in expansion labelled by RNA-SPLIT in Ciz-1 KO cells (top), visualised by 3D-SIM. Single cross-sections. Scale bar corresponds to 2 μm. Small inserts show 'coupled' Xist in detail. Arrows indicate 'coupled' Xist that are enlarged in the lower panels. Scale bars correspond to 200 nm. NNA of newly synthesised RNA to pre-synthesised RNA signal obtained by RNA-SPLIT during expansion and steady state in Ciz-1 KO cells (bottom), including EdU and randomised control. n = 200 cells.

distances between randomly scrambled molecules (Figure 22d). In fact, the same effect on the 'Random' control could be seen in the autosomal transgene cells, which also exhibit a Xist molecule density defect, albeit to a lesser extent (Figure 19e and 22d). Xist coupling was also observed during steady state in Ciz-1 KO cells with a median distance of 285, which is significantly lower than the 'Random' control (Figure 24). However, it is considerably higher than the respective median distance measured in WT cells of 178 nm. It is therefore possible that coupling in Ciz-1 KO mESCs is slightly reduced in steady state (Figure 19c and 24).

4.5 Xist is fully delocalised in Ciz-1 KO NPCs

Extensive analysis of Xist localisation, dynamics and coupling in Ciz-1 KO cells showed that CIZ-1 only plays a minor role in Xist density and dynamics in mESCs, however, it has been shown that perturbation of CIZ-1 leads to Xist RNA dispersal in some differentiated cell types (Ridings-Figueroa et al. 2017; Sunwoo et al. 2017). Hence, it is reasonable to assume that insights obtained by single Xist foci detection in combination with RNA-SPLIT in differentiated Ciz-1 KO cells might facilitate exploration of CIZ-1 function in the context of XCI. This requires differentiation not only of the Ciz-1 KO mESC line but also of the parental WT mESC line, because fundamental principles of Xist behaviour in differentiated cells need to be assessed in the WT context first in order to make comparisons with CIZ-1KO cells. For this purpose the WT and Ciz-1 KO mESC lines described above were differentiated into NPCs using a differentiation protocol that has been previously developed and optimised in the lab adapted, based on protocols from Conti et al. 2005 and Splinter et al. 2011 (Figure 25a). Although an Xist localisation defect has not specifically been shown in Ciz-1 KO NPCs or neurons, this protocol was chosen because experience has shown that it provides relatively homogenous differentiation compared to other protocols such as embryoid body differentiation. NPCs are especially suitable for imaging experiments due to being flattened and adherent. Using flat cells reduces out of focus light and this is of particular importance for 3D-SIM, since resolution improves with increased proximity of the area of interest to the coverslip. For these experiments NPC differentiation medium was supplemented with doxycycline to maintain Xist induction (Figure 25a). Single

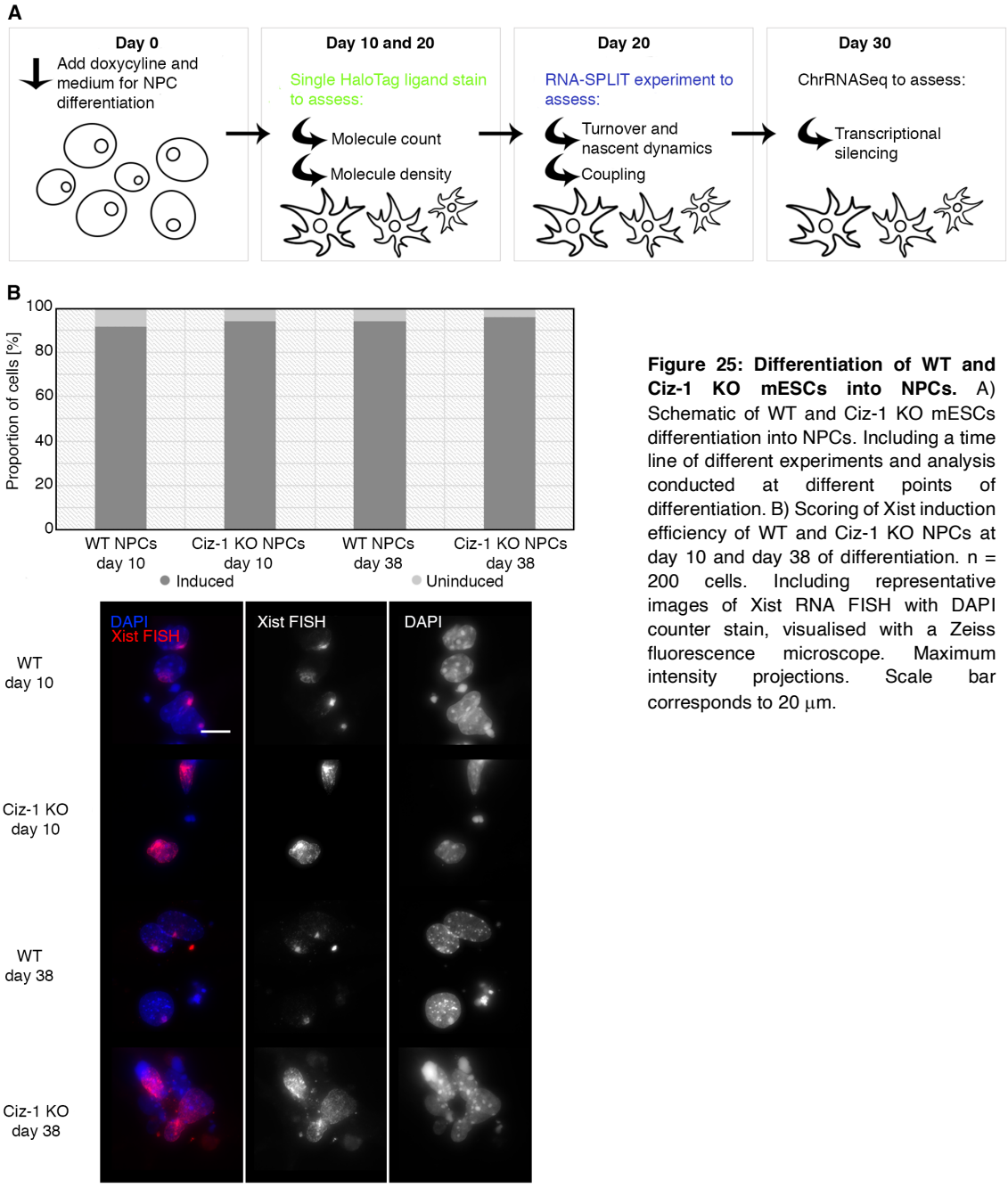

Figure 25: Differentiation of WT and Ciz-1 KO mESCs into NPCs. A) Schematic of WT and Ciz-1 KO mESCs differentiation into NPCs. Including a time line of different experiments and analysis conducted at different points of differentiation. B) Scoring of Xist induction efficiency of WT and Ciz-1 KO NPCs at day 10 and day 38 of differentiation. n = 200 cells. Including representative images of Xist RNA FISH with DAPI counter stain, visualised with a Zeiss fluorescence microscope. Maximum intensity projections. Scale bar corresponds to 20 μm.

HaloTag ligand staining was performed at day 10 and day 20 of differentiation and Xist molecule count as well as Xist molecule density were determined to assess Xist localisation in WT and Ciz-1 KO NPCs (Figure 25a). Moreover, RNA-SPLIT was independently conducted at day 20 of NPC differentiation to examine Xist RNA turnover, transcription dynamics and coupling (Figure 25a). Finally, chromatin RNA

sequencing was performed at day 30 of differentiation in order to assess Xist-mediated transcriptional silencing (Figure 25a).

In order to exclude polyploidy or presence of XO cells, and to evaluate induction efficiency in the WT and Ciz-1 KO NPCs at earlier and later stages of differentiation, Xist was visualised by RNA FISH at day 10 and day 38 of differentiation (Figure 25b). This analysis showed that Xist induction efficiency is very high in WT and Ciz-1 KO NPCs with 91.5% and 94% respectively at day 10 of differentiation, further increasing to 94% and 96% respectively at day 38 of differentiation (Figure 25b). Strikingly, dispersal of Xist throughout the nucleus was visible in the majority of Ciz-1 KO cells at both early and later stages of NPC differentiation, even when visualised at low resolution with widefield fluorescence microscopy (Figure 25b).

The localisation defect of Xist RNA in Ciz-1 KO NPCs became even more apparent when BglG-Halo-Xist was super-resolved by 3D-SIM (Figure 26a). It also became clear that Xist still clusters, even when dispersed across the entire nucleus (Figure 26a). Close examination of single cross-sections showed that Xist primarily clusters at heterochromatic regions around the nuclear/nucleolar periphery. This suggests that Xist might have interactions with heterochromatic regions even when it is not localised to a specific chromosome *in cis*.

In order to quantify the dispersal of Xist, NNA was used to measure the median distances of each Xist molecule to all other Xist molecules in each cell (Figure 26b). This measure describes the density of Xist molecules in WT and Ciz-1 KO NPCs at different stages of differentiation (Figure 26b). Accordingly, a dramatic increase in median distances and, thus, a decrease in Xist molecule density could be quantified

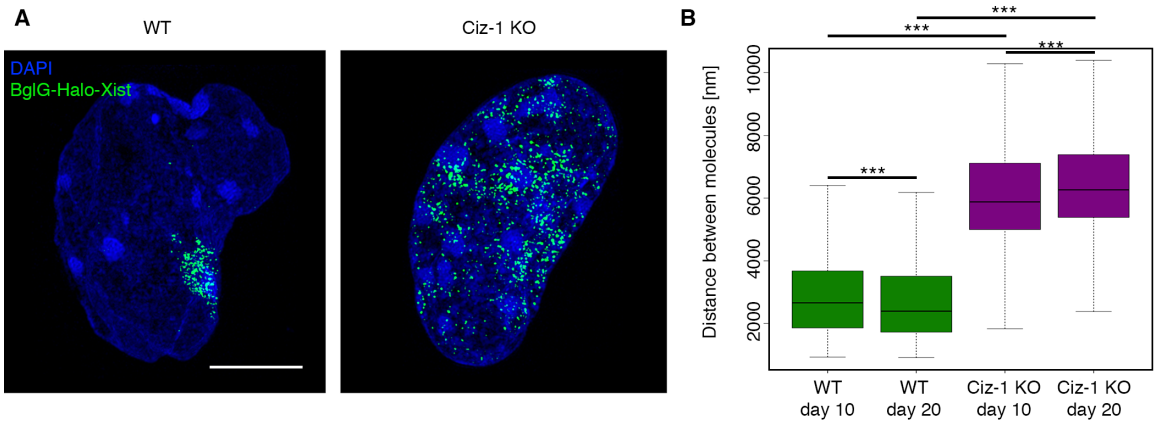

Figure 26: Xist is fully delocalised in Ciz-1 KO NPCs. A) Comparison of representative images of HaloTag staining and DAPI counter stain in WT and Ciz-1 KO NPCs at day 10 of differentiation, visualised by 3D-SIM. Maximum intensity projections. Scale bars correspond to 2 μm. B) Median distances between each Xist molecule and all other Xist molecules in each cell in WT and Ciz-1 KO NPCs at day 10 and day 20 of differentiation, determined by NNA, serving as an indicator of Xist molecule density. n = 200 cells.

in Ciz-1 KO NPCs as compared to WT NPCs (Figure 26b). Interestingly, distances between Xist molecules were found to significantly decrease and density to increase as differentiation progresses in WT NPCs, possibly due to further compaction of the Xi (Figure 26b). In contrast, distances were seen to significantly increase and density to decrease with progression of differentiation in Ciz-1 KO NPCs (Figure 26b). That the Xist dispersal phenotype in Ciz-1 KO NPCs becomes more pronounced with differentiation supports the suggestion that CIZ-1 function in Xist localisation might be redundant in mESCs and become gradually more important with advancement of cellular differentiation and XCI (Figure 26b).

4.6 Minimal effects on silencing in Ciz-1 KO NPCs

Considering the dramatic delocalisation of Xist in Ciz-1 KO NPCs (Figure 26a), the question arises whether this has an impact on Xist-mediated silencing. As a first step in investigating this the recruitment of Polycomb group proteins and hence the enrichment of corresponding histone modifications such as uH2A was assessed. Combined HaloTag staining with immunostaining for uH2A was performed in WT and Ciz-1 KO NPCs (Figure 27a). As expected, uH2A enrichment at the Xist territory could be clearly seen in WT NPCs, indicating ongoing Polycomb group protein recruitment and histone modification deposition (Figure 27a). In Ciz-1 KO NPCs, however, uH2A enrichment could not be observed (Figure 27a). Enrichment was seen at sites where dispersed Xist localises, for example at heterochromatin of the nuclear periphery and surrounding the nucleoli in comparison to WT NPCs (Figure 27a). This suggests that the delocalised Xist might still be able to recruit Polycomb group proteins to chromatin to deposit histone modifications, and potentially that delocalised Xist maintains a silencing function (see also below).

To directly test how Xist RNA dispersal in Ciz-1 KO NPCs affects Xi silencing allelic chromatin RNA sequencing of WT and Ciz-1 KO NPCs was carried out (Figure 27b). Analysis of WT and Ciz-1 KO mESCs as in Figure 21b was repeated to provide a reference control. Xist-mediated silencing of the Xi progressed significantly after 30 days of NPC differentiation in both WT and Ciz-1 KO NPCs (Figure 27b). These results indicate that delocalisation of Xist in Ciz-1 KO NPCs does not lead to an obvious reactivation of the Xi, and that silencing can be maintained independently of Xist and enrichment of uH2A at this stage (Figure 27a and 27b). This is consistent

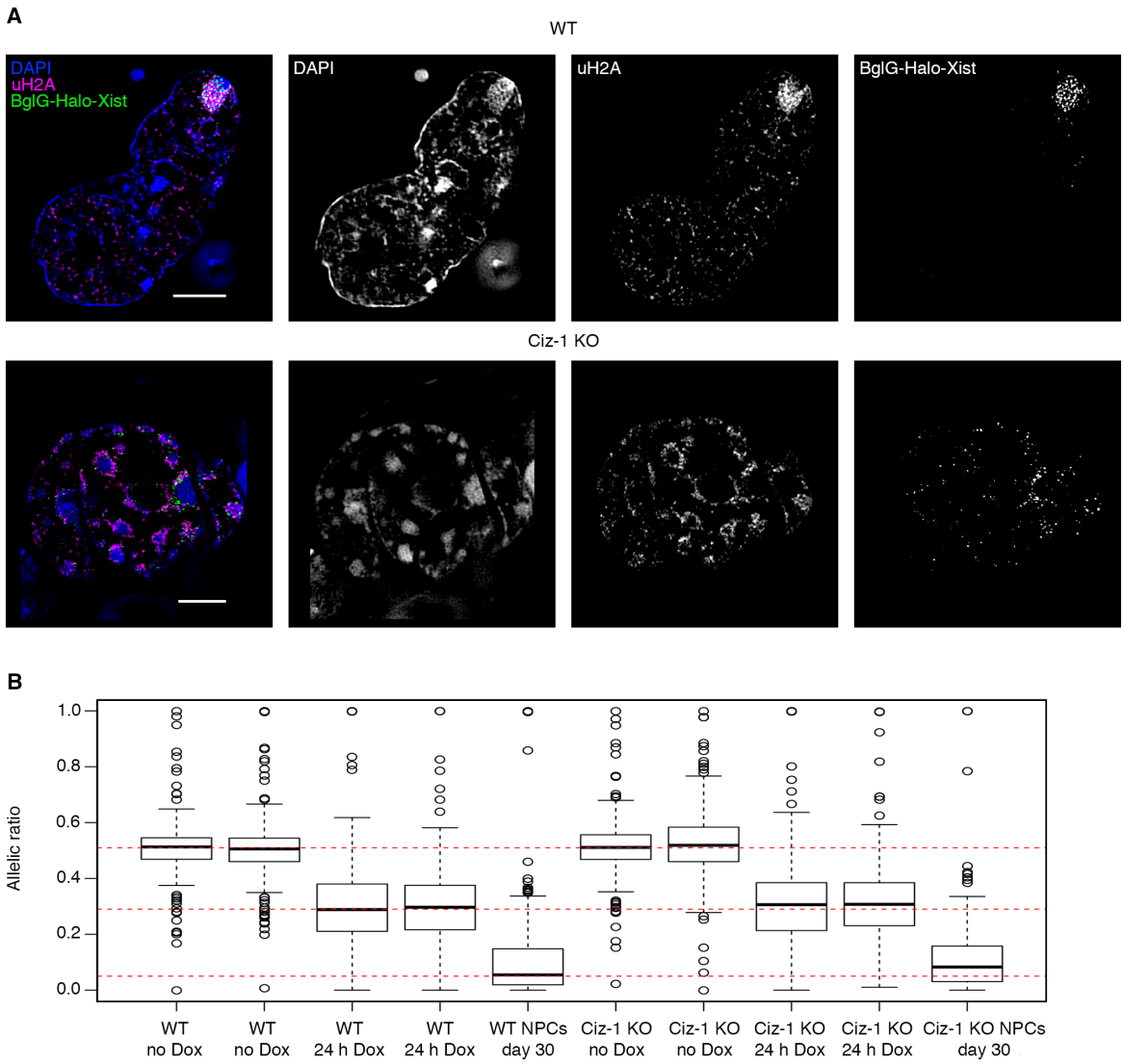

Figure 27: Ciz-1 KO NPCs show no H2AK119ub1 enrichment on the Xi, but with no significant defect in X chromosomal silencing. A) Comparison of representative images of combined HaloTag staining immunostaining for uH2A with DAPI counter stain in WT and Ciz-1 KO NPCs at day 10 of differentiation, visualised by 3D-SIM. Maximum intensity projections. Scale bars correspond to 5 μm. B) Allelic analysis of transcription of X-linked genes in WT and Ciz-1 KO mESCs after 24 h of doxycycline induction, as well as WT and Ciz-1 KO NPCs after 30 days of differentiation determined by chromatin RNA sequencing. Including controls without doxycycline induction.

with previous work using Xist conditional KO cells, which has shown that Xist is dispensable for the maintenance of X chromosomal silencing (Csankovszki, Nagy, and Jaenisch 2001). Presumably perturbation of CIZ-1 leads to Xist delocalisation only after transcriptional silencing of the Xi has been established in NPCs. This is in line with Ciz-1 KO mice not showing any major neurological abnormalities (Ridings-Figueroa et al. 2017). Careful examination of the chromatin RNA-seq data

reveals a slight relaxation of silencing in Ciz-1 KO NPCs as compared to WT NPCs at day 30 of differentiation (Figure 27b). However, in contrast to the mESC chromatin RNA sequencing data, which is based on at least two replicas, only one replica each of WT and Ciz-1 KO NPCs was sequenced to date (Figure 27b). This limits reaching conclusions about the significance of this observed relaxation of silencing, or of the identification of specific genes affected (Figure 27b). Obtaining further data on this point has been stalled by the COVID-19 pandemic. Therefore, it can be concluded that Ciz-1 KO has little or no effect on transcriptional silencing of the Xi in NPCs (Figure 27b).

4.7 Xist transcription is increased in Ciz-1 KO NPCs

Next to the effect of Ciz-1 KO on Xist localisation and density, single HaloTag ligand staining also revealed a dramatic increase in the number of Xist molecules in Ciz-1 KO NPCs as compared to WT NPCs (Figure 28a). Generally, the number of Xist molecules was determined to be more than 2-fold higher in WT NPCs as compared to mESCs with a median of ~250 molecules per cell in NPCs as compared to ~100 molecules per cell in mESCs (Figure 10a and 28a). While Ciz-1 KO did not seem to have a major impact on Xist molecule number in mESCs, perturbation of CIZ-1 in NPCs lead to a dramatic increase in Xist molecule count to over 1000 Xist molecules per cell on average (Figure 28a). This is equivalent to a 4-fold increase of Xist molecules as compared to WT NPCs and a 10-fold increase as compared to WT and Ciz-1 KO mESCs (Figure 28a). Interestingly, Xist molecule numbers decreased somewhat with progression of differentiation from day 10 to day 20 in both WT and Ciz-1 KO NPCs (Figure 28a).

Xist expression data derived from the chromatin RNA sequencing performed in WT and Ciz-1 KO mESCs and NPCs confirmed the striking increase of Xist expression after NPC differentiation (Figure 28b). However, only a slight increase in Xist molecules in Ciz-1 KO NPCs as compared to WT NPCs could be found by analysis of the chromatin RNA sequencing data, indicating that the extracted chromatin fraction likely did not contain the majority of delocalised Xist molecules in Ciz-1 KO NPCs (Figure 28b).

The differences in Xist molecule numbers in WT and Ciz-1 KO NPCs could be due to increased Xist RNA transcription and/or stability. Therefore, RNA-SPLIT was

conducted to examine the effect of NPC differentiation on Xist RNA dynamics in general, as well as the effect of Ciz-1 KO in NPCs on Xist RNA dynamics in particular. A gradual increase of newly synthesised Xist molecules could be observed in both WT and Ciz-1 KO NPCs (Figure 28c). In line with the aforementioned increase in Xist molecule numbers, Xist transcription was increased by almost 2-fold in WT NPCs as compared to WT mESCs (Figure 28c). Considering the constant incubation of cells with doxycycline over the course of 20 days of differentiation, this increase in transcription might be an effect of prolonged doxycycline treatment rather than a biologically relevant effect. However, Xist transcription was even more dramatically increased to approximately 300 Xist molecules/h in Ciz-1 KO NPCs, which is equivalent to a ~6-fold increase over WT mESCs and a ~3-fold increase over WT NPCs (Figure 28c). This suggests that, while perturbation of CIZ-1 does not have a major impact on Xist transcription in mESCs, it does lead to deregulated Xist transcription in NPCs (compare Figure 23c and 28c).

As described in chapter 3 section 3.4, Xist RNA stability and degradation rates are defined by the rate of Xist transcription. Hence, it is feasible to hypothesize that the increase of Xist transcription in NPCs in general, and in Ciz-1 KO NPCs in particular, would lead to an alteration in Xist RNA stability. To examine this issue, RNA-SPLIT was performed to assess Xist RNA turnover in WT and Ciz-1 KO NPCs. Unexpectedly, pre-synthesised Xist RNA molecules could still be detected after 220 min in both cell lines (Figure 28d). This suggests that Xist stability in both WT and Ciz-1 KO NPCs is increased as compared to WT and Ciz-1 KO mESCs, which

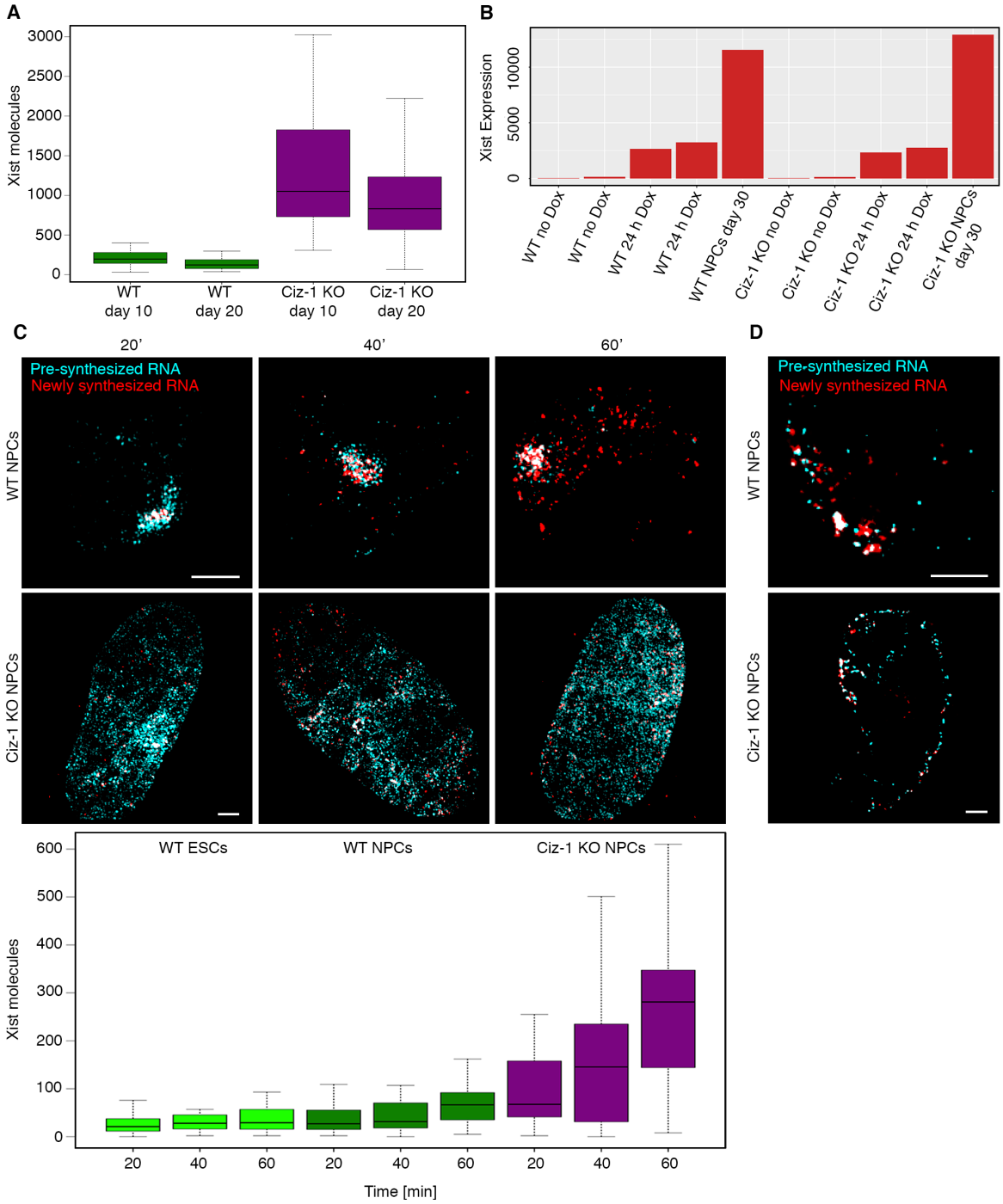

Figure 28: Xist transcription dynamics and stability in WT and Ciz-1 KO NPCs assessed by RNA-SPLIT. A) Quantification of Xist molecules in WT and Ciz-1 KO NPCs after 10 and 20 days of differentiation. n = 200 cells. B) Xist expression in WT and Ciz-1 KO mESCs after 24 h of doxycycline induction, as well as WT and Ciz-1 KO NPCs after 30 days of differentiation, determined by chromatin RNA sequencing. Including controls without doxycycline induction. C) Representative RNA-SPLIT images at different staining times with HaloTag ligand 2 in WT and Ciz-1 KO NPCs after 20 days of differentiation (top). Images were acquired using 3D-SIM. Maximum intensity projections. Scale bars correspond to 2 μm. Quantification of Xist RNA transcription in WT mESCs after 3 h of doxycycline induction, as well as WT NPCs and Ciz-1 KO NPCs after 20 days of differentiation (bottom), obtained by scoring the number of newly synthesised Xist molecules over time. n = 20 cells/ time point. D) Representative RNA-SPLIT images of pre-synthesised Xist still present after 220 min in WT and Ciz-1 KO NPCs after 20 days of differentiation, visualised by 3D-SIM. Single cross-sections. Scale bars correspond to 2 μm.

showed a complete turnover of Xist RNA after 220 min (compare Figure 23b and 28d). The timepoint of complete turnover of Xist RNA in WT and Ciz-1 KO NPCs could not be determined due to concerns that stable binding of BglG-Halo proteins to the Bgl-stem-loop array cannot be guaranteed for experiments longer than 220 min. Thus, potential differences in Xist RNA stability between WT and Ciz-1 KO NPCs will have to be determined by alternative methods, such as SLAM-seq, in the future. It is unclear if these results are because the feedback mechanism linking Xist transcription and turnover in mESCs is no longer active in NPCs, or whether they represent an outcome of using the artificial doxycycline promoter to drive Xist expression through differentiation. To resolve this point future studies should investigate Xist dynamics in NPCs in which Xist expression is driven from the natural promoter.

4.8 Xist coupling is evident in NPCs and is independent of Xist localisation to the X chromosome in Ciz-1 KO cells

It has been suggested that Xist RNA spreads differently at later stages of XCI than at earlier stages (Simon et al. 2013). Additionally, the above-mentioned results show that Xist RNA dynamics differ in NPCs as compared to mESCs. This prompts the question whether the phenomenon of Xist coupling observed in WT, autosomal transgene and Ciz-1 KO mESCs, can also be found in NPCs. Initial assessment of RNA-SPLIT images of WT NPCs after 20 days of differentiation by eye showed that Xist coupling indeed occurs (Figure 29a). The RNA-SPLIT data was subsequently analysed by NNA to quantify this observation (Figure 29a). EdU and 'Random' control were set up as described previously in section 4.4 (Figure 29a). NNA showed a median distance of 176 nm between newly synthesised Xist RNA molecules and pre-synthesised Xist RNA molecules in WT NPCs as compared with 164 nm in WT mESCs, suggesting that Xist coupling occurs regardless of cell differentiation (Figure 19c and 29a). The median distance in WT NPCs was found to be 2.8-fold higher than the EdU control, which is only slightly larger than the fold change of 2.6 seen in WT mESCs (compare Figure 19c and 29a). As in previous experiments, these findings exclude double labelling of the same molecule. Furthermore, the quantified median distance between newly synthesised Xist RNA molecules and pre-synthesised Xist RNA molecules in WT NPCs was determined to be significantly shorter than in the 'Random' control, which showed a median distance of 524 nm (Figure 29a).

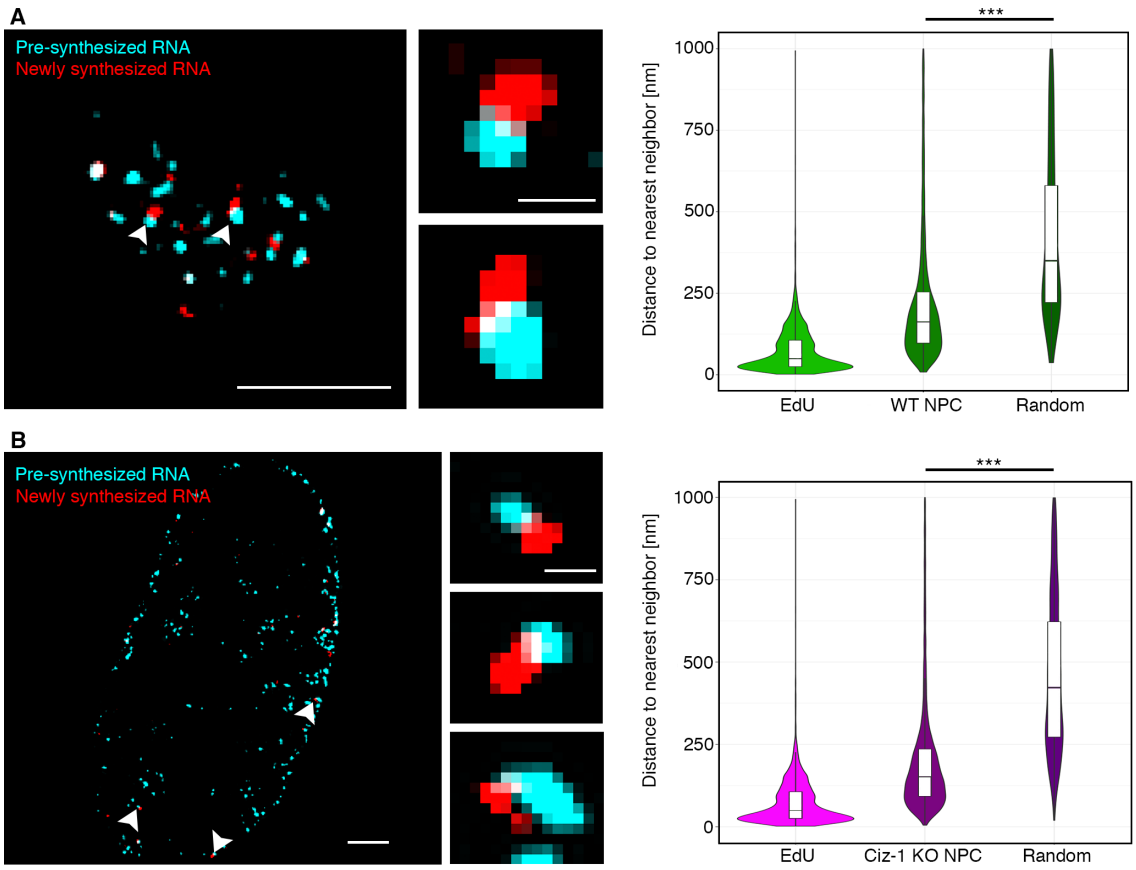

Figure 29: Xist coupling occurs in WT and Ciz-1 KO NPCs. A) NNA of newly synthesised RNA to pre-synthesised RNA signal obtained by RNA-SPLIT WT NPCs after 20 days of differentiation, including EdU and randomised control. n = 150 cells. Includes an example image of pre-synthesised and newly synthesised Xist labelled by RNA-SPLIT in WT NPCs after 20 days of differentiation, visualised by 3D-SIM. Single cross-sections. Scale bar corresponds to 2 μm. Small inserts show 'coupled' Xist in detail. Scale bar corresponds to 200 nm. B) NNA of newly synthesised RNA to pre-synthesised RNA signal obtained by RNA-SPLIT Ciz-1 KO NPCs after 20 days of differentiation, including EdU and randomised control. n = 150 cells. Includes an example image of pre-synthesised and newly synthesised Xist labelled by RNA-SPLIT in Ciz-1 KO NPCs after 20 days of differentiation, visualised by 3D-SIM. Single cross-sections. Scale bar corresponds to 2 μm. Small inserts show 'coupled' Xist in detail. Scale bar corresponds to 200 nm.

After establishing that Xist coupling can be observed in NPCs in general, RNA-SPLIT and NNA were performed in order to assess Xist coupling in NPCs when CIZ-1 is perturbed (Figure 29b). Strikingly, Xist coupling could be observed by eye when assessing RNA-SPLIT images despite the complete dispersal of Xist molecules throughout the nucleus (Figure 29b). A median distance of 163 nm between newly synthesised Xist RNA molecules and pre-synthesised Xist RNA molecules could be determined in Ciz-1 KO NPCs, compared with 176 nm in WT NPCs, suggesting that Xist coupling occurs normally in Ciz-1 KO NPCs (Figure 29a

and 29b). Comparison with EdU random controls support this conclusion (compare Figure 19c, 29a and 29b). That delocalised Xist is able to couple speaks against the notion that Xist coupling reflects molecular crowding in the interchromatin channels of a given chromosome *in cis*, and rather suggests that either a secondary factor, or the biophysical properties of Xist itself might be responsible for Xist coupling at the chromatin binding site. To conclude, Xist coupling is independent of CIZ-1 function, stage of XCI and differentiation, as well as Xist spreading across the X chromosome or an autosome *in cis*.

4.9 Summary: New insights into the role of CIZ-1 in Xist localisation and dynamics

Here, RNA-SPLIT was applied to assess the role of CIZ-1, recently implicated in Xist localisation to the Xi (Ridings-Figueroa et al. 2017; Sunwoo et al. 2017). Ciz-1 KO cells were successfully generated by CRISPR/Cas9 mediated deletion of the majority of the *CIZ-1* locus in the background of XX mESCs with endogenous inducible BglG-Halo-Xist (Figure 20a). Successful perturbation of CIZ-1 was confirmed by Western blot, immunostaining and chromatin RNA sequencing (Figure 20). H3K27me3 enrichment could be observed in both WT and Ciz-1 KO cells, and chromatin RNA sequencing with allelic analysis showed that Xist mediated silencing of X-linked genes is unaffected upon perturbation of CIZ-1 (Figure 20c and 21b). This indicates that CIZ-1 perturbation neither alters Xist function to recruit PRC-mediated histone modifications in mESCs and induce transcriptional silencing of the Xi, nor affects other parts of the early stages of XCI such as SPEN recruitment. Considering that CIZ-1 deficiency in mice has previously been shown not to affect embryogenesis, early postnatal development, or cell viability *ex vivo,* these findings further underline that CIZ-1 is dispensable for the establishment of a transcriptionally silent Xi (Ridings-Figueroa et al. 2017).

Single HaloTag ligand staining and visualisation of BglG-Halo-Xist by 3D-SIM allowed for the assessment of Xist localisation in Ciz-1 KO mESCs. A decrease of Xist territory volume in steady state as compared to expansion, as seen in WT cells before, was found in Ciz-1 KO mESCs (Figure 22b). This suggests that Xist territory compaction with progression of XCI is intact in Ciz-1 KO mESCs, which is in line

with the observation that transcriptional silencing is unaffected. Indeed, the subtle decrease of Xist territory volume in Ciz-1 KO as compared to WT cells during steady state could be attributed to a general decrease in Xist molecules (Figure 22b and 22c). Additionally, perturbation of CIZ-1 in mESCs was shown to result in a decreased Xist RNA density, determined by a variation of NNA (Figure 22d). This analysis, where the median distance of each Xist molecule to the 10 nearest neighbouring Xist molecules is quantified in order to assess molecule density, proved to be a valuable method for comparing chromosomal Xist coverage in different cell lines (Figure 22d). A significant density defect was also observed in the autosomal transgene cells, which in general are thought to display attenuated Xist spreading and inefficient Xist coverage (Popova et al. 2006). Similar to autosomal transgene cells, no increase in Xist territory volume was observed in Ciz-1 KO mESCs, suggesting that there is no delocalisation of Xist from the Xi, but instead a less dense Xist coverage (Figure 22b and 22d). CIZ-1 has been implicated in anchoring Xist to the chromatin (Sunwoo et al. 2017). Hence, less Xist molecules may stay bound to chromatin in Ciz-1 KO mESCs, leading to less dense Xist coverage of the Xi. Less efficient compaction of the Xi, however, can likely be ruled out as a reason, since Xist territory volumes were shown to still be significantly reduced as XCI advances (Figure 22b). Alternatively, the defect in Xist density could be due to a change in Xist dynamics, which would agree with a general reduction in Xist molecule numbers (Figure 22c).

RNA-SPLIT was conducted to assess Xist stability and transcription rates in Ciz-1 KO mESCs during expansion and steady state. Xist RNA stability was found to

increase significantly from expansion to steady state in Ciz-1 KO mESCs, which agrees with the observations made in WT mESCs (Figure 23b). Thus, increasing stability with progression of XCI is independent of CIZ-1 function. No significant changes in Xist stability could be detected in the Ciz-1 KO mESCs, which also nicely underlines the robustness of the newly developed RNA-SPLIT method (Figure 23b). While CIZ-1 does not seem to play a major role in Xist stability in mESCs, a somewhat earlier decrease of Xist molecule numbers during steady state might explain the slightly reduced Xist molecule number in Ciz-1 KO cells during that time (Figure 22c and 23b). Further confirming the interconnectivity of Xist transcription and stability seen in WT mESCs, Xist transcription was found to decrease with progression of XCI in Ciz-1 KO cells (Figure 23c). A minor decrease in transcription in Ciz-1 KO cells during expansion might contribute to the reduced number of Xist molecules in Ciz-1 KO cells during this phase (Figure 22c and 23c), however, technical variations could also be the reason for these differences and analysis of more than one WT cell line could provide more clarity in the future. Still, the similarities of the observations made in the WT and Ciz-1 KO mESCs can serve as validation of the general reproducibility of RNA-SPLIT results.

Although the role of CIZ-1 in anchoring Xist to the chromatin might suggest that Xist coupling could be disrupted in Ciz-1 KO cells (Sunwoo et al. 2017), coupling was found to be unaffected in Ciz-1 KO mESCs using RNA-SPLIT followed by NNA (Figure 24). In conclusion, perturbation of CIZ-1 has no major effect on Xist RNA localisation, dynamics or coupling in mESCs. This is in line with previous research

suggesting that CIZ1 is dispensable for the establishment phase of a transcriptionally silent Xi (Ridings-Figueroa et al. 2017).

It has been shown that perturbation of CIZ-1 leads to Xist RNA dispersal in some differentiated cell types such as mouse fibroblasts as well as B- and T-lymphocytes (Ridings-Figueroa et al. 2017; Sunwoo et al. 2017). Hence, differentiation of the Ciz-1 KO mESC line was carried out using an NPC differentiation protocol, which has been known to show particularly homogenous differentiation. However, Xist RNA behaviour has been suggested to differ generally between mESCs and differentiated cells (Engreitz et al. 2013; Simon et al. 2013). Therefore, the parental WT mESC line was also differentiated and assessed for comparison.

Extensive Xist RNA dispersal throughout the nucleus was indeed observed in Ciz-1 KO NPCs (Figure 26a). Despite the obvious delocalisation of Xist in Ciz-1 KO NPCs, Xist was found to accumulate at heterochromatic regions at the nuclear and nucleolar periphery (Figure 26a). This localisation may be mediated by other factors such as hnRNPU, which has previously been described to anchor Xist to chromatin (Hasegawa et al. 2010; Sunwoo et al. 2017). The dispersal of Xist was quantified by measuring the molecule density using NNA and demonstrated a dramatic decrease in Xist molecule density in Ciz-1 KO NPCs (Figure 26b). As an aside, density was found to increase as differentiation progresses in WT NPCs, while it decreasing in Ciz-1 KO NPCs (Figure 26b). Together, these results suggest that CIZ-1 function is largely redundant in mESCs and becomes progressively more important with the advancement of XCI.

In line with the delocalisation of Xist from the Xi in Ciz-1 KO NPCs, immunostaining for uH2A revealed the lack of enrichment of the Polycomb-mediated histone modification on the Xi (Figure 27a). Instead, uH2A enrichment was found at those sites that dispersed Xist localises to, i.e. the nuclear and nucleolar periphery, suggesting that Xist might still recruit Polycomb group proteins and maintain silencing function in Ciz-1 KO NPCs (Figure 27a). However, potential Xist-mediated silencing across the genome would likely affect genes on different chromosomes in a random fashion and therefore be difficult to pick up by chromatin RNA sequencing for example. Notwithstanding the lack of uH2A enrichment, no major deficiency in Xist-mediated silencing of the Xi could be found in Ciz-1 KO NPCs by chromatin RNA sequencing, similar to findings in Ciz-1 KO mESCs (Figure 27b). Hence, transcriptional silencing of the Xi is largely independent of CIZ-1, Xist localisation and uH2A enrichment in NPCs. This is likely because CIZ-1 function in Xist localisation only becomes essential after transcriptional silencing of the Xi has been established, consistent with the observation that Ciz-1 KO mice do not show any major abnormalities. A minor relaxation of silencing in Ciz-1 KO NPCs was observed which is in line with minor defects in X-linked gene silencing that have been reported for PEFs derived as well as B-/T-lymphocytes from CIZ-1 deficient mice (Ridings-Figueroa et al. 2017). This finding, however, will have to be confirmed as it is based on only a single biological replicate (Figure 27b). Considering the dramatic phenotype of Ciz-1 KO NPCs, it would also be interesting to examine whether subtle neurological or behavioural phenotypes can be found in Ciz-1 KO mice.

RNA-SPLIT and chromatin RNA sequencing analysis uncovered a 2-fold increase of both Xist molecule numbers and Xist transcription in WT NPCs as compared to WT mESCs (Figure 28). It is possible that prolonged incubation of cells with doxycycline may be responsible for this effect. However, Xist molecule numbers and transcription were found to be even more dramatically increased in Ciz-1 KO NPCs, meaning that perturbation of CIZ-1 leads to deregulated Xist transcription in NPCs but not in mESCs (Figure 23c and 28c). Limitations of RNA-SPLIT experiments to ~4 h due to concerns of turnover of BglG-Halo on the stem loops, meant that Xist RNA stability in WT and Ciz-1 KO NPCs could not be accurately quantified. It could however be noted that stability is generally increased to more than 220 min in both cell lines (Figure 28d). In the future, this may be further investigated by alternative methods, which can determine longer turnover rates, such as SLAM-seq.

Together, these results suggest that CIZ-1 either has a direct role in the transcriptional regulation of Xist in NPCs, or an indirect role, where the delocalisation of Xist from the Xi leads to an increase in Xist transcription. The discrepancy between Xist expression determined by RNA-SPLIT and chromatin RNA sequencing can be explained by the assumption that a significant fraction of delocalised Xist is likely not picked up in the chromatin fraction during the chromatin RNA sequencing experiment. This has potential implications for future biochemistry experiments, where tight association of Xist with the chromatin hinders the effort to purify Xist RNPs. Recruitment of uH2A to Xist binding sites indicates that, while

delocalised, the Xist RNP may be otherwise functional in CIZ-1 NPCs, making it a good potential candidate for such biochemistry experiments.

Finally, Xist coupling was assessed in WT and Ciz-1 KO NPCs by RNA-SPLIT and NNA. Despite the differences in Xist dynamics between WT NPCs and WT mESCs, Xist coupling was found to be unaffected in WT NPCs, suggesting that this phenomenon is independent of the stage of cell differentiation (Figure 29a). Remarkably, Xist coupling was also found in Ciz-1 KO NPCs, despite Xist being fully delocalised (Figure 29b). This indicates that Xist coupling is not a result of Xist crowding in the interchromatin channels of a given chromosome or localisation to specific sites on the Xi. Instead it is likely mediated by a secondary factor, or the biophysical properties of Xist itself. That coupling nearly always involves a newly synthesised RNA molecule with a bound pre-synthesised RNA molecule suggests that this happens at the chromatin binding site of Xist, rather than at the Xist transcription site. Hence, it can be established that Xist coupling is a phenomenon independent of CIZ-1, stage of XCI and Xist localisation *in cis*, which is likely mediated by a secondary factor or Xist physical properties at Xist chromatin binding sites.

To conclude, perturbation experiments of CIZ-1 in both mESCs and NPCs have revealed that CIZ-1 deficiency has little to no effect on Xist localisation, dynamics and coupling in mESCs, but that CIZ-1 plays a major role in Xist localisation and transcription in differentiated cells.

CHAPTER V

5 SPEN plays a key role in Xist localisation, dynamics and coupling

5.1 Generation of SPEN RRM deletion in BglG-Halo-Xist mESCs

XCI is an essential developmental process and hence many factors involved in Xist-mediated transcriptional silencing of the X chromosome have redundant roles. For instance, perturbation of known silencing factors RNA Binding Motif Protein 15 (Rbm15) and LBR, as well as deletion of the XR-PID, which is essential for Polycomb group protein recruitment, do not fully abrogate silencing of Xi-linked genes (Nesterova et al. 2019). An exception is the RNA binding protein SPEN, homolog of Drosophila split ends, which has a critical role in establishing Xist-mediated transcriptional repression of X-linked genes. SPEN has been found to interact directly with the Xist RNA A-repeats, similarly critical for establishment of silencing, via its RRMs (Monfort et al. 2015; Moindrot et al. 2015; Chu et al. 2015; Lu et al. 2016). SPEN functions as a platform to recruit silencing or repressive factors to the Xist coated chromosome. Critically, SPEN has been shown to interact with the N-CoR via its SPOC domain, recruiting HDAC3, which accounts at least in part for its role in gene silencing by maintaining histone deacetylation on the Xi, thus resulting in reduced gene expression (McHugh et al. 2015; Żylicz et al. 2019; Dossin et al. 2020). The SPOC domain may also contribute to silencing through interaction with another co-repressor complex, NuRD and/or by direct interaction with RNA

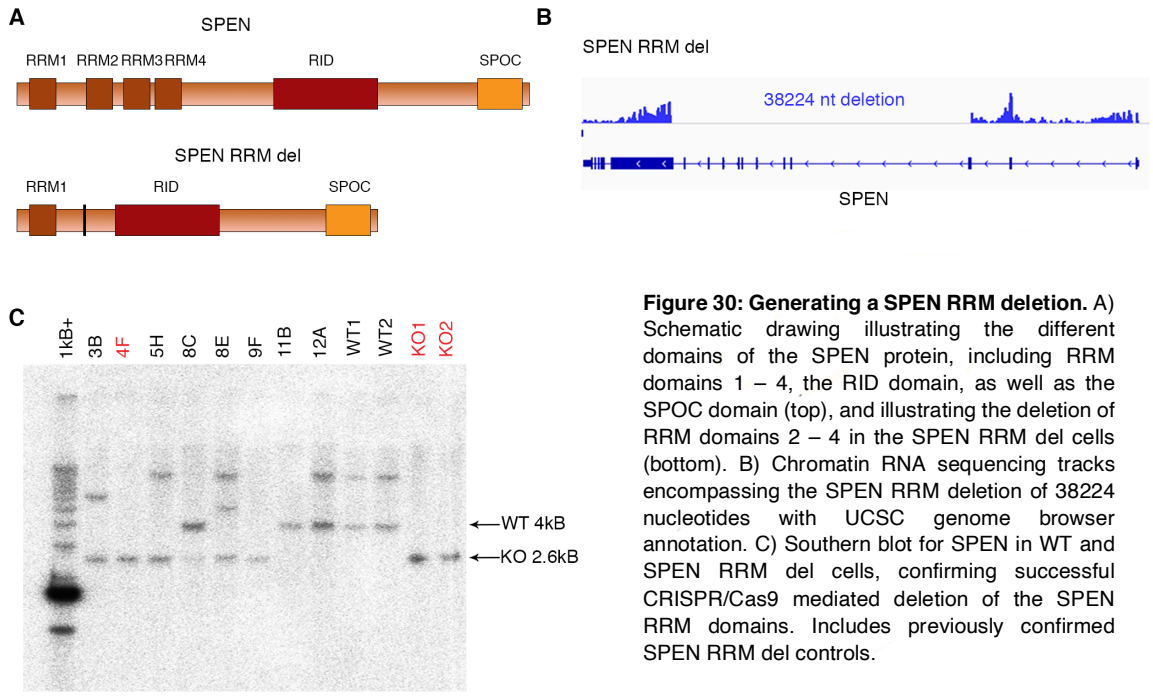

Figure 30: Generating a SPEN RRM deletion. A) Schematic drawing illustrating the different domains of the SPEN protein, including RRM domains 1 – 4, the RID domain, as well as the SPOC domain (top), and illustrating the deletion of RRM domains 2 – 4 in the SPEN RRM del cells (bottom). B) Chromatin RNA sequencing tracks encompassing the SPEN RRM deletion of 38224 nucleotides with UCSC genome browser annotation. C) Southern blot for SPEN in WT and SPEN RRM del cells, confirming successful CRISPR/Cas9 mediated deletion of the SPEN RRM domains. Includes previously confirmed SPEN RRM del controls.

polymerase II (Dossin et al. 2020). In recent work analysing mESCs, in which the SPEN RRM domains were deleted by CRISPR/Cas9 mediated genome engineering, aberrant Xist territories were found to occur (Nesterova et al. 2019), indicating that there might be some function of SPEN in Xist localisation. Similar findings were reported for a deletion of the Xist A-repeat with which SPEN interacts (Nesterova et al. 2019).

To quantify effects of SPEN on Xist RNA localisation, a SPEN RRM deletion was engineered in mESCs containing endogenous inducible BglG-Halo-Xist using CRISPR/Cas9 mediated genome engineering with sgRNAs used previously (Nesterova et al. 2019) (Figure 30a and 30b). Cells containing a deletion of the RRM domains were first selected by PCR screening of gDNA (gDNA). Then, 8 clones were further analysed by Southern blot along with samples from WT cells and as a

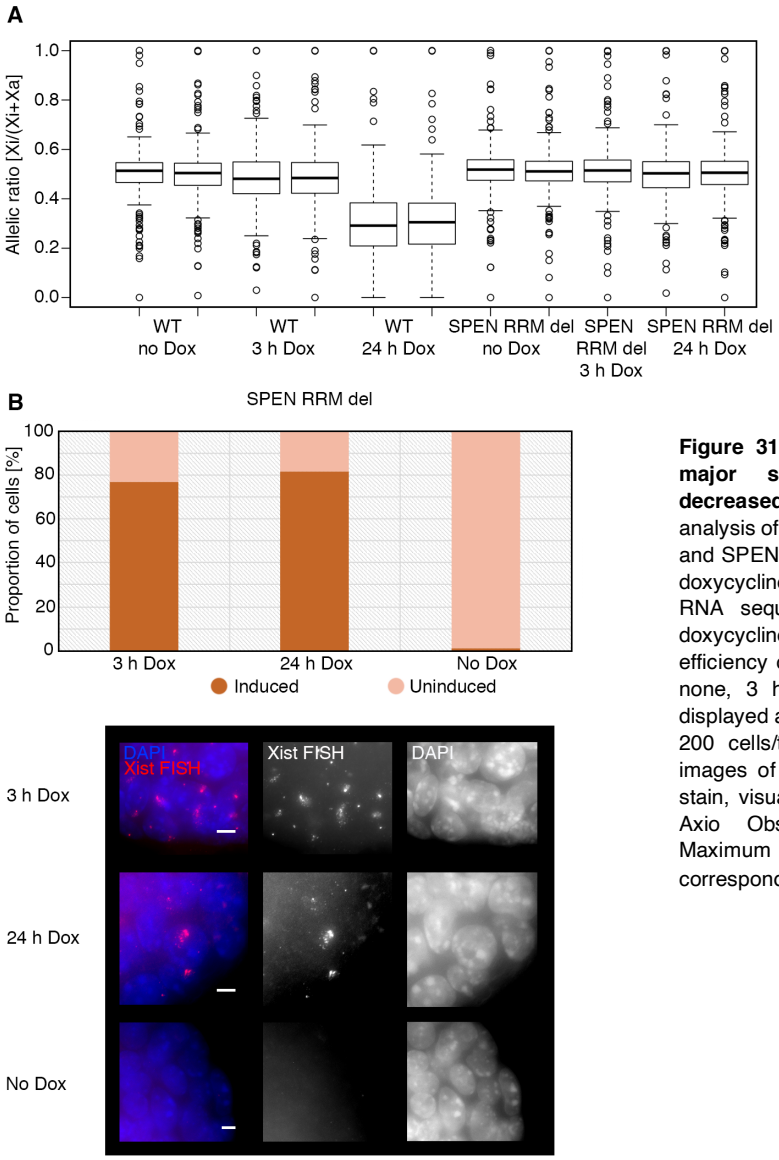

Figure 31: SPEN RRM del cells display a major silencing defect and slightly decreased induction efficiency. A) Allelic analysis of transcription of X-linked genes in WT and SPEN RRM del cells after 3 h and 24 h of doxycycline induction, determined by chromatin RNA sequencing. Includes controls without doxycycline induction. B) Scoring of induction efficiency of the SPEN RRM del cell line after none, 3 h and 24 h doxycycline induction, displayed as proportion of induced cells [%]. n = 200 cells/time point. Includes representative images of Xist RNA FISH with DAPI counter stain, visualised with an inverted fluorescence Axio Observer Z.1 microscope (Zeiss). Maximum intensity projections. Scale bars correspond to 5 μm.

further control, cells previously confirmed to contain SPEN RRM KO (Figure 30c). Based on this, one homozygous clone was chosen and chromatin RNA sequencing performed, which confirmed the 38,224 nucleotide deletion of RRM domains 2 – 4 (Figure 30b). Allelic analysis of the chromatin RNA sequencing data also showed a major silencing defect both 3 h and 24 h post-induction of Xist, consistent with prior studies (Figure 31a). Moreover, Xist RNA FISH visualised using a standard Zeiss microscope was performed to exclude the presence of polyploid and XO cells, as

well as to assess the efficiency of Xist induction (Figure 31b). The latter was slightly reduced as compared to WT cells with 77% and 81.5% after 3 h and 24 h of doxycycline induction respectively (Figure 31b). Only 1% of the cells showed Xist territory formation without the addition of doxycycline, suggesting a negligible leakiness of the inducible Xist promoter (Figure 31b). Hence, Xist territories were formed in the majority of SPEN RRM del cells despite a more dispersed Xist RNA distribution (Figure 31b). It could also be observed that Xist territories were of a smaller size in the SPEN RRM del as compared to WT cells during steady state (Figure 31b).

5.2 Generation of SPEN SPOC domain mutations in BglG-Halo-Xist mESCs

A second SPEN mutant was generated to investigate if the gene silencing activity of SPEN is linked to its role in Xist RNA localisation. Accordingly, the SPOC domain of SPEN was mutated so as to abrogate recruitment of downstream co-repressors. Specifically, mESCs with endogenous inducible BglG-Halo-Xist were engineered with two point mutations in the SPOC domain, generated by CRISPR/Cas9 facilitated homologous recombination, in order to dissect potentially differing roles of the SPOC domain and the rest of the SPEN protein (Figure 32a). The said mutations, substitutions of amino acids R3552A and R3554A, have previously been shown to disrupt interaction of SPEN with N-CoR/HDAC3 (Ariyoshi and Schwabe 2003). These mutations are therefore predicted to disrupt SPEN catalytic activity essential for Xist-mediated silencing without affecting SPEN binding to Xist RNA itself. This second SPEN mutant cell line is referred to herein as SPOC mut.

Successful amino acid substitution was screened for by two different gDNA PCR analyses. The resulting PCR fragments were sequenced (Sanger Sequencing, Figure 32b), and 4 clones with the correct substitutions were taken forward for further analysis. Chromatin RNA sequencing confirmed successful amino acid substitution for 3 of the clones and allowed for the assessment of transcriptional silencing of X-linked genes by allelic analysis (Figure 32c). In line with recent research (Dossin et al. 2020), the SPOC domain mutation was found to strongly abrogate Xist-mediated gene silencing, but not to the same extent as seen for deletion of the SPEN RRM domain, suggesting SPEN has SPOC domain

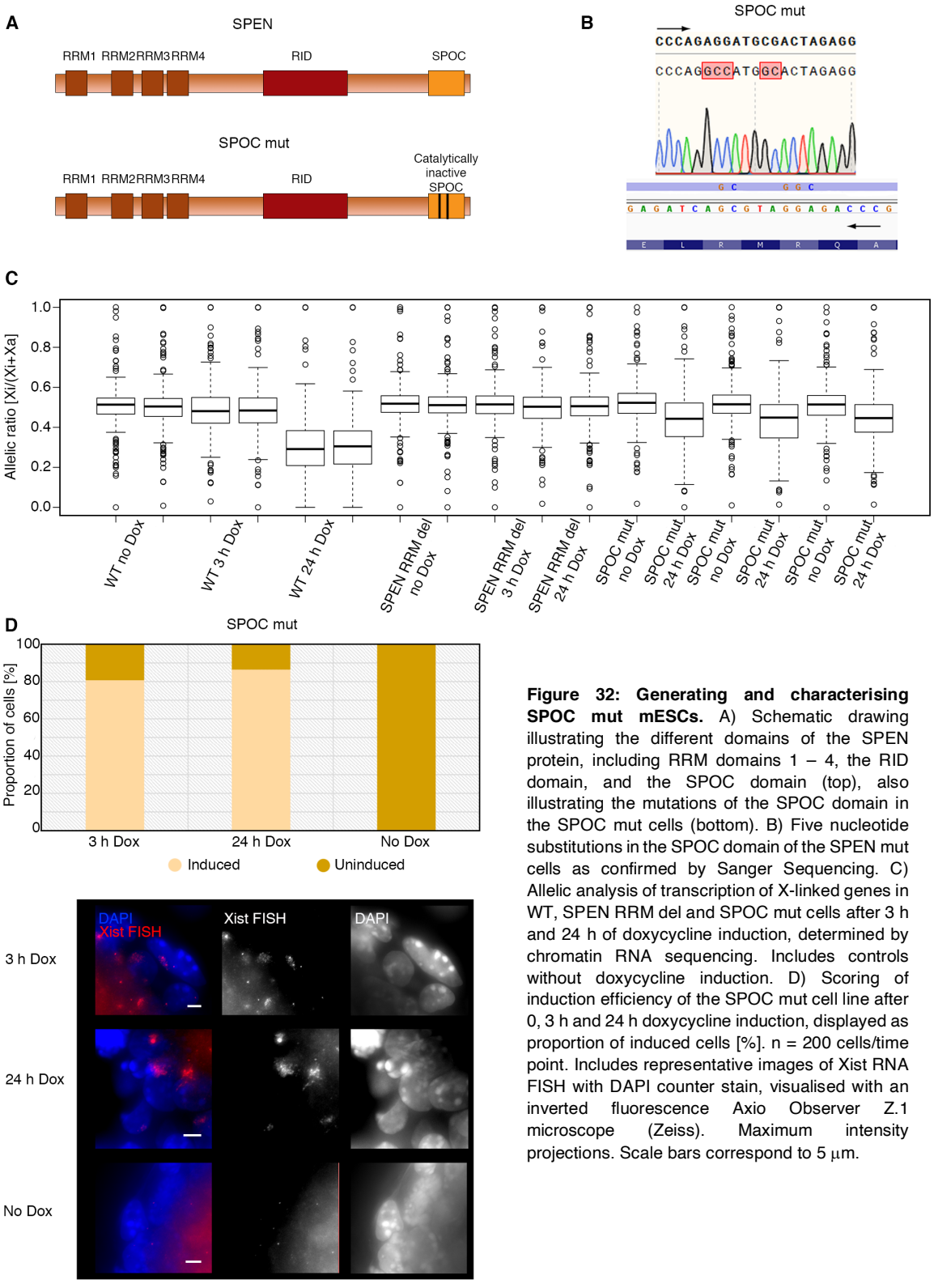

Figure 32: Generating and characterising SPOC mut mESCs. A) Schematic drawing illustrating the different domains of the SPEN protein, including RRM domains 1 – 4, the RID domain, and the SPOC domain (top), also illustrating the mutations of the SPOC domain in the SPOC mut cells (bottom). B) Five nucleotide substitutions in the SPOC domain of the SPEN mut cells as confirmed by Sanger Sequencing. C) Allelic analysis of transcription of X-linked genes in WT, SPEN RRM del and SPOC mut cells after 3 h and 24 h of doxycycline induction, determined by chromatin RNA sequencing. Includes controls without doxycycline induction. D) Scoring of induction efficiency of the SPOC mut cell line after 0, 3 h and 24 h doxycycline induction, displayed as proportion of induced cells [%]. n = 200 cells/time point. Includes representative images of Xist RNA FISH with DAPI counter stain, visualised with an inverted fluorescence Axio Observer Z.1 microscope (Zeiss). Maximum intensity projections. Scale bars correspond to 5 μm.

independent functions in XCI (Figure 32c). It was therefore particularly intriguing to explore whether this discrepancy could be due to potential changes in Xist RNA behaviour and localisation in SPEN RRM del cells using RNA-SPLIT.

The presence of polyploid and XO cells in SPOC mut cells was excluded by Xist RNA FISH (Figure 32d), and a final clone for analysis was chosen based on suitable BglG-Halo expression levels as examined by single HaloTag staining followed by 3D-SIM. No cells showed Xist territory formation without doxycycline induction and, hence, leakiness of the inducible promoter was ruled out (Figure 32b). Scoring of Xist territories demonstrated a higher induction efficiency than SPEN RRM del cells with 81% after 3 h and 86.5% after 24 h doxycycline induction (compared to 77% and 81.5% in SPEN RRM del cells, Figure 31b), similar to WT cells (Figure 32d). Moreover, Xist localisation seemed to be unaffected in SPOC mut cells at this resolution, contrasting with SPEN RRM del cells (compare Figure 31b and Figure 32b). To investigate apparent differences in Xist localisation observed for SPEN RRM del and SPOC mut cells using conventional imaging, 3D-SIM and RNA SPLIT were performed, as described in sections below.

5.3 SPEN plays an important role in Xist localisation

Following the observation of aberrant Xist territories in the SPEN RRM del cells at lower resolution, HaloTag staining in combination with 3D-SIM was performed to study Xist localisation in SPEN RRM del and SPOC mut cells at super-resolution. Indeed, Xist was found dispersed throughout the nucleus both during expansion and steady state in SPEN RRM del cells (Figure 33a). Xist territories could still be detected, but seemed to occupy strikingly larger parts of the total nuclear volume with an increased number of Xist molecules as compared to WT cells during expansion (Figure 33a). Moreover, stray single Xist molecules could be found outside of clearly defined Xist territories more than in WT cells (Figure 33a). Xist territories in SPEN RRM del cells also appeared to decrease in size as compared to WT cells during steady state, while the number of fully dispersed Xist molecules further increased (Figure 33a). Interestingly, the aforementioned findings were not apparent in SPOC mut cells. Here, Xist territories seemed to be enlarged as compared to WT cells during expansion, but Xist territories were found to be of similar size to those in WT cells during steady state, and dispersed Xist molecules were not seen in either of the phases (Figure 33a). This suggests that SPEN may have a novel role in Xist localisation, which is separable from the recruitment of downstream factors through the SPOC domain. In order to confirm these observations, Xist territory volumes, nuclear occupancy, molecule numbers and density were quantified using the previously described image processing and analysis tools.

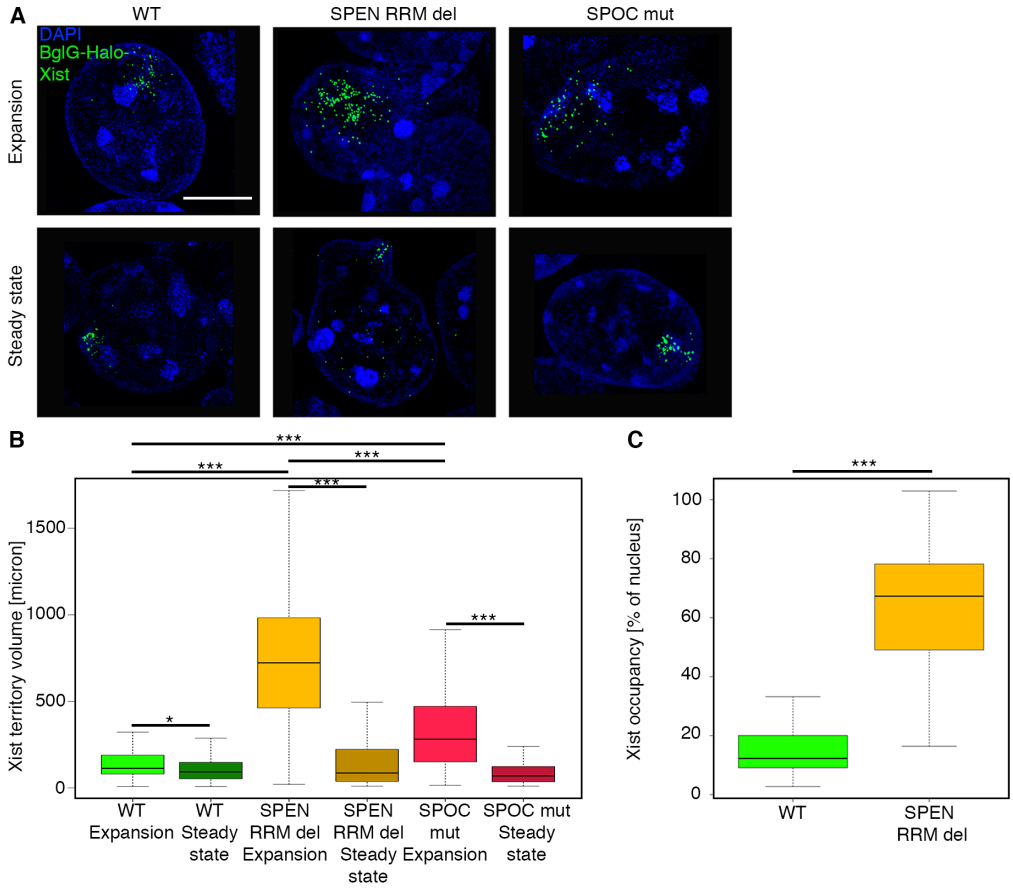

Figure 33: Analysis of Xist localisation in SPEN RRM del and SPOC mut cells. A) Comparison of representative images of HaloTag staining and DAPI counter stain of WT, SPEN RRM del and SPOC mut cells during expansion and steady state shows pronounced Xist localisation defect in SPEN RRM del cells, visualised by 3D-SIM. Maximum intensity projections. Scale bar corresponds to 2 μm. B) Quantification of Xist territory volume in WT, SPEN RRM del and SPOC mut cells during expansion and steady state. n = 200 cells/time point. C) Quantification of Xist delocalisation from the Xi in SPEN RRM del cells. Xist occupancy of the nucleus in WT and SPEN RRM del cells was determined by expressing the Xist territory volume as fraction of the total nuclear volume for each cell. n = 120 cells/cell line.

The volume of Xist territories was found to be dramatically increased in SPEN RRM del cells during expansion, and was surprisingly not reduced during steady state despite the previously observed decrease in Xist territory size at lower resolution (Figure 33b). The latter could be attributed to the aforementioned detection of dispersed molecules in SPEN RRM del cells using 3D-SIM (Figure 33a). In line with earlier observations, Xist territory volumes in the SPOC mutant were found to be significantly closer to WT cell volumes during expansion, albeit still significantly increased (Figure 33b). No significant difference could be determined between Xist territory volumes in SPOC mut and WT cells (Figure 33b). Furthermore, comparison

of Xist occupancy of the nuclear volume during expansion in WT and SPEN RRM del cells showed that, while Xist only occupies around 10% of the nuclear volume in WT cells, Xist could be found in around 70% of the nuclear volume in SPEN RRM del cells, indicating that Xist is significantly delocalised from the Xi (Figure 33c). Together, these results confirm a novel role of SPEN in Xist localisation to the Xi, which at least in part can be separated from its function in SPOC-mediated transcriptional silencing of the Xi.

Quantification of Xist molecule numbers in the different mutant cell lines showed a significant increase of Xist molecules in SPEN RRM del as compared to WT cells during expansion, but not in SPOC mut cells (Figure 34a). During steady state, however, Xist molecule numbers were found to be significantly decreased in SPEN RRM del cells as compared to WT cells, while no significant difference could be detected between SPOC mut and WT cells (Figure 34a). These results were confirmed by Xist expression data obtained by chromatin RNA sequencing, which showed that Xist expression was markedly decreased in SPEN RRM del cells, but not in SPOC mut cells during steady state (Figure 34b). Overall, this suggests that Xist RNA abundance is deregulated in SPEN RRM del, but not in SPOC mut cells.

RNA-SPLIT was performed to give more insight as to changes in Xist transcription and/or degradation rates. NNA was performed using the RNA-SPLIT data to determine the median distance of each Xist molecule to its ten nearest neighbouring Xist molecules as an indicator of Xist density (Figure 34c). Surprisingly, given the distinct Xist localisation phenotype of SPEN RRM del and SPOC mut cells, distances were significantly increased and, hence, Xist density decreased in both

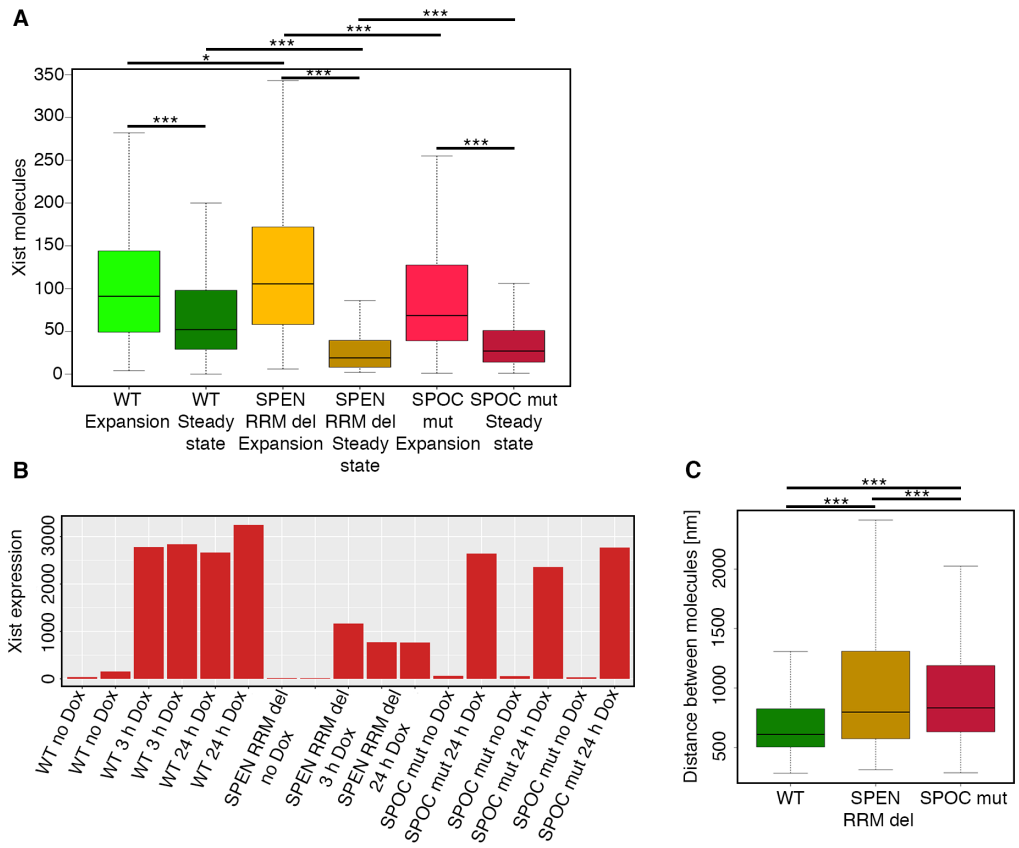

Figure 34: Perturbation of SPEN binding to Xist affects Xist expression and density. A) Quantification of Xist molecules in WT, SPEN RRM del and SPOC mut cells during expansion and steady state shows a pronounced change in Xist molecule numbers upon deletion of the SPEN RRM domains, but less so upon mutation of the SPEN SPOC domain. n = 200 cells/time point. B) Xist expression in WT, SPEN RRM del and SPOC mut cells after 3 h or 24 h of doxycycline induction, determined by ChrRNA-seq. Includes controls without doxycycline induction. C) Quantification of the Xist coverage defect in SPEN RRM del and SPOC mut cells. Median distances between each Xist molecule and its ten nearest neighbouring Xist molecules were determined by NNA after RNA-SPLIT, and serve as an indicator of Xist molecule density. n = 240 cells/cell line.

the SPEN RRM del and SPOC mut as compared to WT cells (Figure 34c). This suggests that, in addition to its SPOC domain independent role in Xist localisation to the Xi, SPEN also has a SPOC domain dependent function in efficient Xist RNA coverage of the Xi.

5.4 Perturbation of SPEN binding to Xist leads to increased Xist transcription and decreased stability

RNA-SPLIT allows for the discrimination of pools of newly synthesised and pre-synthesised RNA and their observation over time to study Xist RNA dynamics, as described in chapter 3 section 3. This can be used to assess both Xist RNA stability and transcription rates. The latter can be determined by counting the gradual increase of newly synthesised Xist RNA molecules in short time intervals during expansion and steady state. Here, RNA-SPLIT and subsequent analysis of Xist RNA transcription were performed in SPEN RRM del and SPOC mut cells, and the results were compared to WT cells in order to examine a potential role of SPEN in Xist transcription / degradation kinetics predicted based on differences in Xist molecule numbers in the mutant cells as described above. During expansion, a gradual increase of newly synthesised Xist molecules could be observed in SPEN RRM del cells similar to WT cells (Figure 35a). Also similar to WT cells, there was a general reduction in Xist transcription with progression of XCI from expansion to steady state (Figure 35b). However, Xist transcription rates were increased in SPEN RRM del compared to WT cells both during expansion and steady state (Figure 35b). This result is quite unexpected, since Xist molecule numbers were found to be significantly lower during steady state in SPEN RRM del cells than in WT (Figure 34a and 34b). Interestingly, in SPOC mut cells Xist transcription was rather slightly reduced both during expansion and steady state (Figure 35c). This suggests that SPEN has a role in regulating Xist RNA transcription, which is independent of its SPOC domain and, hence, the recruitment of HDAC3. Given that the changes in

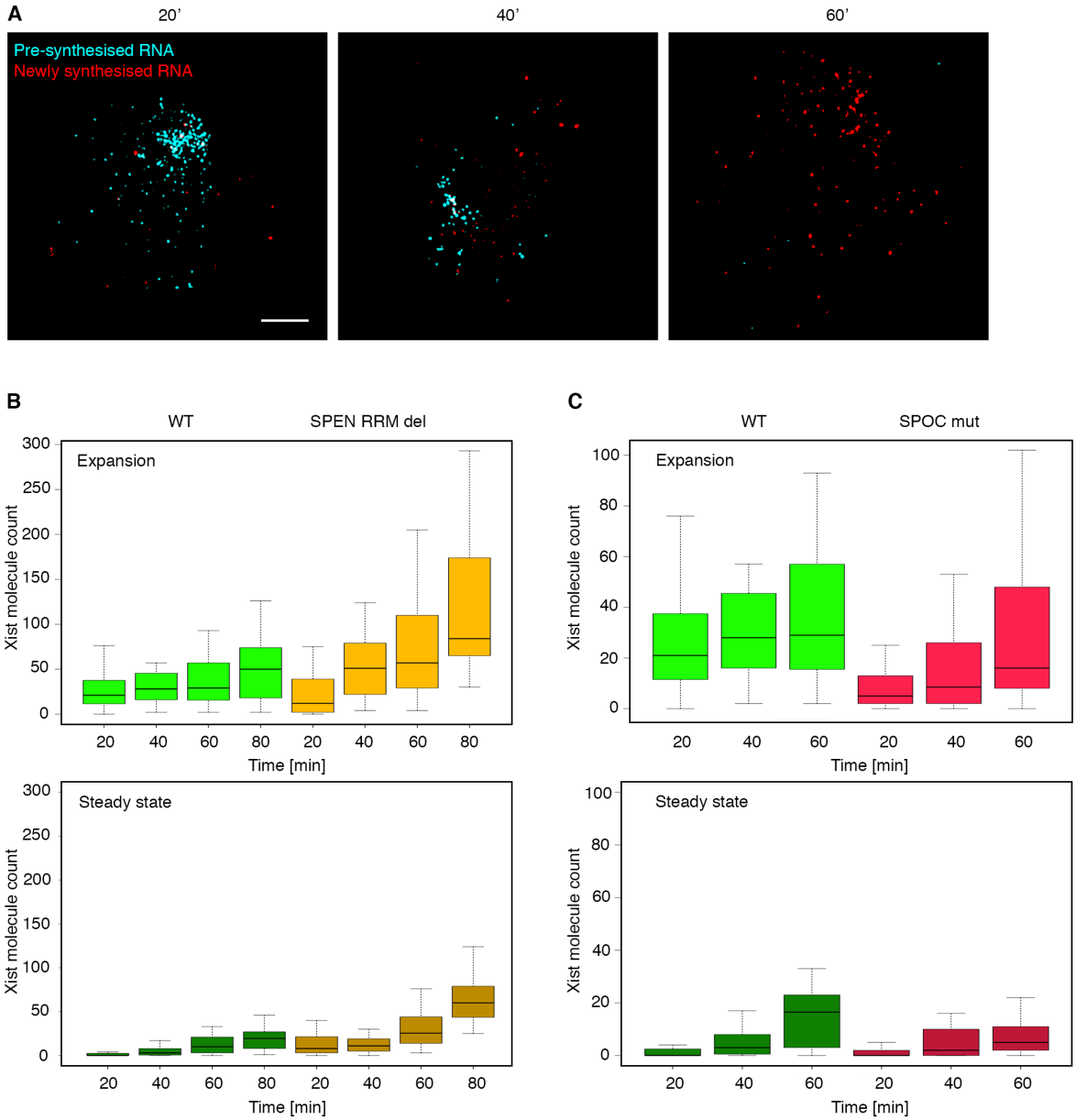

Figure 35: SPEN RRM del but not SPOC mut cells show increased Xist RNA transcription. A) Representative RNA-SPLIT images of SPEN RRM del cells during expansion show gradual increase of newly synthesised Xist RNA molecules, acquired by 3D-SIM. Maximum intensity projections. Scale bar corresponds to 2 μm. B) Xist RNA transcription is upregulated in SPEN RRM del as compared to WT cells during expansion and steady state, quantified by scoring the number of newly synthesised Xist molecules over time. n = 20 cells/ time point. C) Xist transcription rates are unaffected by mutation of the SPEN SPOC domain. Quantification of Xist RNA transcription in WT and SPOC mut cells during expansion and steady state, obtained by scoring the number of newly synthesised Xist molecules over time. n = 20 cells/ time point.

Xist transcription rate cannot account for the low Xist molecule count in SPEN RRM del cells during steady state, it seems feasible to further propose that Xist degradation must increase.

In order to test this hypothesis, RNA-SPLIT was conducted to study the turnover of Xist RNA by determination of the number of pre-synthesised RNA molecules while increasing the staining time for newly synthesised RNA molecules until no more pre-synthesised RNA molecules are present (Figure 36a). Here, Xist turnover was assessed in SPEN RRM del and SPOC mut cells during expansion and steady state. Initial assessment of the RNA-SPLIT images by eye revealed that pre-synthesised Xist RNA molecules could no longer be detected after 80 min in SPEN RRM del cells during expansion, as compared to 140 min in WT cells, while pre-synthesised Xist RNA molecules could still be seen after 80 min in SPOC mut cells (Figure 13c and 36a). Quantification of the pre-synthesised Xist RNA molecule numbers over time by centroid determination and counting confirmed this observation. Whilst SPOC mut and WT cells showed a complete turnover of Xist RNA after 140 min during expansion and 220 min during steady state, Xist RNA in SPEN RRM del cells was found to have a significantly decreased stability with a complete turnover after 80 min and 100 min during expansion and steady state respectively (Figure 36b). Thus, the dramatic increase in Xist stability as XCI progresses from expansion to steady state was not seen in SPEN RRM del cells, although it was observed in SPOC mut cells (Figure 36b). Overall, SPOC mut cells showed Xist stability comparable to WT cells (Figure 36b). As previously described in chapter 3 section 8, experiments in WT cells suggest a feedback mechanism, where Xist transcription rates determine Xist degradation rates. It is therefore likely that deregulation of Xist transcription in SPEN RRM del cells causes an increase in Xist degradation. To conclude, these results reveal a novel, SPOC domain

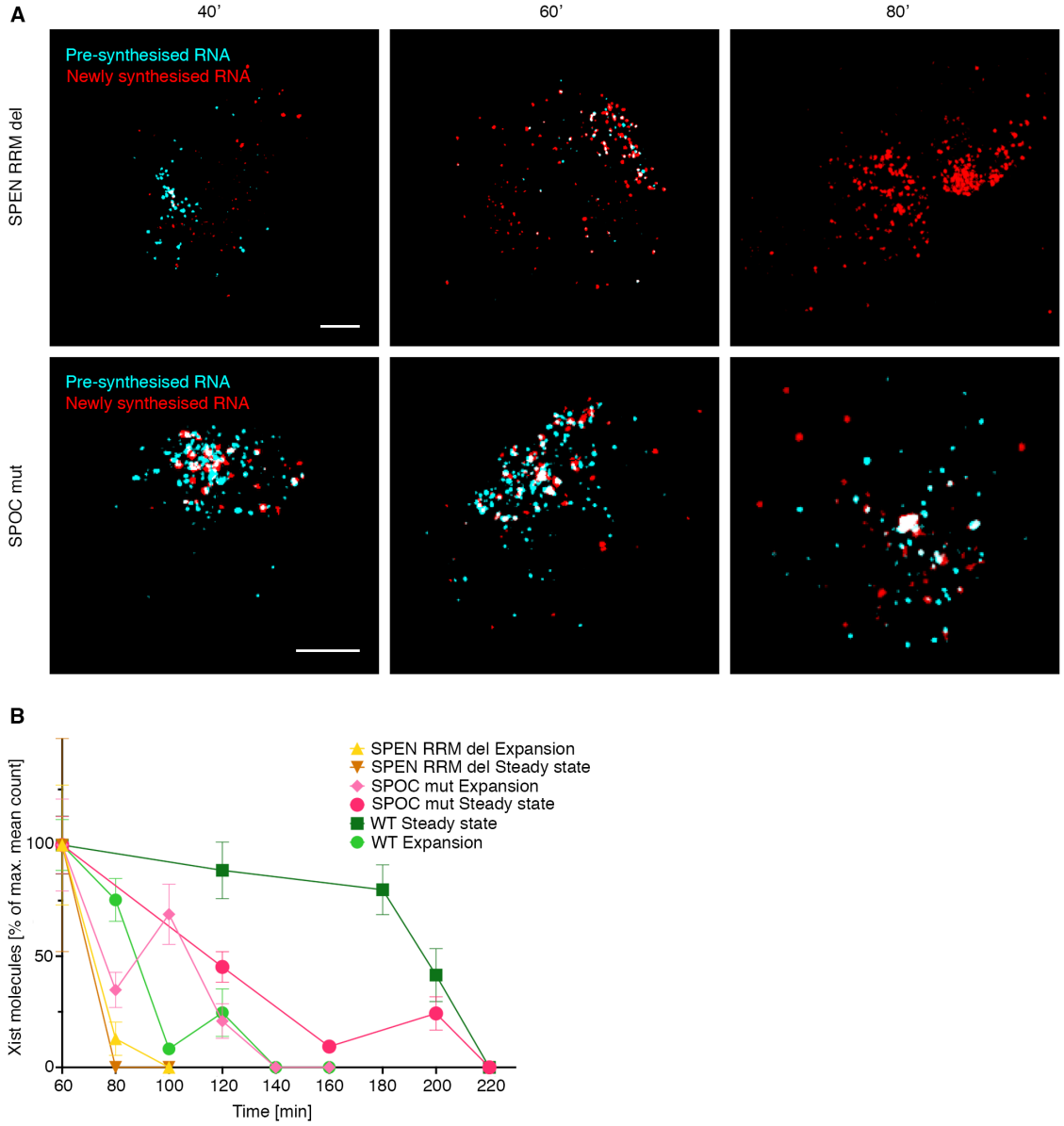

Figure 36: SPEN RRM del but not SPOC mut cells show significantly decreased Xist RNA stability. A) pre-synthesised RNA signal is lost over time: representative RNA-SPLIT images at different staining times with HaloTag ligand 2 in SPEN RRM del and SPOC mut cells during expansion. Images were acquired using 3D-SIM. Maximum intensity projections. Scale bars correspond to 2 μm. B) Quantification of Xist turnover in WT, SPEN RRM del and SPOC mut cells during expansion and steady state shows decreased Xist stability in SPEN RRM del but not SPOC mut cells, obtained by scoring pre-synthesised Xist molecules over time and plotting as percentage of max. mean molecule count for each dataset. n = 20 cells/time point.

independent role of SPEN in the regulation of Xist RNA transcription, stability, abundance and accordingly, silencing ability.

5.5 SPEN binding to Xist but not SPOC domain function is essential for Xist coupling

In a final series of experiments the effect of SPEN mutation on Xist coupling was investigated. Indeed, initial observations suggested that newly synthesised and pre-synthesised Xist RNA molecules occupy distinct bindings sites in SPEN RRM del cells, contrasting with SPOC mut cells and, as noted above WT cells (Figure 37a). Quantification of coupling by NNA of the RNA-SPLIT data confirmed this observation (Figure 37b and 37c). Here, NNA was used to measure the distances between newly synthesised Xist RNA molecules and their respective nearest neighbouring pre-synthesised Xist RNA molecules. Female C127 cells pulsed with EdU were used as technical control, and x, y, and z coordinates of newly synthesised Xist RNA molecule localisations were scrambled before NNA to function as 'Random' control (Figure 37b and 37c). However, contrary to previous analyses, 'Random' controls were generated separately for expansion and steady state in SPEN RRM del cells, because of the striking differences in Xist territory size, particularly in Xist RNA abundance between the two phases (Figure 37b).

NNA showed a median distance of 238 nm between newly synthesised Xist RNA molecules and pre-synthesised Xist RNA molecules during expansion in SPEN RRM del cells as compared to 164 nm in WT cells, suggesting that Xist coupling is partially disrupted (Figure 19c and 37b). The median distance between newly synthesised Xist RNA molecules and pre-synthesised Xist RNA molecules was still significantly less than in the respective 'Random' control (Figure 37b). This observation suggests that whilst Xist coupling is disrupted in SPEN RRM del cells

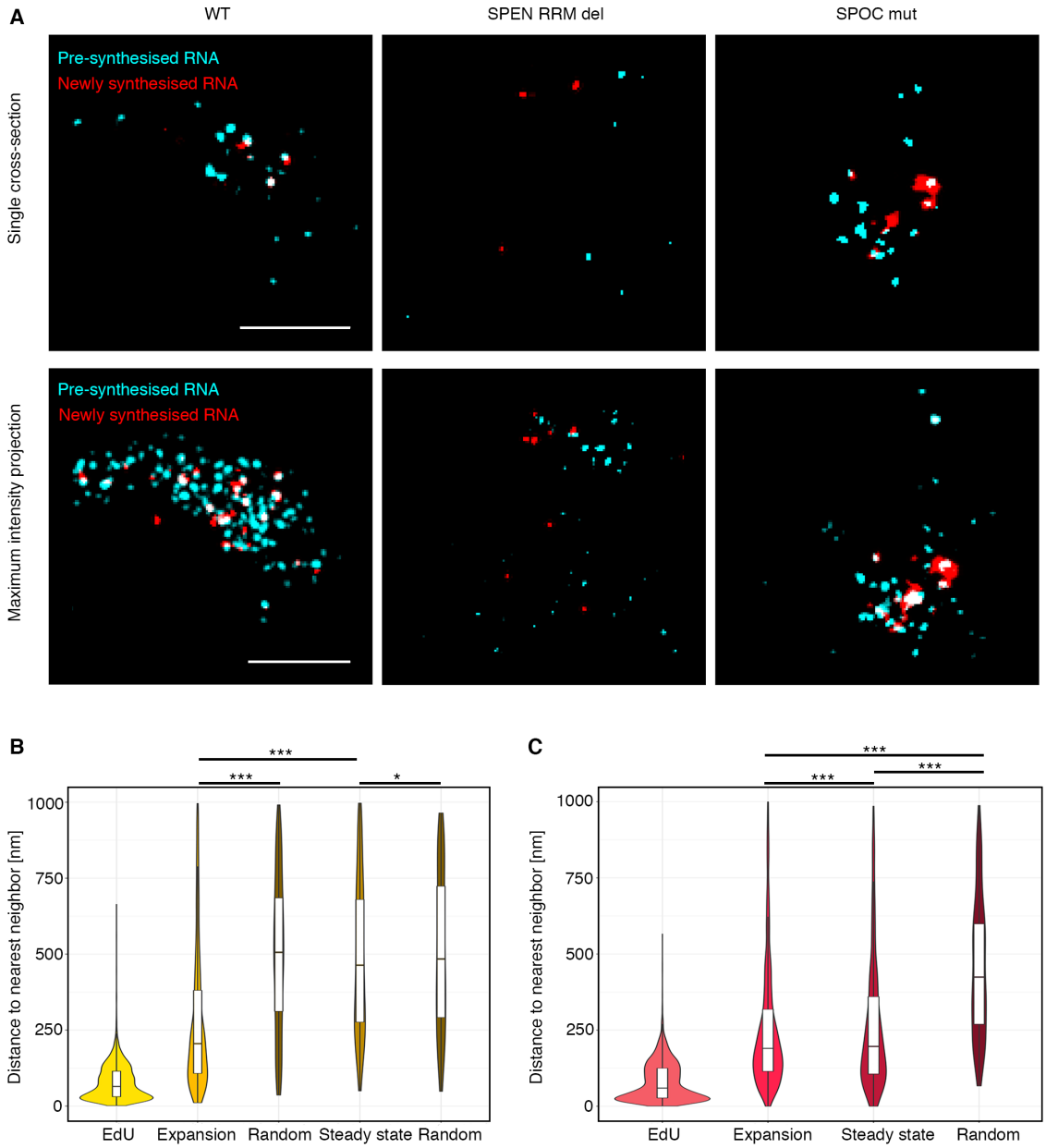

Figure 37: Deletion of the SPEN RRM domains but not mutation of the SPOC domain leads to abrogated Xist coupling. A) Xist coupling is abrogated in SPEN RRM del cells: representative RNA-SPLIT images of WT, SPEN RRM del and SPOC mut cells during expansion. Images were acquired using 3D-SIM. Single cross-sections (top) and maximum intensity projections (bottom). Scale bars correspond to 2 μm. B) NNA of RNA-SPLIT data shows abrogated Xist coupling in SPEN RRM del cells. Distances of each newly synthesised Xist RNA molecule to its nearest pre-synthesised Xist RNA molecule during expansion and steady state in SPEN RRM del cells are displayed in violin plots, including EdU and randomized control. n = 200 cells/time point. C) NNA of RNA-SPLIT data shows coupling behaviour of Xist in SPOC mut cells. Distances of each newly synthesised Xist RNA molecule to its nearest neighbouring pre-synthesised Xist RNA molecule during expansion and steady state in SPOC mut cells are displayed in violin plots, including EdU and randomized

during expansion, it is not entirely abolished (Figure 37b). Assessment of the RNA-SPLIT images by eye indicates that this partial coupling appears to happen

particularly around the Xist transcription site, where Xist is highly enriched (Figure 37a).

Intriguingly, Xist coupling was found to be further disrupted during steady state in SPEN RRM del cells with a median distance of 480 nm. This figure is higher than the respective 'Random' control, suggesting that newly synthesised Xist RNA molecules might actually bind to sites spatially separate from pre-synthesised Xist RNA molecules in a non-random manner (Figure 37b).

Contrasting with the results in SPEN RRM del cells, NNA showed a median distance of 197 nm between newly synthesised Xist RNA molecules and pre-synthesised Xist RNA molecules during expansion in SPOC mut cells similar to 164 nm in WT cells, and indicating that Xist coupling is largely unaffected (Figure 19c and 37c). Xist coupling was slightly affected during steady state in SPOC mut cells, with a median distance of 308 nm, but is nevertheless significantly lower than the 'Random' control and the median distance obtained for SPEN RRM del cells during steady state (Figure 37c).

Together, these results reveal an Xist coupling defect in SPEN RRM del cells, which becomes more dramatic with the progression of XCI from expansion to steady state, and is not apparent in SPOC mut cells. It follows that SPEN has a SPOC domain independent function in Xist coupling. One could speculate that the abrogated Xist coupling in SPEN RRM del cells might be a side effect of disrupted Xist localisation and/or dynamics in SPEN RRM del cells. However, Xist coupling behaviour was found to be independent of Xist localisation to the Xi, since it could be observed in Ciz-1 KO NPCs, where Xist is fully delocalised (Figure 26a and 26b). Moreover, Xist

coupling was found to be intact in autosomal transgene cells, where Xist transcription and degradation rates were altered, suggesting that it is also independent of changes in Xist dynamics (Figure 13c, 15b and 19e). These arguments suggest that the role of SPEN in Xist coupling is separable from its role in Xist localisation and dynamics. Since there is preferential coupling of newly synthesised with pre-synthesised Xist, the phenomenon must take place at the binding site of Xist on the chromatin and not co-transcriptionally. This could be explained either by a secondary factor present only at the binding site, or by a conformational/ biophysical change of Xist that occurs only upon binding to chromatin. In this context, SPEN could either directly mediate Xist coupling through, for instance, dimerization. Alternatively, SPEN could indirectly facilitate Xist coupling. Since the protein constitutes a large part of the Xist RNP it may be essential to the integrity and/or biophysical properties of the RNP or the secondary structure of Xist RNA itself, all of which may be important for Xist coupling.

5.6 Summary: SPEN plays a SPOC domain independent key role in Xist localisation, dynamics and coupling

To investigate a potential role of the Xist silencing factor SPEN in Xist RNA localisation and behaviour, a SPEN RRM deletion was engineered (Figure 30a and 30b). Chromatin RNA sequencing confirmed the 38,224 nucleotide deletion of RRM domains 2 – 4 (Figure 30b), and allelic analysis showed a major silencing defect both 3 h and 24 h post-induction, consistent with prior studies (Nesterova et al. 2019; Dossin et al. 2020) (Figure 31a). As previously mentioned, the aim was to dissect the different SPOC domain dependent and SPOC domain independent roles of SPEN in Xist RNA behaviour. Therefore, mESCs with endogenous inducible BglG-Halo-Xist and two point mutations in the SPOC domain were generated (SPOC mut cells, Figure 32a). These mutations involved the substitution of the two amino acids R3552A and R3554A in the SPOC domain of SPEN and were previously shown to disrupt the interaction of SPEN with N-CoR/HDAC3 (Ariyoshi and Schwabe 2003). Successful substitution was confirmed by restriction digest followed by Sanger Sequencing (Figure 32b). In line with recent research (Dossin et al. 2020), allelic analysis of chromatin RNA sequencing data showed that the SPOC domain mutation strongly abrogates Xist-mediated gene silencing, but not to the same extent as in the deletion of the SPEN RRM domains, indicating the likelihood of a SPOC domain independent role of SPEN in silencing (Figure 32c). Analysis of both mutant cell lines was carried out to explore whether this discrepancy could be due to changes in Xist RNA behaviour and localisation.

First, Xist RNA FISH showed a slightly reduced induction efficiency in SPEN RRM del cells, but not SPOC mut cells, compared to WT during both expansion and steady state (Figure 31b and 32d). Considering the latter findings, it seems feasible that this discrepancy in detected Xist territories might not be due to a change in induction efficiency itself, but due to dispersal of Xist throughout the nucleus and altered transcription/degradation kinetics in SPEN RRM del but not SPOC mut cells. Despite a slightly more dispersed Xist RNA distribution, visible even at lower resolution, Xist territories were formed in the majority of SPEN RRM del cells (Figure 31b). This is in line with previous observations of aberrant Xist territories in SPEN RRM del cells at conventional resolution (Nesterova et al. 2019). 3D-SIM analysis demonstrated that Xist territories were smaller in the SPEN RRM del as compared to WT cells during steady state (Figure 31b). HaloTag staining in combination with 3D-SIM confirmed that Xist was dispersed throughout the nucleus both during expansion and steady state in SPEN RRM del cells (Figure 33a). These observations were confirmed by the quantification of Xist territory volumes, nuclear occupancy, molecule numbers and density. Xist territories were found to be dramatically increased in SPEN RRM del cells during expansion (Figure 33b). Comparison of Xist occupancy of nuclear volume during expansion showed that while Xist only occupies around 10% of the nuclear volume in WT cells, Xist could be found in around 70% of the nucleus in SPEN RRM del cells, indicating that Xist is delocalised from the Xi (Figure 33c). Residual accumulation of Xist around the TS during steady state (Figure 33a), suggests that Xist may still be able to localise to proximal regions of the Xi at first, but is then unable to spread to sites more distant from the Xist TS. Considering the gradual expansion of Xist in 3D in WT cells

described in chapter 3, this may indicate that Xist is still capable of initial binding to the chromatin near the TS, but fails to spread and re-locate to more distal sites over time.

In contrast to SPEN RRM del cells, Xist territories were not found to be abnormal in SPOC mut cells both at conventional resolution and also when examined using 3D-SIM followed by HaloTag staining (Figure 32b and 33a). Quantification of Xist territory volumes in the SPOC mutant showed that they were significantly closer to WT cells during expansion than in SPEN RRM del cell. Together, these results confirm a novel role of SPEN in Xist localisation and spreading across the Xi, which is at least in part SPOC domain independent.

RNA-SPLIT and subsequent NNA was performed to determine the median distance of each Xist molecule to its ten nearest neighbouring Xist molecules as an indicator of Xist density (Figure 34c). Surprisingly, given the previous observation of Xist territories having a normal appearance in SPOC mut cells, Xist density was significantly decreased in both the SPEN RRM del and SPOC mut as compared to WT cells (Figure 34c). This suggests that, in addition to its SPOC domain independent role in Xist localisation and spreading across the Xi, SPEN also has a SPOC domain dependent function in the efficient Xist RNA coverage of the Xi. This could be due to incomplete compaction of the chromatin in both SPEN RRM del and SPOC mut cells, since the SPOC domain is thought to mediate co-repressor recruitment and thus histone deacetylation (Bhaskara et al. 2010; Żylicz et al. 2019; Nesterova et al. 2019; Dossin et al. 2020).

Quantification of Xist molecule numbers in the different mutant cell lines showed a significant increase of Xist molecules in the SPEN RRM del as compared to WT cells during expansion (Figure 34a). During steady state, however, Xist molecule numbers were found to be significantly decreased compared to WT cells (Figure 34a). No such differences could be detected in SPOC mut cells (Figure 34b). These results were confirmed by analysis of Xist expression based on chromatin RNA sequencing data (Figure 34b). Overall, this suggests that Xist RNA abundance is deregulated in SPEN RRM del, but not SPOC mut cells.

RNA-SPLIT was performed to help answer whether Xist transcription and/ or degradation rates change in SPEN mutants. As observed in WT cells before, a general reduction in Xist transcription with progression of XCI from expansion to steady state could be observed in SPEN RRM del and SPOC mut cells (Figure 35b and 35c). However, Xist transcription rates were increased both during expansion and steady state in SPEN RRM del as compared to WT cells and could therefore not account for the decreased Xist molecule numbers during steady state (Figure 35b). Interestingly, the same effect could not be found in SPOC mut cells, suggesting that SPEN has a SPOC domain independent role in regulating Xist RNA transcription (Figure 35c). Recently, SPEN has been implicated in directing silencing factors and Xist to active gene promoters through its SPOC domain (Dossin et al. 2020). The RNA-SPLIT results indicate that this may also include the Xist promoter itself, and that SPEN thereby dampens Xist transcriptions in WT cells, but in a SPOC domain independent manner. Indeed, Xist RAP data has found Xist binding enriched around the Xic, particularly at early stages of XCI (Engreitz et al.

2013). However, the resolution of said data does not allow for the confirmation of Xist binding to its own promoter specifically (see further discussion in chapter 6).

Next, RNA-SPLIT was used to assess the Xist turnover in SPEN RRM del and SPOC mut cells during expansion and steady state. Whilst SPOC mut and WT cells showed a complete turnover of Xist RNA after 140 min during expansion and 220 min during steady state, Xist RNA in SPEN RRM del cells was found to have a significantly decreased stability with a complete turnover after 80 min and 100 min during expansion and steady state respectively (Figure 36b). Thus, the dramatic increase in Xist stability as XCI progresses from expansion to steady state was not seen in SPEN RRM del cells, but could be observed in SPOC mut cells (Figure 36b). Based on the earlier finding (see chapter 3) that Xist transcription rates determine Xist degradation rates, it can be proposed that deregulation of Xist transcription in SPEN RRM del cells caused an increase in Xist degradation. To conclude, these results reveal a novel, SPOC domain independent role of SPEN in the regulation of Xist RNA transcription, and hence stability as well as abundance.

RNA-SPLIT revealed the fascinating phenomena of Xist coupling at different stages of XCI, and in the context of the Xi and chromosome 15, and that this is independent of CIZ-1 function (Figure 19, 21 and 29a-b). Considering the major disruption of Xist-mediated gene silencing and Xist behaviour in SPEN RRM del cells, this raised the question whether Xist coupling is affected by perturbation of SPEN. Indeed, quantification of Xist coupling by NNA of the RNA-SPLIT showed that Xist coupling was severely disrupted in SPEN RRM del cells during expansion and steady state (Figure 37b). In contrast, Xist coupling was found to be intact in SPOC mut cells

during both expansion and steady state (Figure 37c). Overall, the results revealed that the Xist coupling defect in SPEN RRM del cells becomes more dramatic with the progression of XCI from expansion to steady state and that SPEN's function in Xist coupling is SPOC domain independent. Given that Xist coupling behaviour is independent of Xist localisation to the Xi in Ciz-1 KO NPCs, and independent of Xist dynamics in autosomal transgene cells (Figure 13c, 15b and 19e), the novel role of SPEN in Xist coupling is apparently separable from its role in Xist localisation and dynamics. Since there is preferential coupling of newly synthesised with pre-synthesised Xist, the phenomenon must take place at the binding site of Xist on the chromatin and not co-transcriptionally. This can only be explained either by a secondary factor present only at the binding site, or by a conformational change of Xist that occurs only upon binding to chromatin. In this context, SPEN could either facilitate Xist coupling directly or indirectly. The latter seems more probable, since dimerization, for instance, would more likely take place before Xist binding to the chromatin and, hence, could not account for preferred coupling of temporally separate Xist molecules. Moreover, SPEN constitutes a large part of the Xist RNP and may thus influence its integrity and/or biophysical properties, as well as the secondary structure of Xist RNA itself, which all might be required for Xist coupling.

The aim of these perturbation experiments was to examine the role of SPEN in Xist RNA behaviour, while carefully distinguishing between SPOC domain dependent and independent functions. Indeed, three novel and SPOC domain independent functions of SPEN, namely in Xist localisation, dynamics and coupling, were revealed by RNA-SPLIT analysis. This is surprising, since previous studies

concluded that SPEN is dispensable for Xist localisation (Monfort et al. 2015; Dossin et al. 2020), although presence of aberrant Xist territories in SPEN RRM del cells has been mentioned recently (Nesterova et al. 2019). This discrepancy is most likely due to previous studies employing conventional imaging approaches and qualitative analysis. Accordingly, these findings on the role of SPEN in Xist RNA behaviour highlight the importance and extraordinary sensitivity of super-resolution microscopy in combination with HaloTag labelling, as well as the necessity for unbiased quantification of imaging data.

As established in chapter 4, Xist localisation to the Xi in general does not appear to affect Xist coupling. However, intact Xist coupling and / or dynamics may be essential for Xist localisation. Whether or not the newly identified functions of SPEN are interdependent remains to be determined. It is, however, tempting to speculate that it is the loss of Xist coupling that causes aberrant Xist RNA localisation and decreased stability in SPEN RRM del cells.

CHAPTER VI

6 Discussion

Labelling nuclear RNAs such as Xist to study localisation and dynamics is challenging. Here, the BgI-stem-loop system allowed for efficient labelling of inducible endogenous Xist RNA on the X chromosome and autosomal transgenic Xist RNA on chromosome 15 to study Xist behaviour without altering Xist-mediated silencing or functionality. In combination with HaloTag technology and 3D-SIM, this system enabled the detection of distinct Xist foci. The time window from 1.5 h until 5 h and the timepoint 24 h post-induction were identified for the assessment of initial Xist spreading across the chromosome territory (expansion) and the maintenance of Xist *in cis* (steady state), respectively. This chapter will discuss the development of RNA-SPLIT and its application to the study of Xist RNA localisation, dynamics and spreading, both in the endogenous and autosomal transgenic context. Additionally, insights gained by perturbation experiments of the Xist localisation factor CIZ-1 and the Xist silencing factor SPEN and their role in the aforementioned aspects of Xist behaviour will be considered.

6.1 RNA-SPLIT – a powerful tool to study Xist RNA behaviour

Initially, the aim of the project was to study Xist RNA dynamics by super-resolution live cell imaging of BglG-Halo-Xist, but technical barriers limited what could be achieved in this regard. 3D-SIM live cell imaging yielded sufficient resolution for the detection of single Xist foci, but the speed of acquisition was limiting and did not enable the capture of Xist RNA dynamics. Single particle PALM/TIRF was used as an alternative to capture highly dynamic Xist particles, but required the use of photoactivatable ligands, and, hence, stem-loop bound and unbound BglG-Halo proteins could no longer be distinguished. The option of using RNA aptamers such as Mango for background reduction was also ruled out due to issues with generating stable integrants in mESCs. Development of a new method, RNA-SPLIT (sequential pulse localisation imaging over time), where different HaloTag ligands are added to live cells sequentially, helped overcome the technical challenges posed by live cell imaging and enabled extensive analysis of Xist RNA dynamics, localisation and spreading behaviour at super-resolution using 3D-SIM.

SLAM-seq analysis of the degradation kinetics of Xist was successfully used to cross-validate the RNA-SPLIT results and proved that RNA-SPLIT is a reliable method to assess RNA kinetics. In fact, variability was higher when using SLAM-seq, and analysis of Xist-mediated silencing under SLAM-seq conditions showed that Xist did not fully silence after 4SU incorporation following the SLAM-seq protocol, raising questions about of the physiological relevance of these results. Chromatin RNA sequencing analysis, on the other hand, confirmed that silencing is generally unaffected by the insertion of the Bgl-stem-loop array, suggesting that

RNA-SPLIT is a more native method to assess RNA kinetics than SLAM-seq. Moreover, RNA-SPLIT does not require the addition of reagents to halt transcription and, hence, does not have detrimental effects on cell metabolism. While only one clonal line of WT cells has been studied in the context of this project, similarities in the WT and Ciz-1 KO, as well as SPEN SPOC mutant mESCs serve as validation of the general high reproducibility of RNA-SPLIT.

In contrast to conventional localisation microscopy techniques, RNA-SPLIT provides temporally resolved 3D localisation information, and therefore allows for the observation of RNA kinetics, and Xist RNA spreading and localisation over time, making it a versatile and broadly applicable tool. Different staining times could be adjusted to suit the characteristics of the different measurements being undertaken. Furthermore, the data sets contain added information regarding chromatin states, for example based on DAPI density, which has not been used to date, but could be used in subsequent studies. To conclude, RNA-SPLIT represents a robust, versatile and native tool to study Xist RNA behaviour at high spatial and temporal resolution.

Since RNA-SPLIT only requires the use of two channels to image newly synthesised and pre-synthesised RNA molecules, different labels could be added to study other XCI factors at the same time. For example, the SnapTag labelling system could be used to visualise Xist interacting proteins, such as CIZ-1 and SPEN in tandem with Xist RNPs, and to examine their interaction over time. Application of another stem-loop based labelling system, such as MS2, in combination with SnapTag labelling technology could moreover be used to study other lncRNAs involved in XCI, such as Jpx, Ftx, Tsix and Linx together with Xist RNA.

RNA-SPLIT can not only be used for the study of Xist RNA, but could be applied to examine localisation, kinetics and behaviour of other RNAs as well. As described previously, labelling and study of nuclear RNAs at high spatial and temporal resolution is challenging. Here, RNA-SPLIT provides a powerful set of tools without the need for live cell imaging or highly disruptive treatment. This new method would be especially applicable to highly localised RNAs, such as nuclear paraspeckle assembly transcript 1 (NEAT1). Moreover, RNA-SPLIT analysis of another lncRNA could serve as validation of the method itself, and comparison of the results could yield important insights into Xist RNA specific behaviour, which distinguishes it from other lncRNAs. RNA-SPLIT experiments are limited to a time course of up to 4 h due to the concern of turnover of the BglG fusion protein on the stem loops and therefore are particularly suitable for dynamic RNAs with rapid turnover. However, in cases where turnover exceeds the restricted time window for RNA-SPLIT, alternative approaches such as SLAM-seq would be required.

To be more broadly applicable, RNA-SPLIT needs to be further improved. At this point the methodology depends on the manual acquisition of extremely large data sets, followed by partially manual image processing relying on the thresholding of each image by hand. Only the data analysis part of the workflow is currently fully automated. This makes the acquisition, processing and analysis of each dataset time and labour intensive, with each dataset requiring around three to four months of full-time work. Considering the extreme variability of Xist territories in WT cells, and especially in the different cellular backgrounds, as well as the importance of the selection of cells with suitable BglG fusion protein expression levels for optimal

image quality, it would be highly challenging to automate the image acquisition. However, recent progress in the use of artificial intelligence for high-resolution imaging is promising and could deliver solutions for highly diverse datasets. Work produced and manually processed in this project could be used as training datasets for neural networks in the future. A similar approach could be chosen for the automation of the manual thresholding of background signal by unbound BglG fusion protein.

In addition to the applications of the newly developed system in the advanced imaging of Xist RNA, the use of HaloTag labelling technology also allows for pull-down experiments through the use of biotinylated ligands. This could allow for Xist RAP / CHART-seq like approaches to study the binding of Xist RNA to the chromatin, which has the potential for single cell analysis. Although this has been explored in the WT context (Engreitz et al. 2013; Simon et al. 2013), and following deletion of the Xist A-repeat (Engreitz et al. 2013), in the future it will be very interesting to explore how perturbation of different factors, such as SPEN, affects chromosome sites for Xist binding and spreading.

Whilst RNA-SPLIT has allowed for the extensive study of Xist behaviour, some questions still remain unanswered. RNA-SPLIT confirmed Xist spreading in 3D, but could not reveal the mechanism of spreading. Despite indications that Xist might spread through a series of binding and unbinding events, only live cell imaging of single Xist foci can ultimately uncover how Xist is spreading *in cis*. The main reason that single-particle tracking experiments were not achievable was the signal stemming from unbound BglG fusion proteins. Therefore, it will be of utmost

importance to find a way of reducing this signal to ensure successful live cell imaging in the future. In these experiments the BglG protein expression was controlled by a doxycycline inducible promoter. Previous attempts in the lab to titrate the doxycycline concentration to reduce expression have not been successful. Additionally, Xist RNA was controlled by a doxycycline inducible promoter, making it impossible to delay the induction of the BglG fusion protein to reduce background levels. Hence, a future model system for live cell imaging should disconnect the BglG expression from Xist RNA expression by the use of an alternative induction system, which should ideally be titratable. This would also resolve the issue around variability of expression levels in different cell lines. Recently, the GeneSwitch system (Wang et al. 1994) has been shown to be titratable and this might provide a good alternative induction system for BglG fusion protein in the future.

6.2 *Cis*-limited localisation of Xist RNA

Initial experiments found the 3' end of Xist to be more closely associated with the chromatin boundary, while Xist in general was located in the interchromatin space, which agrees with previous 3D-SIM studies (Smeets et al. 2014). The nuclear matrix protein CIZ-1 has recently been implicated in Xist localisation to the X chromosome territory (Ridings-Figueroa et al. 2017). 3D-SIM analysis showed that CIZ-1 closely associates with Xist towards the 3' end very early after Xist induction. This agrees with previous research, which established that CIZ-1 binds to Xist at the E-repeats (Ridings-Figueroa et al. 2017; Sunwoo et al. 2017). Together, these observations indicated that Xist RNPs may be tethered to the chromatin at their 3' end through CIZ-1. Thus, perturbation experiments involving CIZ-1 seemed ideal to study *cis*-limited Xist RNA localisation.

Ciz-1 KO mESCs were generated by CRISPR/Cas9 mediated genome engineering. Allelic analysis of chromatin RNA sequencing data showed that Xist-mediated silencing of X-linked genes is unaltered upon perturbation of CIZ-1. CIZ-1 deficiency in mice has previously been shown not to affect embryogenesis, early postnatal development, or cell viability *ex vivo* (Ridings-Figueroa et al. 2017). Together these results suggest that CIZ-1 is dispensable for the initiation and establishment of XCI. The Xist territory volume was found to decrease with progression of XCI from expansion to steady state in WT and Ciz-1 KO mESCs, indicating gradual Xist territory compaction with progression of XCI. This is in line with the observation that transcriptional silencing is unaffected in Ciz-1 KO mESCs. Additionally, image processing tools and NNA of the 3D-SIM data allowed for the measurement of Xist

RNA density: The median distance of each Xist molecule to the 10 nearest neighbouring Xist molecules was determined in order to assess molecule density. This proved to be a valuable method for comparing chromosomal Xist coverage in different cell lines: perturbation of CIZ-1 in mESCs was shown to result in decreased Xist RNA density, and a significant density defect was detected in autosomal transgene cells as well. The latter is in line with previous studies, which suggest that transgenic Xist can display attenuated Xist spreading and inefficient Xist coverage (Popova et al. 2006). Neither autosomal transgene nor Ciz-1 KO mESCs, however, were found to have an increased Xist territory volume as compared to WT cells, implying a coverage defect rather than delocalisation of Xist from the inactive Xi (Figure 38a). Considering that CIZ-1 has been implicated in anchoring Xist to the chromatin, it seems plausible that less Xist molecules might be bound to chromatin in Ciz-1 KO mESCs, leading to less dense Xist coverage of the Xi (Sunwoo et al. 2017). However, the fact that Xist-mediated transcriptional silencing is unaffected in Ciz-1 KO mESCs and that no delocalised Xist could be found throughout the nucleus, argues against this idea. As described earlier, less efficient compaction of the Xi could be ruled out as a reason for the density defect as well. An alternative explanation, that the decreased Xist RNA density on the Xi is linked to a change in Xist kinetics, agrees with the finding of a general reduction in Xist molecule numbers and was later confirmed by RNA-SPLIT experiments.

It has been shown that perturbation of CIZ-1 leads to Xist RNA dispersal in some differentiated cell types such as mouse fibroblasts as well as B- and T-lymphocytes (Ridings-Figueroa et al. 2017; Sunwoo et al. 2017). Thus, differentiation of the Ciz-

1 KO mESCs was performed using an NPC differentiation protocol. A clear Xist localisation defect was seen in Ciz-1 KO NPCs, consistent with results obtained previously for other differentiated cell types (Ridings-Figueroa et al. 2017), and NPC differentiation offers a synchronous and homogeneous cell culture model. Xist RNA behaviour has been proposed to differ generally between mESCs and differentiated cells (Engreitz et al. 2013; Simon et al. 2013), hence parental WT mESCs were also differentiated for comparison.

Whilst Xist RNA dispersal throughout the nucleus could be observed in Ciz-1 KO NPCs (Figure 38a), Xist was found to accumulate at specific regions, heterochromatin of the nuclear and nucleolar periphery (Figure 38a). This localisation may be mediated by other factors such as hnRNPU, which has previously been described to anchor Xist to chromatin (Hasegawa et al. 2010; Sunwoo et al. 2017), or may be an inherent property of Xist (Figure 38a). Similar to the delocalisation of Xist in Ciz-1 KO NPCs, hnRNPU knock down in MEFs has been shown to cause Xist RNA dispersal (Sunwoo et al. 2017), indicating an inter-dependency of hnRNPU and CIZ-1 in differentiated cells. In fact, it has been proposed that hnRNPU works as a scaffold attachment factor for Xist to the nuclear matrix, while CIZ-1 may function as a bridging factor interacting both with hnRNPU and Xist RNA (Brockdorff 2019). In undifferentiated cells, there might be an unknown alternative anchoring factor, possibly the highly homologous protein hnRNPUL1 or even SPEN, with a similar function to CIZ-1, making the latter dispensable at this stage (Figure 38a).

The dramatic dispersal of Xist in Ciz-1 KO NPCs was quantified and confirmed by measuring the molecule density. Interestingly, density was discovered to increase with the progression of differentiation in WT NPCs, while it decreased in Ciz-1 KO NPCs. Together, these results suggest that whilst CIZ-1 function is largely redundant in mESCs it becomes progressively more important with the advancement of XCI. When exactly CIZ-1 becomes essential for *cis*-limited Xist localisation during differentiation, and what triggers this change, remains to be explored. In the future, RNA-SPLIT could help answer these questions. For instance, it would be interesting to further explore *cis*-limited Xist RNA localisation by perturbing hnRNPU in the existing Ciz-1 KO cell line. Since hnRNPU KO mESCs are not viable, one could instead utilise one of the recently developed degron systems, such as the dTAG system (Nabet et al. 2018).

In line with the delocalisation of Xist from the Xi in Ciz-1 KO NPCs, uH2A was no longer enriched on the Xi. However, uH2A enrichment was still found at those sites that dispersed Xist localised to, i.e. the nuclear and nucleolar periphery (Figure 38a), suggesting that Xist still recruits Polycomb group proteins and may accordingly maintain its silencing function in Ciz-1 KO NPCs. Despite the lack of uH2A enrichment on Xi in Ciz-1 KO NPCs, there was no major deficiency in silencing Xi genes. This agrees with previous findings that loss of Xist after XCI is established does not interfere with the maintenance of the inactive state, and the suggestion that stable epigenetic marks are sufficient for the maintenance of XCI (Costanzi et al. 2000; Csankovszki, Nagy, and Jaenisch 2001). Still, the localisation of Xist to heterochromatic regions and the enrichment of uH2A at the same sites,

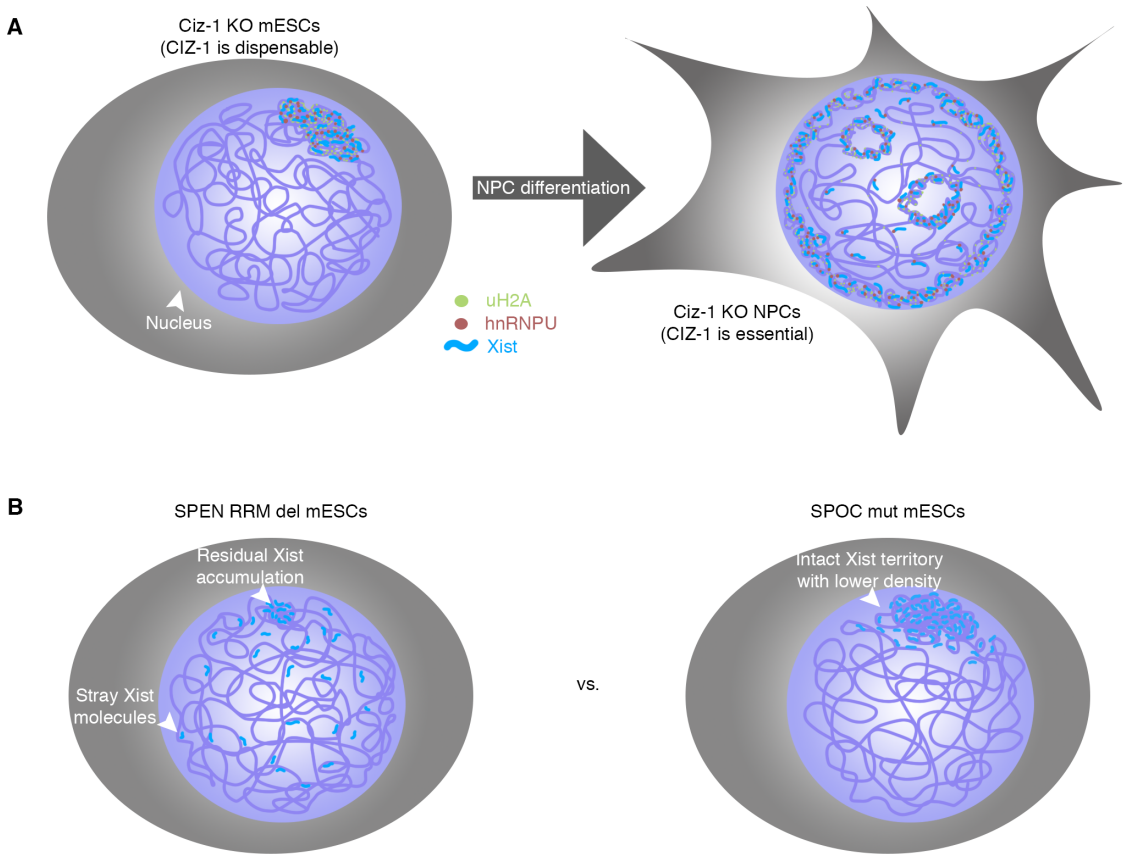

Figure 38: CIZ-1 and SPEN play a role in *cis*-limited Xist localisation. A) Schematic illustrating Xist localisation in Ciz-1 KO mESCs (left) and Ciz-1 KO NPCs (right). B) Schematic illustrating Xist localisation in SPEN RRM del mESCs (left) and SPOC mut mESCs (right).

raises the question whether Xist might silence off-target genes in Ciz-1 KO NPCs, specifically those located close to constitutive heterochromatin. Such an effect would likely differ from cell to cell and would therefore be difficult to pick up by, RNA sequencing of cell populations. To test this hypothesis, one could therefore compare XX and XY Ciz-1 KO NPCs, which would allow for the discrimination of changes related to Xist RNA dispersal from other gene expression changes caused by the KO of CIZ-1.

To summarise, transcriptional silencing of the Xi is independent of CIZ-1, Xist localisation to the Xi and uH2A enrichment in NPCs, suggesting that CIZ-1 function

in Xist localisation only becomes essential after transcriptional silencing of the Xi has already been established (Figure 38a). This is in line with Ciz-1 KO mice not showing any major neurological abnormalities, and with primary embryonic fibroblasts derived from CIZ-1 deficient mice as well as B / T-lymphocytes only showing minor effects on X-linked gene repression (Ridings-Figueroa et al. 2017). Although a minor relaxation of silencing was seen in Ciz-1 KO NPCs, but this was based on only one biological replica, and thus needs to be confirmed in the future. Addition of more replicas would also allow for further analysis and potentially classification of the genes with reduced silencing. Considering the dramatic phenotype of Ciz-1 KO NPCs, where Xist was found dispersed through the nucleus, it would also be interesting to examine whether a minor neurological phenotype can be found in Ciz-1 KO mice. More generally, the above described experiments involved NPC differentiation with Doxycycline addition to induce Xist expression, which could impact the results. Generation of new cell lines to allow for a side-by-side comparison with a non-inducible system for differentiation could resolve this issue in the future.

As described in chapter 5, analysis of SPEN mutant mESCs revealed a role for SPEN in Xist localisation that is independent of its SPOC domain and Xist-mediated gene silencing. Despite SPEN RRM del cells forming visible Xist territories, a slightly more dispersed Xist RNA distribution was seen, even at conventional resolution, in line with a previous report (Nesterova et al. 2019). HaloTag staining and 3D-SIM analysis demonstrated that Xist territories were smaller in the SPEN RRM del as compared to WT cells during steady state, and confirmed that Xist was dispersed

throughout the nucleus both during expansion and steady state (Figure 38b). These observations were quantified by the measurement of Xist territory volumes, nuclear occupancy, molecule numbers and density. For instance, comparison of Xist occupancy of nuclear volume during expansion showed that while Xist only occupies around 10% of the nuclear volume in WT cells, Xist could be found in around 70% of the nucleus in SPEN RRM del cells, indicating that Xist is delocalised from the Xi. Residual accumulation of Xist around the TS during steady state suggests that Xist is still capable of initial binding to chromatin, but fails to spread and re-locate to more distal sites over time, implicating SPEN in directly or indirectly facilitating Xist spreading across the Xi (Figure 38b and 40b). Interestingly, ChIP experiments to analyse the distribution of Polycomb histone modification on the Xi at equivalent timepoints representing expansion (3 h) and steady state (24 h) show a clear deficit at sites further away from the Xist locus in SPEN RRM del but not SPOC mut cell lines (Joe Bowness, personal communication). Given that Polycomb mediated histone modifications provide a surrogate mark for Xist localisation, this observation adds to the mounting evidence that the localisation defect seen in SPEN RRM del cells is due to a deficiency in Xist spreading rather than an inability to tether Xist to the chromatin, as was seen in the Ciz-1 KO NPCs. In the future, it may be interesting to examine this apparent spreading defect in SPEN mutant mESCs by RAP or CHART-seq experiments.

Despite the observation of apparently normal Xist territories in SPOC mut cells, Xist density was significantly decreased compared to WT cells, suggesting an additional SPOC domain dependent role of SPEN in the efficient Xist RNA coverage of the Xi

(Figure 38b). This could be due to incomplete compaction of the chromatin in both SPEN RRM del and SPOC mut cells, since the SPOC domain is thought to mediate HDAC3 recruitment and thus deacetylation (Bhaskara et al. 2010; Żylicz et al. 2019; Nesterova et al. 2019; Dossin et al. 2020). However, the lack of a marker for the Xi territory hinders determination of whether a density defect is due to dispersal of Xist RNA from the Xi territory or due to a decondensed Xi. Still, that the Xist territory volume is less affected in SPOC mutant mESCs argues for the latter explanation. In the future, chromosome painting using X chromosome specific probe sets might provide further insights into the different Xist localisation phenotypes found in SPEN RRM del and SPOC mutant mESCs. However, this is complicated by the harsh experimental conditions of chromosome painting, which might not allow for the parallel labelling of Xist RNA by RNA FISH or HaloTag staining. Recently, a non-denaturing form of FISH, RASER (resolution after single-strand exonuclease resection)-FISH has been developed to visualise chromosomal loci without denaturing DNA (Brown et al. 2018). These gentler conditions might either allow for direct labelling of Xist RNA by HaloTag staining, or indirect labelling of Xist RNA or a surrogate marker by immunofluorescence staining. Hence, RASER-FISH is a promising method to explore Xist RNA localisation with reference to the Xi territory in the future. Furthermore, application of Hi-C could enable examination of the potential changes to the chromosome structure of the Xi in the different mutant cell lines in the future.

As experience studying the SPEN RRM del cell line has shown, conventional imaging approaches are often not sensitive enough and do not yield sufficient

resolution to detect subtler Xist localisation defects. Moreover, analysis of the large datasets with thousands of data points obtained by RNA-SPLIT reduce bias and help capture effects across cell populations. Therefore, other factors involved in Xist-mediated silencing, which have thus far not been implicated in Xist localisation, could also be re-evaluated. For instance, deletion of the Xist B repeat has recently been described to cause dispersal of Xist in mouse embryonic fibroblasts (MEFs) (Colognori et al. 2019). The Xist B repeat is required to recruit PRC complexes (Pintacuda et al. 2017), and indeed deletion of PRC1 Polycomb group proteins had a similar apparent effect on Xist localisation (Colognori et al. 2019). Although PRC complexes have been implicated in Xist-mediated silencing and not Xist localisation or kinetics before, previous methods might not have been sensitive enough to have picked up the effects of their perturbation similar to defects in SPEN RRM del cells reported here. It would therefore be interesting to use RNA-SPLIT to analyse Xist behaviour upon perturbation of PRC1/PRC2 in the future.

6.3 New insights into Xist RNA kinetics

RNA-SPLIT was applied to assess Xist RNA turnover. Both endogenous and autosomal transgenic Xist RNA stability was significantly increased in steady state as compared to expansion, suggesting that Xist stability increases with progression of XCI independently of the chromosomal context (Figure 39). However, stability was found to be generally decreased in autosomal transgene cells, indicating that Xist is generally more stable in its endogenous context. Increased stability of endogenous Xist could be explained by the different chromatin environment of the Xi compared to chromosome 15, and/or factors specifically enriched on the X chromosome. Decreased stability of autosomal Xist could partially account for the reduced silencing efficiency reported previously (Tang et al. 2010; Loda et al. 2017). Likewise, the increase in stability over time could be triggered by a change of the physical chromatin environment or secondary protein factors present only during the steady state phase of XCI. This seems likely, since both chromatin environment, factors enriched on the Xi and dependency on Xist have been shown to change substantially with the progression of XCI. However, the aforementioned observations were made using only one autosomal transgene integration site. In order to exclude variability between cell lines, due to integration site and/or copy number, further analysis of independent autosomal integrations will be necessary.

Measurement of Xist transcription dynamics by RNA-SPLIT revealed that both endogenous and autosomal transgenic Xist transcription is significantly decreased in steady state as compared to expansion (Figure 39), while Xist transcription was found to be generally increased in the autosomal transgene cell line, suggesting a

feedback mechanism may control Xist stability depending on transcription rates. Indeed, previous research has suggested such a feedback mechanism, based on experiments where interruption of transcription by Actinomycin D treatment resulted in a dramatic increase in Xist stability (Ng et al. 2011). In this work, using doxycycline washout, Xist stability was also dramatically increased (Figure 39). Since endogenous and autosomal transgenic Xist analysed in this study are under the control of a doxycycline inducible promoter, this feedback mechanism must be promoter independent. Whilst the basis for this effect is currently unknown, some possibilities are discussed below. In summary, Xist RNA stability is defined by its chromatin environment and, through an unknown feedback mechanism, its rate of transcription (Figure 39).

RNA-SPLIT was also used to assess Xist stability and transcription rates in Ciz-1 KO mESCs during expansion and steady state, and to explore whether perturbation of *cis*-limited localisation might relate to deregulation of Xist kinetics and therefore abundance. Xist RNA stability was found to increase significantly from expansion to steady state in Ciz-1 KO mESCs, while Xist RNA transcription decreased significantly, just like in WT mESCs, indicating that the feedback mechanism connecting transcription and degradation of Xist is independent of CIZ-1 function in undifferentiated cells. This was not surprising, since Xist localisation was also found to be largely unaffected in Ciz-1 KO mESCs.

However, RNA-SPLIT and chromatin RNA sequencing experiments showed a dramatic increase of both Xist molecule numbers and Xist transcription in WT NPCs as compared to WT mESCs. While, it is possible that prolonged incubation of cells

with doxycycline may be responsible for this effect, Xist molecule numbers and transcription were found to be even more dramatically increased in Ciz-1 KO NPCs. The latter observation suggests that perturbation of CIZ-1 leads to deregulated Xist kinetics in differentiated but not undifferentiated cells. Experiments using non-inducible differentiation could clarify the effect of Doxycycline induction in the future. Together, these results suggest that CIZ-1 either has a direct role in the transcriptional regulation of Xist in NPCs, or an indirect role, where delocalisation of Xist from the Xi leads to an increase in Xist transcription. Since CIZ-1 has not previously been implicated in regulating transcription, it is tempting to speculate that the delocalisation of Xist from the Xi itself might cause the deregulation of the feedback mechanism controlling Xist kinetics. This would argue for a model where tight regulation of Xist kinetics and a resulting equilibrium of transcription and degradation ensure a constant RNA abundance for in cis-localisation throughout the different stages of XCI (Figure 39).

The results in Ciz-1 KO NPCs raise the question of whether SPEN RRM del cells, where Xist was delocalised from the Xi, would also display deregulated Xist kinetics. Recently, SPEN has been implicated in directing silencing factors to active gene promoters through its SPOC domain, potentially including the Xist promoter itself (Dossin et al. 2020). Indeed, RAP data has found Xist binding enriched around the Xic particularly at early stages of XCI (Engreitz et al. 2013), although the resolution prevents specific localisation of Xist to its own promoter. Quantification of Xist molecule numbers by RNA-SPLIT and chromatin RNA sequencing showed a significant increase in the SPEN RRM del as compared to WT cells during

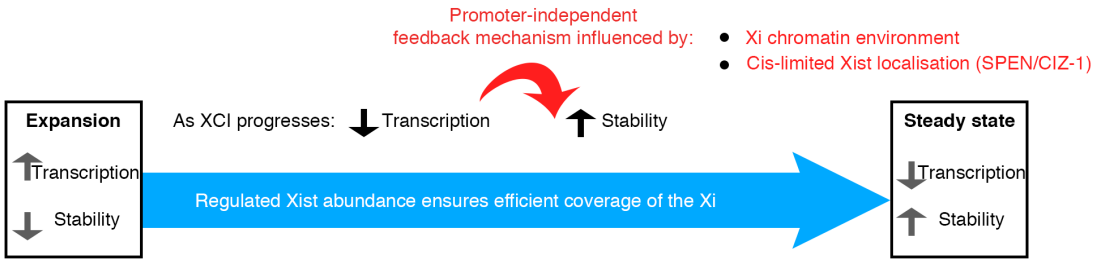

Figure 39: A novel promoter-independent feedback mechanism regulates Xist stability in response to Xist transcription rates throughout XCI. A) Schematic illustrating how Xist stability and abundance is regulated from expansion to steady state by a transcription rate dependent feedback mechanism.

expansion, while no such significant differences could be detected in SPOC mut cells. This suggests that Xist RNA abundance is indeed deregulated in SPEN RRM del, but not SPOC mut cells (Figure 39). Certainly, Xist transcription rates were increased both during expansion and steady state in SPEN RRM del as compared to WT cells, and this could not be found in SPOC mut cells, suggesting that SPEN has a SPOC domain independent role in regulating Xist RNA transcription. The idea that SPEN dampens Xist transcription in WT cells in a SPOC domain independent manner is somewhat counterintuitive, but may make sense in the context of the hypothesis that Xist RNA localisation regulates Xist transcription and/or degradation (Figure 39).

In agreement with a feedback mechanism between Xist transcription and degradation, RNA-SPLIT showed that Xist stability is dramatically decreased in SPEN RRM del cells during both expansion and steady state. Considering the earlier finding that Xist transcription rates determine Xist degradation rates, it can be proposed that deregulation of Xist transcription in SPEN RRM del cells caused an increase in Xist degradation. Further adding to the hypothesis that this feedback

mechanism might be dependent on *cis*-limited spreading of Xist across the Xi, SPOC mut cells did not show deregulated Xist kinetics.

The indications that *cis*-limited Xist RNA localisation and abundance might influence the above described feedback, make it tempting to speculate about its potential mechanism. For instance, a threshold abundance of *cis*-limited Xist RNPs could saturate Xist binding sites on the Xi, crowding the interchromatin channels. The decrease in available binding sites and/or the specific local concentration of Xist RNPs might initiate a dampening of Xist RNA transcription and increased degradation through a yet unknown molecular sensor. Interestingly, RNA-SPLIT experiments revealed that Xist RNA is degraded more readily at the periphery of the Xi territory. This might indicate that peripheral regions of the Xi territory may be more accessible for the degradation machinery. The finding that escapees, which retain access to the transcription machinery throughout XCI, are often found at the periphery of the Xi (Giorgetti et al. 2016), supports this proposition.

Recently, several sites of N6-Methyladenosine (m6A) deposition have been found in Xist RNA, and have been implicated in Xist-mediated silencing (Patil et al. 2016; Dominissini et al. 2012; Ke et al. 2015; Moindrot et al. 2015). The m6A modification has been widely associated with RNA stability (Yang Wang et al. 2014; X. Wang et al. 2014). Moreover, the m6A reader YTHDC1 has been shown to facilitate degradation of m6A-modified RNAs through the nuclear exosome (Liu et al. 2020). Therefore, it seems plausible to propose that the nuclear exosome is responsible for Xist RNA degradation at the periphery of the Xi territory. In the future, it would be interesting to know whether and how perturbation of the m6A machinery, for

instance by degradation of the N6-adenosine-methyltransferase 70 kDa subunit (METTL3), would influence Xist RNA kinetics.

To conclude, these results reveal that Xist transcription and degradation rates are interconnected by a novel promoter-independent feedback mechanism, which is dependent on the stage of XCI (Figure 39). A new, SPOC domain independent role of SPEN in the regulation of Xist RNA transcription, and hence stability as well as abundance, was identified, and CIZ-1 was implicated in the regulation of Xist kinetics in differentiated cells (Figure 39). Since deregulated Xist kinetics were observed exclusively in cellular backgrounds where *cis*-limited Xist localisation and/or spreading was found to be impaired, it may be possible that the tight regulation of Xist transcription and degradation rates is dependent on the Xi specific chromatin environment, as well as *cis*-limited Xist localisation (Figure 39). To establish causality of these different factors and how they relate to the newly identified feedback mechanism between Xist transcription and stability, it would be interesting to explore ways to artificially alter Xist localisation and stability separately. For instance, a recent study has found that incorporation of adenylate-uridylate-rich elements (AU-rich elements; AREs) into the 3'-UTR can decrease RNA stability (Koh, Porter, and Batchelor 2019), and another study has explored miRNA treatment to knock down Xist RNA (Yao et al. 2015).

6.4 Xist RNA spreading across the Xi

The aforementioned results have shown that Xist is highly dynamic, being constantly transcribed and rapidly degraded within hours. This is in line with FRAP experiments that have shown that Xist is very dynamic with recovery times of approximately 30 min (Ng et al. 2011). The fact that live cell 3D-SIM analysis fails to capture Xist RNA movements suggests that the rate of transport between bound sites is much faster than the frame rate in these experiments. Xist RAP experiments have shown that Xist spreading across the X chromosome is mainly correlated to Hi-C data, indicating that Xist spreads first from its transcription site to 3D proximal sites (Engreitz et al. 2013). RNA-SPLIT provides temporally resolved 3D localisation information, and thus enables different insights into Xist spreading.

The location of the Xist transcription site was approximated based on the density and fluorescence intensity of the signal from newly transcribed Xist RNA, and the distances that RNA molecules travelled from the transcription site in 3D over time were measured. In agreement with Engreitz et al (2013), newly transcribed Xist was found to spread in 3D from the transcription site towards the periphery of the Xi territory during expansion (Figure 40a). The finding that during expansion the range of newly synthesised Xist molecules relative to pre-synthesised Xist molecules increases over time, indicates either that saturation of nearby binding sites is required to open up further binding sites, or that individual Xist molecules move between chromatin binding sites in a series binding and unbinding events (Figure 40). The observation that Xist localised to the periphery of the Xist territory appears

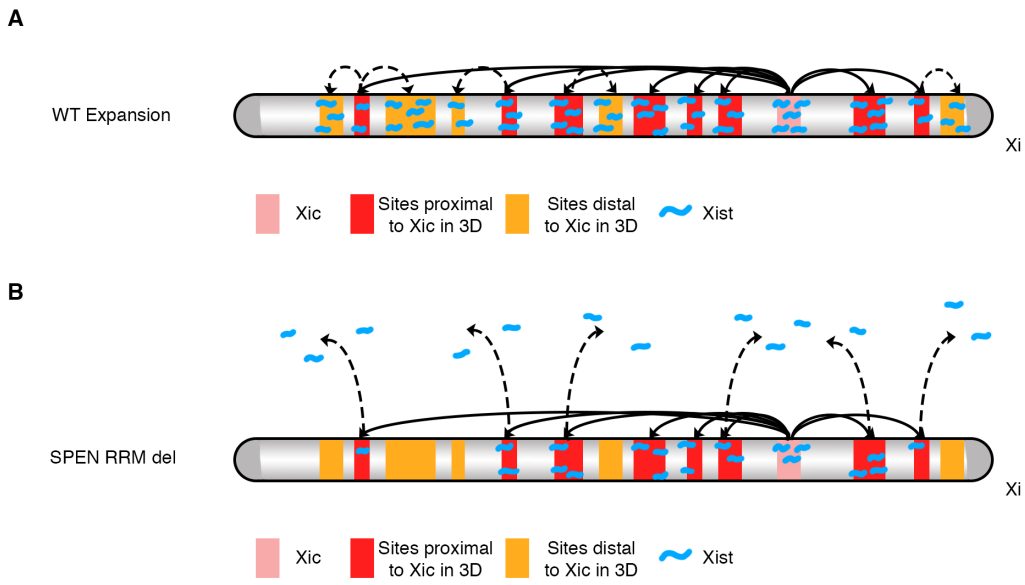

Figure 40: Model of Xist spreading in WT mESCs and upon perturbation of SPEN. A) Schematic illustrating Xist RNA spreading across the Xi in WT mESCs during expansion. B) Schematic illustrating Xist RNA spreading and localisation defect in SPEN RRM del cells.

to be degraded before centrally localised Xist, favours the latter interpretation. RNA-SPLIT did not show 3D Xist spreading during steady state, in line with CHART-seq experiments showing that Xist RNA spreads to all regions of the Xi without preference after locked nucleic acid treatment at later stages of XCI (Simon et al. 2013).

Considering the finding that the chromatin environment influences Xist RNA density and kinetics, it would be exciting in the future to explore whether chromatin remodellers such as cohesin and condensin play a role in Xist spreading behaviour, transcription and stability. Engreitz and colleagues found that the only factor they could correlate to Xist spreading was distance in 3D as indicated by Hi-C data (Engreitz et al. 2013), and the interactions of chromatin in 3D seen with Hi-C have been found to be highly dependent on cohesin (Schwarzer et al. 2017; Rao et al.

2017). This raises the question whether degradation of cohesin / condensin by, for instance, the dTAG degron system, just before Xist RNA induction would alter Xist RNA spreading. Preliminary RNA-SPLIT experiments, where cells were depleted of ATP after Xist RNA induction, have indicated that Xist might be dispersed under these conditions (data not shown). This might possibly point towards importance of the ATP dependent cohesin / condensin complexes in Xist RNA localisation behaviour.

As mentioned in section 6.2, RNA-SPLIT data as well as recent ChIP experiments in the lab using Polycomb histone modifications as a surrogate mark for Xist RNA spreading revealed a spreading defect in SPEN RRM del cells, but not in SPOC mut cells, uncovering a novel SPOC domain independent role of SPEN in Xist spreading (Figure 40b). This is in line with Xist RAP experiments by Engreitz et al. (2013), showing that Xist RNA with a deletion of the A-repeats, which are essential for SPEN binding to Xist RNA, fails to spread to active genes. Moreover, the RAP experiment was conducted 3 h after Xist induction, matching the timeframe of the previously described RNA-SPLIT and ChIP experiments. These results indicate that the Xist A-repeat deletion phenocopies the Xist RNA spreading and localisation defect seen in SPEN RRM del mESCs. That Xist spreading and localisation was found largely unaffected in SPOC mutant mESCs further implies that this is not because of the absence of Xist-mediated silencing. Interestingly coupling was also distinctly affected in SPEN RRM del cells and not in SPOC mutant cells, suggesting that coupling could be linked to the spreading of Xist RNA beyond initial 3D proximal sites (see below for further discussion of this point).

6.5 About the curious phenomenon of Xist coupling

RNA-SPLIT enabled the observation of a fascinating spatial colocalisation of individual newly synthesised with pre-synthesised Xist RNA molecules, referred to as coupling, which had not previously been described (Figure 41a). Quantification by NNA confirmed the curious phenomena of newly transcribed Xist coupling with previously bound Xist. Double-labelling of Xist with different HaloTag ligands was ruled out by a dual-colour control. Experiments employing a combination of HaloTag labelling and traditional RNA FISH labelling of Xist indicate that this was not seen previously because coupled Xist molecules are detected as one single Xist RNA FISH domain, even when visualised by super-resolution microscopy. Coupling was observed during both expansion and steady state phase, as well as in WT and autosomal transgene cells, suggesting that it is independent of the stage of XCI, chromosomal context, as well as accompanying changes in Xist stability and transcription rate. The predominant occurrence of coupled newly synthesised and pre-synthesised, as opposed to coupled newly synthesised or coupled pre-synthesised Xist RNA molecules, indicates that newly synthesised molecules do not couple as soon as they are transcribed and search for chromatin binding sites in couplets, but rather that coupling happens at the chromatin binding site, which has been marked by an existing molecule (Figure 41a).

RNA-SPLIT experiments followed by NNA show that coupling is unaffected in Ciz-1 KO mESCs and NPCs, in the latter case despite Xist being extensively delocalised. These findings suggest that Xist coupling is not a result of Xist crowding in the interchromatin channels of a given chromosome, or due to localisation to

specific binding sites on the Xi. Instead, it can only be explained either by a secondary factor present only at the binding site, or by a conformational/ biophysical change of Xist that occurs upon binding to chromatin. Indeed, analysis of the SPEN RRM del and SPOC mut cells showed that coupling is dependent on SPEN (Figure 41b). Thus, quantification of Xist coupling by NNA of the RNA-SPLIT showed that Xist coupling was disrupted in SPEN RRM del cells independently of the stage of XCI. In contrast, Xist coupling was found to be generally intact in SPOC mut cells, establishing that SPEN's function in Xist coupling is SPOC domain independent. The results also revealed that the Xist coupling defect in SPEN RRM del cells intensifies with the progression of XCI from expansion to steady state. Hence, it can be recognised that Xist coupling is a phenomenon independent of CIZ-1, stage of XCI and Xist localisation *in cis*, which is likely mediated by SPEN in a SPOC domain independent manner (Figure 41). While perturbation of SPEN abrogated Xist coupling, it also affected Xist localisation and kinetics, and as a result it is not straightforward to establish causality.

Since the above described results in Ciz-1 KO NPCs indicate that Xist coupling behaviour is independent of Xist localisation to the Xi, the novel role of SPEN in Xist coupling is separable from its role in Xist localisation and dynamics. Here, SPEN could either facilitate Xist coupling directly by association/dimerization of SPEN proteins bound to different Xist molecules, or indirectly by altering the conformation or biophysical properties of Xist (Figure 41). In the context of temporally separated coupling of Xist molecules, the latter seems more probable, since dimerization, for instance, would more likely take place before Xist binding to the chromatin.

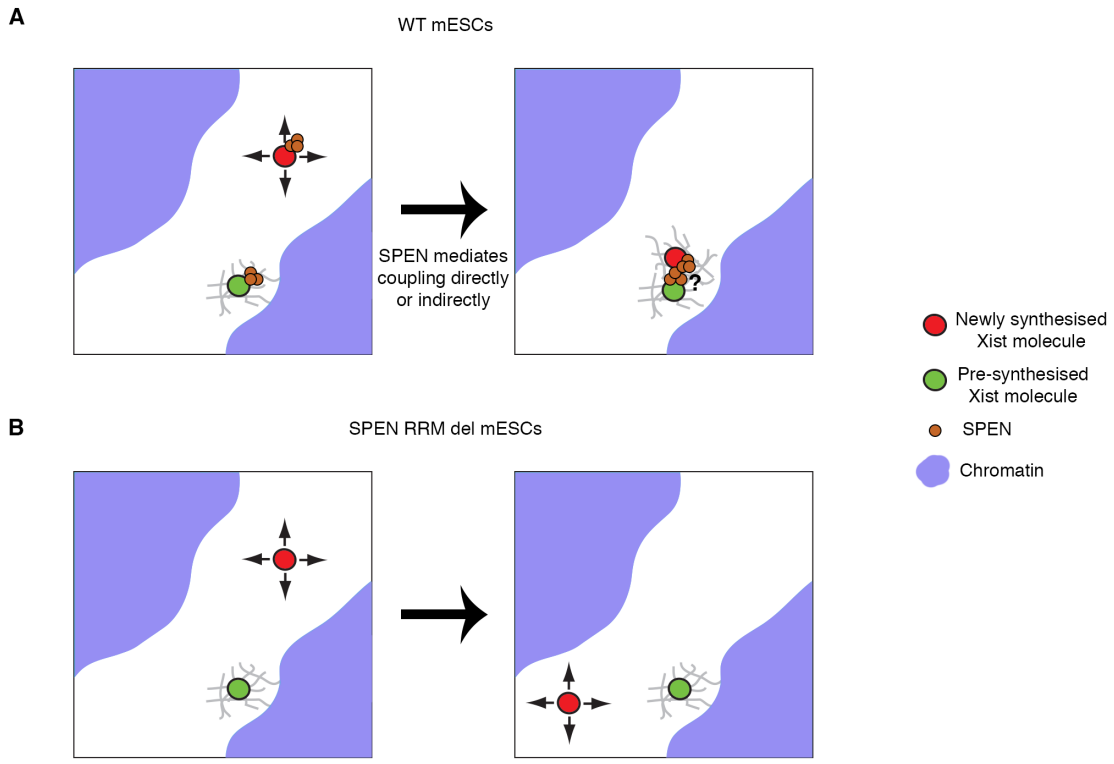

Figure 41: Model of coupling of newly synthesised and pre-synthesised Xist molecules. A) Schematic illustrating Xist RNA coupling in WT mESCs facilitated by SPEN. B)) Schematic illustrating Xist RNA coupling defect in SPEN RRM del mESCs.

Moreover, SPEN constitutes a large part of the Xist RNP and may thus influence its integrity and/or biophysical properties, as well as the secondary structure of Xist RNA itself, which all might be required for Xist coupling. In addition, the Xist A-repeats harbour several potential binding sites for SPEN and up to four SPEN molecules could bind a single Xist molecule at any given time (Lu et al. 2016) (Figure 41a), increasing the likelihood that the presence or absence of SPEN binding to Xist might have a major impact on the biophysical properties and conformation of Xist. In addition, Rbm15, which is essential for the recruitment of the m6A RNA methyltransferase complex to Xist RNA (Ariyoshi and Schwabe 2003; Moindrot et al. 2015; Lu et al. 2016), shares binding sites with SPEN in the Xist A-

repeat, making it possible that in the absence of SPEN, Rbm15 binding to Xist RNA would increase, further altering the properties of the Xist RNP.

The discovery of SPEN dependent Xist coupling raises the question of what the biological function of this unique phenomenon is. As described in section 6.4, there might be a link between coupling and spreading beyond initial 3D proximal sites, since SPEN RRM del cells show a distinct SPOC domain independent defect in Xist spreading and coupling. Although the results in Ciz-1 KO NPCs have shown that coupling is not dependent on *cis*-limited Xist localisation, an absence of coupling could still cause dispersal of Xist from the Xi, as seen in SPEN RRM del cells. Another striking observation is the temporal aspect of coupling with newly synthesized Xist RNA localising to pre-synthesized Xist RNA. This might indicate that the previously bound Xist RNPs mark Xist anchoring sites, and therefore help direct newly synthesized Xist RNA molecules to specific chromatin regions. One might speculate that there could be a 'handover' like mechanism, where newly synthesized Xist RNPs localise to previously occupied sites, freeing up the pre-synthesised Xist RNP to move to a new binding site, before another Xist RNP can bind etc.

In order to study coupling and its function in the future, one might hope to perturb Xist coupling in a more targeted fashion. One approach would be to identify which domains of SPEN are essential for Xist coupling, for example using a deletional analysis by CRISPR/Cas9-mediated genome editing, or to use different minimal rescue constructs in SPEN RRM del cells to potentially rescue coupling. The identification of the responsible SPEN domain might then give an indication as to

whether SPEN facilitates coupling directly or indirectly. A finding that no specific domain can be implicated in coupling would speak for the latter.

Other protein factors or specific regions of Xist RNA itself might be involved in facilitating coupling. Therefore it would be interesting to perform a large scale deletional analysis of Xist RNA, as well as perturbation of different known XCI factors in the future. Here, a single timepoint of an RNA-SPLIT experiment could be sufficient to establish whether coupling is affected in different mutant cells in order to decrease workload. One could also consider artificially coupling Xist, e.g. by expressing two molecules of transgenic Xist connected by a linker. This would couple newly synthesised Xist RNA molecules instead of newly and pre-synthesised Xist molecules and could therefore help to further examine the temporal aspect of Xist coupling.

In summary further studies are required both to determine the molecular basis of Xist coupling and its functional significance. Further application of RNA-SPLIT will play an important role in achieving these aims.

References

Ainscough, Justin F.X., Faisal Abdel Rahman, Heather Sercombe, Alicia Sedo, Bjorn Gerlach, and Dawn Coverley. 2007. “C-Terminal Domains Deliver the DNA Replication Factor Ciz1 to the Nuclear Matrix.” *Journal of Cell Science*. https://doi.org/10.1242/jcs.03327.

Allderdice, P. W., O. J. Miller, D. A. Miller, and H. P. Klinger. 1978. “Spreading of Inactivation in an (X;14) Translocation.” *American Journal of Medical Genetics*. https://doi.org/10.1002/ajmg.1320020304.

Ariyoshi, Mariko, and John W.R. Schwabe. 2003. “A Conserved Structural Motif Reveals the Essential Transcriptional Repression Function of Spen Proteins and Their Role in Developmental Signaling.” *Genes and Development*. https://doi.org/10.1101/gad.266203.

Avner, P, and E Heard. 2001. “X-Chromosome Inactivation: Counting, Choice and Initiation.” *Nat Rev Genet* 2 (1): 59–67. https://doi.org/10.1038/35047580.

Aymerich, S., and M. Steinmetz. 1992. “Specificity Determinants and Structural Features in the RNA Target of the Bacterial Antiterminator Proteins of the BglG/SacY Family.” *Proceedings of the National Academy of Sciences of the United States of America*. https://doi.org/10.1073/pnas.89.21.10410.

Ball, Graeme, Justin Demmerle, Rainer Kaufmann, Ilan Davis, Ian M. Dobbie, and Lothar Schermelleh. 2015. “SIMcheck: A Toolbox for Successful Super-Resolution Structured Illumination Microscopy.” *Scientific Reports*. https://doi.org/10.1038/srep15915.

Barakat, Tahsin Stefan, Friedemann Loos, Selma Van Staveren, Elvira Myronova,

Mehrnaz Ghazvini, J. Anton Grootegoed, and Joost Gribnau. 2014. “The Trans-Activator RNF12 and Cis-Acting Elements Effectuate X Chromosome Inactivation Independent of X-Pairing.” *Molecular Cell* 53 (6): 965–78. https://doi.org/10.1016/j.molcel.2014.02.006.

Barr, Murray L., and Ewart G. Bertram. 1949. “A Morphological Distinction between Neurones of the Male and Female, and the Behaviour of the Nucleolar Satellite during Accelerated Nucleoprotein Synthesis [2].” *Nature*. https://doi.org/10.1038/163676a0.

Bauman, J. G.J., J. Wiegant, P. Borst, and P. van Duijn. 1980. “A New Method for Fluorescence Microscopical Localization of Specific DNA Sequences by in Situ Hybridization of Fluorochrome-Labelled RNA.” *Experimental Cell Research*. https://doi.org/10.1016/0014-4827(80)90087-7.

Beach, Dale L., E. D. Salmon, and Kerry Bloom. 1999. “Localization and Anchoring of MRNA in Budding Yeast.” *Current Biology*. https://doi.org/10.1016/S0960-9822(99)80260-7.

Beletskii, Anton, Young Kwon Hong, John Pehrson, Michael Egholm, and William M. Strauss. 2001. “PNA Interference Mapping Demonstrates Functional Domains in the Noncoding RNA Xist.” *Proceedings of the National Academy of Sciences of the United States of America*. https://doi.org/10.1073/pnas.161173098.

Belyaev, Nikolai D., Ann M. Keohane, and Bryan M. Turner. 1996. “Differential Underacetylation of Histones H2A, H3 and H4 on the Inactive X Chromosome in Human Female Cells.” *Human Genetics*. https://doi.org/10.1007/BF02281863.

Bemmel, Joke G. van, Rafael Galupa, Chris Gard, Nicolas Servant, Christel Picard, James Davies, Anthony James Szempruch, et al. 2019. “The Bipartite TAD

Organization of the X-Inactivation Center Ensures Opposing Developmental Regulation of Tsix and Xist." *Nature Genetics*. https://doi.org/10.1038/s41588-019-0412-0.

Berletch, Joel B., Wenxiu Ma, Fan Yang, Jay Shendure, William S. Noble, Christine M. Disteche, and Xinxian Deng. 2015. "Escape from X Inactivation Varies in Mouse Tissues." *PLoS Genetics*. https://doi.org/10.1371/journal.pgen.1005079.

Bertrand, Edouard, Pascal Chartrand, Matthias Schaefer, Shailesh M. Shenoy, Robert H. Singer, and Roy M. Long. 1998. "Localization of ASH1 MRNA Particles in Living Yeast." *Molecular Cell*. https://doi.org/10.1016/S1097-2765(00)80143-4.

Bhaskara, Srividya, Sarah K. Knutson, Guochun Jiang, Mahesh B. Chandrasekharan, Andrew J. Wilson, Siyuan Zheng, Ashwini Yenamandra, et al. 2010. "Hdac3 Is Essential for the Maintenance of Chromatin Structure and Genome Stability." *Cancer Cell*. https://doi.org/10.1016/j.ccr.2010.10.022.

Blewitt, Marnie E., Anne Valerie Gendrel, Zhenyi Pang, Duncan B. Sparrow, Nadia Whitelaw, Jeffrey M. Craig, Anwyn Apedaile, et al. 2008. "SmcHD1, Containing a Structural-Maintenance-of-Chromosomes Hinge Domain, Has a Critical Role in X Inactivation." *Nature Genetics*. https://doi.org/10.1038/ng.142.

Boettiger, Alistair N., Bogdan Bintu, Jeffrey R. Moffitt, Siyuan Wang, Brian J. Beliveau, Geoffrey Fudenberg, Maxim Imakaev, Leonid A. Mirny, Chao Ting Wu, and Xiaowei Zhuang. 2016. "Super-Resolution Imaging Reveals Distinct Chromatin Folding for Different Epigenetic States." *Nature*. https://doi.org/10.1038/nature16496.

Borsani, Giuseppe, Rossana Tonlorenzi, M. Christine Simmler, Luisa Dandolo, Danielle Arnaud, Valeria Capra, Markus Grompe, et al. 1991. "Characterization of a Murine Gene Expressed from the Inactive X Chromosome." *Nature*.

https://doi.org/10.1038/351325a0.

Bousard, Aurélie, Ana Cláudia Raposo, Jan Jakub Żylicz, Christel Picard, Vanessa Borges Pires, Yanyan Qi, Cláudia Gil, et al. 2019. " The Role of Xist -mediated Polycomb Recruitment in the Initiation of X-chromosome Inactivation ." *EMBO Reports*. https://doi.org/10.15252/embr.201948019.

Brideau, Nicholas J, Heather Coker, Anne-Valerie Gendrel, C Alistair Siebert, Karel Bezstarosti, Jeroen Demmers, Raymond A Poot, Tatyana B Nesterova, and Neil Brockdorff. 2015. "Independent Mechanisms Target SMCHD1 to Trimethylated Histone H3 Lysine 9-Modified Chromatin and the Inactive X Chromosome." *Molecular and Cellular Biology* 35 (23): 4053–68. https://doi.org/10.1128/MCB.00432-15.

Brockdorff, Neil. 2019. "Localized Accumulation of Xist RNA in X Chromosome Inactivation." *Open Biology*. https://doi.org/10.1098/rsob.190213.

Brockdorff, Neil, Alan Ashworth, Graham F. Kay, Penny Cooper, Sandy Smith, Veronica M. McCabe, Dominic P. Norris, Graeme D. Penny, Dipika Patel, and Sohaila Rastan. 1991. "Conservation of Position and Exclusive Expression of Mouse Xist from the Inactive X Chromosome." *Nature*. https://doi.org/10.1038/351329a0.

Brockdorff, Neil, Alan Ashworth, Graham F. Kay, Veronica M. McCabe, Dominic P. Norris, Penny J. Cooper, Sally Swift, and Sohaila Rastan. 1992. "The Product of the Mouse Xist Gene Is a 15 Kb Inactive X-Specific Transcript Containing No Conserved ORF and Located in the Nucleus." *Cell* 71 (3): 515–26. https://doi.org/10.1016/0092-8674(92)90519-I.

Brockdorff, Neil, Joseph S. Bowness, and Guifeng Wei. 2020. "Progress toward Understanding Chromosome Silencing by Xist RNA." *Genes & Development*.

https://doi.org/10.1101/gad.337196.120.

Brockdorff, Neil, and Bryan M. Turner. 2015. “Dosage Compensation in Mammals.” *Cold Spring Harbor Perspectives in Biology*. https://doi.org/10.1101/cshperspect.a019406.

Brown, Carolyn J., Andrea Ballabio, James L. Rupert, Ronald G. Lafreniere, Markus Grompe, Rossana Tonlorenzi, and Huntington F. Willard. 1991. “A Gene from the Region of the Human X Inactivation Centre Is Expressed Exclusively from the Inactive X Chromosome.” *Nature*. https://doi.org/10.1038/349038a0.

Brown, Carolyn J., Brian D. Hendrich, Jim L. Rupert, Ronald G. Lafrenière, Yigong Xing, Jeanne Lawrence, and Huntington F. Willard. 1992. “The Human XIST Gene: Analysis of a 17 Kb Inactive X-Specific RNA That Contains Conserved Repeats and Is Highly Localized within the Nucleus.” *Cell* 71 (3): 527–42. https://doi.org/10.1016/0092-8674(92)90520-M.

Brown, Jill M., Nigel A. Roberts, Bryony Graham, Dominic Waithe, Christoffer Lagerholm, Jelena M. Telenius, Sara De Ornellas, et al. 2018. “A Tissue-Specific Self-Interacting Chromatin Domain Forms Independently of Enhancer-Promoter Interactions.” *Nature Communications*. https://doi.org/10.1038/s41467-018-06248-4.

Brown, Stephen D.M. 1991. “XIST and the Mapping of the X Chromosome Inactivation Centre.” *BioEssays*. https://doi.org/10.1002/bies.950131112.

Buzin, Carolyn H., Jeffrey R. Mann, and Judith Singer-Sam. 1994. “Quantitative RT-PCR Assays Show Xist RNA Levels Are Low in Mouse Female Adult Tissue, Embryos and Embryoid Bodies.” *Development*.

Cawte, Adam D., Peter J. Unrau, and David S. Rueda. 2020. “Live Cell Imaging of Single RNA Molecules with Fluorogenic Mango II Arrays.” *Nature Communications*.

https://doi.org/10.1038/s41467-020-14932-7.

Chadwick, Brian P. 2008. “DXZ4 Chromatin Adopts an Opposing Conformation to That of the Surrounding Chromosome and Acquires a Novel Inactive X-Specific Role Involving CTCF and Antisense Transcripts.” *Genome Research*. https://doi.org/10.1101/gr.075713.107.

Chaumeil, Julie, Patricia Le Baccon, Anton Wutz, and Edith Heard. 2006. “A Novel Role for Xist RNA in the Formation of a Repressive Nuclear Compartment into Which Genes Are Recruited When Silenced.” *Genes and Development*. https://doi.org/10.1101/gad.380906.

Chen, C.-K., M. Blanco, C. Jackson, E. Aznauryan, N. Ollikainen, C. Surka, A. Chow, A. Cerase, P. McDonel, and M. Guttman. 2016. “Xist Recruits the X Chromosome to the Nuclear Lamina to Enable Chromosome-Wide Silencing.” *Science* 354 (6311): 468–72. https://doi.org/10.1126/science.aae0047.

Chen, Jianbo, Olga Nikolaitchik, Jatinder Singh, Andrew Wright, Craig E. Bencsics, John M. Coffin, Na Ni, Stephen Lockett, Vinay K. Pathak, and Wei Shau Hu. 2009. “High Efficiency of HIV-1 Genomic RNA Packaging and Heterozygote Formation Revealed by Single Virion Analysis.” *Proceedings of the National Academy of Sciences of the United States of America*. https://doi.org/10.1073/pnas.0906822106.

Chen, Mingming, Zhao Ma, Xiaotian Wu, Shiqi Mao, Yantao Yang, Jie Tan, Christopher J. Krueger, and Antony K. Chen. 2017. “A Molecular Beacon-Based Approach for Live-Cell Imaging of RNA Transcripts with Minimal Target Engineering at the Single-Molecule Level.” *Scientific Reports*. https://doi.org/10.1038/s41598-017-01740-1.

Chow, Jennifer C., Constance Ciaudo, Melissa J. Fazzari, Nathan Mise, Nicolas Servant, Jacob L. Glass, Matthew Attreed, et al. 2010. “LINE-1 Activity in Facultative

Heterochromatin Formation during X Chromosome Inactivation." *Cell*. https://doi.org/10.1016/j.cell.2010.04.042.

Chu, Ci, Qiangfeng Cliff Zhang, Simão Teixeira Da Rocha, Ryan A. Flynn, Maheetha Bharadwaj, J. Mauro Calabrese, Terry Magnuson, Edith Heard, and Howard Y. Chang. 2015. "Systematic Discovery of Xist RNA Binding Proteins." *Cell* 161 (2): 404–16. https://doi.org/10.1016/j.cell.2015.03.025.

Chureau, Corinne, Sophie Chantalat, Antonio Romito, Angélique Galvani, Laurent Duret, Philip Avner, and Claire Rougeulle. 2011. "Ftx Is a Non-Coding RNA Which Affects Xist Expression and Chromatin Structure within the X-Inactivation Center Region." *Human Molecular Genetics*. https://doi.org/10.1093/hmg/ddq516.

Cirillo, Davide, Mario Blanco, Alexandros Armaos, Andreas Buness, Philip Avner, Mitchell Guttman, Andrea Cerase, and Gian Gaetano Tartaglia. 2016. "Quantitative Predictions of Protein Interactions with Long Noncoding RNAs: To the Editor." *Nature Methods*. https://doi.org/10.1038/nmeth.4100.

Clemson, Christine Moulton, John A. McNeil, Huntington F. Willard, and Jeanne Bentley Lawrence. 1996. "XIST RNA Paints the Inactive X Chromosome at Interphase: Evidence for a Novel RNA Involved in Nuclear/Chromosome Structure." *Journal of Cell Biology*. https://doi.org/10.1083/jcb.132.3.259.

Cohen, Dena E., Lance S. Davidow, Jennifer A. Erwin, Na Xu, David Warshawsky, and Jeannie T. Lee. 2007. "The DXPas34 Repeat Regulates Random and Imprinted X Inactivation." *Developmental Cell*. https://doi.org/10.1016/j.devcel.2006.11.014.

Colognori, David, Hongjae Sunwoo, Andrea J. Kriz, Chen Yu Wang, and Jeannie T. Lee. 2019. "Xist Deletional Analysis Reveals an Interdependency between Xist RNA and Polycomb Complexes for Spreading along the Inactive X." *Molecular Cell*.

https://doi.org/10.1016/j.molcel.2019.01.015.

Conti, Luciano, Steven M. Pollard, Thorsten Gorba, Erika Reitano, Mauro Toselli, Gerardo Biella, Yirui Sun, et al. 2005. “Niche-Independent Symmetrical Self-Renewal of a Mammalian Tissue Stem Cell.” *PLoS Biology*. https://doi.org/10.1371/journal.pbio.0030283.

Copeland, Nikki A., Heather E. Sercombe, Justin F.X. Ainscough, and Dawn Coverley. 2010. “Ciz1 Cooperates with Cyclin-A-CDK2 to Activate Mammalian DNA Replication in Vitro.” *Journal of Cell Science*. https://doi.org/10.1242/jcs.059345.

Copeland, Nikki A., Heather E. Sercombe, Rosemary H.C. Wilson, and Dawn Coverley. 2015. “Cyclin-A-CDK2-Mediated Phosphorylation of CIZ1 Blocks Replisome Formation and Initiation of Mammalian DNA Replication.” *Journal of Cell Science*. https://doi.org/10.1242/jcs.161919.

Costanzi, Carl, Paula Stein, Diane M. Worrad, Richard M. Schultz, and John R. Pehrson. 2000. “Histone MacroH2A1 Is Concentrated in the Inactive X Chromosome of Female Preimplantation Mouse Embryos.” *Development*.

Coverley, Dawn, Jackie Marr, and Justin Ainscough. 2005. “Ciz1 Promotes Mammalian DNA Replication.” *Journal of Cell Science*. https://doi.org/10.1242/jcs.01599.

Csankovszki, Györgyi, András Nagy, and Rudolf Jaenisch. 2001. “Synergism of Xist RNA, DNA Methylation, and Histone Hypoacetylation in Maintaining X Chromosome Inactivation.” *Journal of Cell Biology*. https://doi.org/10.1083/jcb.153.4.773.

Daigle, Nathalie, and Jan Ellenberg. 2007. “ΛN-GFP: An RNA Reporter System for Live-Cell Imaging.” *Nature Methods*. https://doi.org/10.1038/nmeth1065.

Darrow, Emily M., Miriam H. Huntley, Olga Dudchenko, Elena K. Stamenova, Neva C.

Durand, Zhuo Sun, Su Chen Huang, et al. 2016. “Deletion of DXZ4 on the Human Inactive X Chromosome Alters Higher-Order Genome Architecture.” *Proceedings of the National Academy of Sciences of the United States of America*. https://doi.org/10.1073/pnas.1609643113.

Debrand, E., C. Chureau, D. Arnaud, P. Avner, and E. Heard. 1999. “Functional Analysis of the DXPas34Locus, a 3′ Regulator of Xist Expression.” *Molecular and Cellular Biology*. https://doi.org/10.1128/mcb.19.12.8513.

Deng, Xinxian, Wenxiu Ma, Vijay Ramani, Andrew Hill, Fan Yang, Ferhat Ay, Joel B. Berletch, et al. 2015. “Bipartite Structure of the Inactive Mouse X Chromosome.” *Genome Biology*. https://doi.org/10.1186/s13059-015-0728-8.

Disteche, Christine M. 2012. “Dosage Compensation of the Sex Chromosomes.” *Annual Review of Genetics*. https://doi.org/10.1146/annurev-genet-110711-155454.

Dobin, Alexander, Carrie A. Davis, Felix Schlesinger, Jorg Drenkow, Chris Zaleski, Sonali Jha, Philippe Batut, Mark Chaisson, and Thomas R. Gingeras. 2013. “STAR: Ultrafast Universal RNA-Seq Aligner.” *Bioinformatics*. https://doi.org/10.1093/bioinformatics/bts635.

Dolgosheina, Elena V., Sunny C.Y. Jeng, Shanker Shyam S. Panchapakesan, Razvan Cojocaru, Patrick S.K. Chen, Peter D. Wilson, Nancy Hawkins, Paul A. Wiggins, and Peter J. Unrau. 2014. “RNA Mango Aptamer-Fluorophore: A Bright, High-Affinity Complex for RNA Labeling and Tracking.” *ACS Chemical Biology*. https://doi.org/10.1021/cb500499x.

Dominissini, Dan, Sharon Moshitch-Moshkovitz, Schraga Schwartz, Mali Salmon-Divon, Lior Ungar, Sivan Osenberg, Karen Cesarkas, et al. 2012. “Topology of the Human and Mouse M6A RNA Methylomes Revealed by M6A-Seq.” *Nature*.

https://doi.org/10.1038/nature11112.

Dossin, François, Inês Pinheiro, Jan J. Żylicz, Julia Roensch, Samuel Collombet, Agnès Le Saux, Tomasz Chelmicki, et al. 2020. “SPEN Integrates Transcriptional and Epigenetic Control of X-Inactivation.” *Nature*. https://doi.org/10.1038/s41586-020-1974-9.

Duthie, Sarah M., Tatyana B. Nesterova, Emma J. Formstone, Ann M. Keohane, Bryan M. Turner, Suren M. Zakian, and Neil Brockdorff. 1999. “Xist RNA Exhibits a Banded Localization on the Inactive X Chromosome and Is Excluded from Autosomal Material in Cis.” *Human Molecular Genetics* 8 (2): 195–204. https://doi.org/10.1093/hmg/8.2.195.

Ellington, Andrew D., and Jack W. Szostak. 1990. “In Vitro Selection of RNA Molecules That Bind Specific Ligands.” *Nature*. https://doi.org/10.1038/346818a0.

Engreitz, J. M., A. Pandya-Jones, P. McDonel, A. Shishkin, K. Sirokman, C. Surka, S. Kadri, et al. 2013. “The Xist LncRNA Exploits Three-Dimensional Genome Architecture to Spread Across the X Chromosome.” *Science* 341 (6147): 1237973–1237973. https://doi.org/10.1126/science.1237973.

Filonov, Grigory S., Jared D. Moon, Nina Svensen, and Samie R. Jaffrey. 2014. “Broccoli: Rapid Selection of an RNA Mimic of Green Fluorescent Protein by Fluorescence-Based Selection and Directed Evolution.” *Journal of the American Chemical Society*. https://doi.org/10.1021/ja508478x.

Franco, Brunella, and Andrea Ballabio. 2006. “X-Inactivation and Human Disease: X-Linked Dominant Male-Lethal Disorders.” *Current Opinion in Genetics and Development*. https://doi.org/10.1016/j.gde.2006.04.012.

Gall, J. G., and M. L. Pardue. 1969. “Formation and Detection of RNA-DNA Hybrid Molecules in Cytological Preparations.” *Proceedings of the National Academy of Sciences of the United States of America*. https://doi.org/10.1073/pnas.63.2.378.

Galupa, Rafael, Elphège Pierre Nora, Rebecca Worsley-Hunt, Christel Picard, Chris Gard, Joke Gerarda van Bemmel, Nicolas Servant, et al. 2020. “A Conserved Noncoding Locus Regulates Random Monoallelic Xist Expression across a Topological Boundary.” *Molecular Cell*. https://doi.org/10.1016/j.molcel.2019.10.030.

Garcia, Jennifer F., and Roy Parker. 2016. “Ubiquitous Accumulation of 3′ MRNA Decay Fragments in Saccharomyces Cerevisiae MRNAs with Chromosomally Integrated MS2 Arrays.” *RNA*. https://doi.org/10.1261/rna.056325.116.

Gdula, Michal R., Tatyana B. Nesterova, Greta Pintacuda, Jonathan Godwin, Ye Zhan, Hakan Ozadam, Michael McClellan, et al. 2019. “The Non-Canonical SMC Protein SmcHD1 Antagonises TAD Formation and Compartmentalisation on the Inactive X Chromosome.” *Nature Communications*. https://doi.org/10.1038/s41467-018-07907-2.

Gendrel, Anne-Valerie, Y. Amy Tang, Masako Suzuki, Jonathan Godwin, Tatyana B. Nesterova, John M. Greally, Edith Heard, and Neil Brockdorff. 2013. “Epigenetic Functions of Smchd1 Repress Gene Clusters on the Inactive X Chromosome and on Autosomes.” *Molecular and Cellular Biology* 33 (16): 3150–65. https://doi.org/10.1128/MCB.00145-13.

Gilbert, C. W., S. Muldal, L. G. Lajtha, and Janet Rowley. 1962. “Time-Sequence of Human Chromosome Duplication.” *Nature*. https://doi.org/10.1038/195869a0.

Giorgetti, Luca, Bryan R. Lajoie, Ava C. Carter, Mikael Attia, Ye Zhan, Jin Xu, Chong Jian Chen, et al. 2016. “Structural Organization of the Inactive X Chromosome in the

Mouse." *Nature* 535 (7613): 575–79. https://doi.org/10.1038/nature18589.

Gontan, Cristina, Eskeatnaf Mulugeta Achame, Jeroen Demmers, Tahsin Stefan Barakat, Eveline Rentmeester, Wilfred Van Ijcken, J. Anton Grootegoed, and Joost Gribnau. 2012. "RNF12 Initiates X-Chromosome Inactivation by Targeting REX1 for Degradation." *Nature*. https://doi.org/10.1038/nature11070.

Grate, Dilara, and Charles Wilson. 1999. "Laser-Mediated, Site-Specific Inactivation of RNA Transcripts." *Proceedings of the National Academy of Sciences of the United States of America*. https://doi.org/10.1073/pnas.96.11.6131.

Graves, Jennifer A.Marshall. 2016. "Evolution of Vertebrate Sex Chromosomes and Dosage Compensation." *Nature Reviews Genetics*. https://doi.org/10.1038/nrg.2015.2.

Grimm, Jonathan B., Anand K. Muthusamy, Yajie Liang, Timothy A. Brown, William C. Lemon, Ronak Patel, Rongwen Lu, et al. 2017. "A General Method to Fine-Tune Fluorophores for Live-Cell and in Vivo Imaging." *Nature Methods*. https://doi.org/10.1038/nmeth.4403.

Grünwald, David, Robert H. Singer, and Michael Rout. 2011. "Nuclear Export Dynamics of RNA-"protein Complexes." *Nature*. https://doi.org/10.1038/nature10318.

Guenther, Matthew G., Orr Barak, and Mitchell A. Lazar. 2001. "The SMRT and N-CoR Corepressors Are Activating Cofactors for Histone Deacetylase 3." *Molecular and Cellular Biology*. https://doi.org/10.1128/mcb.21.18.6091-6101.2001.

Ha, Norbert, Lan Tian Lai, Rosi Chelliah, Yashu Zhen, Seet Pei Yi Vanessa, Soak Kuan Lai, Hoi Yeung Li, et al. 2018. "Live-Cell Imaging and Functional Dissection of Xist RNA Reveal Mechanisms of X Chromosome Inactivation and Reactivation."

IScience. https://doi.org/10.1016/j.isci.2018.09.007.

Harrison, P. R., D. Conkie, J. Paul, and K. Jones. 1973. “Localisation of Cellular Globin Messenger RNA by in Situ Hybridisation to Complementary DNA.” *FEBS Letters*. https://doi.org/10.1016/0014-5793(73)80749-5.

Hasegawa, Yuko, Neil Brockdorff, Shinji Kawano, Kimiko Tsutui, Ken Tsutui, and Shinichi Nakagawa. 2010. “The Matrix Protein HnRNP U Is Required for Chromosomal Localization of Xist RNA.” *Developmental Cell*. https://doi.org/10.1016/j.devcel.2010.08.006.

Heard, Edith, Claire Rougeulle, Danielle Arnaud, Philip Avner, C. David Allis, and David L. Spector. 2001. “Methylation of Histone H3 at Lys-9 Is an Early Mark on the X Chromosome during X Inactivation.” *Cell*. https://doi.org/10.1016/S0092-8674(01)00598-0.

Heinrich, Stephanie, Corinne L. Sidler, Claus M. Azzalin, and Karsten Weis. 2017. “Stem-Loop RNA Labeling Can Affect Nuclear and Cytoplasmic MRNA Processing.” *RNA*. https://doi.org/10.1261/rna.057786.116.

Helbig, Roger, and Frank O. Fackelmayer. 2003. “Scaffold Attachment Factor A (SAF-A) Is Concentrated in Inactive X Chromosoe Territories through Its RGG Domain.” *Chromosoma*. https://doi.org/10.1007/s00412-003-0258-0.

Herzog, Veronika A., Brian Reichholf, Tobias Neumann, Philipp Rescheneder, Pooja Bhat, Thomas R. Burkard, Wiebke Wlotzka, Arndt Von Haeseler, Johannes Zuber, and Stefan L. Ameres. 2017. “Thiol-Linked Alkylation of RNA to Assess Expression Dynamics.” *Nature Methods*. https://doi.org/10.1038/nmeth.4435.

Higgins, Gillian, Katherine M. Roper, Irene J. Watson, Fiona H. Blackhall, William N. Rom,

Harvey I. Pass, Justin F.X. Ainscough, and Dawn Coverley. 2012. “Variant Ciz1 Is a Circulating Biomarker for Early-Stage Lung Cancer.” *Proceedings of the National Academy of Sciences of the United States of America*. https://doi.org/10.1073/pnas.1210107109.

Hollander, Petra Den, Suresh K. Rayala, Dawn Coverley, and Rakesh Kumar. 2006. “Ciz1, a Novel DNA-Binding Coactivator of the Estrogen Receptor α, Confers Hypersensitivity to Estrogen Action.” *Cancer Research*. https://doi.org/10.1158/0008-5472.CAN-06-2336.

Horakova, Andrea H., J. Mauro Calabrese, Christine R. McLaughlin, Deanna C. Tremblay, Terry Magnuson, and Brian P. Chadwick. 2012. “The Mouse DXZ4 Homolog Retains Ctcf Binding and Proximity to Pls3 despite Substantial Organizational Differences Compared to the Primate Macrosatellite.” *Genome Biology*. https://doi.org/10.1186/gb-2012-13-8-r70.

Jansz, Natasha, Tatyana Nesterova, Andrew Keniry, Megan Iminitoff, Peter F. Hickey, Greta Pintacuda, Osamu Masui, et al. 2018. “Smchd1 Targeting to the Inactive X Is Dependent on the Xist-HnrnpK-PRC1 Pathway.” *Cell Reports*. https://doi.org/10.1016/j.celrep.2018.10.044.

Jeon, Yesu, and Jeannie T. Lee. 2011. “YY1 Tethers Xist RNA to the Inactive X Nucleation Center.” *Cell*. https://doi.org/10.1016/j.cell.2011.06.026.

Jeppesen, Peter, and Bryan M. Turner. 1993. “The Inactive X Chromosome in Female Mammals Is Distinguished by a Lack of Histone H4 Acetylation, a Cytogenetic Marker for Gene Expression.” *Cell*. https://doi.org/10.1016/0092-8674(93)90419-Q.

Jonkers, Iris, Tahsin Stefan Barakat, Eskeatnaf Mulugeta Achame, Kim Monkhorst, Annegien Kenter, Eveline Rentmeester, Frank Grosveld, J. Anton Grootegoed, and

Joost Gribnau. 2009. “RNF12 Is an X-Encoded Dose-Dependent Activator of X Chromosome Inactivation.” *Cell* 139 (5): 999–1011. https://doi.org/10.1016/j.cell.2009.10.034.

Jonkers, Iris, Kim Monkhorst, Eveline Rentmeester, J. Anton Grootegoed, Frank Grosveld, and Joost Gribnau. 2008. “Xist RNA Is Confined to the Nuclear Territory of the Silenced X Chromosome throughout the Cell Cycle.” *Molecular and Cellular Biology*. https://doi.org/10.1128/mcb.02269-07.

Jürges, Christopher, Lars Dölken, and Florian Erhard. 2018. “Dissecting Newly Transcribed and Old RNA Using GRAND-SLAM.” In *Bioinformatics*. https://doi.org/10.1093/bioinformatics/bty256.

Kay, Graham F., Graeme D. Penny, Dipika Patel, Alan Ashworth, Neil Brockdorff, and Sohaila Rastan. 1993. “Expression of Xist during Mouse Development Suggests a Role in the Initiation of X Chromosome Inactivation.” *Cell*. https://doi.org/10.1016/0092-8674(93)90658-D.

Ke, Shengdong, Endalkachew A. Alemu, Claudia Mertens, Emily Conn Gantman, John J. Fak, Aldo Mele, Bhagwattie Haripal, et al. 2015. “A Majority of M6A Residues Are in the Last Exons, Allowing the Potential for 3′ UTR Regulation.” *Genes and Development*. https://doi.org/10.1101/gad.269415.115.

Koh, Woo Seuk, Joshua R. Porter, and Eric Batchelor. 2019. “Tuning of MRNA Stability through Altering 3′-UTR Sequences Generates Distinct Output Expression in a Synthetic Circuit Driven by P53 Oscillations.” *Scientific Reports*. https://doi.org/10.1038/s41598-019-42509-y.

Kohlmaier, Alexander, Fabio Savarese, Monika Lachner, Joost Martens, Thomas Jenuwein, and Anton Wutz. 2004. “A Chromosomal Memory Triggered by Xist

Regulates Histone Methylation in X Inactivation." *PLoS Biology*. https://doi.org/10.1371/journal.pbio.0020171.

Kraus, Felix, Ezequiel Miron, Justin Demmerle, Tsotne Chitiashvili, Alexei Budco, Quentin Alle, Atsushi Matsuda, Heinrich Leonhardt, Lothar Schermelleh, and Yolanda Markaki. 2017. "Quantitative 3D Structured Illumination Microscopy of Nuclear Structures." *Nature Protocols*. https://doi.org/10.1038/nprot.2017.020.

Larson, Daniel R., Daniel Zenklusen, Bin Wu, Jeffrey A. Chao, and Robert H. Singer. 2011. "Real-Time Observation of Transcription Initiation and Elongation on an Endogenous Yeast Gene." *Science*. https://doi.org/10.1126/science.1202142.

Larsson, Chatarina, Ida Grundberg, Ola Söderberg, and Mats Nilsson. 2010. "In Situ Detection and Genotyping of Individual MRNA Molecules." *Nature Methods*. https://doi.org/10.1038/nmeth.1448.

Lee, J T, L S Davidow, and D Warshawsky. 1999. "Tsix, a Gene Antisense to Xist at the X-Inactivation Centre." *Nature Genetics* 21 (april): 400–404. https://doi.org/10.1038/7734.

Lee, Jeannie T., and Rudolf Jaenisch. 1997. "Long-Range Cis Effects of Ectopic X-Inactivation Centres on a Mouse Autosome." *Nature*. https://doi.org/10.1038/386275a0.

Lee, Jeannie T., William M. Strauss, Jessica A. Dausman, and Rudolf Jaenisch. 1996. "A 450 Kb Transgene Displays Properties of the Mammalian X-Inactivation Center." *Cell*. https://doi.org/10.1016/S0092-8674(00)80079-3.

Lee, Jeannie T, and Naifang Lu. 1999. "Targeted Mutagenesis of Tsix Leads to Nonrandom X Inactivation One X from Inactivation through a " Blocking Factor "

(Neg- Ative Factor). Finally, the Choice of Active and Inactive X May Involve Purposeful Selection of Each through Both." *Cell* 99: 47–57. https://doi.org/10.1016/S0092-8674(00)80061-6.

Li, Heng, Bob Handsaker, Alec Wysoker, Tim Fennell, Jue Ruan, Nils Homer, Gabor Marth, Goncalo Abecasis, and Richard Durbin. 2009. "The Sequence Alignment/Map Format and SAMtools." *Bioinformatics*. https://doi.org/10.1093/bioinformatics/btp352.

Lieberman-aiden, Erez, Nynke L Van Berkum, Louise Williams, Maxim Imakaev, Tobias Ragoczy, Agnes Telling, Ido Amit, et al. 2009. "Comprehensive Mapping of Long-Range Interactions Reveals Folding Principles of the Human Genome" 33292 (October): 289–94.

Liu, Jun, Xiaoyang Dou, Chuanyuan Chen, Chuan Chen, Chang Liu, Meng Michelle Xu, Siqi Zhao, et al. 2020. "N6-Methyladenosine of Chromosome-Associated Regulatory RNA Regulates Chromatin State and Transcription." *Science*. https://doi.org/10.1126/science.aay6018.

Loda, Agnese, Johannes H. Brandsma, Ivaylo Vassilev, Nicolas Servant, Friedemann Loos, Azadeh Amirnasr, Erik Splinter, et al. 2017. "Genetic and Epigenetic Features Direct Differential Efficiency of Xist-Mediated Silencing at X-Chromosomal and Autosomal Locations." *Nature Communications* 8 (1): 690. https://doi.org/10.1038/s41467-017-00528-1.

Loda, Agnese, and Edith Heard. 2019. "Xist RNA in Action: Past, Present, and Future." *PLoS Genetics*. https://doi.org/10.1371/journal.pgen.1008333.

Loos, Friedemann, Cheryl Maduro, Agnese Loda, Johannes Lehmann, Gert-Jan Kremers, Derk ten Berge, J. Anton Grootegoed, and Joost Gribnau. 2016. " Xist and Tsix Transcription Dynamics Is Regulated by the X-to-Autosome Ratio and Semistable

Transcriptional States .” *Molecular and Cellular Biology*. https://doi.org/10.1128/mcb.00183-16.

Los, Georgyi V., Lance P. Encell, Mark G. McDougall, Danette D. Hartzell, Natasha Karassina, Chad Zimprich, Monika G. Wood, et al. 2008. “HaloTag: A Novel Protein Labeling Technology for Cell Imaging and Protein Analysis.” *ACS Chemical Biology*. https://doi.org/10.1021/cb800025k.

Lowary, Peggy T., and Olke C. Uhlenbeck. 1987. “An RNA Mutation That Increases the Affinity of an RNA - Protein Interaction.” *Nucleic Acids Research*. https://doi.org/10.1093/nar/15.24.10483.

Lu, Zhipeng, Qiangfeng Cliff Zhang, Byron Lee, Ryan A. Flynn, Martin A. Smith, James T. Robinson, Chen Davidovich, et al. 2016. “RNA Duplex Map in Living Cells Reveals Higher-Order Transcriptome Structure.” *Cell*. https://doi.org/10.1016/j.cell.2016.04.028.

Luikenhuis, S, A Wutz, and R Jaenisch. 2001. “Antisense Transcription through the Xist Locus Mediates Tsix Function in Embryonic Stem Cells.” *Molecular and Cellular Biology* 21 (24): 8512–20. https://doi.org/10.1128/MCB.21.24.8512-8520.2001.

Lyon, Mary F. 1998. “X-Chromosome Inactivation: A Repeat Hypothesis.” *Cytogenetics and Cell Genetics*. https://doi.org/10.1159/000014969.

Lyon, Mary F. 1961. “Gene Action in the X-Chromosome of the Mouse (Mus Musculus L.).” *Nature* 189: 775–76.

Makhlouf, Mélanie, Jean-François Ouimette, Andrew Oldfield, Pablo Navarro, Damien Neuillet, and Claire Rougeulle. 2014. “A Prominent and Conserved Role for YY1 in Xist Transcriptional Activation.” *Nature Communications* 5: 4878.

https://doi.org/10.1038/ncomms5878.

Masui, Osamu, Edith Heard, and Haruhiko Koseki. 2018. “Live Imaging of Xist RNA.” In *Methods in Molecular Biology*. https://doi.org/10.1007/978-1-4939-8766-5_6.

Matsuda, Atsushi, Lothar Schermelleh, Yasuhiro Hirano, Tokuko Haraguchi, and Yasushi Hiraoka. 2018. “Accurate and Fiducial-Marker-Free Correction for Three-Dimensional Chromatic Shift in Biological Fluorescence Microscopy.” *Scientific Reports*. https://doi.org/10.1038/s41598-018-25922-7.

McHugh, Colleen A, Chun-Kan Chen, Amy Chow, Christine F Surka, Christina Tran, Patrick McDonel, Amy Pandya-Jones, et al. 2015. “The Xist LncRNA Interacts Directly with SHARP to Silence Transcription through HDAC3.” *Nature* 521 (7551): 232–36. https://doi.org/10.1038/nature14443.

Mermoud, Jaqueline E., Carl Costanzi, John R. Pehrson, and Neil Brockdorff. 1999. “Histone MacroH2A1.2 Relocates to the Inactive X Chromosome after Initiation and Propagation of X-Inactivation.” *Journal of Cell Biology*. https://doi.org/10.1083/jcb.147.7.1399.

Mitsui, Kaoru, Akira Matsumoto, Satoshi Ohtsuka, Motoaki Ohtsubo, and Akihiko Yoshimura. 1999. “Cloning and Characterization of a Novel P21(Cip1/Waf1)-Interacting Zinc Finger Protein, Ciz1.” *Biochemical and Biophysical Research Communications*. https://doi.org/10.1006/bbrc.1999.1516.

Moindrot, Benoit, Andrea Cerase, Heather Coker, Osamu Masui, Anne Grijzenhout, Greta Pintacuda, Lothar Schermelleh, Tatyana B. Nesterova, and Neil Brockdorff. 2015. “A Pooled ShRNA Screen Identifies Rbm15, Spen, and Wtap as Factors Required for Xist RNA-Mediated Silencing.” *Cell Reports* 12 (4): 562–72. https://doi.org/10.1016/j.celrep.2015.06.053.

Monfort, Asun, Giulio Di Minin, Andreas Postlmayr, Remo Freimann, Fabiana Arieti, St??phane Thore, and Anton Wutz. 2015. “Identification of Spen as a Crucial Factor for Xist Function through Forward Genetic Screening in Haploid Embryonic Stem Cells.” *Cell Reports* 12 (4): 554–61. https://doi.org/10.1016/j.celrep.2015.06.067.

Monkhorst, Kim, Iris Jonkers, Eveline Rentmeester, Frank Grosveld, and Joost Gribnau. 2008. “X Inactivation Counting and Choice Is a Stochastic Process: Evidence for Involvement of an X-Linked Activator.” *Cell* 132 (3): 410–21. https://doi.org/10.1016/j.cell.2007.12.036.

Nabet, Behnam, Justin M. Roberts, Dennis L. Buckley, Joshiawa Paulk, Shiva Dastjerdi, Annan Yang, Alan L. Leggett, et al. 2018. “The DTAG System for Immediate and Target-Specific Protein Degradation.” *Nature Chemical Biology*. https://doi.org/10.1038/s41589-018-0021-8.

Napoles, Mariana de, Jacqueline E. Mermoud, Rika Wakao, Y. Amy Tang, Mitusuhiro Endoh, Ruth Appanah, Tatyana B. Nesterova, et al. 2004. “Polycomb Group Proteins Ring1A/B Link Ubiquitylation of Histone H2A to Heritable Gene Silencing and X Inactivation.” *Developmental Cell* 7 (5): 663–76. https://doi.org/10.1016/j.devcel.2004.10.005.

Naughton, Catherine, Duncan Sproul, Charlotte Hamilton, and Nick Gilbert. 2010. “Analysis of Active and Inactive X Chromosome Architecture Reveals the Independent Organization of 30 Nm and Large-Scale Chromatin Structures.” *Molecular Cell*. https://doi.org/10.1016/j.molcel.2010.10.013.

Navarro, Pablo, Ian Chambers, Violetta Karwacki-Neisius, Corinne Chureau, Céline Morey, Claire Rougeulle, and Philip Avner. 2008. “Molecular Coupling of Xist Regulation and Pluripotency.” *Science (New York, N.Y.)* 321 (5896): 1693–95.

https://doi.org/10.1126/science.1160952.

Navarro, Pablo, Michael Moffat, Nicholas P. Mullin, and Ian Chambers. 2011. “The X-Inactivation Trans-Activator Rnf12 Is Negatively Regulated by Pluripotency Factors in Embryonic Stem Cells.” *Human Genetics*. https://doi.org/10.1007/s00439-011-0998-5.

Navarro, Pablo, Andrew Oldfield, Julie Legoupi, Nicola Festuccia, Agnã S. Dubois, Mikael Attia, Jon Schoorlemmer, Claire Rougeulle, Ian Chambers, and Philip Avner. 2010. “Molecular Coupling of Tsix Regulation and Pluripotency.” *Nature*. https://doi.org/10.1038/nature09496.

Nesterova, Tatyana B., Sergey Ya Slobodyanyuk, Eugene A. Elisaphenko, Alexander I. Shevchenko, Colette Johnston, Marina E. Pavlova, Igor B. Rogozin, Nikolay N. Kolesnikov, Neil Brockdorff, and Suren M. Zakian. 2001. “Characterization of the Genomic Xist Locus in Rodents Reveals Conservation of Overall Gene Structure and Tandem Repeats but Rapid Evolution of Unique Sequence.” *Genome Research*. https://doi.org/10.1101/gr.174901.

Nesterova, Tatyana B., Guifeng Wei, Heather Coker, Greta Pintacuda, Joseph S. Bowness, Tianyi Zhang, Mafalda Almeida, et al. 2019. “Systematic Allelic Analysis Defines the Interplay of Key Pathways in X Chromosome Inactivation.” *Nature Communications*. https://doi.org/10.1038/s41467-019-11171-3.

Ng, K., N. Daigle, A. Bancaud, T. Ohhata, P. Humphreys, R. Walker, J. Ellenberg, and A. Wutz. 2011. “A System for Imaging the Regulatory Noncoding Xist RNA in Living Mouse Embryonic Stem Cells.” *Molecular Biology of the Cell* 22 (14): 2634–45. https://doi.org/10.1091/mbc.E11-02-0146.

Nora, Elphège P., Anton Goloborodko, Anne Laure Valton, Johan H. Gibcus, Alec

Uebersohn, Nezar Abdennur, Job Dekker, Leonid A. Mirny, and Benoit G. Bruneau. 2017. “Targeted Degradation of CTCF Decouples Local Insulation of Chromosome Domains from Genomic Compartmentalization.” *Cell* 169 (5): 930-944.e22. https://doi.org/10.1016/j.cell.2017.05.004.

Nora, Elphège P., Bryan R. Lajoie, Edda G. Schulz, Luca Giorgetti, Ikuhiro Okamoto, Nicolas Servant, Tristan Piolot, et al. 2012. “Spatial Partitioning of the Regulatory Landscape of the X-Inactivation Centre.” *Nature*. https://doi.org/10.1038/nature11049.

Norris, Dominic P., Neil Brockdorff, and Sohaila Rastan. 1991. “Methylation Status of CpG-Rich Islands on Active and Inactive Mouse X Chromosomes.” *Mammalian Genome*. https://doi.org/10.1007/BF02443782.

Paige, Jeremy S., Karen Y. Wu, and Samie R. Jaffrey. 2011. “RNA Mimics of Green Fluorescent Protein.” *Science*. https://doi.org/10.1126/science.1207339.

Patil, Deepak P., Chun-Kan Chen, Brian F. Pickering, Amy Chow, Constanza Jackson, Mitchell Guttman, and Samie R. Jaffrey. 2016. “M6A RNA Methylation Promotes XIST-Mediated Transcriptional Repression.” *Nature* 537 (7620): 369–73. https://doi.org/10.1038/nature19342.

Pintacuda, Greta, Guifeng Wei, Chloe Roustan, Burcu Anil Kirmizitas, Nicolae Solcan, Andrea Cerase, Alfredo Castello, et al. 2017. “HnRNPK Recruits PCGF3 / 5-PRC1 to the Xist RNA B-Repeat to Establish Polycomb-Mediated Chromosomal Silencing.” *Molecular Cell* 68: 955–69. https://doi.org/10.1016/j.molcel.2017.11.013.

Plath, Kathrin, Jia Fang, Susanna K. Mlynarczyk-Evans, Ru Cao, Kathleen A. Worringer, Hengbin Wang, Cecile C. De la Cruz, Arie P. Otte, Barbara Panning, and Yi Zhang. 2003. “Role of Histone H3 Lysine 27 Methylation in X Inactivation.” *Science*.

https://doi.org/10.1126/science.1084274.

Popova, Bilyana C, Takashi Tada, Nobuo Takagi, Neil Brockdorff, and Tatyana B Nesterova. 2006. “Attenuated Spread of X-Inactivation in an X;Autosome Translocation.” *Proceedings of the National Academy of Sciences of the United States of America* 103 (20): 7706–11. https://doi.org/10.1073/pnas.0602021103.

Pullirsch, Dieter, Renate Härtel, Hiroyuki Kishimoto, Martin Leeb, Günter Steiner, and Anton Wutz. 2010. “The Trithorax Group Protein Ash2l and Saf-A Are Recruited to the Inactive X Chromosome at the Onset of Stable X Inactivation.” *Development*. https://doi.org/10.1242/dev.035956.

Rahman, Faisal A., Naveed Aziz, and Dawn Coverley. 2010. “Differential Detection of Alternatively Spliced Variants of Ciz1 in Normal and Cancer Cells Using a Custom Exon-Junction Microarray.” *BMC Cancer*. https://doi.org/10.1186/1471-2407-10-482.

Raj, Arjun, Patrick van den Bogaard, Scott A. Rifkin, Alexander van Oudenaarden, and Sanjay Tyagi. 2008. “Imaging Individual MRNA Molecules Using Multiple Singly Labeled Probes.” *Nature Methods*. https://doi.org/10.1038/nmeth.1253.

Rao, Suhas S.P., Su Chen Huang, Brian Glenn St Hilaire, Jesse M. Engreitz, Elizabeth M. Perez, Kyong Rim Kieffer-Kwon, Adrian L. Sanborn, et al. 2017. “Cohesin Loss Eliminates All Loop Domains.” *Cell*. https://doi.org/10.1016/j.cell.2017.09.026.

Rao, Suhas S.P., Miriam H. Huntley, Neva C. Durand, Elena K. Stamenova, Ivan D. Bochkov, James T. Robinson, Adrian L. Sanborn, et al. 2014. “A 3D Map of the Human Genome at Kilobase Resolution Reveals Principles of Chromatin Looping.” *Cell*. https://doi.org/10.1016/j.cell.2014.11.021.

Rastan, S. 1983. “Non-Random X-Chromosome Inactivation in Mouse X-Autosome

Translocation Embryos - Location of the Inactivation Centre." *Journal of Embryology and Experimental Morphology*.

Reynolds, Nicola, Mali Salmon-Divon, Heidi Dvinge, Antony Hynes-Allen, Gayan Balasooriya, Donna Leaford, Axel Behrens, Paul Bertone, and Brian Hendrich. 2012. "NuRD-Mediated Deacetylation of H3K27 Facilitates Recruitment of Polycomb Repressive Complex 2 to Direct Gene Repression." *EMBO Journal*. https://doi.org/10.1038/emboj.2011.431.

Ridings-Figueroa, Rebeca, Emma R. Stewart, Tatyana B. Nesterova, Heather Coker, Greta Pintacuda, Jonathan Godwin, Rose Wilson, et al. 2017. "The Nuclear Matrix Protein CIZ1 Facilitates Localization of Xist RNA to the Inactive X-Chromosome Territory." *Genes and Development* 31 (9): 876–88. https://doi.org/10.1101/gad.295907.117.

Rocha, Simão T da, and Edith Heard. 2017. "Novel Players in X Inactivation: Insights into Xist-Mediated Gene Silencing and Chromosome Conformation." *Nature Structural & Molecular Biology* 24 (3): 197–204. https://doi.org/10.1038/nsmb.3370.

Rocha, Simão Teixeira da, Valentina Boeva, Martin Escamilla-Del-Arenal, Katia Ancelin, Camille Granier, Neuza Reis Matias, Serena Sanulli, et al. 2014. "Jarid2 Is Implicated in the Initial Xist-Induced Targeting of PRC2 to the Inactive X Chromosome." *Molecular Cell*. https://doi.org/10.1016/j.molcel.2014.01.002.

Sado, T., E. Li, and H. Sasaki. 2002. "Effect of Tsix Disruption on Xist Expression in Male ES Cells." *Cytogenetic and Genome Research* 99 (1–4): 115–18. https://doi.org/10.1159/000071582.

Sado, Takashi, Yuko Hoki, and Hiroyuki Sasaki. 2005. "Tsix Silences Xist through Modification of Chromatin Structure." *Developmental Cell* 9 (1): 159–65.

https://doi.org/10.1016/j.devcel.2005.05.015.

Sarma, Kavitha, Pierre Levasseur, Alexander Aristarkhov, and Jeannie T. Lee. 2010. "Locked Nucleic Acids (LNAs) Reveal Sequence Requirements and Kinetics of Xist RNA Localization to the X Chromosome." *Proceedings of the National Academy of Sciences of the United States of America*. https://doi.org/10.1073/pnas.1009785107.

Schulz, Edda G., Johannes Meisig, Tomonori Nakamura, Ikuhiro Okamoto, Anja Sieber, Christel Picard, Maud Borensztein, Mitinori Saitou, Nils Blüthgen, and Edith Heard. 2014. "The Two Active X Chromosomes in Female ESCs Block Exit from the Pluripotent State by Modulating the ESC Signaling Network." *Cell Stem Cell*. https://doi.org/10.1016/j.stem.2013.11.022.

Schwarzer, Wibke, Nezar Abdennur, Anton Goloborodko, Aleksandra Pekowska, Geoffrey Fudenberg, Yann Loe-Mie, Nuno A. Fonseca, et al. 2017. "Two Independent Modes of Chromatin Organization Revealed by Cohesin Removal." *Nature*. https://doi.org/10.1038/nature24281.

Sheardown, Steven A., Sarah M. Duthie, Colette M. Johnston, Alistair E.T. Newall, Emma J. Formstone, Ruth M. Arkell, Tatyana B. Nesterova, Gian Carlo Alghisi, Sohaila Rastan, and Neil Brockdorff. 1997. "Stabilization of Xist RNA Mediates Initiation of X Chromosome Inactivation." *Cell*. https://doi.org/10.1016/S0092-8674(01)80012-X.

Silva, Jose, Winifred Mak, Ilona Zvetkova, Ruth Appanah, Tatyana B. Nesterova, Zoe Webster, Antoine H F M Peters, Thomas Jenuwein, Arie P. Otte, and Neil Brockdorff. 2003. "Establishment of Histone H3 Methylation on the Inactive X Chromosome Requires Transient Recruitment of Eed-Enx1 Polycomb Group Complexes." *Developmental Cell* 4 (4): 481–95. https://doi.org/10.1016/S1534-5807(03)00068-6.

Simon, Matthew D., Stefan F. Pinter, Rui Fang, Kavitha Sarma, Michael Rutenberg-

Schoenberg, Sarah K. Bowman, Barry A. Kesner, Verena K. Maier, Robert E. Kingston, and Jeannie T. Lee. 2013. “High-Resolution Xist Binding Maps Reveal Two-Step Spreading during X-Chromosome Inactivation.” *Nature* 504 (7480): 465–69. https://doi.org/10.1038/nature12719.

Singer, R. H., and D. C. Ward. 1982. “Actin Gene Expression Visualized in Chicken Muscle Tissue Culture by Using in Situ Hybridization with a Biotinated Nucleotide Analog.” *Proceedings of the National Academy of Sciences of the United States of America*. https://doi.org/10.1073/pnas.79.23.7331.

Smeets, Daniel, Yolanda Markaki, Volker J Schmid, Felix Kraus, Anna Tattermusch, Andrea Cerase, Michael Sterr, et al. 2014. “Three-Dimensional Super-Resolution Microscopy of the Inactive X Chromosome Territory Reveals a Collapse of Its Active Nuclear Compartment Harboring Distinct Xist RNA Foci.” *Epigenetics & Chromatin* 7 (1): 8. https://doi.org/10.1186/1756-8935-7-8.

Splinter, Erik, Elzo de Wit, Elphège P. Nora, Petra Klous, Harmen J.G. van de Werken, Yun Zhu, Lucas J.T. Kaaij, et al. 2011. “The Inactive X Chromosome Adopts a Unique Three-Dimensional Conformation That Is Dependent on Xist RNA.” *Genes and Development*. https://doi.org/10.1101/gad.633311.

Stavropoulos, Nicholas, Naifung Lu, and Jeannie T. Lee. 2001. “A Functional Role for Tsix Transcription in Blocking Xist RNA Accumulation but Not in X-Chromosome Choice.” *Proceedings of the National Academy of Sciences of the United States of America*. https://doi.org/10.1073/pnas.171243598.

Strack, Rita L., Matthew D. Disney, and Samie R. Jaffrey. 2013. “A Superfolding Spinach2 Reveals the Dynamic Nature of Trinucleotide Repeat-Containing RNA.” *Nature Methods*. https://doi.org/10.1038/nmeth.2701.

Sun, Bryan K., Aimée M. Deaton, and Jeannie T. Lee. 2006. “A Transient Heterochromatic State in Xist Preempts X Inactivation Choice without RNA Stabilization.” *Molecular Cell*. https://doi.org/10.1016/j.molcel.2006.01.028.

Sunwoo, Hongjae, David Colognori, John E. Froberg, Yesu Jeon, and Jeannie T. Lee. 2017. “Repeat E Anchors Xist RNA to the Inactive X Chromosomal Compartment through CDKN1A-Interacting Protein (CIZ1).” *Proceedings of the National Academy of Sciences* 114 (40): 10654–59. https://doi.org/10.1073/pnas.1711206114.

Sunwoo, Hongjae, John Y. Wu, and Jeannie T. Lee. 2015. “The Xist RNA-PRC2 Complex at 20-Nm Resolution Reveals a Low Xist Stoichiometry and Suggests a Hit-and-Run Mechanism in Mouse Cells.” *Proceedings of the National Academy of Sciences* 112 (31): E4216–25. https://doi.org/10.1073/pnas.1503690112.

Takagi, N., O. Sugawara, and M. Sasaki. 1982. “Regional and Temporal Changes in the Pattern of X-Chromosome Replication during the Early Post-Implantation Development of the Female Mouse.” *Chromosoma*. https://doi.org/10.1007/BF00294971.

Takagi, Nobuo, and Motomichi Sasaki. 1975. “Preferential Inactivation of the Paternally Derived X Chromosome in the Extraembryonic Membranes of the Mouse.” *Nature*. https://doi.org/10.1038/256640a0.

Tang, Y. Amy, Derek Huntley, Giovanni Montana, Andrea Cerase, Tatyana B. Nesterova, and Neil Brockdorff. 2010. “Efficiency of Xist-Mediated Silencing on Autosomes Is Linked to Chromosomal Domain Organisation.” *Epigenetics and Chromatin*. https://doi.org/10.1186/1756-8935-3-10.

Taniguchi, Yuichi, Paul J. Choi, Gene Wei Li, Huiyi Chen, Mohan Babu, Jeremy Hearn, Andrew Emili, and X. Sunney Xie. 2010. “Quantifying E. Coli Proteome and

Transcriptome with Single-Molecule Sensitivity in Single Cells." *Science*. https://doi.org/10.1126/science.1188308.

Teller, Kathrin, Doris Illner, Stefanie Thamm, Corella S. Casas-Delucchi, Rogier Versteeg, Mireille Indemans, Thomas Cremer, and Marion Cremer. 2011. "A Top-down Analysis of Xa- and Xi-Territories Reveals Differences of Higher Order Structure at ≥20 Mb Genomic Length Scales." *Nucleus*. https://doi.org/10.4161/nucl.2.5.17862.

Tian, Di, Sha Sun, and Jeannie T. Lee. 2010. "The Long Noncoding RNA, Jpx, Is a Molecular Switch for X Chromosome Inactivation." *Cell*. https://doi.org/10.1016/j.cell.2010.09.049.

Tuerk, Craig, and Larry Gold. 1990. "Systematic Evolution of Ligands by Exponential Enrichment: RNA Ligands to Bacteriophage T4 DNA Polymerase." *Science*. https://doi.org/10.1126/science.2200121.

Tyagi, Sanjay, and Fred Russell Kramer. 1996. "Molecular Beacons: Probes That Fluoresce Upon Hybridization." *Nature Biotechnology*. https://doi.org/10.1038/nbt0396-303.

Wang, Siyuan, Jun-han Su, Brian J Beliveau, Bogdan Bintu, Jeffrey R Moffitt, and Xiaowei Zhuang. 2016. "Spatial Organization of Chromatin Domains and Compartments in Single Chromosomes." *Science* 353 (6299): 598–602. https://doi.org/10.1126/science.aaf8084.Spatial.

Wang, Xiao, Zhike Lu, Adrian Gomez, Gary C. Hon, Yanan Yue, Dali Han, Ye Fu, et al. 2014. "N 6-Methyladenosine-Dependent Regulation of Messenger RNA Stability." *Nature*. https://doi.org/10.1038/nature12730.

Wang, Yang, Yue Li, Julia I. Toth, Matthew D. Petroski, Zhaolei Zhang, and Jing Crystal

Zhao. 2014. “N6 -Methyladenosine Modification Destabilizes Developmental Regulators in Embryonic Stem Cells.” *Nature Cell Biology*. https://doi.org/10.1038/ncb2902.

Wang, Yaolin, Bert W. O’Malley, Sophia Y. Tsai, and Bert W. O’Malley. 1994. “A Regulatory System for Use in Gene Transfer.” *Proceedings of the National Academy of Sciences of the United States of America*. https://doi.org/10.1073/pnas.91.17.8180.

Wutz, A, and R Jaenisch. 2000. “A Shift from Reversible to Irreversible X Inactivation Is Triggered during ES Cell Differentiation.” *Molecular Cell* 5 (4): 695–705. https://doi.org/10.1016/S1097-2765(00)80248-8.

Wutz, Anton, Theodore P. Rasmussen, and Rudolf Jaenisch. 2002. “Chromosomal Silencing and Localization Are Mediated by Different Domains of Xist RNA.” *Nature Genetics*. https://doi.org/10.1038/ng820.

Xiao, Jianfeng, Satya R. Vemula, Yi Xue, Mohammad M. Khan, Korah P. Kuruvilla, Esther M. Marquez-Lona, Madison R. Cobb, and Mark S. LeDoux. 2016. “Motor Phenotypes and Molecular Networks Associated with Germline Deficiency of Ciz1.” *Experimental Neurology*. https://doi.org/10.1016/j.expneurol.2016.05.006.

Yamada, Norishige, Yuko Hasegawa, Minghui Yue, Tomofumi Hamada, Shinichi Nakagawa, and Yuya Ogawa. 2015. “Xist Exon 7 Contributes to the Stable Localization of Xist RNA on the Inactive X-Chromosome.” *PLoS Genetics* 11 (8): 1–21. https://doi.org/10.1371/journal.pgen.1005430.

Yao, Yilong, Jun Ma, Yixue Xue, Ping Wang, Zhen Li, Jing Liu, Liangyu Chen, et al. 2015. “Knockdown of Long Non-Coding RNA XIST Exerts Tumor-Suppressive Functions in Human Glioblastoma Stem Cells by up-Regulating MiR-152.” *Cancer Letters*.

https://doi.org/10.1016/j.canlet.2014.12.051.

Żylicz, Jan Jakub, Aurélie Bousard, Kristina Žumer, Francois Dossin, Eusra Mohammad, Simão Teixeira da Rocha, Björn Schwalb, et al. 2019. “The Implication of Early Chromatin Changes in X Chromosome Inactivation.” *Cell*. https://doi.org/10.1016/j.cell.2018.11.041.